University of South Carolina
Scholar Commons

Theses and Dissertations

Spring 2019

Development of Scalable and Tunable Super-Hydrophilic and - Hydrophobic Coatings on the CU Substrate for Phase Change Heat Transfer Applications

Raikan Saad Dawas

Follow this and additional works at: https://scholarcommons.sc.edu/etd

Part of the Mechanical Engineering Commons

DEVELOPMENT OF SCALABLE AND TUNABLE SUPER-HYDROPHILIC AND - HYDROPHOBIC COATINGS ON THE CU SUBSTRATE FOR PHASE CHANGE HEAT TRANSFER APPLICATIONS

by

Raikan Saad Dawas

Bachelor of Science
University of Baghdad, 1998

Master of Science
University of Baghdad, 2001

Submitted in Partial Fulfillment of the Requirements

For the Degree of Doctor of Philosophy in

Mechanical Engineering

College of Engineering and Computing

University of South Carolina

2019

Accepted by:

Chen Li, Major Professor

Jamil Khan, Committee Member

Tanvir Farouk, Committee Member

Guiren Wang, Committee Member

Jasim Imran, Committee Member

Cheryl L. Addy, Vice Provost and Dean of the Graduate School

DEDICATION

I would like to dedicate this work to my parents, my wife, my children Rawan, Zainab, Hussein, Hawraa, Aaya and Muhammad as well as to my brothers and sisters especially to my brother; Khalid my God has mercy on him. Also, I will not forget all my sincere friends and relatives.

ACKNOWLEDGEMENTS

I would also like to thank all my labmates at the Micro/Nanoscale Transport Lab, Mehdi Famouri, Benli Peng, Mohammad Alwazzan, Ahmad Abdulshaheed, Tamanna Alam, Wenming Li, Mostafa Mobli, Wei Chang, GuanHan Huang, Yueyang Zhao, Congcong Ren, and Jiaxuan Ma as well as special thanks to all the Iraqi students at the University of South Carolina for their continuous support, encouragements, and advice.

I would like to express my deepest thank to my family, my parents, my wife, my brothers, my sisters and my children, Rawan, Zainab, Hussein, Hawraa, Aaya, and Muhammad who unconditionally supported me with their worm love. I would also like to thank all my friends and relatives for their support and encouragements.

ABSTRACT

The aim of this study is to enhance and sustain the thin liquid film evaporation (TLFE) as well as dropwise condensation (DWC) on scalable copper substrates. The current dissertation consists of two sections. The objective of the first section is to enhance the dry cooling technology which is widely used in industrial applications such as in the air side of power plants, AC unit, or electronic cooling. However, the thermal dissipation performance is limited with low heat transfer coefficients (HTCs) due to the low thermal conductivity and density of the air. Inspired by the phase change heat transfer during the perspiration of mammals, a sweating-boosted air cooling strategy was proposed to improve the thermal dissipation during the dry cooling process. In our previous research, we have demonstrated the effectiveness of a nanoscale ALD TiO_2 and CuO wick structures with grooves on copper on the sweating-boosted air cooling performance. The results showed that this technique could effectively enhance the heat transfer rates much higher than the dry cooling. However, for practical applications, developing practical heating surfaces with high wettability and for the long-term use against organic contamination is a critical issue. Therefore, it is crucial to develop robust superhydrophilic surfaces with excellent mechanical and chemical stability for long-term operations.

In this study, durable superhydrophilic green patina microstructures were successfully fabricated over large surfaces on the copper substrate by a two-step chemical oxidization process. Scanning electron microscopy (SEM), Energy dispersive

vi

spectroscopy (EDS), X-ray photoelectron spectroscopy (XPS), and Nanoindentation tests were employed to analyze the morphology, the surface chemical compositions, and the mechanical properties of these green patina microstructures, respectively. The effect of the green patina thickness on the mechanical properties, liquid spreading, and the capillary rise was investigated. The results showed the high wettability of the green patina surface, and the highest capillary rise was achieved with the thinner green patina thickness. Additionally, Experiments were conducted in a wind tunnel system to evaluate the convective and evaporative heat transfer enhancement using different green patina surfaces at various air flow velocity, water dripping rate, and thermal loads. The optimized heat transfer coefficients were achieved at the saturated wetting condition, where the thin liquid film covers the whole heat transfer surface. As a summary of the results obtained by this research, the superhydrophilic green patina surfaces showed the high durability and reliability after testing each sample more than one month, which demonstrates that the green patina surface can be implemented for long-term operation with high performance in phase change heat transfer applications. In this study, we have demonstrated 614.17 % enhancement of HTC, which is about 6 times higher than that of the dry cooling process. Therefore, an enormous benefit in environment and energy efficiency of air cooling can be increased an order of magnitude due to the current research

The objective of the second section of this dissertation is to enhance dropwise condensation (DWC) on scalable copper substrates. In the past several decades, DWC on metal and metal oxides surfaces had aroused significant attention due to 10 folds higher heat transfer rate than that of filmwise condensation (FWC). Recently, numerous effects

have been made to enhance DWC by fabricating superhydrophobic surfaces due to their chemical stability and high droplet mobility. However, the application of these surfaces for long-term operations has been hindered due to the highly pinned condensate droplets into the micro/nanostructures, which could turn the mobile Cassie state to Wenzel state and then shifting the condensation from DWC to unfavorable FWC.

In this study, to systematically understand hydrophobic porous coatings in promoting DWC, a series of studies have been carried out to examine effects of key parameters such as coating thickness, pore size, surface chemistry, and additional thermal resistance from coatings. The study consists of three parts. **In part (I)**, thickness effects and role of oxygen of the superhydrophobic coatings on DWC has been investigated. Two types of coatings, i.e., microstructured green patina ($Cu_4SO_4(OH)_6$) and nanostructured copper oxide (CuO) have been employed. Experimental results clearly showed that the coating thickness of the superhydrophobic patina plays a critical role in determining the condensation heat transfer rate. When coating thickness exceeds 1.0 $\boldsymbol{\mu}$m, the condensation rate would greatly decrease. At the low and high subcooling degrees, the condensation heat transfer rate was downgraded below FWC by 12.08-29.6 % with patina coating thicknesses of about 50.0 $\boldsymbol{\mu}$m. However, the performance was enhanced by 40.1-87.1 % on the patina surface with a coating thickness less than or about 1.0 $\boldsymbol{\mu}$m. **In part (II)**, sub-microscale thick (300 nm-1.6 μm) cuprite (Cu_2O) coatings were developed to further promote DWC owing to small thickness and nanoscale pore size. The maximum improvement in terms of heat flux on the fresh samples of the cuprite surface is 212.04% compared to FWC, but still lower than complete DWC on smooth copper surfaces. The cuprite coating with the sub microscale porous structures and nanoscale

viii

pores size can generate high capillary pressure and hence prevents the droplets from sucking into pores In addition, further oxidization of cuprite surface in the hydrogen peroxide solution could greatly improve the chemical stability of the surface. **In part (III)**, in order to maximize DWC performance, the cuprite coatings were completely removed to eliminate the additional thermal resistance from coatings. The cuprite coatings were removed ultrasonically by acid, acetone, and ethanol, and then washed with distilled water to form a yellow rough copper surface. As a result, a novel superhydrophobic copper surface has been created with microscale porous and microgrooves structures. Compared to FWC, DWC heat transfer rate was enhanced 332.8 %, on the superhydrophobic copper surface. Furthermore, the enhancements in terms of heat flux and the heat transfer coefficient (HTC) compared to the plain hydrophobic surface were about 12.65 % and 13.43 %, respectively. The maximum heat flux and HTC were about 797.05 KW/m^2 and 76.72 KW/m$^2 \cdot$K, respectively, at a subcooling degree of 10.6 ℃.

In this study, the effects of key parameters of porous coatings on DWC have been systematically and successfully characterized. This systematical study eventually leads to the development of an innovative superhydrophobic surface with microscale porous and microgrooves structures, which outperforms completely DWC on smooth hydrophobic copper surfaces. It is because of two primary reasons: first, the additional thermal resistance of coatings has been removed; the other one is that the porous structures with microgrooves can also generate high capillary pressure and prevent droplets from penetration into the cavities of the structures.

TABLE OF CONTENTS

xi

LIST OF TABLES

xiii

LIST OF FIGURES

xxiii

xxvi

PART I: EVAPORATION

CHAPTER 1

INTRODUCTION

1.1 Background

Dry cooling technology is widely used in industrial applications such as in the air side of power plants, AC unit, or electronic cooling. However, its thermal dissipation performance is limited with low heat transfer coefficients (HTCs) due to the low thermal conductivity and density of the air. Inspired by the phase change heat transfer during the perspiration of mammals, a sweating-boosted air cooling strategy could be implemented to improve the thermal dissipation during the dry cooling process. One important example of applying this technique is for the power plants condensers. In thermal power plants, the condenser plays a significant role to define the overall thermal efficiency. For optimal performance, it is required to efficiently cool the low-pressure steam in the condenser. However, a huge amount of freshwater is withdrawn and consumed for the cooling purpose. In the US, approximately 143,000 million gallons per day was accounted in 2005 [1, 2]. To enable green economy, the US federal government pursuits for reducing the annual water usage by 2% by developing advanced cooling technologies with less or no water consumption [3]. One alternative way is to replace the water cooled condenser (WCC) with an air cooled condenser (ACC), which can drastically reduce water usage, but has up to 10% power generation penalty [4]. Additionally, the performance of the air-cooled condensers is limited with a lower heat transfer coefficient (HTC) (typically ~20–50 W/m^2·K) due to the low thermal conductivity and density of the

2

air compared to water used in WCCs. Consequently, large surface areas are required, which lead to a large footprint and costly air cooled condenser (about 3–5 times that of water cooled condenser [4]). However, the efficient phase change heat transfer can hold a promise to address this challenge. Inspired by the phase change during the perspiration process of mammals, a sweating-boosted air cooling strategy can be proposed to augment HTC in the air-cooled condenser (ACC), and significantly decrease the water consumption. The mechanism of the sweating-boosted air cooling approach is the convective water evaporation promoted by a forced air flow as illustrated in Figure 1.1 [5]. When a droplet of water is dripped on a superhydrophilic heated surface, it spreads laterally and forms a thin liquid film. Then the water evaporates into vapor which is carried away by the air flow.
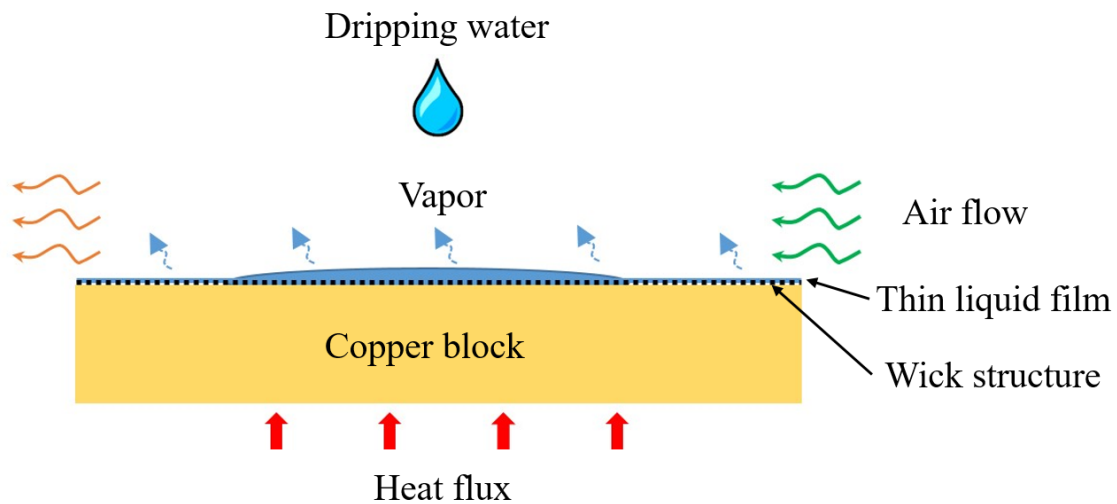
Figure 1.1 Schematic of the sweating-boosted air cooling strategy [5].

It was well-verified that the thin film evaporation on the heated surface is the key feature to enhance the heat dissipation for evaporative cooling processes [6]. The transport of latent heat associated with the convective mass and heat transfer in liquid film evaporation can dramatically augment the convective heat transfer. Yan et al. [7]

3

numerically investigated the effect of the liquid film evaporation on laminar mixed convection heat and mass transfer enhancement. They found that the magnitude of evaporative latent heat flux was five times greater than that of sensible heat flux. In inclined square ducts, Jiang et al. [8] studied the mixed convective heat transfer enhanced by liquid film evaporation and reported that the heat transfer rate due to the latent heat transport associated with film evaporation is higher and could be magnified to be ten times of that without mass transfer. Saha et al.[9] studied numerically the effect of the liquid film thickness under a laminar flow condition on the sweating boosted air cooling performance. They demonstrated that the overall HTC increases with increasing the Reynolds number and decreasing the liquid film thickness. They found that the enhancement in the overall HTC has increased by a factor of five in comparison to the pure forced convection process. The maximum enhancement was about 332 W/m2K and achieved at the Reynolds number of 97,974 and 50 μm liquid film thickness. Additionally, extensive experimental and numerical studies have been implemented to examine the factors that can affect the evaporation rates. These factors include (a) flow conditions: natural [10], laminar [11], and turbulent convection [12]; (b) geometries, such as vertical channel [13], inclined planes [8], and tube bundles [14]; (c) coolants, such as water, R134a [15], and ammonia-water mixtures [16]; and (d) ambient conditions, such as air velocity, ambient temperature and air relative humidity [17].

Even though the liquid film evaporation has extensively been investigated experimentally, theoretically, and numerically, major inconsistencies were remarked between these results due to the challenge in achieving a homogeneous liquid film [18]. The liquid film was experimentally accomplished by sliding the liquid over vertical or

4

inclined plates using gravitational force; while it was theoretically and/or numerically employed as a boundary condition with an assumption of zero thickness [19]. Recent studies by Yan [7] and Debbissi et al. [20] reported that this assumption can be valid only for low mass flow rate of liquid film, but for higher values the assumption becomes inappropriate. However, this challenge can be partially treated by changing the surface morphology of the heated surface with micro- and/or nano- sized features, such as nanowires [21], thin capillary wicks [22, 23], micropillar arrays [24, 25], and sintered porous media [26]. Another approach is modifying the surface chemistry by fabricating a thin film coating with high surface energy, such as Silica [27, 28], TiO_2 [29], and CuO [30]. In our previous studies, Wang et al. [5, 31] prepared a nanoscale ALD TiO_2 and CuO wick structures with grooves on copper substrates to examine the effect of the superhydrophilic surfaces on the sweating-boosted air cooling. The results showed that this technique can effectively enhance the heat transfer rates by 182.6% and drastically reduce the water consumption of ACC. However, due to surface heating and organic contamination, those fabricated surfaces are not durable and reliable for long term operation.

1.2 Overview of the superhydrophilic coatings fabrication

In both academic research and practical use, super wetting surfaces have aroused lots of attention over the past decade because of their unique functions and potential applications. Superhydrophilic surfaces, which are described with a water contact angle less than 5°, allow ultrafast drying and complete water spreading [32]. Therefore, they have been used for several industrial applications such as anti-fogging surfaces [33, 34], enhancing heat transfer applications [5, 35, 36], bio-fouling devices [37, 38],

5

biomolecular immobilization [39, 40], and drag reduction [41]. There are several fundamental techniques for the superhydrophilic surface fabrication based on the phenomena of the surface wettability, which is governed by the chemical composition and surface structure roughness [42]. Fujishima et al. [43] discussed the photo-induced hydrophilic (PIH) effect to fabricate TiO_2 surface which changes from hydrophilic to superhydrophilic after irradiating by Ultraviolet (UV) light. However, this surface can lose its superhydrophilicity gradually if it is stored in dark place. The same PIH mechanism has been recognized for TiO_2, ZnO and WO_3 surfaces [44-46]. Additionally, there are different ways to fabricate the superhydrophilic surfaces such as Sol-gel method [47], Layer-by-Layer (LbL) assembly [48], Plasma vapor deposition process [49], Electrospinning method [50, 51], Electrochemical method [52], Chemical and hydrothermal methods [53, 54].

1.2.1 Fabricating superhydrophilic coatings on copper substrates

Copper is a basic material for industrial applications due to its superior mechanical and electrical properties and low cost. Therefore, the fabrication of superhydrophilic copper surfaces has attracted lots of attention because of their special functions and wide applications. To synthesize superhydrophilic micro- and nanostructures on copper substrates, the convenient way is to change its surface energy and morphology via thermal or chemical oxidization methods. Youngsuk et al. [30] reported the fabrication of controlled wettability of micro/nanostructure of Cu_2O and CuO surfaces using different chemical and thermal oxidization methods. They showed that CuO nanostructure surface could improve the capillary and heat transfer performance. As a result, it can be used significantly for phase change heat transfer applications. For

6

efficient separation of oil and water process, Zhang et al. [55] presented the preparation of superhydrophilic of $Cu(OH)_2$ membranes with nanowire-haired structure via chemical oxidization. Tang et al. [53] reported the fabrication of superhydrophilic Cu_2O and CuO membranes with a contact angle less than 1 ° via the reduction or calcination of the parent $Cu(OH)_2$ membranes, which are affected by the reaction conditions. Additionally, with various morphology, the fabrication of cupric oxide nanostructures using chemical oxidization methods has been presented, such as nanobelts [56], 3D flower-like network [57], sharp needle-like nanowires [58, 59], and nano-rods and ribbons [53, 60, 61].

Although superhydrophilic surfaces show high surface energy and a certain degree of self-cleaning properties, those surfaces can easily be contaminated if they employed in a harsh environment [32]. Therefore, for industrial applications, it is crucial to develop robust and durable superhydrophilic surfaces with excellent mechanical and chemical stability for long-term operations. Moreover, because of the complicated process, expensive equipment, and low interfacial strength, it is necessary to develop new economic technology for fabricating large -scale superhydrophilic surfaces with stable properties. Additionally, although recent studies exhibited the advantages of the superhydrophilic surfaces with high wettability for the high performance of capillary and heat transfer rates, the developing of practical heating surfaces with high wettability is still a big challenge and that hindered their applications in industrial applications [30].

Inspired by nature, after exposing the copper surface to a moist atmosphere or marine environmental for long periods, the surface is covered with a green corrosion called patina as found on the Statue of Liberty [62]. It consists of an inner layer of cuprite (Cu_2O) and an outer layer of brochantite ($Cu_4SO_4(OH)_6$) [63, 64], which plays a

7

significant role in protecting the copper metal from further corrosion [65-68]. Since the development of the patina on copper surface is a natural process and takes years, many techniques have been developed to accelerate the fabrication intentionally via cold or hot chemical oxidization methods [66, 69-75]. However, most of the patina coatings prepared previously have non-uniform of brochantite structures and poor adhesion on the copper substrate, resulting in concerns in potential applications. Recently, Cho et al. [76] reported a new method for producing a uniform and robust superhydrophilic and superhydrophobic green patina surfaces on copper substrates. The chemical process involves two-step oxidization to develop first a cuprous oxide as a base oxide on copper substrate and then the brochantite surface. The as-prepared surfaces exhibited superior corrosion resistance and mechanical durability and could be applied for separation of oil and water efficiently.

1.3 The objective of this study

Even though the patina coating was fabricated before many years artificially, it has not been utilized for heat transfer applications. In the present study, durable superhydrophilc green patina coatings on copper substrates have been developed based on the recipe presented by Ref. [76] with some modifications. The effect of the green patina thickness on the mechanical properties, liquid spreading, capillary rise, and heat transfer applications has been systematically investigated. The change of the patina thickness has been carried out by modifying the temperature and the concentration of the chemical reaction. The mechanical properties of the different coatings have been tested by measuring the surface hardness and the modulus of the coatings using Nanoindentation tests. Furthermore, to characterize the morphology, and the surface

8

chemical compositions of the green patina microstructures on the copper substrate, Scanning electron microscopy (SEM), Energy dispersive spectroscopy (EDS) and X-ray photoelectron spectroscopy (XPS) tests were achieved. Additionally, the effect of the different green patina coatings on the heat dissipation performance of the sweating-boosted air cooling is experimentally studied under various dripping rates, thermal loads, air velocities and patina thicknesses.

9

CHAPTER 2

EXPERIMENTAL ENVESTIGATION

2.1 Fabrication of the green patina surface

To enhance the heat dissipation during the sweating boosted air cooling, a superhydrophilic surface is required to efficiently induce liquid spreading and form a thin liquid film over the heat transfer surface. For this purpose, a superhydrophilc green patina surface with high surface energy and durability is fabricated. As shown in Figure 2.1, the copper sample (purity 99.9%) with dimensions of 50 mm $\times$ 50 mm $\times$ 3 mm was first polished by 500 and 1000 silicon carbide papers. Then the sample was dipped in 10 wt. % of sulfuric acid solution and ultrasonically cleaned for 10 min to remove the native oxides on the surface. After that, it was ultrasonically cleaned in acetone, ethanol and distilled water for 10 min. respectively. After finishing the cleaning process, the prepared sample was first immersed in a 0.04 M $KClO_3$ solution at 60 ℃ for 12 h to be oxidized and form a reddish film of Cuprite (Cu_2O) on the copper substrate based on the following reaction [76, 77];

$$6Cu + ClO3^- \rightarrow 3Cu_2O + Cl^- \tag{2.1}$$

The pH of the solution was adjusted to a value of 3, which is measured by PH meter (PHH222, OMEGA), by adding drops of Sulfuric acid (10 % wt) to the solution. Second, after completing the first reaction to prepare the cuprite film, 0.1 M copper sulfate pentahydrate $(CuSO_4.5H_2O$) was added to the solution with stirring at 60 rpm. Then after

60 hrs, the as-prepared cuprite was transformed to establish greenish crystalline structures of brochantite ($Cu_4SO_4(OH)_6$) on the surface based on the following reaction [78];

$$2Cu_2O + SO_4{}^{2-} + 4H_2O \rightarrow Cu_4SO_4(OH)_6 + 2H^+ + 4e^- \qquad (2.2)$$
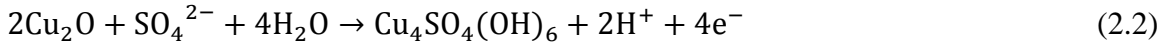
Finally, the as-prepared coating was removed, rinsed with distilled water and heated on a hot plate repeatedly at 60 °C for 5 minutes for two or three times.

Table 2.1 : The different recipes for green patina coating preparation.

Sample	First Reaction	Second Reaction
A	0.02 M $KClO_3$, 60 °C, pH =3, 12 hours	0.1 M $CuSO_4.5H_2O$, 60 °C, Stirring at 60 rpm, 60 hours
B1	0.04 M $KClO_3$, 60 °C, pH =3, 12 hours	0.1 M $CuSO_4.5H_2O$, 60 °C, Stirring at 60 rpm, 60 hours
B2	0.04 M $KClO_3$, 60 °C, pH =3, 12 hours	0.1 M $CuSO_4.5H_2O$, 40 °C, Stirring at 60 rpm, 60 hours
B3	0.04 M $KClO_3$, 60 °C, pH =3, 12 hours	0.1 M $CuSO_4.5H_2O$, 25 °C, Stirring at 60 rpm, 60 hours

2.2 Characterization of the green patina surface

The surface morphology of the as-prepared green patina surface was characterized by a field-emission scanning electron microscopy (SEM, TESCAN Vega-3 SBU, USA). The thickness of the coating was measured from the SEM image of the cross-sectional area. The chemical compositions of the patina substrate were also analyzed using X-ray photoelectron spectroscopy (AXIS Ultra DLD XPS, Kratos Analytical Ltd., U.K) and energy dispersive spectroscopy (EDS), which is performed with the same field-emission scanning electron microscope. The mechanical properties of the as-prepared coating were evaluated using a Nanoindentation test by measuring the modulus and surface hardness.

11

A high-speed camera (Micro-EX4, Phantom) operating at 100 frames per seconds was used to analyze the liquid spreading and the capillary rise on different patina coatings.
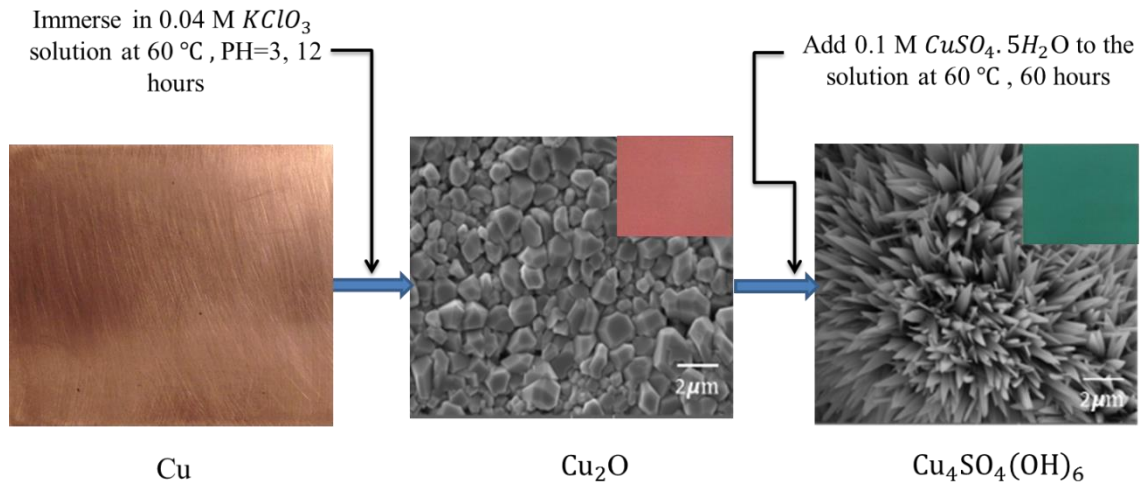
Figure 2.1:Illustration of the fabrication process of the green patina surface on the copper substrate, and the SEM images of the cubic microstructures of cuprite and the dandelion-like microstructures of brochantite at a length scale of 2 μm.
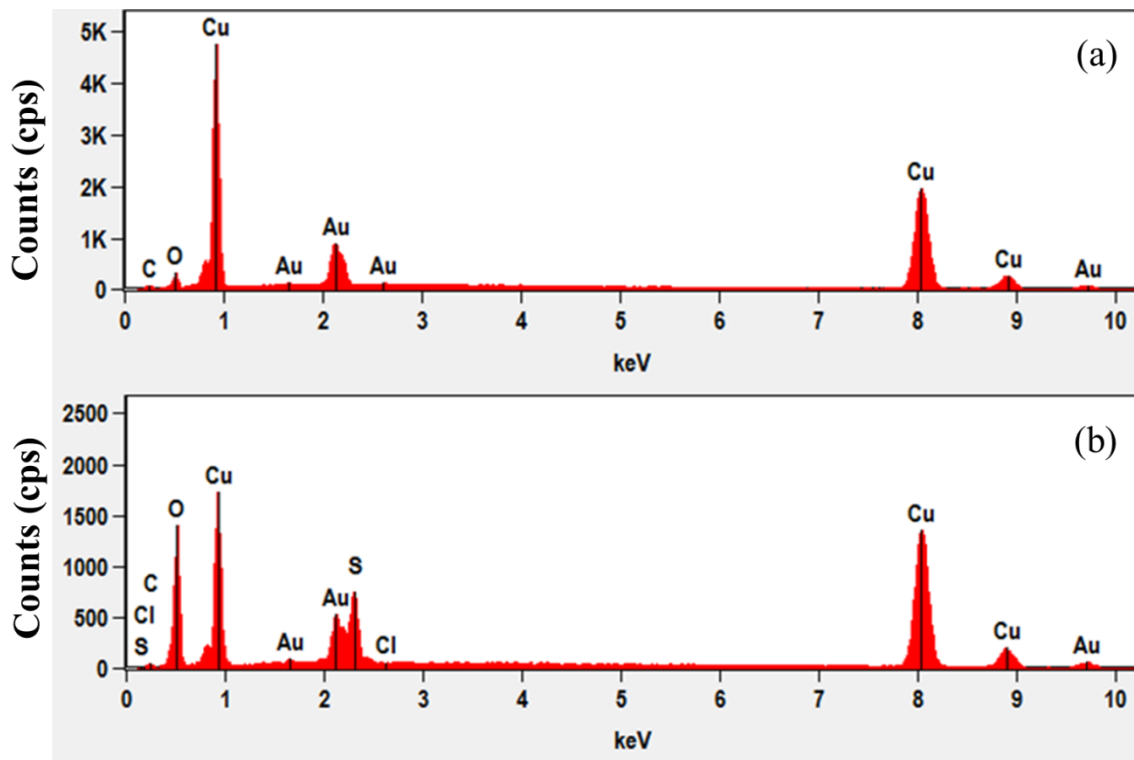
Figure 2. 2: EDS spectrum of the (a) Cu_2O , and (b) brochantite surfaces on the copper substrate

12
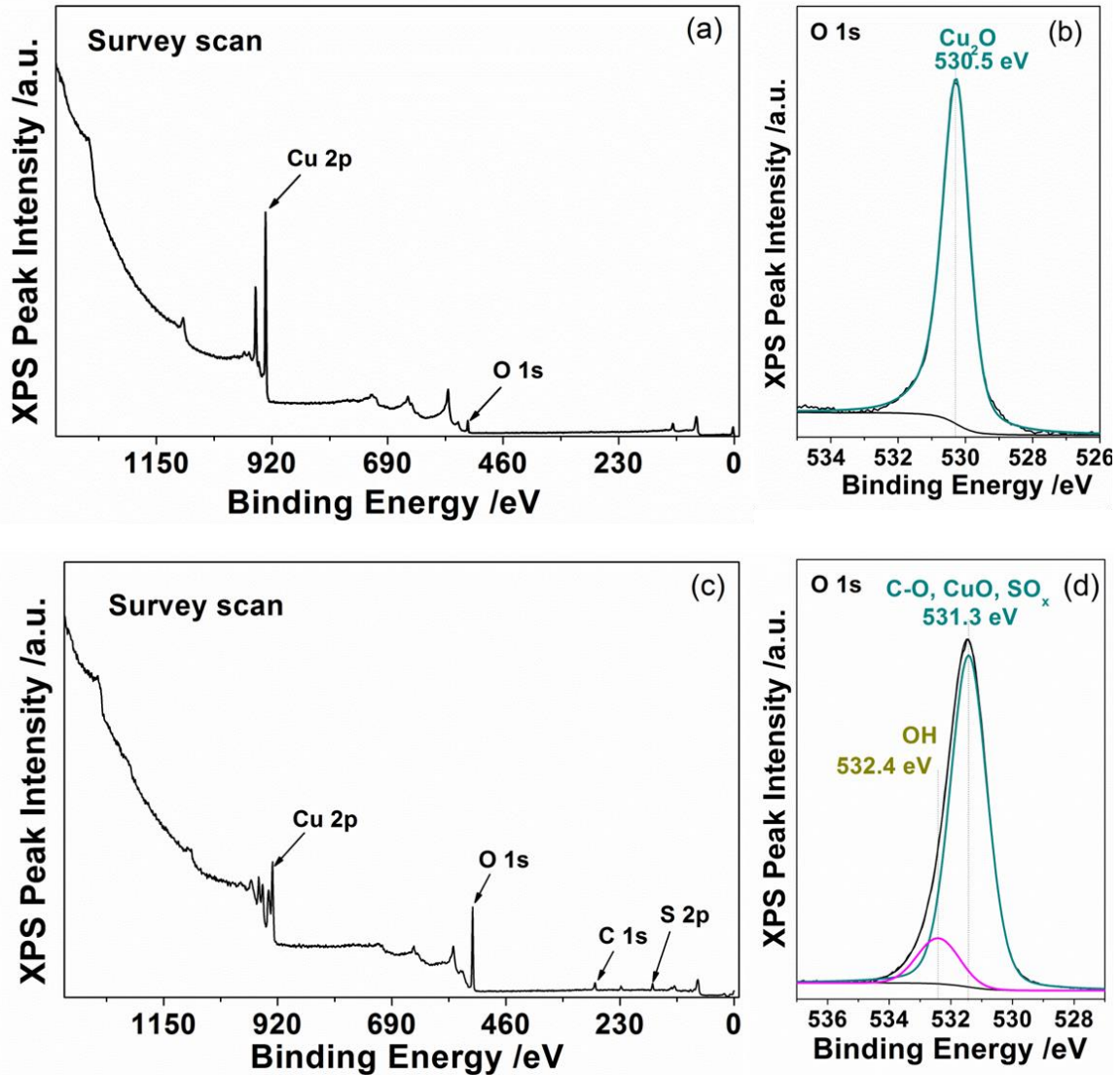
Figure 2.3:(a) the XPS survey scan of the as prepared Cuprite after Argon sputter cleaning, (b) O (1s) XPS spectra of cuprite surface, (c) the XPS survey scan of the as prepared brochantite surface, and (d) O (1s) XPS spectra of the brochantite surface.

2.2.1 The morphology and surface chemistry of green patina coating

The surface morphology of the as-prepared green patina surface is characterized by a field-emission scanning electron microscopy (SEM, TESCAN Vega-3 SBU, USA). As shown in Figure 2.1, the scanning electron microscope (SEM) images taking at a scale length of 2 µm and 10 KV SEM HV reveals that a reddish film of Cuprite (Cu_2O) with cubic microstructures is formed on the copper substrate after 12 hours in the first-step

13

reaction. The SEM image also exhibits large and small crystal cubic grains in micron and submicron meters on the as-prepared cuprite surface (300 nm-1.6 μm). Additionally, after 60 hours from adding copper (II) sulfate pentahydrate ($CuSO_4.5H_2O$) in the solution, the surface was completely coated with greenish three dimensional (3D) crystalline dandelion-like (flower-like) microstructures of brochantite ($Cu_4SO_4(OH)_6$) with dimensions between 10 µm and 20 µm.

The chemical compositions of the patina substrate are analyzed using X-ray photoelectron spectroscopy (AXIS Ultra DLD XPS, Kratos Analytical Ltd., U.K), and energy dispersive spectroscopy (EDS). As shown in Figure 2. **2**, the (EDS) spectrum results reported at 20 KV show that the as-prepared cuprite surface is mainly composed of Cu and O elements. While the EDS spectrum result for the brochantite surface reveals that the surface consists of Cu, O, and S elements. Additionally, As shown in Figure 2.3(a), the (XPS) survey scan analysis of the cuprite surface reveals Cu (2p) peak at 932.3 eV, O (1s) peak at 530.5 eV, and there is no carbon contamination detected on the cuprite surface after the Argon sputtering process. Moreover, as shown in Figure 2.3(b), O (1s) XPS spectra of the cuprite surface exhibits that after the Argon sputtering only one chemical state of oxygen on the surface at 530.5eV was observed, which is attributed to the Cu_2O compound of the surface. Furthermore, the XPS analysis of the brochantite surface as shown in Figure 2.3(c) reveals Cu (2p) peak at 934.3eV, O (1s) peak at 530.9eV, C (1s) peak at 284.6 eV and S (2p) peak at 168.2 eV. The S (2p) peak indicates to the amount of oxidized sulfur created on the surface, and provides evidence to the presence of brochantite components on the surface. Also, for the O (1s) XPS spectra of the brochantite surface, Figure 2.3(d) shows the formation of the copper oxide, sulfur

14

oxide and a small value of carbon contamination on the surface. It is clear that according to the (EDS) and (XPS) characterization, a carbon contamination was formed on the oxide layer of the cuprite and brochantite due to the environmental or the vacuum chambers contamination. The other ratio of the gold originated on the surfaces was due to the layer coated using sputter cleaning to perform high resolution of SEM images.

Figure 2.4: Effect of the 5 minutes ultrasonic cleaning on the adhesion strength for the green patina samples A and B1.

2.2.2 The thickness of green patina coating

As shown in **Table 2.1**, the green patina coatings were fabricated in different recipes by changing the concentration of Potassium Chlorate concentration ($KClO_3$) in the solution and the temperature of the second reaction to form the brochantite. Sample A was prepared with the same recipe presented by Ref. [76], while Sample B1 was developed after doubling the concentration of $KClO_3$ from 0.02 to 0.04 M. As shown in Figure 2.4, the two samples A and B1 were ultrasonically cleaned for 5 min. The brochantite coating was removed from sample A showing the reddish cuprite film; while

Sample B1 exhibits that the Cuprite was transformed to create the brochantite coating with high adhesion strength after touching and scratching the surface by hand. Also, since the green patina was produced in a cold chemical process which takes about three weeks or a hot process with a shorter time [79], we observed that reducing the temperature of the second reaction can decrease the brochantite thickness. Therefore, samples B2 and B3 were developed with changing the temperature of the solution from 60 ℃ to 40 and 25 ℃ respectively.
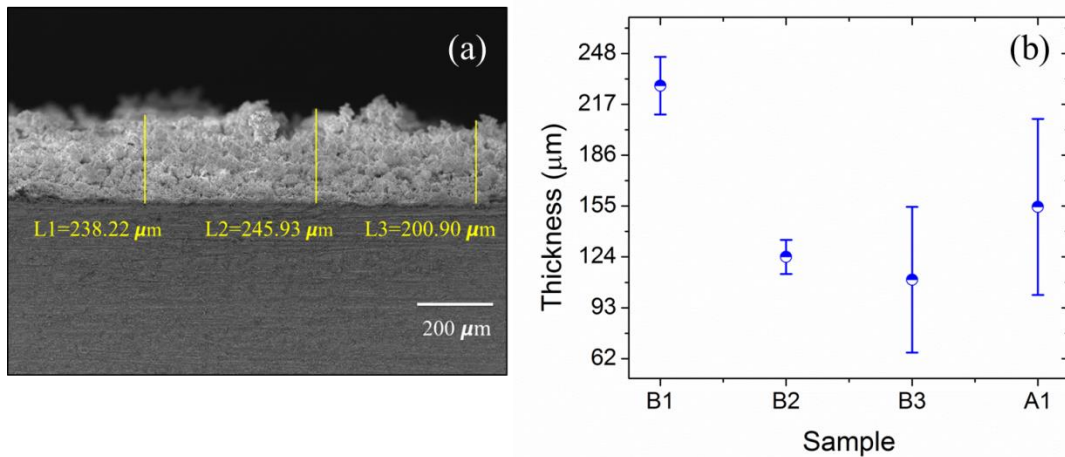
Figure 2.5: (a) The SEM image to the side view of the cross section of the green patina sample B1, and (b) the measured thickness of the patina samples A, B1, B2 and B3.

The thickness of the coating was characterized from the SEM image of the cross-sectional area as shown in Figure 2.5(a). The measured thickness reported is the average value at three different locations, which are 154.4667 ± 53.62, 228.35 ± 17.58, 124.016 ± 10.36, and 110.13 ± 44.38 μm for samples A, B1, B2, and B3 respectively. As can be seen in Figure 2.5(b), the thickness of samples B1, B2, and B3 reduces with the decrease of the solution temperature as explained above. The thickness value of sample A is less than the value of sample B1 due to the difference in the Potassium Chlorate concentration.
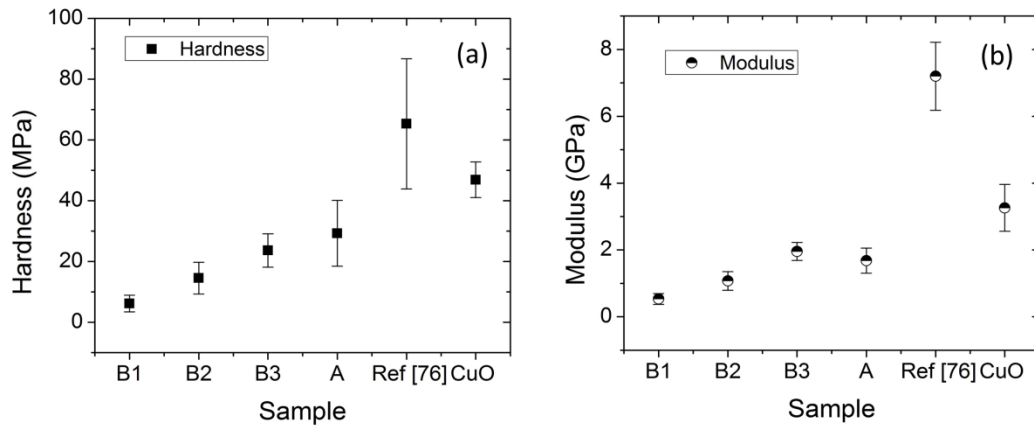
Figure 2.6: (a) The measured surface hardness and (b) the modulus for green patina coatings compared with the patina and copper oxide results presented by Ref. [76].

2.2.3 The mechanical properties of green patina coatings

The mechanical properties of green patina samples A, B1, B2, and B3 were investigated by measuring the surface hardness and modulus using a Nanoindentation test at a maximum load of 1 mN and compared with the results given by Ref. [76] for the green patina and copper oxide coatings. For patina samples A, B1, B2, and B3, the measured surface hardness is 29.281 ± 10.85 MPa, 6.16 ± 2.72 MPa, 14.534 ± 5.22 MPa, 23.62 ± 5.5 MPa, and the modulus is 1.68 ± 0.37 GPa, 0.533 ± 0.16 GPa, 1.074 ± 0.28 GPa, 1.953 ± 0.27 GPa, respectively. As shown in Figure 2.6, for group B coatings, sample B3 has the highest values of the surface hardness and modulus because it has the lowest thickness value as explained in Figure 2.5b. However, the results also reveal that sample A has a higher value of surface hardness and lower value of modulus than sample B3. Additionally, it is clear that the results presented in this work are less than those given by Ref. [45] for the green patina and copper oxide surfaces even though sample A was prepared with the same recipe and applying the stirring during the second chemical process. It was also of great interest to find that the cuprite surface has superior

17

mechanical properties compared to the copper oxide and patina surfaces. The modulus and the surface hardness of the cuprite surface are 24.02 $\pm$ 4.6 GPa, and 732.97 $\pm$ 292.75 MPa, respectively.

Time = 0.001 sec   Time = 0.037 sec   Time = 0.178 sec

Time = 0.736 sec   Time = 1.647 sec   Time = 3.503 sec
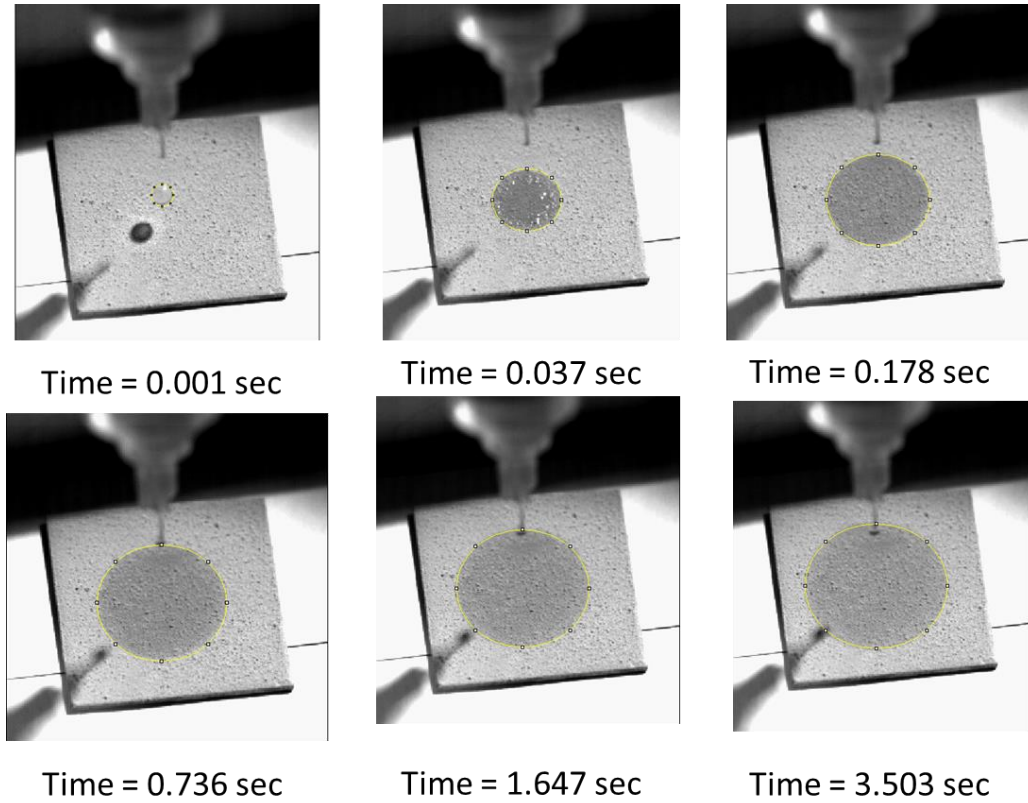
Figure 2.7: The droplet spreading with time for sample B1 after heating at 100 ˚C for 1 h.

2.2.4 The wettability of the green patina coating

The wettability of a surface can be controlled by changing its surface chemistry and surface roughness [42]. The surface chemistry determines whether the surface has high or low surface energy. In general, a surface with high surface energy is hydrophilic, and a surface with low surface energy is hydrophobic. According to Wenzel [80] and Cassie–Baxter [81] models, the surface roughness will also make a hydrophilic surface even more hydrophilic, and a hydrophobic surface even more hydrophobic. The high surface energy of the green patina is due to the high value of oxygen which refers to the

18

high value of hydroxide group in the chemical composition of the brochantite as reported by the XPS analysis. Moreover, the SEM images show that the growth of the crystalline microstructures implies to the increase of the surface roughness. Therefore, the wettability of the patina surface increased according to the Wenzel model.
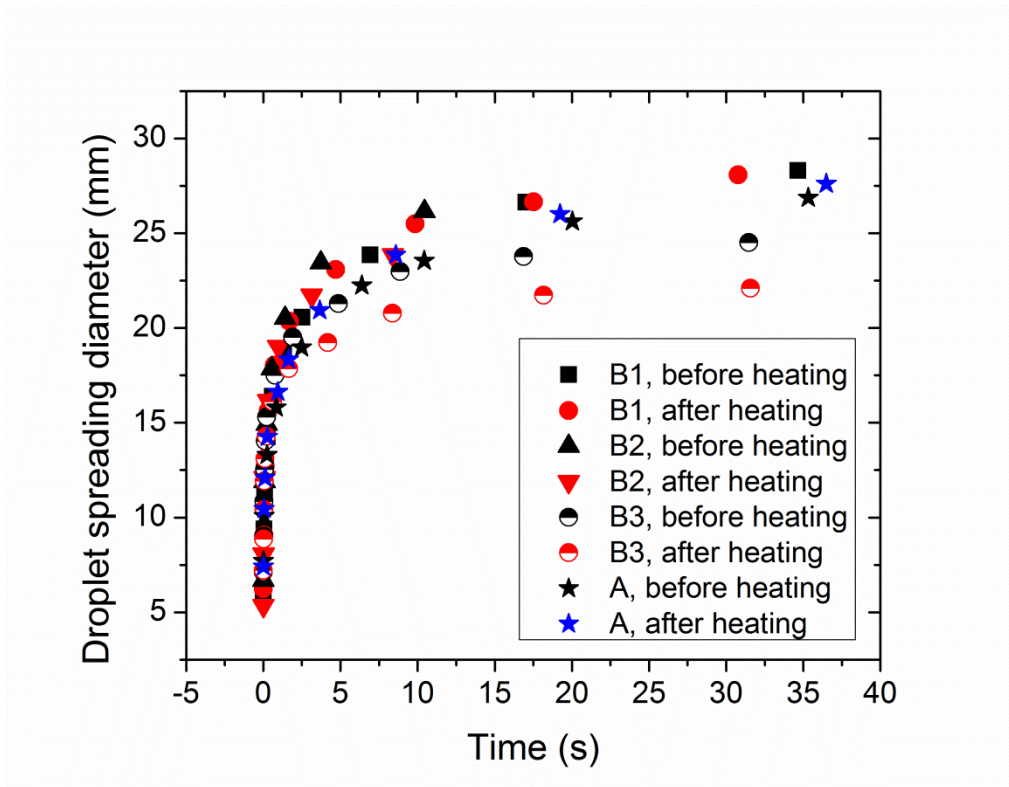
Figure 2.8: The droplet spreading with time for different patina samples (a droplet volume of 10 μl).

In this research, the high wettability of the green patina surface was studied by investigating the liquid spreading and examining the capillary rise over the different patina samples. A high-speed camera (Micro-EX4, Phantom) operating at 100 frames per second was utilized to analyze the liquid spreading on the different patina coatings. The tests were reported before and after heating the samples at 100 ℃ for 1 h. With 5 μl of a water droplet volume, Figure 2.7 demonstrates the liquid spreading on sample B1 with dimension of 20 mm × 20 mm × 1 mm after heating at 100 ℃ for 1 h. The results exhibit

19

the superhydrophilicity of the patina coating with a contact angle close to zero before and after heating the sample. Moreover, Figure 2.8 shows the droplet spreading diameter with time on the different patina samples with dimension of 50 mm × 50 mm × 3 mm before and after heating with 10 μl of a water droplet volume. The results obtained show that the liquid spreading diameters on the patina samples reach about 20-25 mm after 5 seconds.

Time = 0.07 sec   Time = 2.44 sec

Time = 8.91 sec   Time = 16.9 sec
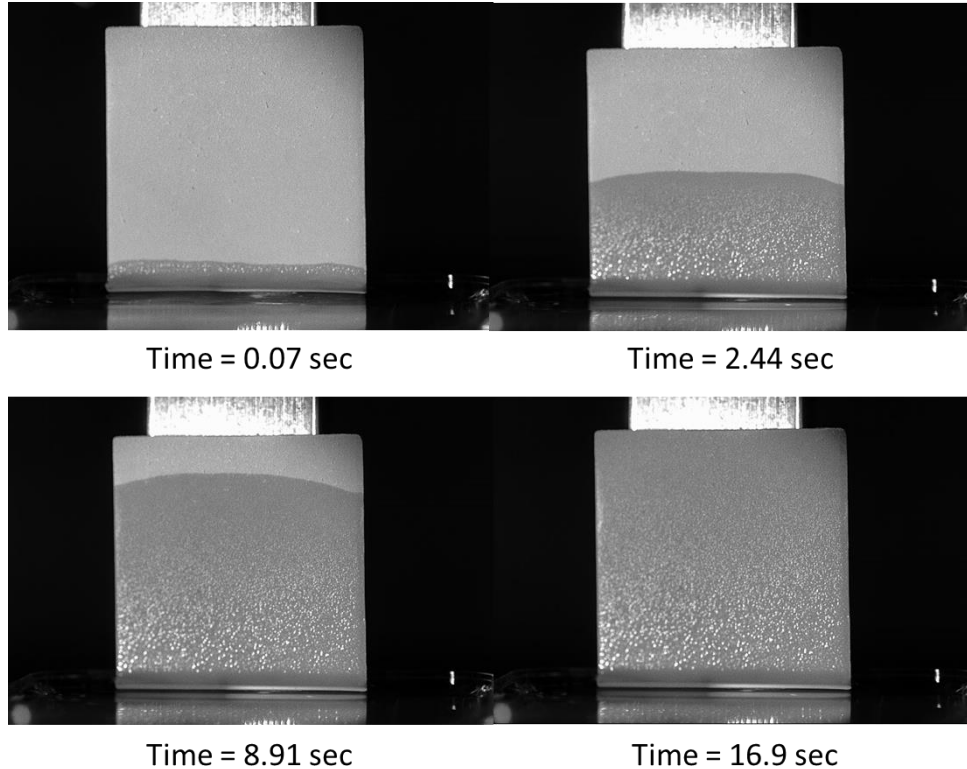
Figure 2.9: The capillary rise height through the patina sample B3, before heating for 1 hr at 100 ℃.

Additionally, the capillary rise effect on the dandelion like microstructures of the patina surface was examined before and after heating the samples at 100 ℃ for 1 h and compared with the results given by Ref. [5] for the copper oxide surface (CuO). The sample with the same dimension of 50 mm × 50 mm × 3 mm was fixed on a sliding block using 3M adhesive tape and slowly moved down vertically into a liquid reservoir. Once, the sample touches the liquid surface, the liquid raises within the microstructures due to

the capillary force. The capillary rise height through the patina substrate as a function of time was recorded by the same high-speed camera (Micro-EX4, Phantom). Figure 2.9 shows the recorded video by the high-speed camera at 100 frames per second to visualize the capillary rise height as a function of time within the patina sample B3 with a coating thickness of 110.13 μm. The water wets the surface and rises very fast to reach the height of 50 mm in 16.9 seconds. The capillary rise height as a function of time for the five patina samples before and after heating up at 100 ℃ for 1 hour is presented in Figure 2.10. The results reveal that as the patina thickness decreases the capillary rise height increases. This behavior can be interpreted based on the capillary action phenomena and liquid transport in porous media. As the thickness of the porous media increases the cross-sectional area which can be brought into contact with the liquid increases and hence the cumulative volume V of the absorbed liquid after a time t is given by the following equation as presented by Ref. [82].

$$V = AS\sqrt{t} \tag{2.3}$$

where S is the sorptivity of the porous media, in units of $m.s^{1/2}$. Therefore the capillary rise increases with decreasing the coating thickness. For Sample B1 with the highest coating thickness of 228.35 μm, the water height reaches the height of 40 mm in 55 seconds, while it reaches 50 mm height in 26.0 seconds for sample B2 with the lower coating thickness of 124.016 μm. However, the water wets the surface and to reach the height of 50 mm in 46.52 seconds for the patina sample A. The obtained patina coatings results were also compared with the results given by Ref. [5] for a flat surface of copper oxide (CuO) with wick structures. The water height within the copper oxide reaches approximately a steady state in one second, corresponding to a capillary rise height of

21

4.73 mm. It is clear that the presented results in this work exhibit the high wettability and durability of the green patina coating compared with the copper oxide nanostructures.
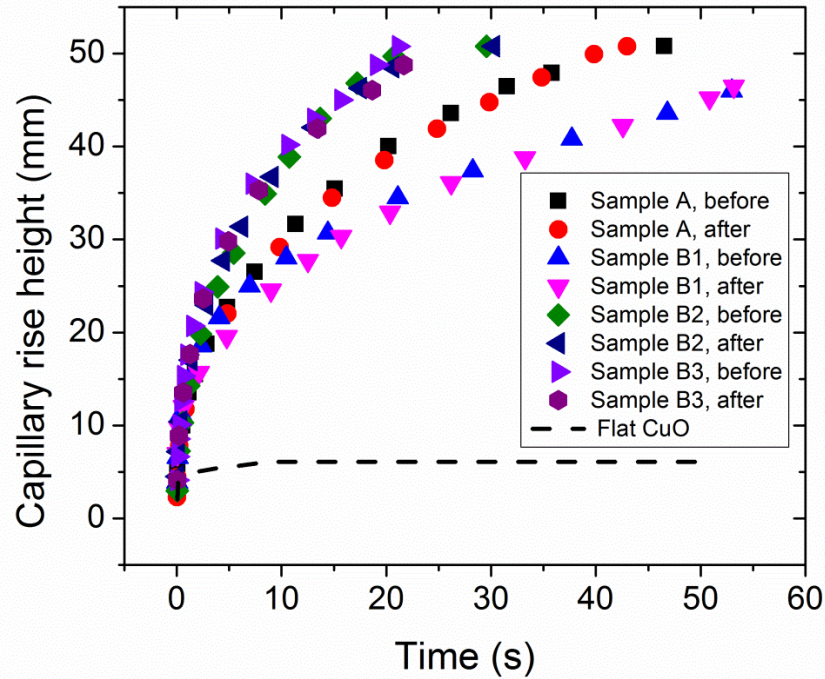
Figure 2.10: The capillary rise height through the patina coatings before and after heating at 100 ℃ for 1 hr and the comparison with the copper oxide coating.

2.3 Experimental system and data processing of sweating-boosted air cooling

2.3.1 The experimental setup

In the present study, as shown in Figure 2.11 and Figure 2.12, the sweating-boosted air cooling experiment was performed in an open wind tunnel system (ScanTEK 200, Aerostream) to evaluate the heat dissipation performance on the different green patina samples. The experiments were conducted under various air flow velocities, thermal loads and water dripping rates. The air flow velocity over the testing sample is in the range of 2.0- 10.0 m/s and measured by an air speed transmitter (FMA904R-V1, Omega). The ambient temperature and the relative humidity are measured by a duct style

relative humidity/temperature transmitter (HX-94C, Omega). A syringe pump (ProSpense, Cole-Parmer) is utilized to deliver and drip distilled water at the center of testing samples. The rates of water dripping on the surface are set at 0, 2.0, 4.0, 6.0, 8.0, 10.0, 12.0, 14.0, and 16.0 ml/h. On the back side of the testing sample with a dimension of 50 mm × 50 mm × 3 mm, three T-type thermal couples (TMQSS-020G-12, Omega) are fixed along the center line with a spacing of 1.5 cm and a depth of 2.0 mm to measure the temperature. A flexible silicone rubber heater (SRFG-202/10-P, Omega) is bonded on the back side of the testing sample using a thermally conductive epoxy (OB-101, Omega), and is connected to a DC power supply to provide a constant heat flux. Then the testing unit, which includes the testing sample, flexible heater, and the thermal couples, is supported with a Lexan block. Also, for an excellent thermal insulation and to ensure a parallel air stream over the testing sample. The testing unit is embedded and adjusted horizontally into an acrylic block. The system is considered in steady state after all the measured parameters remained constant for a period of 30 mins. All the measured data are acquired by an Agilent 34972A and recorded by a LabVIEW program to a PC.

2.3.2. Data processing and uncertainty analysis

The effective heat flux dissipated from the heated surface is given by;

$$q'' = \frac{VI}{A}(1 - \phi) \tag{2.4}$$

where

q'' is the measured heat flux dissipated from the heated surface;

V and I are the voltage and current provided by a DC power supply to the heater;

A is the projected surface area of the testing sample;

ϕ is the conductive heat losses from the side of testing sample to the surroundings.

From the thermal resistance network presented in Figure 2.13, the total thermal resistance of the copper block coated with a green patina structure during the sweating evaporation experiment is given by;

$$R_{total} = R_{Cu} + R_p + R_l + R_{sweat} \qquad (2.5)$$

where

R_{Cu} is the thermal resistance of copper block from the top surface to the location where the thermal couple is fixed;

R_p is the thermal resistance of the patina structure;

R_l is the thermal resistance of the liquid film within the patina structure;

R_{sweat} is the thermal resistance of the convective heat and mass transfer due to the sweating-boosted air cooling.

The thermal resistance of the copper block between the location of thermal couples and the top of copper surface is

$$R_{Cu} = \frac{\Delta x}{k_{Cu}} \qquad (2.6)$$

Where

k_{Cu} is the thermal conductivity of the copper block.

Δx is the distance between the top of the copper block and the location where the thermal couple fixed, and $\Delta x = 1\ mm$;

The thermal resistance of the patina structure is;

$$R_p = \frac{t_p}{k_p} \qquad (2.7)$$

Where

k_p is the thermal conductivity of the green patina;

t_p is the thickness of the green patina coating;

The thermal resistance of the liquid film within the patina structure is given by;

$$R_l = \frac{d}{k_l} \tag{2.8}$$

where

d is the thickness of the liquid film within the structure, and k_l is the thermal conductivity of the liquid film deposited on the patina structure;

The surface temperature (T_s) at the top of the copper block is determined by

$$T_s = T_b + q''.R_{Cu} \tag{2.9}$$

where

T_b is the average wall temperature measured with the three thermal couples;

The effective (measured) heat dissipated from the heated wetted surface in forms of sensible and latent heat can be written as;

$$q = h_{conv} A(T_s - T_\infty) + \dot{m}c_{p,l}(T_s - T_i) + m''h_{fg} = h_{eq} A (T_s - T_\infty) \tag{2.10}$$

Where

q is the measured thermal load;

T_∞ is the temperature of air flow;

h_{conv} is the convective HTC;

m'' is the evaporation rate of water; and $\dot{m}$ is the mass rate of the liquid film;

$c_{p,l}$ is the thermal capacity of water;

T_i is the temperature of dripping water;

h_{fg} is the latent heat of water.

h_{eq} is the equivalent HTC of sweating-boost air cooling.

Where

25

$$h_{eq} = 1/(R_{patina} + R_l + R_{sweat}) \qquad (2.11)$$

The equivalent HTC (h_{eq}) for the sweating cooling can be extracted as follows;

$$h_{eq} = q''/(T_s - T_\infty) \qquad (2.12)$$

In Equation (2.10), the first term presents the convective heat transfer; the second term is the sensible heat for heating up of dripping water, and the third term for the latent heat of water, respectively. The second term is much less than the other two terms and hence it is neglected in this study. Therefore, equation (2.10) can be simplified and written as follow;

$$q = h_{conv} A(T_s - T_\infty) + m''h_{fg} = h_{eq} A (T_s - T_\infty) \qquad (2.13)$$

Then, the evaporation rate (m'') can be calculated in this form;

$$m'' = \frac{(h_{eq} - h_{conv}). \ A(T_s - T_\infty)}{h_{fg}} \qquad (2.14)$$

The convective HTC (h_{conv}) can be determined theoretically as follows;

$$h_{conv} = \frac{\overline{Nu_L}.K}{L} \qquad (2.15)$$

Where $\overline{Nu_L}$ is the average Nusselt number determined by equation (2.19), k is the thermal conductivity of air, and L is the length of the testing sample with a size of 5.0 cm.

The second term in the right hand side in equation (2.13) represents the latent heat and can be defined in this form;

$$m''h_{fg} = h_v A_v (T_s - T_\infty) \qquad (2.16)$$

Where

A_v is the wetted surface area;

h_v is the evaporative HTC;

26

Substituting equation (2.16) into equation (2.13) and then dividing by $A(T_s - T_\infty)$ gives;

$$h_{eq} = h_{conv} + \frac{A_v}{A} h_v \qquad (2.17)$$

In order to simply compare between the influence of the convective heat and mass transfer during the sweating boosted air cooling, the second term in the RHS in equation (2.17) can be defined to represent the effective evaporative HTC (h_{evap}) as follow;

$$h_{evap} = \frac{A_v}{A} h_v = h_{eq} - h_{conv} \qquad (2.18)$$

For all the patina samples, the uncertainties of propagation in the calculated values of the key parameters are listed in **Table 2. 2**. The estimation of uncertainty was derived based on the method of propagation of errors presented by Kline and McClintok [83].
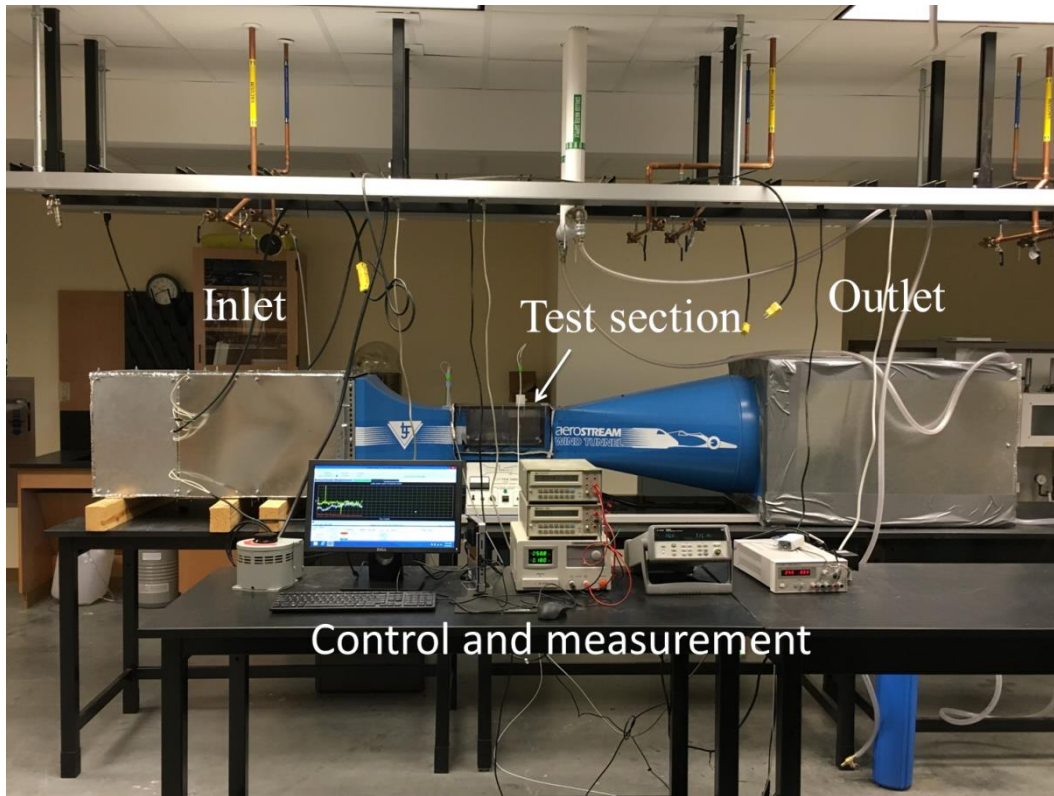
Figure 2.11: The actual experimental setup for for the sweating-boosted air cooling

27
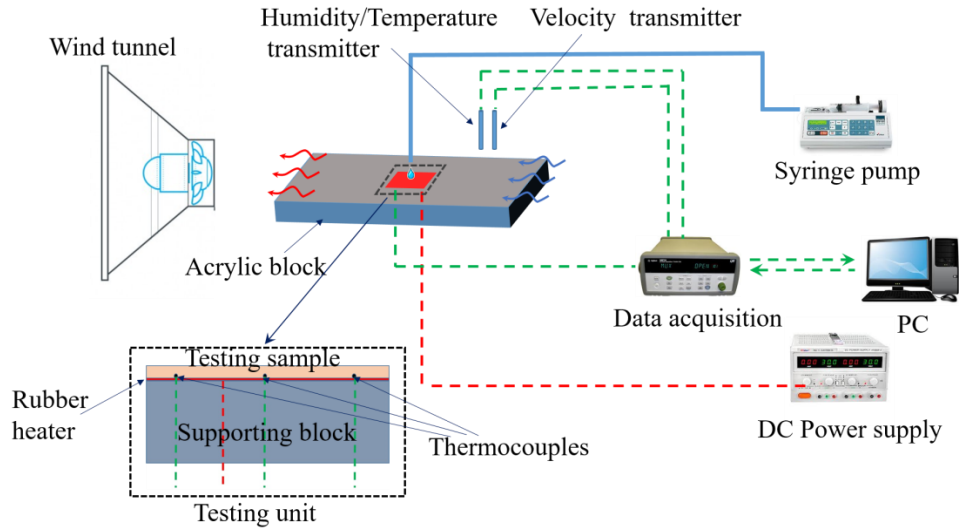
Figure 2.12: A schematic drawing of Experimental setup for the sweating-boosted air cooling [5].

(a)   (b)
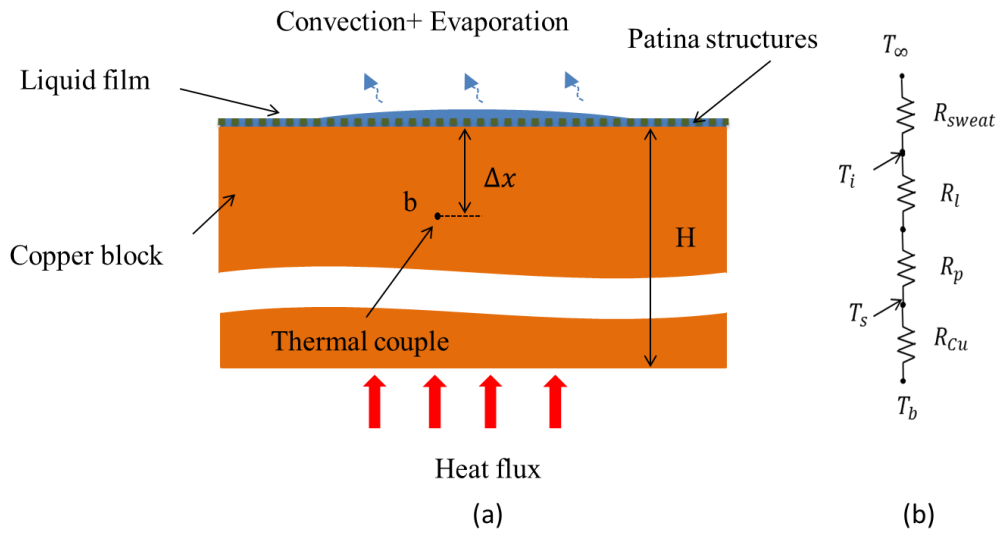
Figure 2.13: Thermal resistance analysis for the green patina testing sample during the sweating-boosted air cooling. (a) Schematic of a unit cell. (b) Thermal resistance network.

2.3.3. Calibration of experimental system

A copper block with a size of 50 mm x 50 mm x 3mm was used as a testing sample to estimate heat losses from the sample sides to the surroundings. There was no evaporation process in this calibration experiment. A thin film heat flux sensor (type

HFS-4, Omega) was mounted on the top of the copper flat surface and bonded using 3M adhesive tape to measure the convective heat flux directly from the surface under the same air flow and heating conditions. The total input powers of the heater, which is bonded on the backside of the copper plate and connected with a DC power supply, are 4.8 W, 7.5 W, and 10.74 W respectively. The air flow velocities are in the range of 2.0 – 10.0 m/s. The values of the heat flux measured by the sensor were subtracted from the values of the input heat flux given by the DC power supply to estimate the heat loss. The measured heat flux was assumed to be the effective heat flux. Consequently, the heat loss was taken into account when calculated the experimental HTC (h_{eq}) by equation (2.12). Additionally, an empirical correlation based on average Nusselt number ($\overline{Nu_L}$) was used to calculate the theoretical HTC given by [84] as;

$$\overline{Nu_L} = 0.906Re_L{}^{1/2}Pr^{1/3} \tag{2.19}$$

where Re and Pr is Reynolds number and Prandtl number of air, respectively. The above correlation is limited for a laminar flow ($Re < 3 \times 10^5$) over a heated flat plate with constant heat flux. The comparison between the experimental and theoretical (HTCs) is shown in Figure 2.14a. as presented in our previous research [5]. A great agreement is obtained, showing an accurate measurement of convective heat flux with using the heat flux sensor.

The heat loss (ϕ), which is estimated from the measured convective heat flux, is given as

$$\phi = \frac{q"_{total} - q"_{conv}}{q"_{total}} \times 100\% \tag{2.20}$$

Where

$q"_{total}$ is the input heat flux of the heater, and $q"_{total} = VI/A$,

$q"_{conv}$ is the convective heat flux measured with the heat flux sensor.

29

Figure 2.14b presents the heat loss evaluated from the measured heat flux for three different heat inputs. The averaged heat losses as a function of Reynolds number for the three heat inputs are expressed using an exponential fitting, as

$$\phi = 23.01\% + 31.80\% \times exp(-2.267 \times 10^{-4} Re) \tag{2.21}$$

The uncertainty for the estimated heat loss for input powers of 4.8 W, 7.5 W, and 10.74 W was less than 3.0 %.
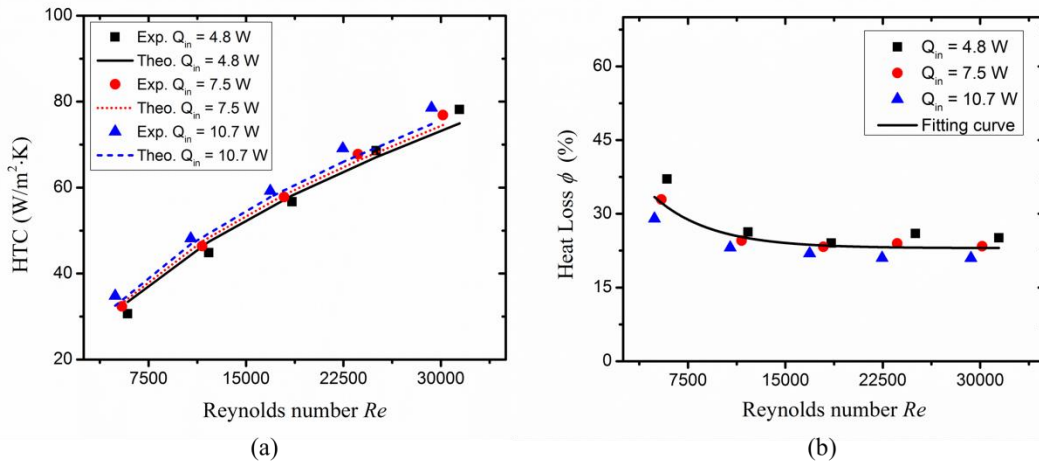
Figure 2.14: (a) The experimental and theoretical HTCs for a flat copper plate. (b) Heat loss estimated with the heat flux sensor.

Table 2. 2: Uncertainties of key parameters

Name of variables	Errors
Length, L	0.01 mm
Wall temperature, T_s	0.5 ºC
Air temperature, T_∞	0.6 °C
Air velocity, U_∞	0.5 m/s
Water dripping rate	2.5 %
Input power of heater, q''_{total}	0.20 %
Heat Loss, ϕ	3.0 %
HTC, h_{eq}	1.0 ~ 10 % with a thermal load of 8.26 W, and up to 37 % with 3.65 W

30

CHAPTER 3

RESULTS AND DISCUSSIONS

The effect of the different superhydrophilic green patina surfaces (A, B1, B2, and B3), which are presented in **Table 2.1**, on the liquid spreading and the capillary rise was studied previously in this research. The results showed that higher spreading and capillary rise are achieved while the green patina thickness decreases. Then, the same examined surfaces with different thicknesses as mentioned were tested during the sweating-boosted air cooling experiment to evaluate the convective evaporation heat transfer enhancement. Each sample was tested two or three times during one month and more. The experimental and theoretical heat transfer results of the plain copper surface (5.0 cm x 5.0 cm x 3 mm) are used as a reference to emphasize the performance enhancement due to the green patina surfaces. The heat transfer results of the patina samples are also compared with the results obtained by Ref.[5] for the sweating-boosted air cooling on CuO wick structures. Note that the error bar for the results presented in this study was hard to be observed.

3.1 Spreading and evaporation behaviors on the green patina microstructures

The evaporation mechanism of a water film on a plain and textured silicon surfaces was described by Ref.[85]. For the plain silicon surface, the evaporation of a water droplet with an initial contact angle continues over a constant wetted area until

reaching the receding contact angle. Then, the contact line recedes, the wetted area decreases, and the contact angle of the liquid film changes to a value between the advancing and receding contact angles. This process repeats until the droplet is completely evaporated. On the contrary, the evaporation-contraction process for the liquid film over the textured silicon surface occurs with holding the original contact line during the evaporation time. This is because the surface tension-induced contraction is balanced off by the capillary force generated by the microstructures. Accordingly, the thinner and larger liquid film over the textured silicon surface provides a higher evaporative heat transfer rate than the plain silicon surface. In the present study, the same behavior of liquid film evaporation is observed over the superhydrophilic green patina surface.

(a) 4 ml/h	(a) 8 ml/h
(c) 12 ml/h	(d) 14 ml/h
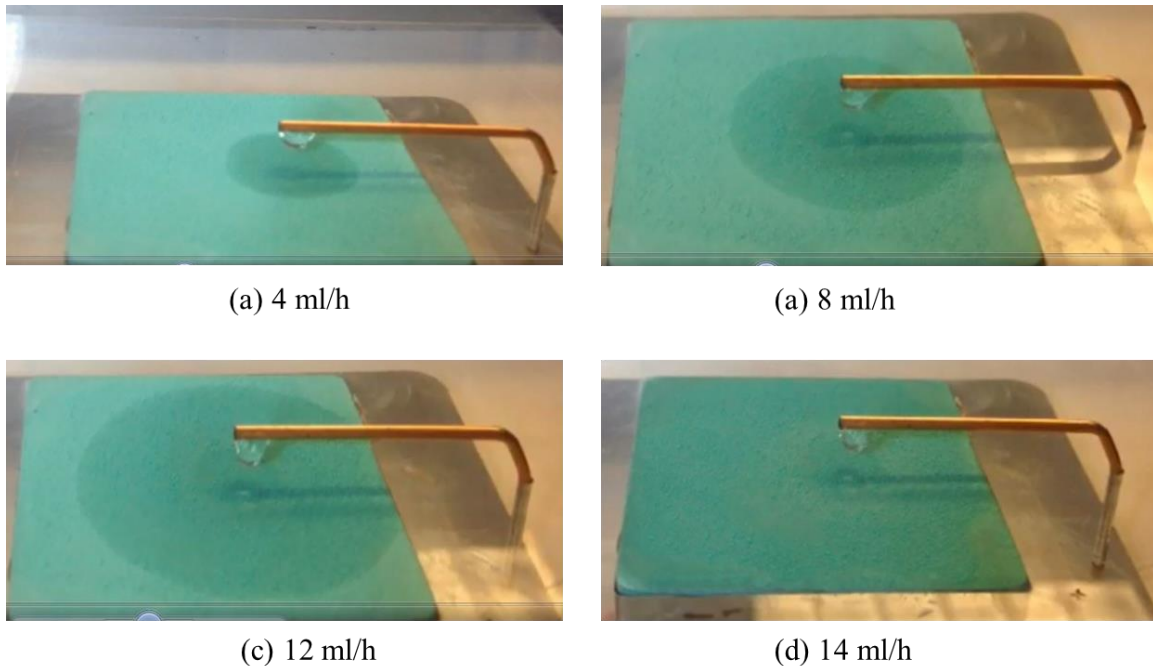
Figure 3.1: The liquid spreading on the green patina surface during the sweating-boosted air cooling experiment with dripping rate of (a) 4 ml/h (b) 8 ml/h (c) 12 ml/h and (d) 14 ml/h at thermal load of 8.263 W (0.32 W/cm^2).
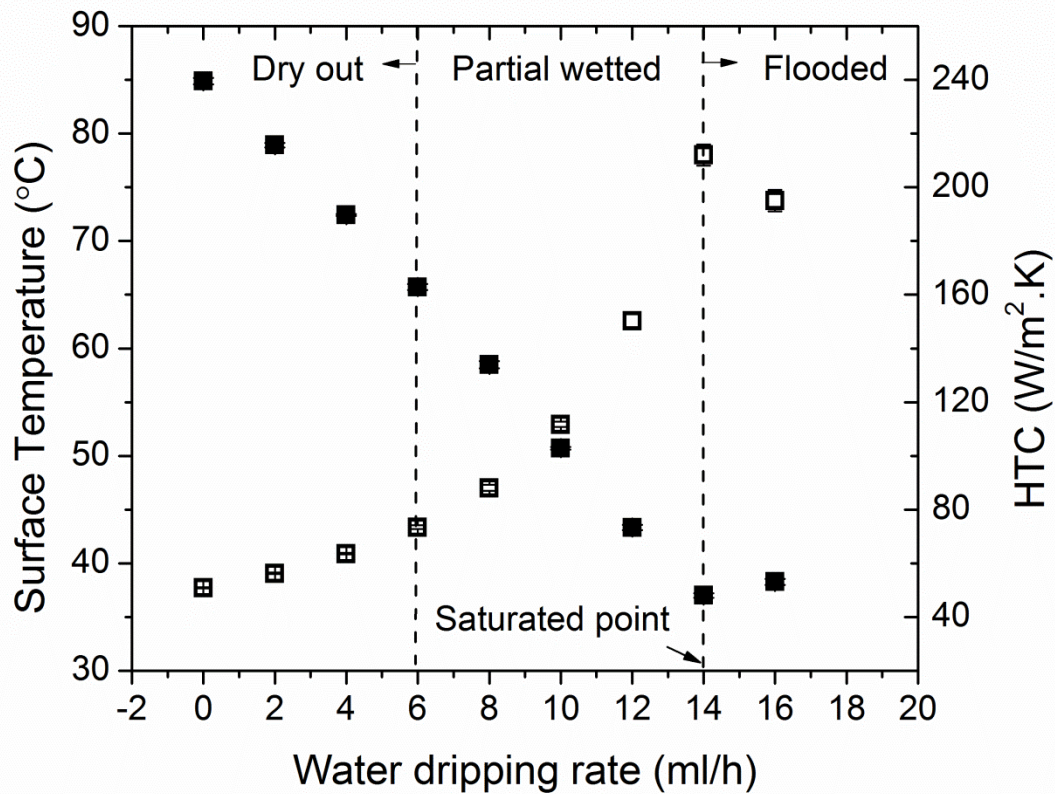
Figure 3.2: Typical thermal performance of the sweating-boosted air cooling. The solid (■) and hollow (□) symbols indicate the surface temperature and the HTC, respectively at 8.263 W (0.32 W/cm^2), $U_\infty = 4\ m/s$, green patina sample B2.

As shown in Figure 3.1, the spreading of a liquid film on the superhydrophilic patina microstructures, which is determined by the capillary force and flow resistance, is generally divided into four distinct regimes during the sweating-boosted air cooling process, namely, dry out, partially wetted, thin film, and flooded regimes. The dry out regime is recognized with the lowest dripping rate, and it continues with a higher dripping rate as the effective heat flux increases. When the water drop touches the testing sample, it forms a small wetted spot where water evaporates completely before the next water drop is delivered. Then a partial wetted area is observed on the heated surface with further increasing the dripping rate. The partial wetted area is continuously enlarged with

www.manaraa.com

the increase of the water dripping rates until a thin liquid film on the whole heat transfer surface is formed. This condition is defined as the saturated wetting point. Beyond this condition, more water drops accumulate to form a thick liquid film on the surface, resulting in a flooding condition and a reduction of heat transfer rate. Therefore, it is desirable to avoid the flooding condition and establish a thinner liquid film on the whole heat transfer surface to achieve the highest performance of the sweating-boosted air cooling.
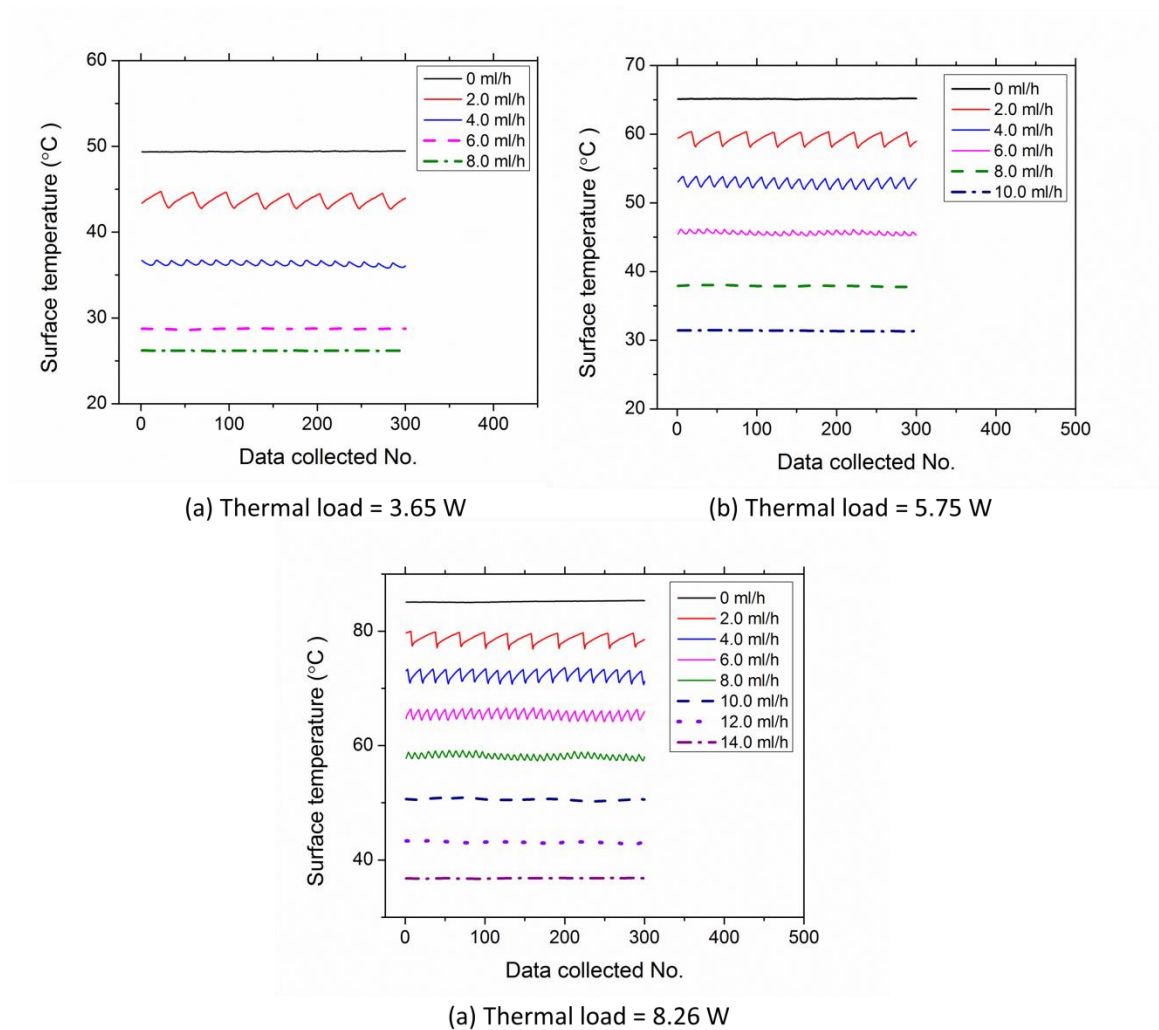
Figure 3.3: The effect of the water dripping rates on the collected data of the measured surface temperature at the steady state, $U_\infty = 4\,m/s$, (a) 3.65 W, (b) 5.75 W, and (c) 8.26 W, for sample B2.

3.2 Typical heat dissipation performance of sweating-boosted air cooling

At the thermal load of 8.26 W (0.32 W/cm^2) and air flow velocity of 4.0 m/s, the thermal performance of sweating-boosted air cooling using green patina sample B2 as a testing sample is characterized by the surface temperature and HTC versus water dripping rates as shown in Figure 3.2. With increasing the water dripping rates from 0 ml/h to 14.0 ml/h, the surface temperature reduces linearly from 84.88 ℃ to 36.99 ℃ while the HTC increases significantly from 50.87 (W/m^2.K) to 212.03 (W/m^2·K). Accordingly, the thermal performance of sweating-boosted air cooling is dramatically enhanced by 316.8 % under the above operating conditions. Additionally, the dry out regime occurs and continues until the dripping rate of 8.0 ml/h, forming a liquid film within a small wetted area on the surface. In this regime, due to the complete evaporation of the liquid film within the small wetted spot before the next delivered water droplet, repeating cycles of the liquid film break up and recovery occurs, which makes the surface temperature is neither spatially uniform nor temporally consistent. During the liquid film breaking up and recovery, the surface temperature accordingly fluctuates in a magnitude of two degrees on the average value as shown in Figure 3.2. From Figure 3.3, at three different thermal loads of 3.65 W, 5.75 W, and 8.26 W, this phenomenon happens during the dry out regime and then it vanished with the dripping rates increasing and a partially wetted condition on the surface being formed, which happens at dripping rates of 4 ml/h, 6 ml/h and 8.0 ml/h with the thermal loads of 3.65 W, 5.75 W, and 8.26 W, respectively. Then, with the partial wetted area expanding, the evaporative heat transfer becomes more dominant, resulting in a further reduction of the surface temperature and enhanced HTCs. For instance, the maximum HTC of 212.03 (W/m^2·K) in this condition is achieved when

a thin liquid film covers the whole heat transfer surface at a dripping rate of 14.0 ml/h as shown in Figure 3.2. This condition is named the saturated wetting point. Beyond this condition, the increase in the dripping rate leads to form a thicker liquid film on the surface, resulting in a flooded condition. This is because the excess dripping water cannot be effectively evaporated and result in additional liquid thermal resistance, the overall HTC is reduced.
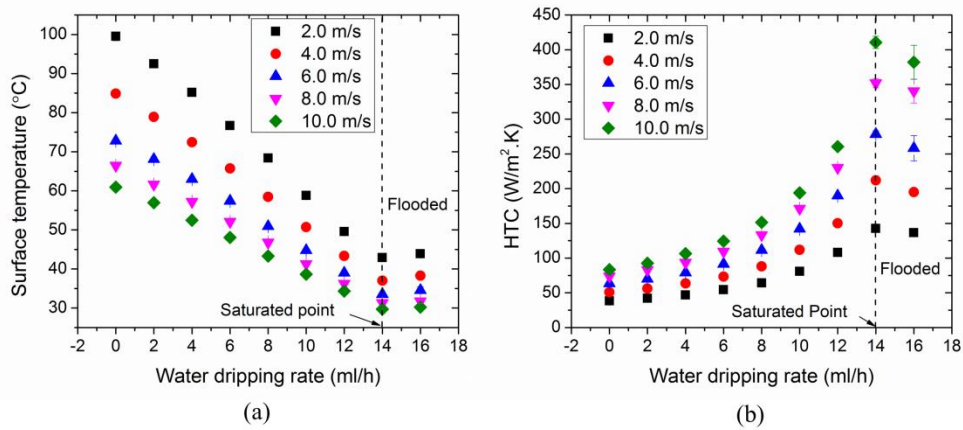
Figure 3.4: The effect of the water dripping rates on (a) the surface temperature, (b) the HTC at 8.263 W (0.32 W/cm^2), green patina sample B2.

3.3 Effect of air velocities

During the sweating-boosted air cooling process, there are two heat transfer phenomena as shown in Figure 3.1. Between the dry surface and air, there is only convection. While between the wet surface and the air, both convection and evaporation contributes. In the present study, the influence of the air flow velocities on the sweating-boosted air cooling performance with using green patina sample B2 is investigated at the measured thermal load of 8.26 W (0.32 W/cm^2). Figure 3.4 shows the effect of air velocities of 2.0, 4.0, 6.0, 8.0, and 10.0 m/s, on the surface temperature and HTC. Without dripping water, the surface temperature drops, and the HTC increases as air flow

36

velocity increases. Then, with increasing the dripping rates of water from 0 ml/h to 14.0 ml/h, higher values of HTCs and lower values of surface temperatures are observed as the air flow velocity increases. Accordingly, compared to the case without water dripping, the surface temperature was reduced from 99.52 ℃ to 29.71 ℃, while the HTC increases from 57.51 to 410.72 (W/m^2.K), showing 614.17 % enhancement of HTC. This enhancement is because that the augmentation of the wetted surface leads to larger evaporation area as shown in Figure 3.5. The evaporation rates increase significantly with the increase of the water dripping rates and slightly with the rise of the air velocities. Therefore, the thin film evaporation contributes more on the HTC enhancements. The maximum values of HTCs, evaporation rates and the minimum values of surface temperatures are observed at the saturated wetted point with a constant dripping rate of 14.0 ml/h at various air flow velocities as shown in Figure 3.4 and Figure 3.5. This indicates that the convective heat transfer is associated with the solid surface, while the convective mass transfer is attributed to the liquid film evaporation on the surface. Higher air velocity leads to higher convective heat transfer, whereas a thinner and larger thin film contributes to increases the evaporation rate, which enhances HTC greater than that of without mass transfer.

It can be concluded that that air flow velocity dominates the mass transfer during the partial wetting and saturated point conditions. This phenomenon was observed by Raimundo et al. [86].They found that over a heated pool, air flow velocity dominates the mass transfer, and temperature differences had much fewer contributions for a forced air flow. The same conclusion was reported by Lecoq et al. [17], when they investigated the influence of the air velocity on the evaporation rate from water droplets on stainless steel

37

plate. They found that as the air flow velocity increases, the HTC increases, which result to more intensive water evaporation. However, there was no obvious effect of the air flow velocity on the temperature difference between the surface and ambient temperatures.
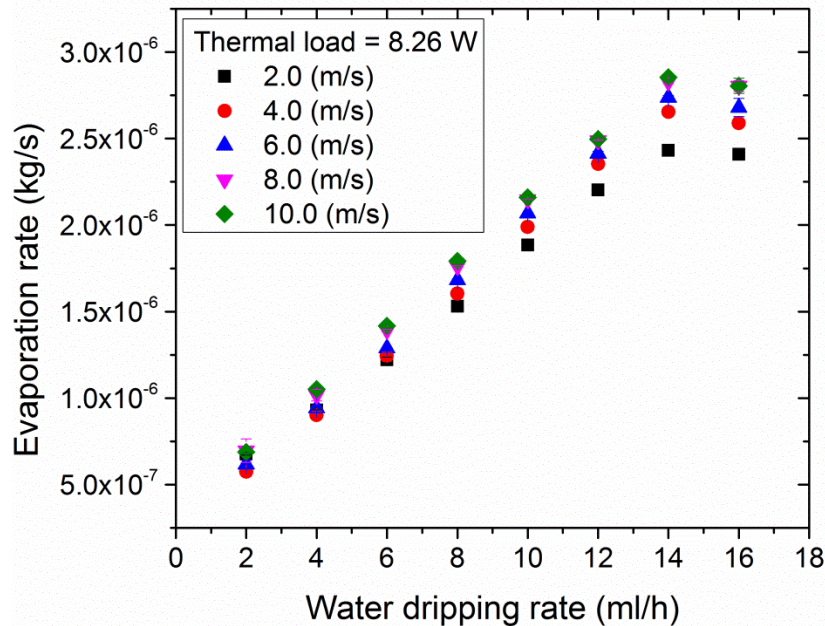
Figure 3.5: The effect of the water dripping rate on the evaporation rate, green patina sample B2 at a thermal load of 8.26 W (0.32 W/cm^2), and various air velocities.

3.4 Effect of thermal loads

The performance of sweating-boosted air cooling using green patina sample B3 was evaluated under different thermal loads (3.65, 5.75 and 8.26 W) and air flow velocities (4.0, 6.0, and 8.0 m/s). Figure 3.6 shows the surface temperature and HTC verse the dripping rates under air flow velocity of 4.0 m/s, and the three different thermal loads. It can be seen that the higher the thermal load, the higher the surface temperature, and the lower HTC. At a thermal load of 8.26 W, the surface temperature reduces linearly from 83.27 ℃ to 35.53 ℃, and HTC rises sharply from 51.82 to 229.34 (W/m2·K) until

reaching the saturated wetted point at water dripping rate of 14.0 ml/h. Then the heat transfer performance recedes beyond this point at the flooded wetted condition.
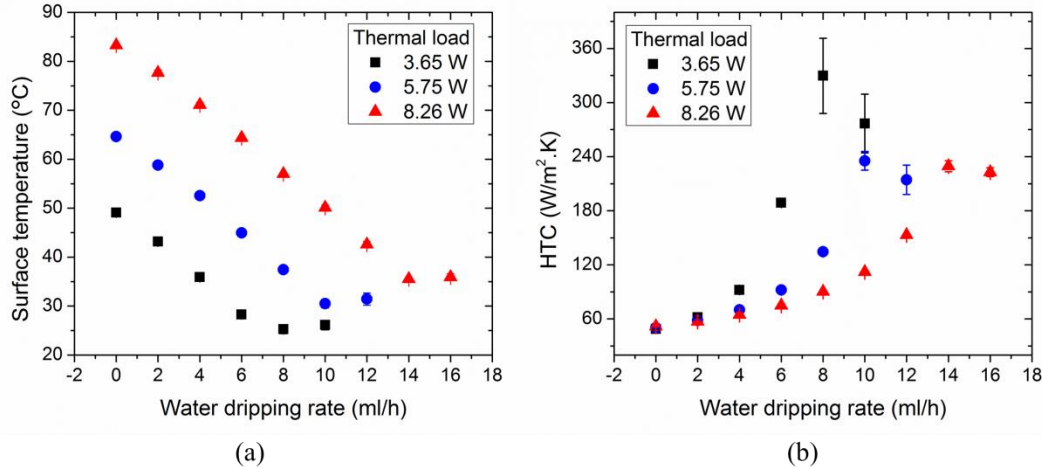
Figure 3.6: The effect of the water dripping rate on (a) the surface temperature, (b) the HTC at different thermal loads, $U_\infty = 4.0\ m/s$, green patina sample B3.

The same typical thermal performance was observed at the lower thermal loads of 3.65 W and 5.75 W. However, the saturated wetted points occur at lower values of water dripping rates. At the thermal loads of 3.65 W and 5.75 W, the saturated wetted points happen with dripping rates of 8 (ml/h) and 10.0 (ml/h) and that result in maximum HTCs of 329.66, and 235.38 (W/m2.K), respectively. This is because that at a higher thermal load, the surface temperature becomes high, and that leads to increasing the evaporation rate. For instance, as shown in Figure 3.7, at a constant air velocity of 6.0 (m/s), the higher thermal load leads to higher evaporation rates. The dry out condition continues with higher dripping rates and the thin liquid film over the entire heat transfer surface is achieved at higher dripping rates compared with the case of the lower thermal load. Moreover, from Figure 3.6, it was found that at the low thermal loads there were large uncertainties in the HTC values. This is due to either the decrease of the relative humidity

from 60.0 to 30.0 % or the rise of the ambient temperature from about 20.0 ℃ to 22.0 ℃

when the experimental tests were repeated two times at each thermal load. Additionally,

even though the high ambient temperature reduces the convective heat transfer, it was

found that the lower relative humidity and higher ambient temperature improve the

evaporative heat transfer significantly at the low thermal load of 3.65 W, leading to low

surface temperatures (which may be close to the ambient temperature) and hence, lower

air-surface temperature difference and higher HTCs.
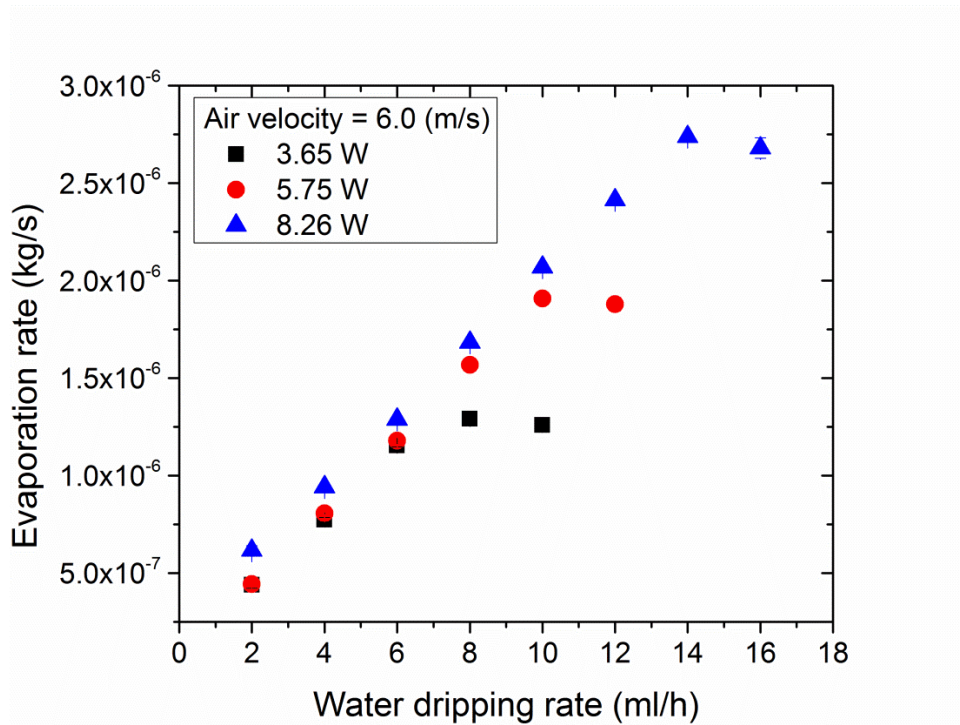
Figure 3.7: The effect of the water dripping rate on the evaporation rate, green patina sample B2 at a constant air velocity of 6 m/s, and different thermal loads.

Figure 3.8 and Figure 3.9 show HTC at higher air flow velocities of 6.0 and 8.0

m/s under the different thermal loads. The maximum HTCs, observed at the low thermal

load of 3.65 W, are 795.7 ± 189.5 and 980.8 ± 360 (W/m2.K) at 6.0 and 8.0 m/s,

respectively. The high HTC should be from the smaller temperature difference between

40

the surface and air temperatures, which leads to large uncertainties as mentioned previously. Moreover, the results exhibit that there is no obvious benefit with the increase of the air velocity on the saturated wetted point at the different thermal loads. However, as shown in Figure 3.8 and Figure 3.9, at thermal loads of 5.75 W and 8.26 W, the saturated wetted points were shifted from 10.0 to 11.0 ml/h and from 14.0 to 15.0 ml/h, at air velocities of 6.0 and 8.0 m/s, respectively. This is due to the same reason explained above. This behavior was also observed by our previous research about the sweating boosted air cooling using nanoscale CuO wick structures presented by Wang et al [5]. As a conclusion, the maximum HTC is achieved when the thin film liquid covers the whole heat transfer surface. Furthermore, the saturated wetted point is affected by the thermal loads, air relative humidity, the ambient temperature and the heat transfer surface area.
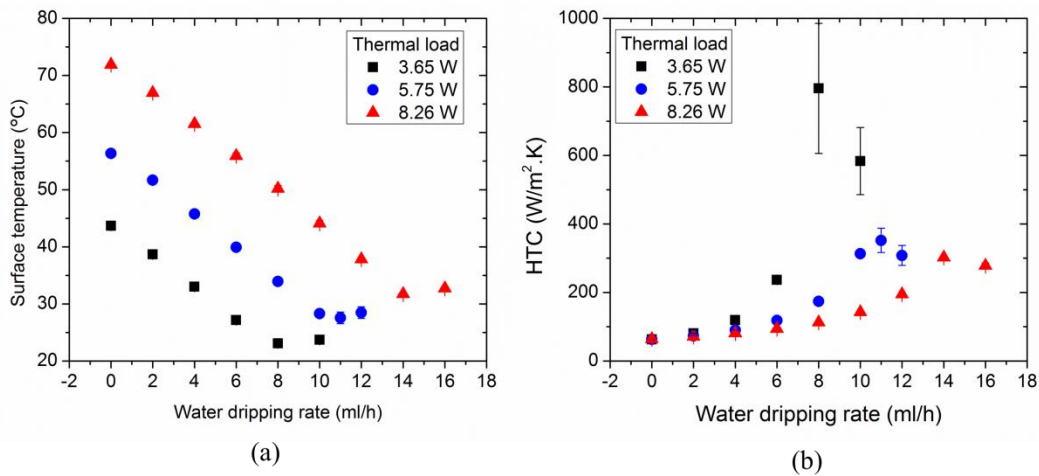
Figure 3.8: The effect of the water dripping rate on (a) the surface temperature, (b) the HTC at different thermal loads, $U_\infty = 6\ m/s$, green patina sample B3.

Sweating-boosted air cooling process includes two conjugated heat transfer modes: convection and evaporation. The measured (total) HTC (h_{eq}), as presented in this study, represents the combination of the convective and evaporative HTCs. Herein, the

convective HTC (h_{conv}) was determined from Equation (2.15); while the evaporative

HTC (h_{evap}) was determined by equation (2.18). The comparison between the measured

HTC and the calculated values of the convective and evaporative HTCs are achieved to

investigate which heat transfer process dominates in enhancing the heat dissipation

during the sweating-boosted air cooling. The comparison is presented in Figure 3.10,

Figure 3.11 and Figure 3.12 at a constant air velocity of 6.0 (m/s) and the three different

thermal loads (3.65, 5.75, and 8.26 W) on the green patina sample B2. As shown in

Figure 3.10, with a thermal load of 3.65 W, the convective heat transfer (h_{conv}) is

approximately constant, but the evaporative HTC (h_{evap}) increases with the water

dripping rate increasing. The value of the evaporative HTC is less than the value of the

convective HTC during the dry out condition. Then they nearly become equal at a

dripping rate of 4.0 (ml/h), referring to the starting of the partial wetting condition.

Beyond this condition, the evaporative HTC increases until reaching the saturated wetting

point, and then it drops in the flooded regime as the water dripping rate increases. The

same behavior was observed as shown in Figure 3.11 and Figure 3.12 for the thermal

loads of 5.75 W and 8.26 W. The matching point between the convective and evaporative

HTC are 6.0 (ml/h) and 8.0 (ml/h), respectively. As a result, it can be concluded that the

convective mass transfer during the sweating-boosted air cooling dominates to improve

the heat dissipation and increase the total HTC. Additionally, as explained previously, the

air flow enhances the mass transfer during the sweating-boosted air cooling; whereas it

dominates the convection heat transfer during the dry cooling. Also, it was great of

interest to notice that the results presented in Figure 3.10, Figure 3.11 and Figure 3.12 at

different thermal loads to compare between the evaporative and convective HTCs are

consistent with the results presented in Figure 3.3 for recognizing the start of the partially wetted conditions during the sweating-boasted air cooling. This wetting condition occurs at the matching point between the convective and evaporative HTC.
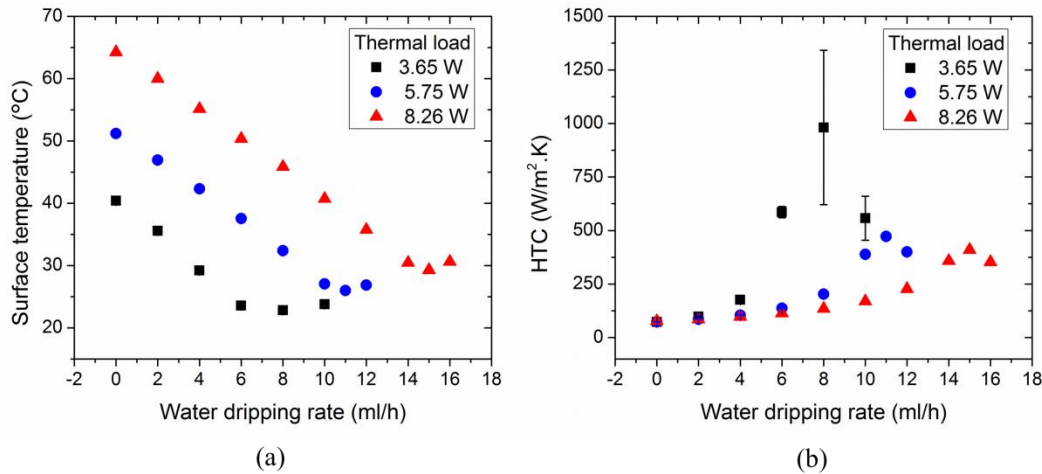
Figure 3.9: The effect of the water dripping rate on (a) the surface temperature, (b) the HTC at different thermal loads, $U_\infty = 8\ m/s$, green patina sample B3.

3.5 Effect of the green patina thickness

The performance of sweating-boosted air cooling using the different green patina samples (A, B1, B2, and B3) was investigated at the thermal load of 8.26 W (0.32 W/cm²). Without water dripping, Figure 3.13a shows the effect of air velocities of 2.0, 4.0, 6.0, 8.0, and 10.0 m/s, corresponding to the average Reynolds numbers of 5358.87, 11060.0, 17313.94, 23459.39 and 32370.22 on the surface temperatures of the flat copper plate on different patina samples. At a given value of Reynolds number, the flat surface without modification displays the highest surface temperature. The lowest surface temperature is observed on the green patina sample B3 with the lowest thickness as explained previously. Additionally, as shown in Figure 3.13b, the effect of Reynolds number on the HTCs at the saturated wetting condition with water dripping rate of 14.0

ml/h was evaluated for the different patina samples. The results were compared with the theoretical and experimental results of the forced convection over a flat copper plate. It was found that at a constant value of Reynolds number, the HTC increase with decreasing the green patina thickness. This is due to the lower thermal resistance and higher capillary rise effects, which lead to promote the evaporation rate and then the heat transfer coefficient (HTC).
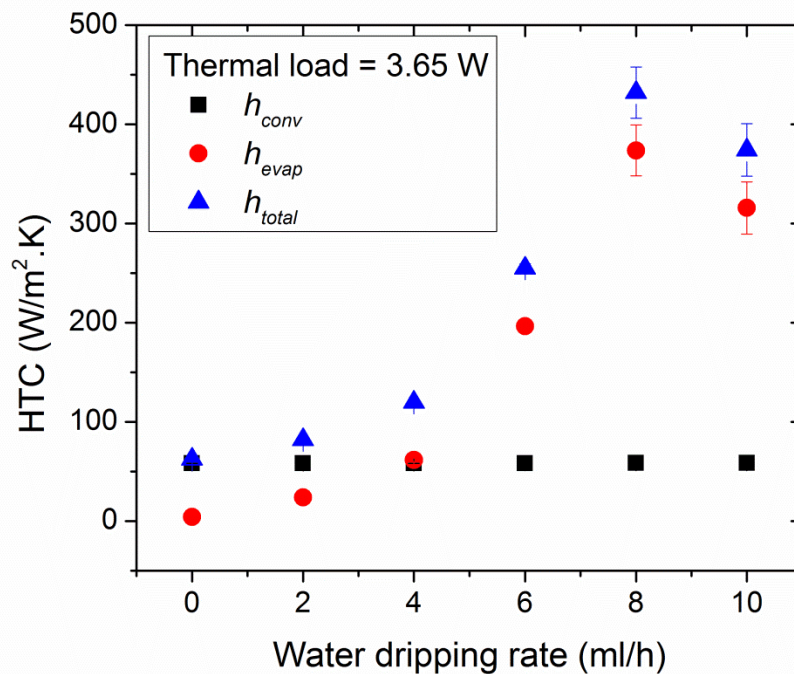
Figure 3.10: The comparison between the total (measured) HTC (h_{total}), the convective HTC (h_{conv}), and the evaporative HTC(h_{evap}) at a constant air velocity of (6 m/s) and a thermal load of 3.65 W.

Moreover, at the average Reynolds number of 23459.39, the maximum values of the HTCs are 359.13, 370.84, 410.72 and 407.34 (W/ $m^2 \cdot$K), on the patina samples A, B1, B2, and B3, respectively. In this case, the HTCs for samples B2 and B3 are close to each other due to the ignorant difference in the coating thickness and the similar capillarity. The same behavior was also observed on the samples A and B1. Therefore, it

44

can be concluded that the smaller the green patina thickness, the lower thermal resistance and the higher HTC.
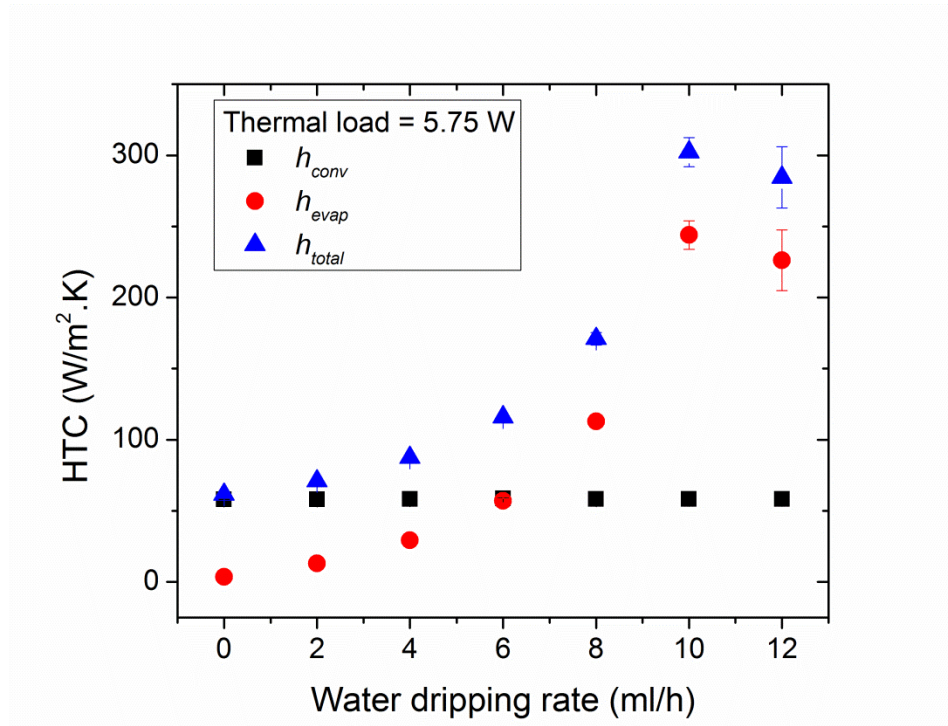
Figure 3.11: The comparison between the total (measured) HTC (h_{total}), the convective HTC (h_{conv}), and the evaporative HTC (h_{evap}) at a constant air velocity of (6 m/s) and a thermal load of 5.75 W.

It is clear from the results presented in this study that the sweating boosted air cooling strategy using the superhydrophilic green patina coating is an effective way to enhance the heat dissipation compared with the dry cooling process over the flat copper surface. For example, the surface temperature is reduced from 108.9 ℃ to 64.4 ℃ , and the HTC is increased from 34.78 to 78.53 W/m²·K for the dry cooling over a flat copper surface. On the other hand, the surface temperature is dropped from 99.4 ℃ to 29.4 ℃, and the HTC improved significantly from 37.99 to 407.33 W/m²·K for the green patina sample B3 when utilizing the sweating boosted air cooling process.
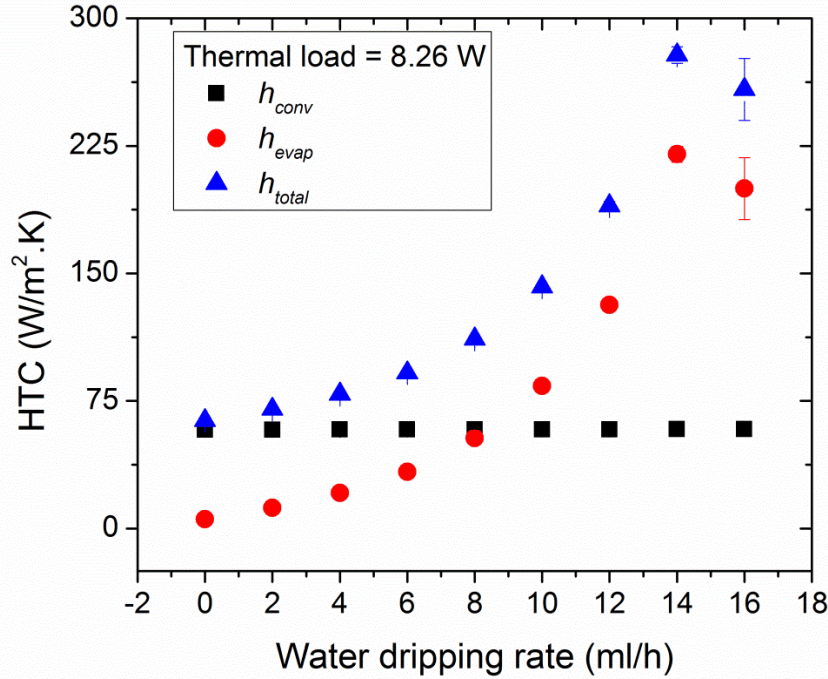
Figure 3.12: The comparison between the total (measured) HTC (h_{total}), the convective HTC (h_{conv}), and the evaporative HTC (h_{evap}) at a constant air velocity of (6 m/s) and a thermal load of 8.26 W.

Furthermore, At a thermal load of 3.65 W, Figure 3.14 exhibits that as the water dripping rate increases, the HTCs for the different coatings rise dramatically until reaching the maximum values with a dripping rate of 8.0 (ml/h) at the saturated wetting point where the thin film covers the whole heat transfer surface. However, the highest value is obtained on the green patina sample B3 with the lowest coating thickness, and compared to the case without water dripping, the HTC increases from 62.67 ± 0.31 W/m^2·K to 795.68 ± 189.5 W/m^2·K. The results herein also show the uncertainty in the HTCs values for the same reason explained previously, which was mainly due to the lower air relative humidity (39.0 ± 8.0 %).

46
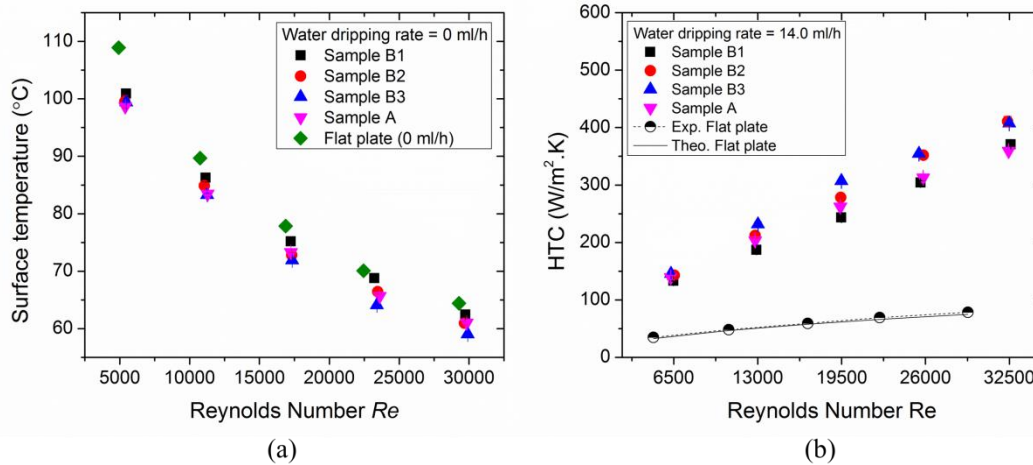
Figure 3.13: The effect of Reynolds number (a) without dripping water on the surface temperature of the plain copper surface and the green patina coatings, (b) with water dripping rate of 14.0 (ml/h) on the HTCs of the green patina surfaces, besides the comparison with theoretical and experimental values on a flat copper surface without dripping.

3.6 Comparisons between the green patina and CuO wick structures

At a constant air velocity of 6.0 m/s, the results of the effect of the different thermal loads on the performance of sweating-boosted air cooling process for the different patina samples and the results presented in Ref. [5] for CuO wick structures with a groove width of 0.75 mm are compared. At a thermal load of 5.75 W, Figure 3.15 shows that at the same conditions, the heat transfer enhancement is higher for the patina surfaces than the CuO wick structures. The maximum HTCs are 317.09, 257.19, 302.22, 352.05 and 185.4 W/m^2.K, corresponding to enhancement of 419.65 %, 338.9 %, 391.8 %, 455.9 % and 182.6 % for the green patina samples A, B1, B2, B3 and CuO wick structures, respectively. Also, it was observed that for the green patina samples A, B1, and B2, the maximum HTCs were obtained at a water dripping rate of 10.0 ml/h, indicating to the saturated wetted point. While for the patina sample B3 and CuO wick structures, the saturated wetted point occurred at a dripping rate of 11.0 ml/h. For sample

47

B3 that was due to the drop in the relative humidity reduced from 55.0 ± 5.0 % to about $40.0 \pm 10.0\%$, which enhanced the water evaporation. With increasing the dripping rates, the HTC for the green patina sample B3 with the lowest coating thickness sharply increases from 63.33 to 352.05 W/m^2.K, whereas the HTC for the CuO wick structures increases from 65.6 to 185.4 W/m^2.K. The lower thermal performance on the CuO surface is due to the lower surface wettability and liquid spreading compared to the patina coatings as demonstrated in Figure 2.10. As a summary, at the effective heat flux of 5.75 W (0.223 W/cm^2), air flow velocity of 6.0 m/s and a dripping rate of 11.0 ml/h, the HTC for the patina coating sample B3 is dramatically enhanced by 455.8 % during the sweating boosted air cooling.

(a)
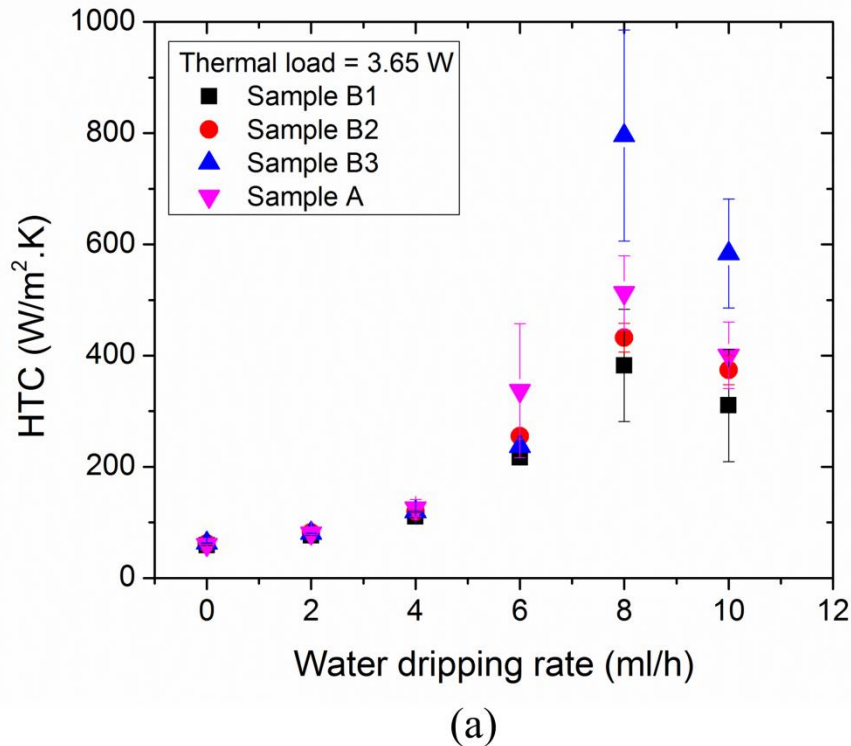
Figure 3.14: The performance of sweating-boosted air cooling process for the different patina samples at $U_\infty = 6\ m/s$ and 3.65 W.

(b)
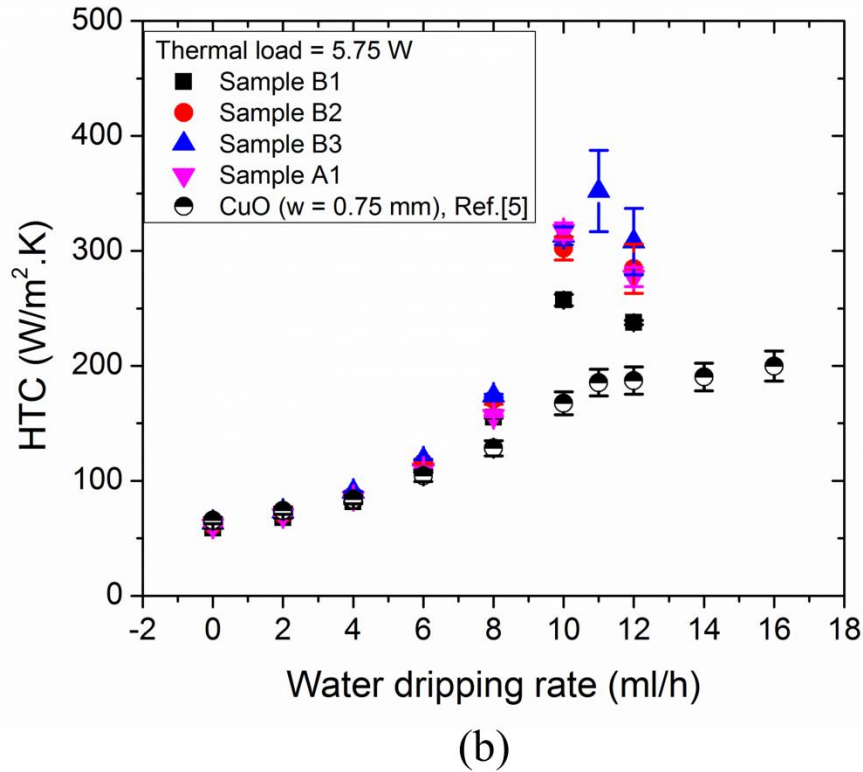
Figure 3.15: The performance of sweating-boosted air cooling process for the different patina samples and the results presented in Ref. [5] for CuO wick structures with a groove width of 0.75 mm at $U_\infty = 6 \ m/s$ and 5.75 W.

Besides, Figure 3.16 shows the effect of the water dripping rates on the HTCs at the thermal load of 8.26 W (0.32 W/cm^2). The saturated wetting point was at 14.0 ml/h for green patina samples B1, B2, and B3, while it was at 15.0 ml/h for samples A and CuO wick structures. For sample A, that was because of the reduction of the relative humidity 35.0 ± 5.0 %. The maximum values of the HTCs were 311.59, 243.23, 278.44, 302.0, and 184.02 W/m^2.K with enhancement of 403.05 %, 302.5 %, 339 %, 372.23 % and 187.53 % for samples A, B1, B2, B3 and CuO, respectively. As a conclusion, it can be seen that as the thermal load increases, the HTC decreases. However, it is still 4 times higher than these without the sweating-boosted air cooling.

www.manaraa.com
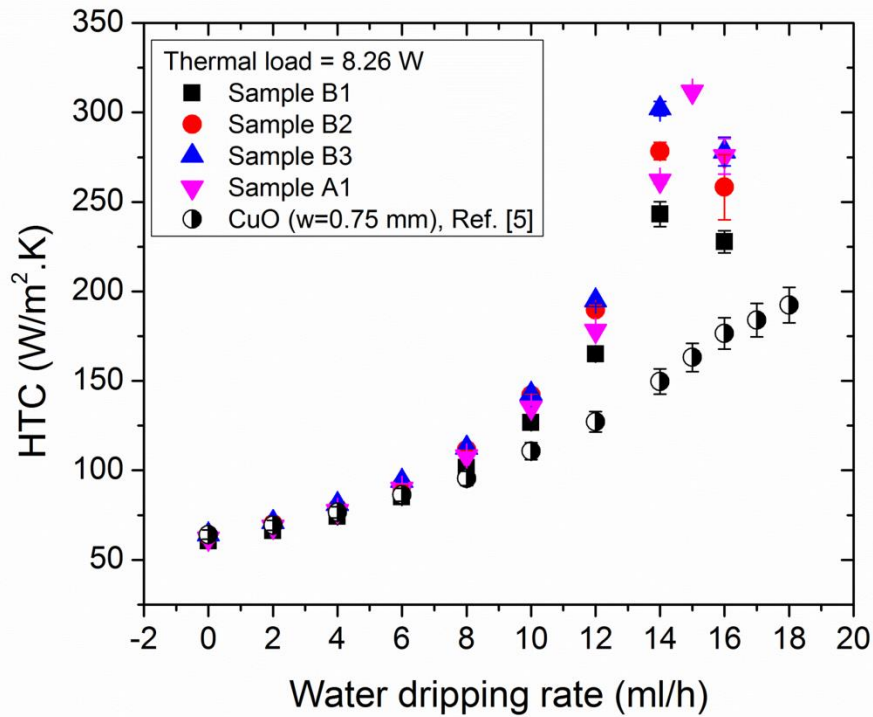
(c)

Figure 3.16: The performance of sweating-boosted air cooling process for the different patina samples and the results presented in Ref. [5] for CuO wick structures with a groove width of 0.75 mm at $U_\infty = 6\ m/s$ and 5.75 W.

3.7 The durability of the green patina coating

To verify the durability of the green patina coating, Sample B2 was stored in a dark place more than three months. Figure 3.17a shows that the patina sample B2 is still durable with high wettability after the three months of fabrication and storing in a dark place. Furthermore, it was a great of interest to observe that after testing the patina samples, the uncertainty of the surface temperature measurements was about 0.5 ℃, and the error bar for the results presented in this study was hard to be observed, which demonstrates the high durability and wettability of this type of coating against the organic contamination problems as shown in Figure 3.17b for sample B1, for example.

50

Furthermore, it was great of interest to see that the green patina sample B2 is still superhydrophilic after more than three years as shown in Figure 3.18.

(a)   (b)
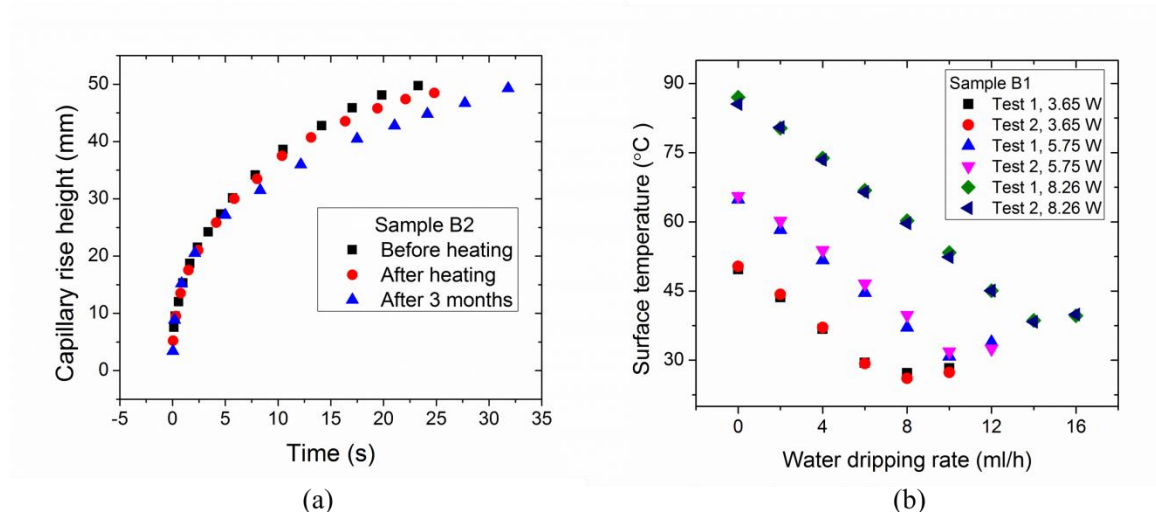
Figure 3.17: (a) Capillary rise height verse time, Sample B2, (b) Effect of the water dripping rate on the surface temperature at different thermal loads, for green patina sample B1 tested during one month.
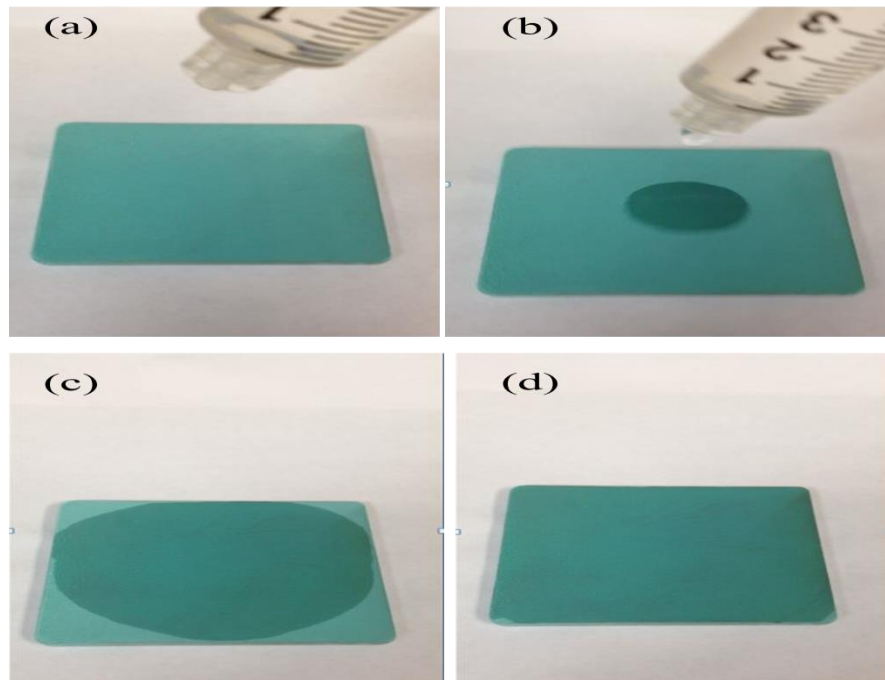
Figure 3. 18: The durability of the liquid spreading on the superhydrophilic green patina coating sample B2 after more than three years (1122 days).

CHAPTER 4

CONCLUSIONS AND FUTURE WORK

4.1 Conclusions

Inspired by the phase change heat transfer during the perspiration of mammals, a sweating-boosted air cooling strategy was adapted to enhance heat dissipation. To enhance the liquid spreading and form the thin liquid film over the heat transfer surface, durable superhydrophilic green patina surfaces were successfully fabricated on copper substrates by two-step chemical oxidization. . The first oxidization was to form a reddish cuprite film (Cu_2O) with cubic microstructures as a base oxide on the copper substrate and the second step was to produce green dandelion-like microstructures of brochantite surface ($Cu_4SO_4(OH)_6$) from oxidization of the cuprite film. The patina thickness was controlled by changing the concentration of potassium chlorate from 0.02 to 0.04 M, and with adjusting the temperature of the second chemical reaction from 60 to 40, and 25 ℃. As the potassium chlorate concentration increased, the patina thickness increased, showing a higher strength bonding after the ultrasonic cleaning test compared with the lower concentration. However, the patina thickness was reduced with the decrease of the chemical reaction temperature. The results exhibited that as the thickness decreases, the surface hardness and modulus of the patina substrate increases. It was also of great interest to find out that the surface hardness and modulus of the cuprite substrate are high compared with the surface hardness and modulus of the copper substrate. Additionally,

52

the results revealed the high wettability of the fabricated green patina surfaces during the liquid spreading and capillary rise tests before and after heating the samples at 100 ℃ for one hour and more. As the thickness of the coating decreases, the capillary rise height increases.

Furthermore, the convective and evaporative heat transfer enhancement using the green patina samples with different coatings thicknesses were evaluated under various air velocities, water dripping rates and thermal loads. The main conclusions are summarized as below:

1. Using the superhydrophilic green patina surface, four distinct wetting conditions associated with increasing the dripping rates, namely, dry out, partially wetted, thin film, and flooded conditions have been identified during the sweating-boosted air cooling process. The optimized HTCs were obtained at the saturated wetting condition. The HTC based on the sweating boosted air cooling technology is more than 6 times higher than that of the dry cooling process.

2. With a constant heat flux and various air velocities, the saturated wetting conditions were achieved at the same water dripping rate. However, this value reduces with the decrease of relative humidity and the increase of ambient temperature due to the enhanced evaporation rate. In the dry out regime, air flow velocity dominates the convective heat transfer; while it enhances the mass transfer during the partial wetting and saturated wetting conditions. The partial wetting condition starts when the evaporative heat transfer coefficient matches the value of the convective heat transfer coefficient as observed and measured in this study.

53

3. As the patina thickness reduces, the HTC increases owing to the reduced coating thermal resistance and high capillary rise effects. Also, the patina surface showed higher HTC compared with the nanoscale CuO wick structures.

4. The superhydrophilic green patina surfaces showed the high durability and reliability after testing each sample three times more than one month during the sweating boosted air cooling experiments. Additionally, the surfaces showed the high surface wettability after the liquid spreading test which is carried out after more than three years.

4.2 Future work

In the current research, the sweating boosted air cooling based on the superhydrophilic green patina coatings was investigated on flat substrates. A significant enhancement for the thin film evaporation and the heat transfer performance was demonstrated. The discovery of the superhydrophilic property and the durability of the green patina coating can open new application areas in the future. Additionally, further studies on this type of coating can be achieved. Some of these studied are discussed below.

1. Investigate the sweating boosted air cooling based on the green patina coatings on fin tubes. Figure 4.1 shows the prepared green patina coating on the fin tube.

2. Study the effect of the green patina on the heat transfer enhancement for other phase change applications such as spray cooling, pool boiling, flow boiling and the evaporation section of the heat pipe.

54

3. Investigate the effect of some refrigerants instead of water on the thin film evaporation using the green patina coating.

4. Try to further understand the reason for the highly superhydropilicity and durability of the green patina coating by characterizing the surface more deeply.
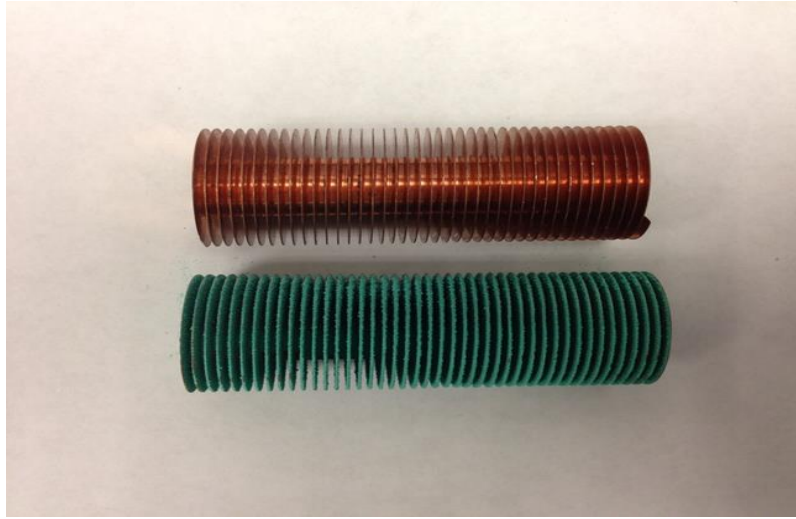
Figure 4.1: The prepared green patina coating on the fin tube

PART II: CONDENSATION

CHAPTER 5

INTRODUCTION

5.1 Background on condensation

Water vapor Condensation is a phase change phenomenon occurring spontaneously in nature [87-90], and it is an essential process for a wide variety of industrial systems, such as power plants [91-97], thermal management [98-108], water desalination [109-111], water harvesting [96, 112-116], HVAC (Heating, Ventilation, and Air Conditioning) [102, 117-120], electronics cooling [121, 122], environmental control [119, 123], and dehumidification [117, 124]. In general, Condensation occurs when steam at saturation temperature comes in touch with a solid surface (condensing surface) whose temperature is lower than the saturation temperature. The latent heat rejected during this phase change process, at a constant temperature and pressure, is defined as the difference between the enthalpy of the saturated steam and the saturated liquid. Consequently, The condensation heat transfer process (vapor-to-liquid phase) is a significant heat transfer mechanism because the latent heat transfer during the condensation process promotes much larger heat flux than sensible heat transfer, and that is essential for the two-phase thermodynamic systems. Therefore, extensive efforts and unlimited developed techniques are in progress to improve the condensation performance efficiency. The enhancement of the condensation heat and mass transfer processes in the industrial systems can lead to considerable savings in energy and natural resources as well as capital and operational costs [125-128]. For instance, approximately 85 % of the

57

global power generation systems and 50 % of desalination plants rely on steam condensers [129]. Therefore, any enhancements in cycle efficiencies of these systems would have a significant effect on global energy consumption.

Accordingly, in order to enhance the condensation heat transfer performance, it is crucial to understand the mechanism of this phase change process. Generally, Water vapor condensation is classified into two main modes, filmwise (FWC) and dropwise condensation (DWC), depending on the interaction between the condensate and the condensing surface, and on the wettability of the condensing surface.
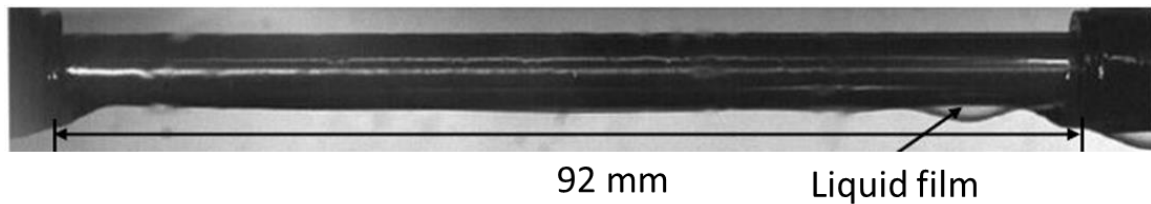
Figure 5.1: Filmwise condensation of water vapor on a hydrophilic horizontal copper tube.

5.2 Filmwise condensation

Filmwise condensation occurs on wetting surfaces called hydrophilic surfaces, which have high surface energy resulting in high wettability, such as clean metals and metal oxides. When the steam condenses on these hydrophilic surfaces, it wets the surface and forms a thin liquid film covering the entire condensing surface as shown in Figure 5.1. This figure shows the filmwise condensation on a horizontal copper tube at a specific subcooling temperature. In practical, in filmwise condensation mode, the heat transfer coefficient is limited by the thermal resistance associated with the formation of the liquid film on the condensing surface. The liquid film provides a barrier to the steam to be condensed on the solid surface, and that leads to a significant decrease in

58

condensation efficiency and heat transfer rates. However, filmwise condensation can be improved by increasing the surface area of the condensing surface, and that can allow more convection heat transfer, and creates a disturbance in the condensing liquid film [130].
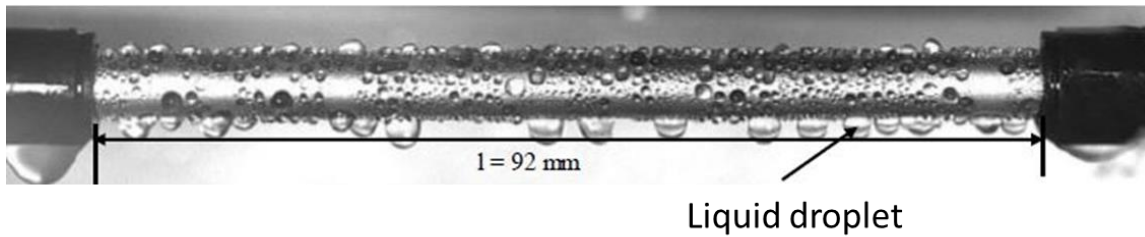
Figure 5.2: Dropwise condensation of water vapor on a hydrophobic horizontal copper tube.

5.3 Dropwise condensation

On the other hand, dropwise condensation (DWC) was first discovered by Schmidt et al. [131, 132], in 1930. This condensation mode can be observed on hydrophobic or superhydrophobic surfaces which have low surface energy. The steam condenses on these non-wetting surfaces in the form of discrete droplets ranging in size from microns to millimeters [133-135]. Figure 5.2 represents the dropwise condensation phenomena on a horizontal copper tube at a certain subcooling temperature. During dropwise condensation mode, the droplets first nucleate at preferred locations called nucleation sites at the atomic scale. Then, the small droplets grow up through direct condensation and coalesce with neighbor droplets until they become large enough to shed off the surface. When the droplets sweep on the surface, they merge with other droplets in their path leaving a bare surface behind it for renucleation. In fact, the droplet can roll off the surface when it reaches a certain critical mass, so its weight can overcome surface

59

adhesion forces. As reported by Ref. [136], this force balance can be expressed by the dimensionless Bond number, which is defined as;

$$Bo = \frac{\Delta \rho g R^2}{\gamma} \tag{5.1}$$

While the characteristic length scale at which both forces are relevant is represented by the capillary length, which is given by;

$$\lambda_c = \sqrt{\frac{\gamma}{\rho g}} \tag{5.2}$$

Where $\boldsymbol{\rho}$ is the density difference between liquid and vapor, g is gravitational acceleration, R is droplet size, and γ is surface tension [137]. It was demonstrated that during dropwise condensation, when the size of the droplets approach the capillary length (~ 2.7 mm for water), they can shed off the condensing surface and clear the surface for renucleation [138, 139].

Compared between filmwise and dropwise condensation modes, it was found that the rate of heat transfer during these two modes is considerably different for the same subcooling temperature. Researchers found that the dropwise condensation yields over an order of magnitude higher heat and mass transfer coefficients than that in filmwise condensation [131, 132, 140, 141]. For instance, dropwise condensation on plain hydrophobic surfaces achieves 5–7 times greater heat transfer coefficients than that for the filmwise condensation [142, 143]. The higher heat transfer performance for dropwise condensation is due to the lower thermal resistance of the discrete condensate drops during dropwise condensation, compared to the higher thermal resistance of the continuous liquid films during the filmwise condensation. Also, during the dropwise condensation, it can be released more bare surface cites for performing more cycles of

60

nucleation, growth, and departure, resulting in increasing the amount of condensing steam and the droplets removal rate [101, 131, 132, 144, 145]. Researchers have investigated experimentally the effect of the departure diameter and the sweeping cycle of the droplets on the heat transfer performance of dropwise condensation, and they found that the heat transfer coefficients increase with the increase of sweeping cycle of the droplets, and decrease with the increase of the drop sizes. This is because the large droplets will hinder heat transfer due to the poor thermal conductance of the liquid condensate [146, 147].
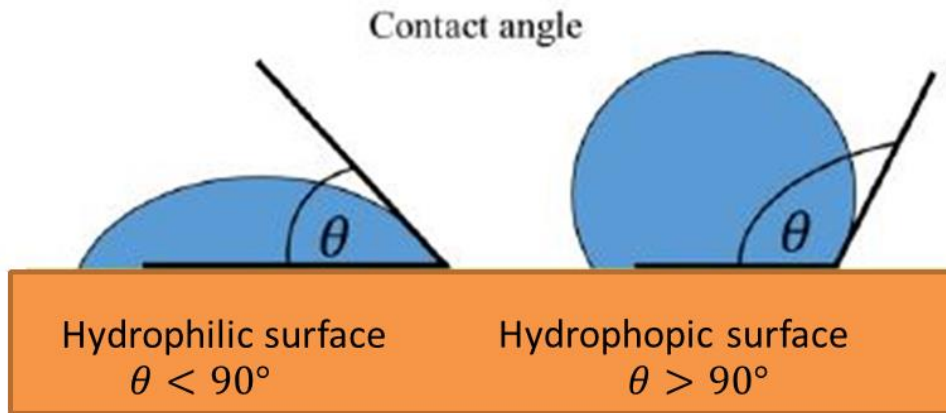
Figure 5.3: The schematic photograph of the apparent contact angle on hydrophobic and hydrophilic surfaces [148].

5.4 Effect of the surface wettability on condensation mode and performance

The surface wettability plays a significant role in understanding condensation phenomena and droplets dynamic. Depending on the wettability of the condensing surface, water vapor will condense in the form of a continuous liquid film (FWC) or individual droplets (DWC). The surface wettability is characterized in terms of the equilibrium contact angle (CA), which is described as the angle that liquid/vapor interface makes with the solid surface, and it is controlled by changing the surface free

61

energy and the surface roughness. For the droplet deposited on an ideal smooth surface, Young [148] first proposed the equilibrium contact angle (θ_y) relation, which demonstrates the force balance at the three-phase contact line of the liquid, solid and vapor phases, as follow;

$$\cos \theta_y = \frac{\gamma_{sv} - \gamma_{sl}}{\gamma_{lv}} \tag{5.3}$$

Where γ_{sv}, γ_{sl} and γ_{lv} are the solid-vapor, solid-liquid, and liquid-vapor interfacial surface energies, respectively. Based on Young's relation [148], if the equilibrium contact angle is higher than 90°, the surface is called hydrophobic and it has low surface energy; whereas if the contact angle is less than 90° the surface is called hydrophilic and it has high surface energy as shown in Figure 5.3. Moreover, it should be noted that the Young equation is applied only to calculate the contact angle for the ideal smooth and homogenous surfaces. However, for the non- ideal rough surfaces, Young's relation cannot be used to calculate the contact angle. Continuing the work of Young, Wenzel [80] and Cassie-Baxter [81] proposed two models to define the contact angle on rough and porous surfaces as shown in Figure 5.4. In Wenzel model, the liquid fills up the grooves of the rough surface, there are no air bubbles underneath the droplet, and the contact angle (θ_w) is defined by the following relation ;

$$\cos \theta_w = r \, \cos \theta_y \tag{5.4}$$

Where r is the surface roughness, which represents the ratio of the total surface area to the projected area, and θ_w is the Wenzel contact angle. It can be noticed by equation (5.4) that $r = 1$ for a smooth surface and $r > 1$ for a rough surface. In contrast, considering the case where the liquid droplet does not penetrate the roughness, which means it rests

on the tips of the roughness, the contact angle (θ_{CB}) is defined by Cassie and Baxter model as follow;

$$\cos\theta_{CB} = f \ \cos\theta_y + (f-1) \tag{5.5}$$

Where, θ_{CB} is the contact angle in Cassie mode, and f is the ratio of the solid area contacting the droplet to the projected area.
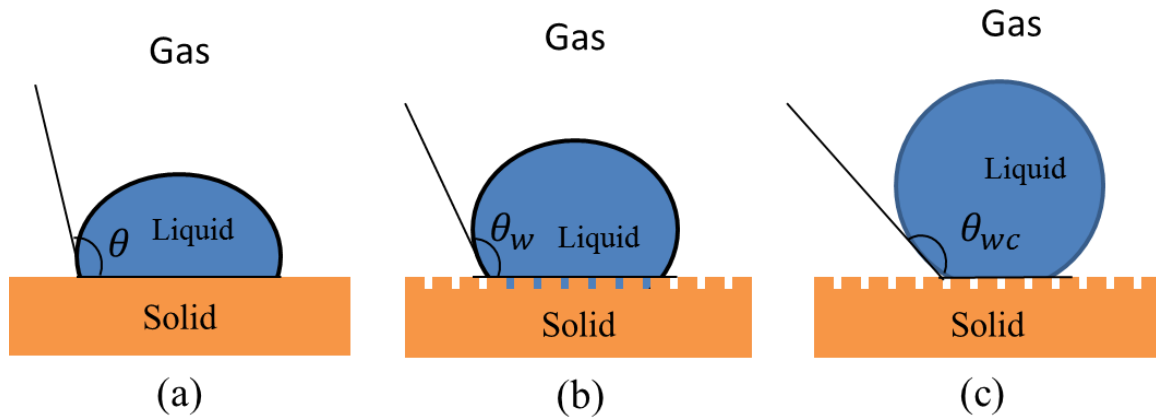
Figure 5.4: The modes of interactions between the solid surface and droplets (a) Young state [148] (b) Wenzel state [80] (c) Cassie-Baxter state [81].

According to Wenzel and Cassie–Baxte models, the wettability of a surface can be controlled by changing its surface roughness. Increasing the surface roughness makes a hydrophilic surface even more hydrophilic by decreasing the contact angle, and when it becomes less than 5°, the surface is called superhydrophilic. However, increasing the roughness of a hydrophobic surface will make it even more hydrophobic. When the contact angle is higher than 150°, the surface is called superhydrophobic. When a water droplet contacts a superhydrophobic surface, it will ball up, while it will spread out completely when it touches a superhydrophilic surface.

It is clear that Wenzel and Cassie wetting modes can both exist on the rough surfaces. However, owing to the lower contact angle hysterias in Cassie-Baxter mode, the

www.manaraa.com

droplets on the substrate have lower adhesion resulting in higher mobility compared to Wenzel mode. As a result, Cassie-Baxter mode is desired to promote efficient dropwise condensation. Accordingly, techniques and focus of research are in progress to improve dropwise condensation (DWC) performance by enhancing droplets mobility.
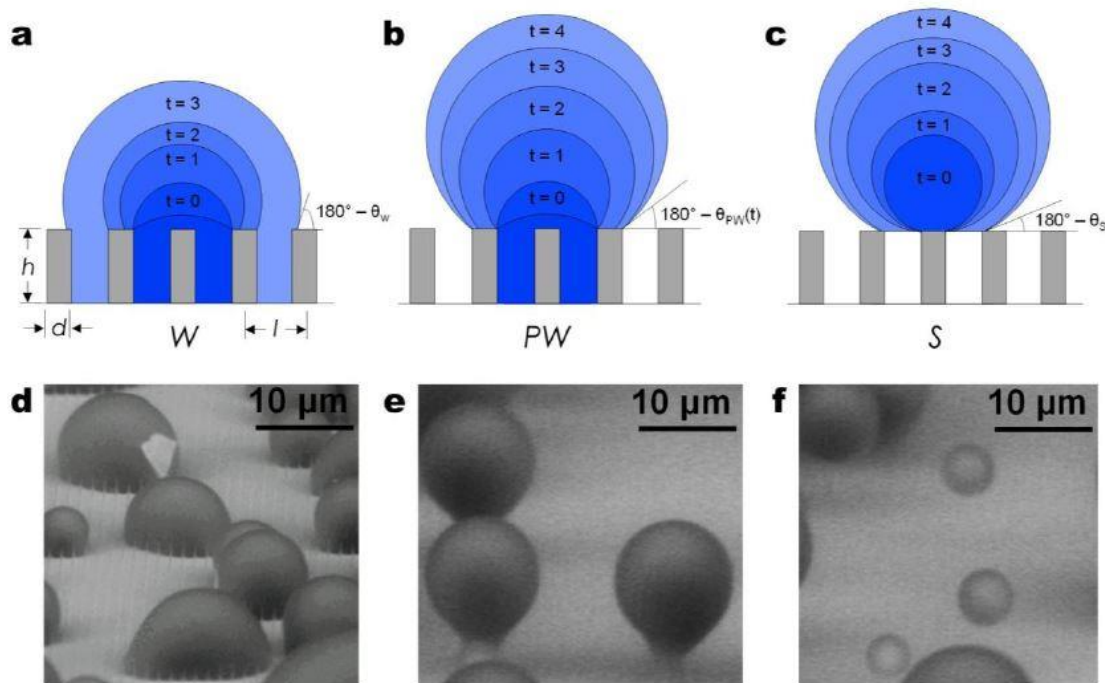
Figure 5.5: Condensing droplet morphologies. Time-lapse schematics of (a) Wenzel (W), (b) partially wetting (PW) , and (c) suspended (S) droplet morphologies. Environmental scanning electron microscopy (ESEM) images of droplets with (d) W, (e) PW, and (f) S morphologies on a nanostructured surface [149].

Over the past decade, Researchers have focused on increasing water repellency and limiting droplet adhesion on condensing surfaces by developing structured superhydrophobic surfaces [150-153]. On these structured superhydrophobic surface, droplets can depart either by gravity if they have small adhesion to the surface, or by coalescence-induced droplet jumping if they have large adhesion to the surface [154]. During dropwise condensation, it was observed three distinct droplet morphologies depending upon the structure geometry and nucleation density [149] for the condensing

64

liquid droplets: Wenzel wetting mode (W) where condensed droplets wet the cavities of the structured surface (Figure 5.5a, d), partially wetting mode (PW) where the droplets form a liquid bridge connecting the base of the droplet (Figure 5.5b, e) or suspended Cassie wetting mode (S) where condensed droplets sit on top of the structured surface (Figure 5.5c, f). For condensation heat transfer enhancement, both the partially droplets (PW) and the suspended droplets (S) are desirable due to their higher mobility compared to that for Wenzel (W) droplets. However, It was demonstrated by Miljkovic et al. [155] that the condensing surface with the partially wetting droplets (PW) has higher growth rates compared to the surface with suspended droplets (S) formation. In their study, they have used a specific geometry and investigated the effect of the droplet morphology on the droplets growth rate and the individual droplet heat transfer. They found an enhancement by 6x and 4-6x in the growth rate and individual droplet heat transfer of PW droplets, respectively compared to that of S droplets. The difference was because that the air in the composite air-solid interface, where the S droplets are suspended on, add more thermal resistance to the droplet growth. It was also demonstrated that for a condensing surface favoring only S droplet formation, the heat transfer performance was degraded by 71% in comparison with a flat hydrophobic surface. Consequently, in order to enhance the dropwise condensation on superhydrophobic surfaces, special designs are required by controlling the surface structure length scale and geometry, droplet morphology, nucleation density, and departure dynamics. In general, in order to maximize the condensation heat transfer performance, the condensing surface should have three characteristics: high nucleation density, low contact angle hysteresis to reduce

65

the droplet departure diameter, and a low apparent contact angle to minimize the conduction thermal resistance of the condensate droplet [108].

CHAPTER 6

LITERATURE REVIEW

During the past several decades, engineering the dropwise condensation of water on metal and metal oxides surfaces has aroused a significant interest due to the higher heat transfer rate compared to filmwise condensation [131, 156]. In order to achieve dropwise condensation (DWC), a low-energy non-wetting coating (promoter) is required to reduce the high surface energy of the typical heat transfer materials such as aluminum, copper, titanium, and stainless steel. Therefore, numerous methods have been developed to achieve suitable DWC promoters [157, 158]. These methods include: (a) applying organic self-assembled monolayers on the condensation surface, (b) Using Various polymer coatings, (c) implementing ion implantation method on metal surfaces, (d) using noble metals such as gold, silver, and chromium due to the natural absorption of hydrocarbons and impurities on their surfaces from the surrounding (e) Applying graphene coating which has hydrophobicity behavior during condensation [159-164]. Furthermore, to achieve effective DWC with highly water droplet mobility, several different approaches have been developed by modifying condensation surfaces, including superhydrophobic surfaces, hierarchical superhydrophobic surfaces, bi-phillic surfaces (hybrid surfaces) and lubricant-infused surfaces [165].

67

6.1 Promoting dropwise condensation by using low surface energy coatings

6.1.1 Self-assembled monolayer coatings

Self-assembled monolayers (SAMs) of organic materials have gained considerable attention for their hydrophobic abilities to promote DWC. These Self-assembled monolayers are composed of a single layer of organic molecules, which strongly chemisorb onto metals/metal oxides surfaces and deposit easily to form a thin molecular film (∼1 nm) [149]. Up to now, two common types of SAM molecules are widely used in scientific research such as alkylthiol [166, 167] (sulfur-based ligand), and alkylsilane (silicon-based ligand) [154, 155, 168]. Due to their negligible thickness, Self-assembled monolayers (SAMs) have negligible heat transfer resistance. Therefore, Researchers have been focused on studying the effect of using self-assembled monolayers on promoting dropwise condensation. Blackman et al. [169, 170] have experimentally investigated the effect of self-assembled monolayers of octadecanethiol, which is a similar compound to n-octadecyl mercaptan, on the ability for promoting DWC. They found effective dropwise condensation for about 500 h of experimentation. However, they have not reported any experimental data for a period over this experimentation time.

Das et al. [166] have been developed self-assembled monolayers (SAMs) on horizontal tubes of gold, copper, and copper-nickel alloy to investigate their condensation characteristics on enhancing dropwise condensation heat transfer. The monolayer coating was created by chemisorption of alkylthiols on these metal surfaces showing strong covalent bonds between alkylthiol and the metal surface. The experimental results showed that, compared to the FWC case, the DWC heat transfer coefficient was

68

improved by a factor of 4 for gold-coated aluminum, and by a factor of 5 for copper and copper-nickel tubes, under vacuum operation (10 kPa). The enhancement values under atmospheric conditions were about a factor of 14 for SAM-on-copper tubes, 14 for SAM-on-copper-nickel tubes, and 9 for SAM-on-gold-coated-aluminum tubes. Figure 6.1 shows the heat transfer coefficient as a function of the surface subcooling at (a) atmospheric and (b) vacuum conditions for the dropwise condensation results compared with FWC and Nusselt theory results.
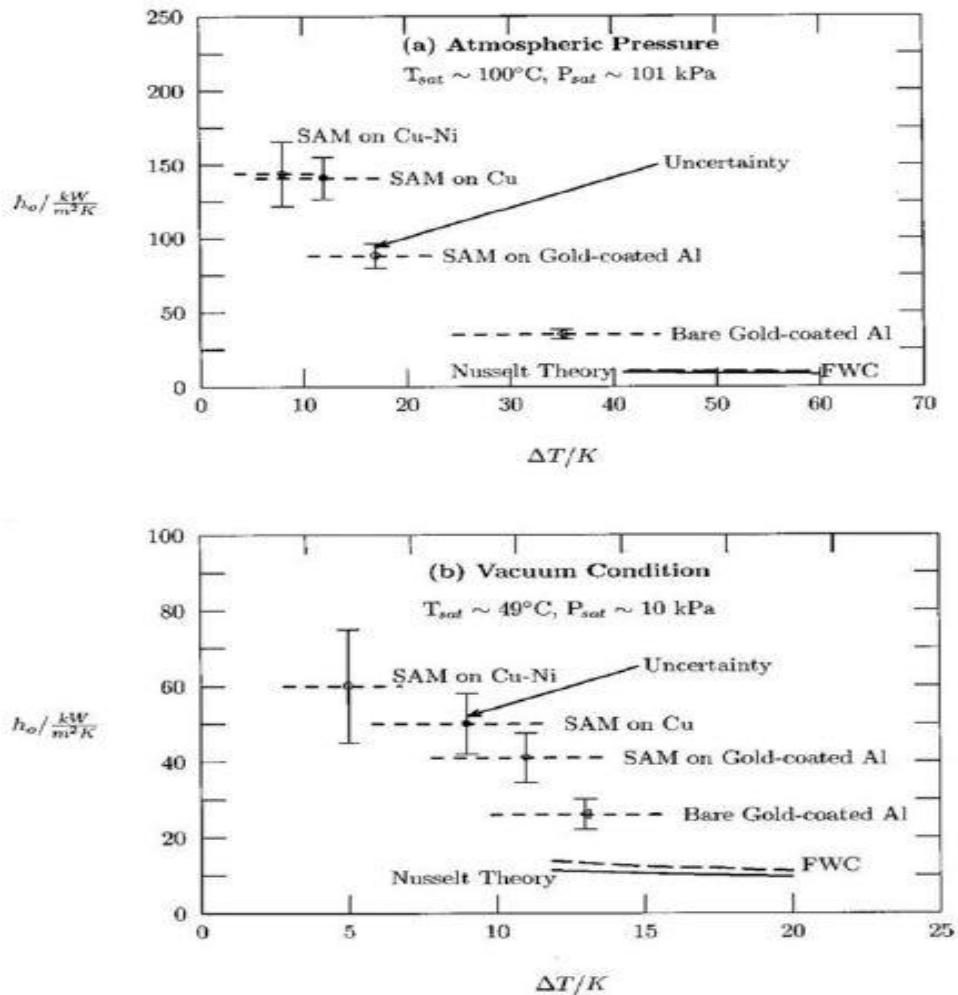
Figure 6.1: The heat transfer coefficient as a function of the surface subcooling at (a) atmospheric and (b) vacuum conditions for dropwise condensation (DWC) of steam on coated tubes [166].
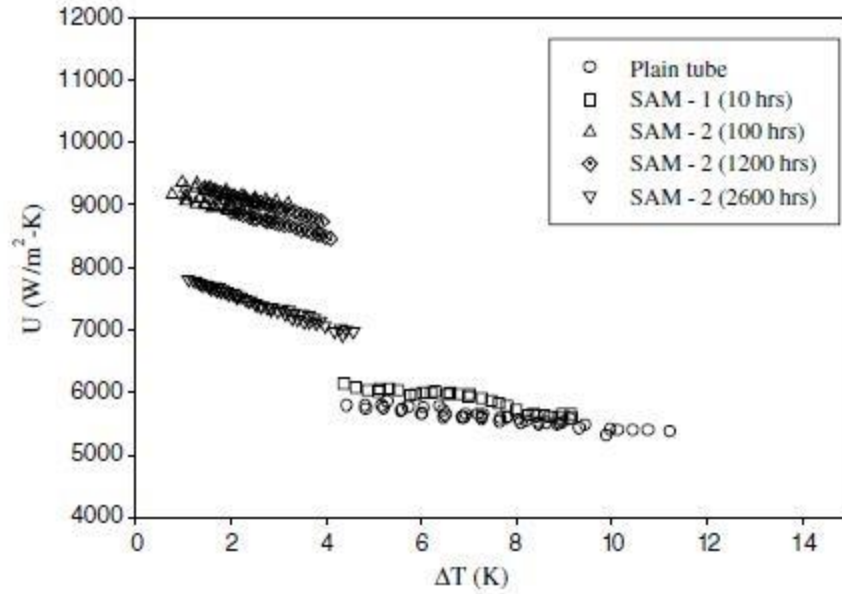
Figure 6.2: Heat transfer coefficient versus vapor to tube wall temperature [167]
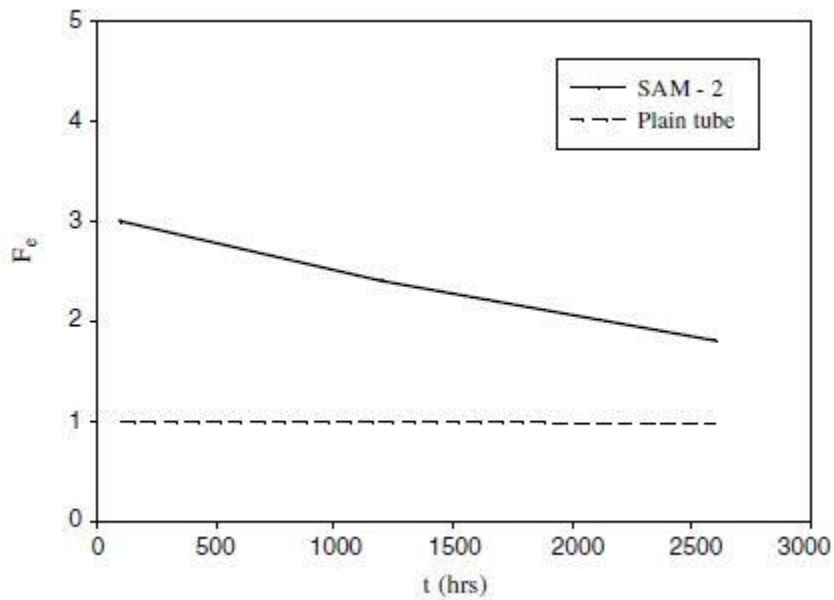
Figure 6.3: Condensation heat transfer coefficient enhancement factor versus the time of operation [167].

Vemuri et al. [167] have been investigated experimentally the effect of two different types of Self-assembled monolayers (SAMs) on the long-term durability of the dropwise condensation heat transfer characteristics. A thin organic hydrophobic film was

70

formed on a copper substrate, using either Stearic acid solution (SAM-1) or n-octadecyl mercaptan solution (SAM-2). The copper substrate was initially immersed in a 30% hydrogen peroxide solution for 8 h to form an oxide layer to improve the bonding between the copper substrate and the SAM coating. Stearic acid (SAM-1) coated surface, which has a contact angle of 155 °, showed dropwise condensation for only 10 h of experimentation, and then gradually changed to filmwise condensation mode with a contact angle of 61.1°. However, By using n-octadecyl mercaptan (SAM-2) coating, the experimental results exhibited that the condensation heat transfer coefficient was enhanced by a factor of 3 after 100 h of experimentation and by a factor of 1.8 after 2600 h of experimentation for copper alloy surfaces, under vacuum condition (33.86 kPa), compared to complete filmwise condensation. Also, for the SAM-2 coated surface, the contact angle changed from 148.5 ° to 111.2 ° after 2600 h of experimentation. From this research, it was proven that achieving lifetime dropwise condensation is substantially dependent on the bonding of the SAM coating to the condensing surface. It was found that n-octadecyl mercaptan (SAM-2) coating, which is bonded by covalent bonding, has high electrostatic attraction resulting in better bonding with the substrate surface and effective DWC compared with stearic acid (SAM-1) coating that is bonded by hydrogen bonding. Figure 6.2 shows the overall heat transfer coefficient versus vapor to the tube wall temperature difference at the vacuum pressure (33.86 kPa). For SAM-2 coating, the overall heat transfer coefficient is improved by a factor of 1.6 times after 100 h of testing and by a factor of 1.5 times after 1200 h of testing and by a factor of 1.3 times after 2600 h of testing when compared to complete filmwise condensation. Figure 6.3 shows the condensation heat transfer coefficient enhancement factor versus the time of operation for

71

the SAM-2 coated surface. Moreover, as compared to FWC, Figure 6.4 shows the heat transfer rate versus vapor to the tube wall temperature difference. It exhibits that when using SAM-2 coatings after 100 h, 1200 h and 2600 h of experimentation, the subcooling temperature was significantly decreased.
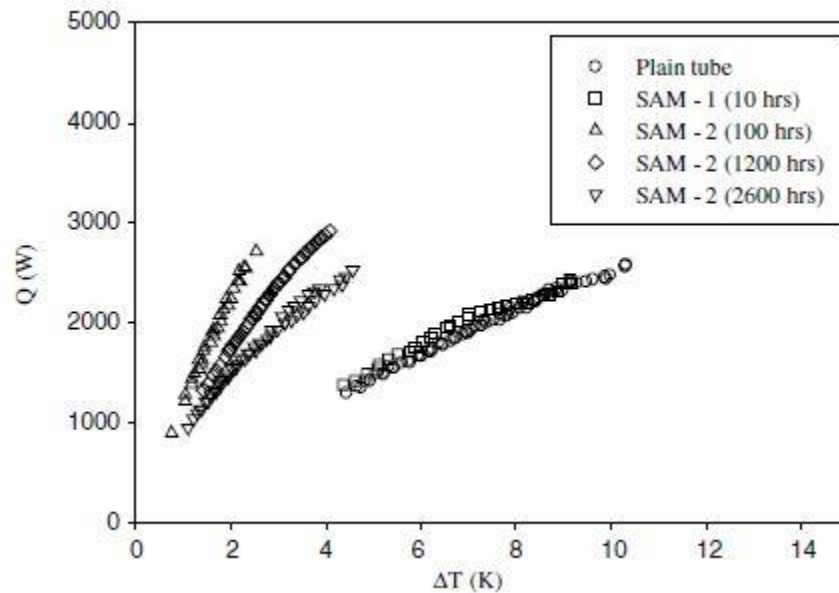
Figure 6.4: Heat transfer rate versus vapor to tube wall temperature difference [167].

6.1.2 Polymer coatings

Another method to reduce the surface energy and achieve DWC on the condensation surface is using polymer coatings such as polytetrafluoroethylene, parylene, and silicones [159, 160, 165, 171-173]. These polymer coatings can be applied on the substrate via sputtering or dip-coating [160, 174, 175]. It was proven that a thicker polymer film (>1 μm) is required to maintain the durability, but that can offset the advantage of DWC due to the increase in the thermal resistance of the polymer film [131]. Recently, developed techniques such as plasma-enhanced chemical vapor deposition (PECVD) and initiated chemical vapor deposition (iCVD) have been used to

72

form thin and ultrathin fluoropolymer coatings (< 40 nm) with success in promoting dropwise condensation [162]. However, the durability of the polymer coatings formed via iCVD and PECVD methods needs more characterization and experimentation to evaluate mechanical wear and chemical stability for long-term condensing applications.

Holden et al. [160] evaluated several polymer coatings for their ability to achieve and sustain DWC of steam at atmospheric pressure. Compared to the complete filmwise condensation, the heat transfer coefficients of steam DWC were enhanced by a factor of 3-8 times when using these polymer coatings. It was also reported that these polymer coatings can successfully promote dropwise condensation for about 22000 h (with polymer film thickness of 60 μm). Furthermore, it was observed that after more than 2 years of direct exposure to steam, some of these polymer coatings still show good quality in promoting dropwise condensation. However, none of the ultra-thin polymer coatings (with a polymer film thickness less than 1 μm) was able to chemically protect reactive substrates (such as copper and its alloys) from a steam/ water environment. Consequently, the continued oxidation of these substrates led to the failure of the polymer coatings.

Yang et al. [176] have investigated experimentally the effect of two different coatings on promoting dropwise condensation, over a vertical copper tube at atmospheric pressure. One was a docosanoic acid monolayer ($C_{21}H_{43}COOH$), which was prepared on the surface using self-assembled monolayers (SAMs) technique. The other one is Ni–P–PTFE composite coatings, which was formed on the copper surface with high and low PTFE contents using electroless plating technique. The results showed that excellent dropwise condensation was achieved on these coated surfaces. The condensation heat

73

transfer coefficient was improved by more than one order of the magnitude compared to complete filmwise condensation. The heat transfer characteristics of the SAM surface are slightly larger than those of Ni–P–PTFE surfaces as shown in Figure 6.5. This is because that the SAM coating has a thickness of 30 Å, leading to a negligible heat transfer resistance, whereas the Ni–P–PTFE coatings have the higher thickness of 4.1–4.3 μm resulting in higher heat transfer resistances. It was also observed that the Ni–P–PTFE coating with high PTFE content has the higher condensation heat transfer rate compared with that has lower PTFE content.
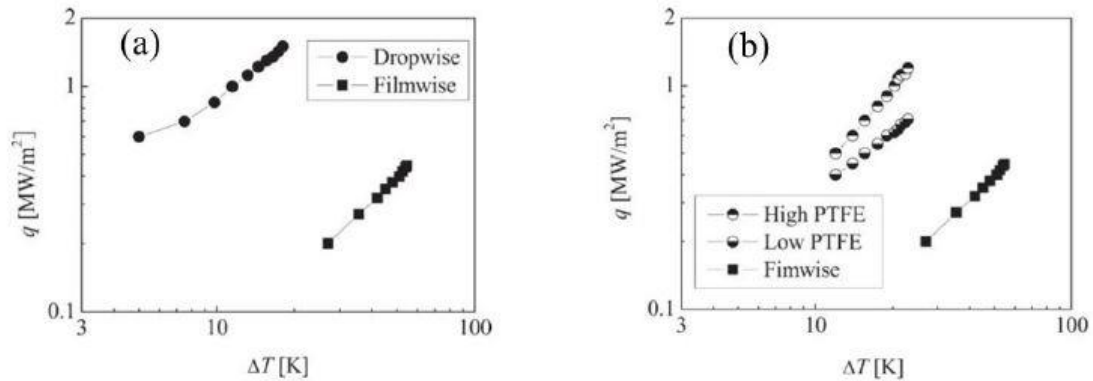
Figure 6.5: Heat flux as a function of the degree of surface subcooling , (a) SAM surface (b) low and high PTFE surfaces compared with filmwise condensation [176].

Ma et al. [161] investigated experimentally the effects of surface processing conditions of the polytetrafluoroethylene (PTFE) films on the dropwise condensation heat transfer of steam under atmospheric pressure. The dynamic ion-beam mixed implantation technique was used to form the polytetrafluoroethylene (PTFE) films on the external surfaces of brass tubes, copper tube, stainless steel tube and carbon steel tube. The experimental results showed that dropwise condensation was efficiently achieved on one of the PTFE coated surfaces at atmospheric pressure. Besides, it was found that,

74

compared to the values of filmwise condensation, heat flux was enhanced by 0.3–4.6 times and condensation heat transfer coefficient by 1.6–28.6 times for the brass tubes treated with various surface processing conditions. It was also concluded that the distribution of chemical components on the coated films is affected by the surface processing conditions, which are crucial to the adhesion between the polymer film and the metal substrate; thereby that significantly affects the condensation heat transfer properties.

Depew et al. [171] applied a polytetrafluoroethylene (Teflon) coating with a thickness of 0.00025-inch on a horizontal Viinch O.D. aluminum tube to investigate its ability in achieving dropwise condensation. Their results indicate that Teflon is a successful coating for promoting dropwise condensation. The enhancement in the heat transfer rates was up to 100% when the Teflon film was made 0.00005 inches thick. Also, they reported that thin Teflon coatings can adhere well to stainless steel and copper, as well as aluminum.

Marto et al. [172] developed new polymer coatings, as well as gold and silver, on various substrates, including square specimens and single horizontal tubes, to evaluate their ability to achieve and sustain long-term dropwise condensation of steam. The experiments have been conducted using two different heat transfer apparatus. The influence of the thermal conductivity and the roughness of the substrate, and the coating thickness on the condensation heat transfer performance were investigated. The experimental results showed that the organic coatings were effective in achieving high quality dropwise condensation for continued experimentation over 12,000 h. The dropwise heat transfer coefficients were enhanced by 3-6 times compared to the filmwise

75

condensation values. Also, it was reported that organic coatings with thicknesses of about 1 μm can successfully promote dropwise condensation for 2 years or perhaps more. The effect of wall thermal conductivity did not affect the experimental data when using these organic coatings. Moreover, the adhesion between the polymer film and the substrate improves when using a roughened substrate.
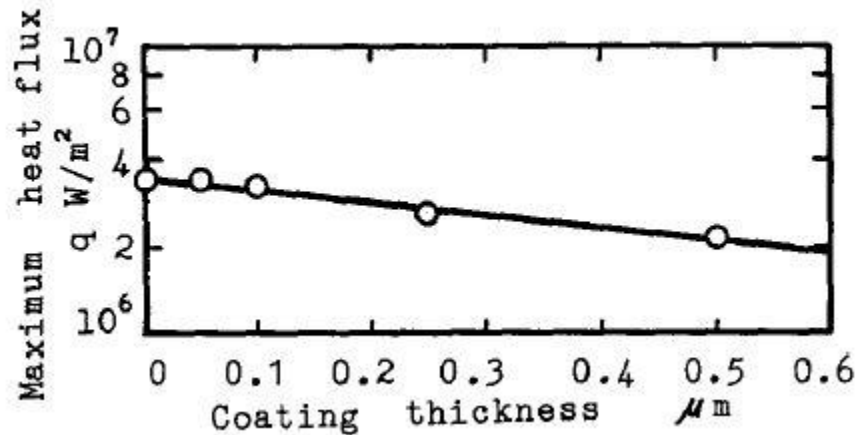
Figure 6.6: Effect of the coating film thickness on the maximum heat flux [159].

Haraguchi et al. [159] have proposed Polyvinylidene chloride coating as a promoter of dropwise steam condensation. The processing cost is much cheaper than the other polymer coatings such as PTFE. Also, this stable polymer coating can be used for large areas with a thickness of 1 A. Their experimental results showed enhancement in the heat transfer coefficient more than 20 times compared with filmwise condensation values. Furthermore, to investigate the effect of this polymer coating on promoting and sustaining dropwise condensation, four different coating thicknesses of 0.05, 0.10, 0.25 and 0.50 μm, were formed on a copper substrate and exposed to steam at atmospheric pressure. Their results were also compared with that presented by other researchers for an oleic acid coated copper surface, an electroplated gold surface, and a gold deposited

76

surface. Figure 6.6 shows that the maximum heat flux decreases with increasing the coating thickness. Moreover, in the large surface subcooling region, it was found that the coating thickness of 0.05 μm yields a dropwise condensation heat transfer performance comparable to that of gold or oleic acid promoting surfaces due to the lower thermal resistance compared with the other thicknesses, as shown in Figure 6.7.
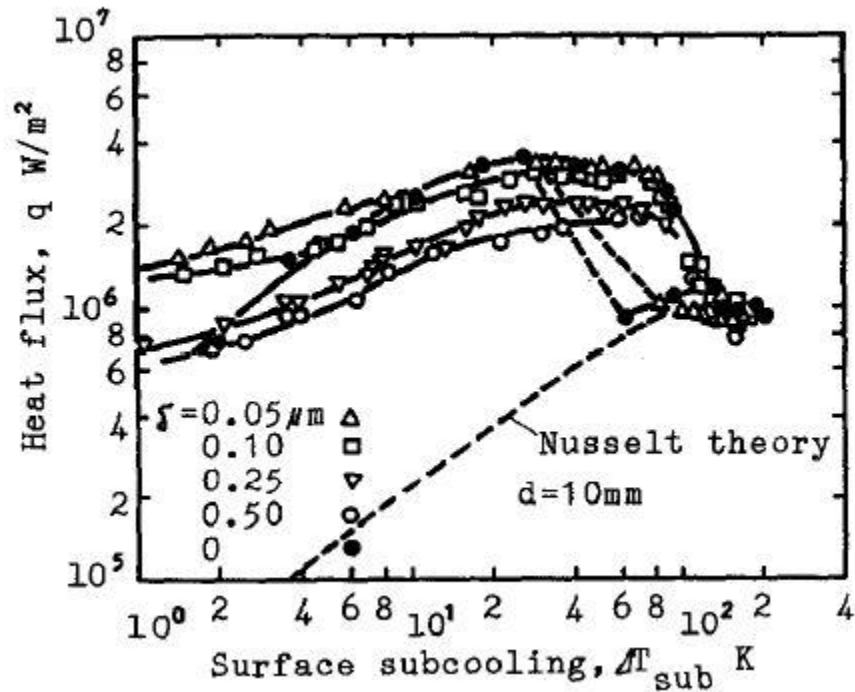
Figure 6.7: Effect of the coating thickness on heat flux [159].

Furthermore, the experimental results as shown in Figure 6.8 indicate that the heat transfer performance was improved with the decrease in the departure droplet diameter. It was found that the heat flux of the gold electroplated surface is lower than the coated surface with a film thickness of 0.05 μm. This is because the departure droplet size of dropwise condensation on the gold electroplated surface was about two times higher than that on the surface with a film thickness of 0.05 μm. Besides, based on durability tests, it was found that polyvinylidene chloride films can be employed in industrial for the

77

condensing applications. The durability test showed that a film with a thickness of 10 μm can sustain dropwise condensation over 21 586 h.
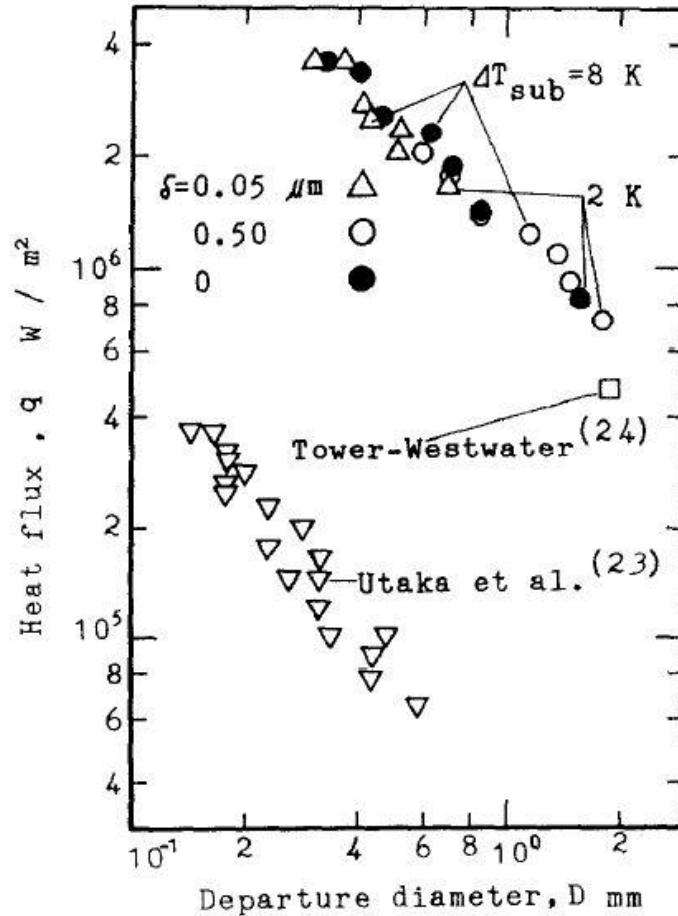
Figure 6.8: Effect of the departure diameter on heat flux [159].

6.1.3 Noble metals

Noble metals such as gold, silver, chromium, etc. have been used as permanent hydrophobic coatings to promote dropwise condensation. These metals have a little additional thermal resistance to heat transfer and the possibility of permanence [177]. Even though these noble metals have high surface energy and give filmwise condensation when exposed to steam [178]. DWC can be promoted on these surfaces due to the presence of physisorbed surface contaminants [179]. Therefore, in recent years,

78

considerable attention has been paid to investigate and understand the variables which influence the long-term durability of these coatings for promoting dropwise condensation. In 1970, Bernett and Zisman [180] revealed that pure water instinctively wets noble metals which are completely free of organic contaminants. However, Erb and Thelen [181] observed excellent dropwise condensation on electroplated gold, silver, rhodium, palladium and platinum surfaces. They found that on thin noble metals, dropwise condensation can be increased by more than half of filmwise condensation, and last more than 10,000 hours of continuous exposure. In this study, it was concluded that there is a critical minimum thickness of those noble metals required to achieve dropwise condensation and smaller thicknesses below these minimum values result in filmwise or mixed condensation.

In 1979, Woodruff and Westwater [182] studied dropwise condensation of steam at atmospheric pressure on electroplated gold surfaces, which are formed on vertical circular surfaces, to find the minimum thickness required to achieve dropwise condensation. They found that a minimum thickness of about 0.2 μm of gold was needed to achieve excellent dropwise condensation for over 2500 h of experimentation. Otherwise, filmwise or mixed condensation would happen on these surfaces Furthermore, the condensation heat-transfer coefficient increased by a factor ranging from 5 to 7 times depending on the subcooling temperature values. It was also observed that promotion of DWC on electroplated gold surfaces was mainly associated to the carbon-to-gold ratio on the surface.

O'Neill and Westwater [183] have conducted experiments to study the effect of electroplated silver surfaces, which were applied on electro-polished copper substrates,

79

on promoting dropwise condensation of steam at atmospheric pressure. The effect of silver plating thicknesses ranging from zero to 3000 nm was investigated. It was found that the endurance of the electroplated silver as a promoter of dropwise condensation depends upon the plating thickness, composition, and the surface preparation of the base metal. Continuous dropwise condensation was observed for about 2400 h on a plating thickness of 300 nm. Also, they found that the minimum thickness of electroplated silver required to achieve excellent dropwise condensation was about 150 nm.
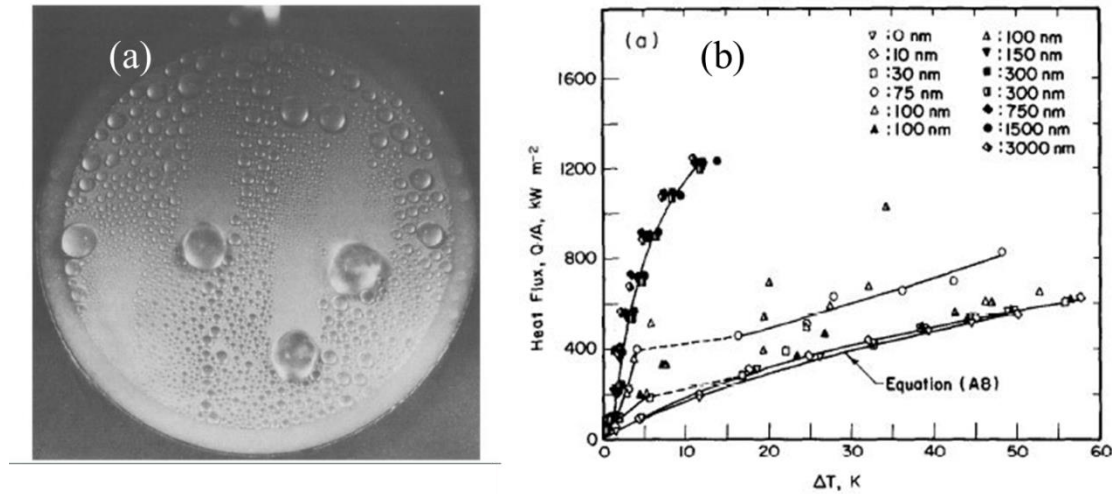
Figure 6.9: (a) Dropwise condensation of steam on electroplated silver coating, (b) Effect of silver plating thickness on the heat transfer during steam condensation [183].

Figure 6.9 shows the dropwise condensation of steam on the electroplating silver surface and the effect of silver plating thicknesses on the heat flux during steam condensation. It can be seen that all electroplates of 150 nm and thicker achieve dropwise condensation, which is attributed to the large amounts of carbon on the electroplated surface. Figure 6.10 reveals that as the plating thickness increased, large amounts of silver and carbon and small amounts of oxygen and copper were produced on the surface, leading to an increase in the heat transfer coefficient. On the other hand, thinner electroplates show higher percentages of copper and oxygen and lower percentages of

80

carbon and silver, resulting in producing either filmwise or mixed condensation. The same behavior was found previously for electroplated gold. Therefore, it can be concluded that the carbon was probably the true promoter of dropwise condensation on these noble metals.
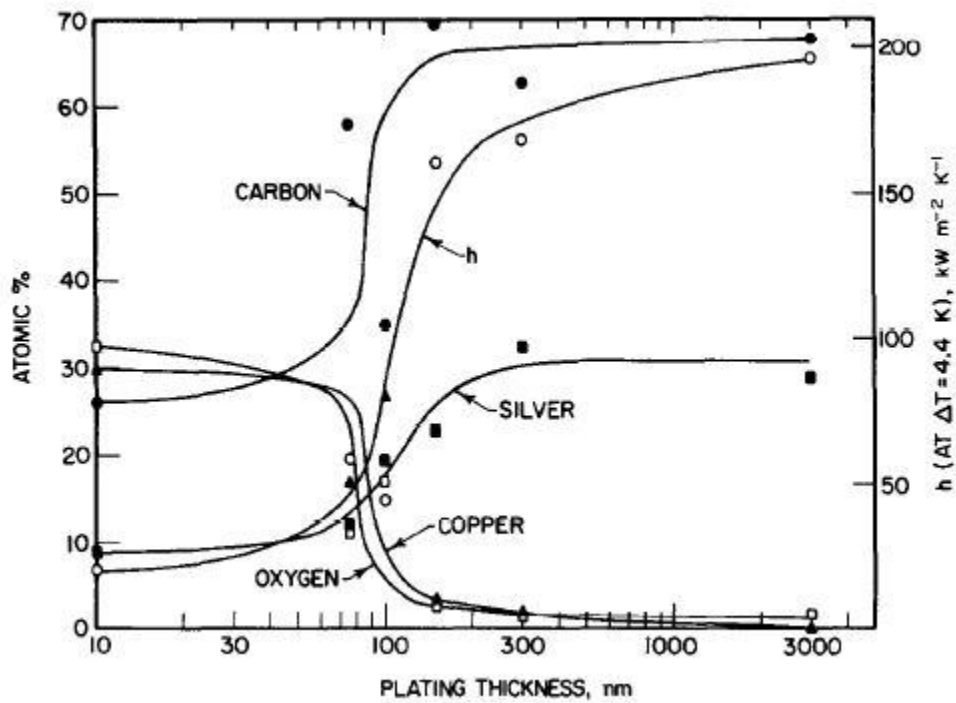
Figure 6.10: The influence of thickness of silver coating on the surface composition and the condensation heat transfer coefficient [183].

Finicum and Westwater [184] have studied experimentally steam condensation at atmospheric pressure on a vertical disc of electroplated chromium coating, and on pure metallic chromium formed by powder metallurgy. The results showed that when there was no air in the condenser chamber, the clean steam condensed in a filmwise manner on the uncontaminated chromium surfaces. It was also found that compared to gold and silver, the clean chromium coating is a poor adsorber of trace organic materials from the surroundings, and that led to filmwise condensation of steam on this surface as shown in Figure 6.11. However, it was observed that with a large amount of air in the condenser,

81

dropwise condensation can be achieved on chromium coating but with low heat transfer coefficient. Moreover, it was found that when pure metallic chromium was vacuum impregnated with the oleic acid promoter, dropwise condensation of steam was achieved and lasted over 3000 h of experimentation. In this study, they concluded that there is no minimum thickness to achieve long-lasting dropwise condensation of steam on chromium surface.
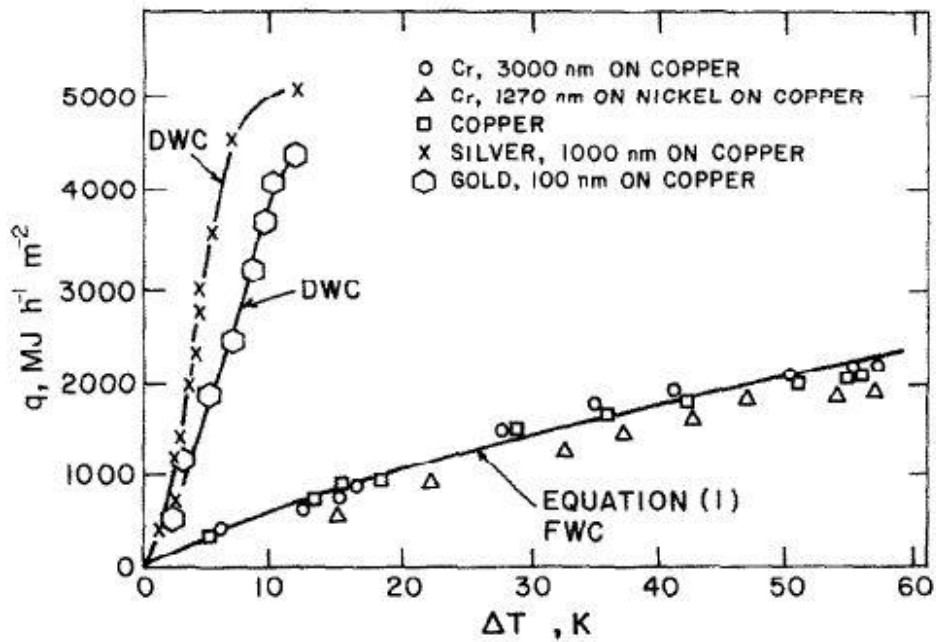
Figure 6.11: Heat flux versus the degree of subcooling for chromium, silver and gold electroplating coatings during steam condensation [184].

6.1.4 Graphene coating

It was recently proven that the graphene coating on the metals (i.e., copper, Nickel, etc.) could promote and sustain the dropwise condensation [127]. The graphene layer consists of carbon atoms which are arranged in a two dimensional hexagonal lattice [185] and shows a hydrophobic behavior due to the existence of the carbon atoms in the surface. This is similar to the behavior of the noble metals that absorbs the carbon

82

contamination from the environmental naturally as explained previously. However, the graphene coating was artificially fabricated on metals surfaces using developed techniques to achieve ultrathin layers with robust chemical stability and lower thermal resistance.
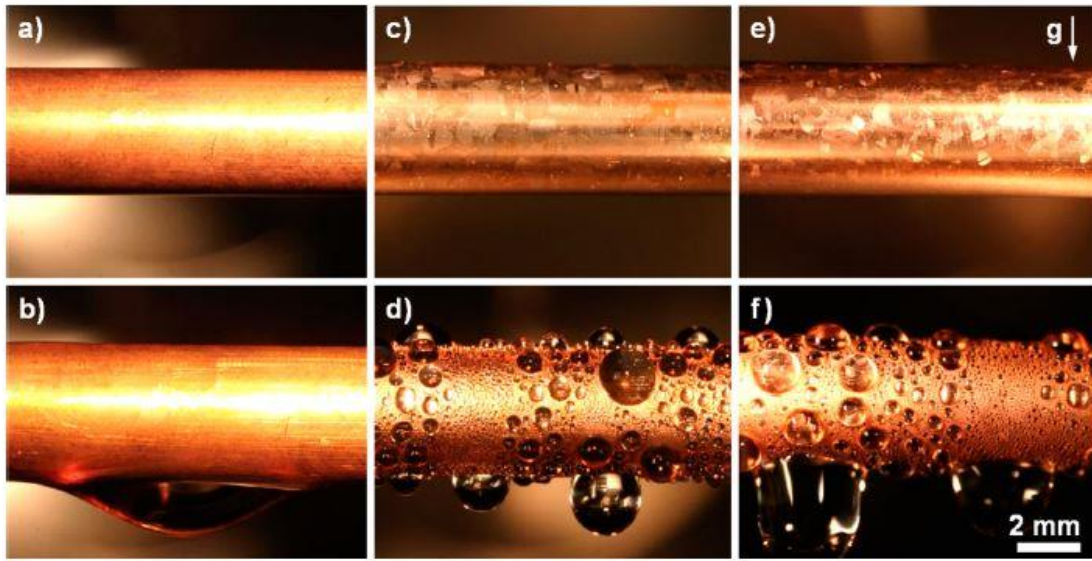
Figure 6.12: Images for filmwise condensation on a copper condenser tube (a) under vacuum and (b) undergoing of deionized and degassed water vapor, images of under vacuum and undergoing of dropwise condensation on LPCVD graphene coating (c,d) and and the APCVD graphene coating in (e,f). [127].

Recently, Preston et al. [127] have fabricated an ultrathin scalable graphene coating on the horizontal copper tubes using chemical vapor deposited method (CVD) to promote the steam dropwise condensation. The comparison between the graphene coating fabricated by low-pressure CVD (LPCVD) and by atmospheric pressure CVD (APCVD) on the condensation heat transfer enhancement was investigated. Figure 6.12 shows the condensation phenomena on the two types of graphene coatings (LPCVD, APCVD). The experimental results demonstrated an enhancement of 4x in the heat transfer rate for both the graphene coatings compared to filmwise condensation as shown in Figure 6.13. Moreover, it was reported that the robustness of the graphene coating using the CVD

technique was superior to the typical hydrophobic long-chain fluorocarbon monolayer coatings. The results showed that the hydrophobic monolayer coating was degraded completely after 12 h of experimentation, whereas a continuous dropwise condensation was observed more than two weeks for the graphene coatings without any degradation.
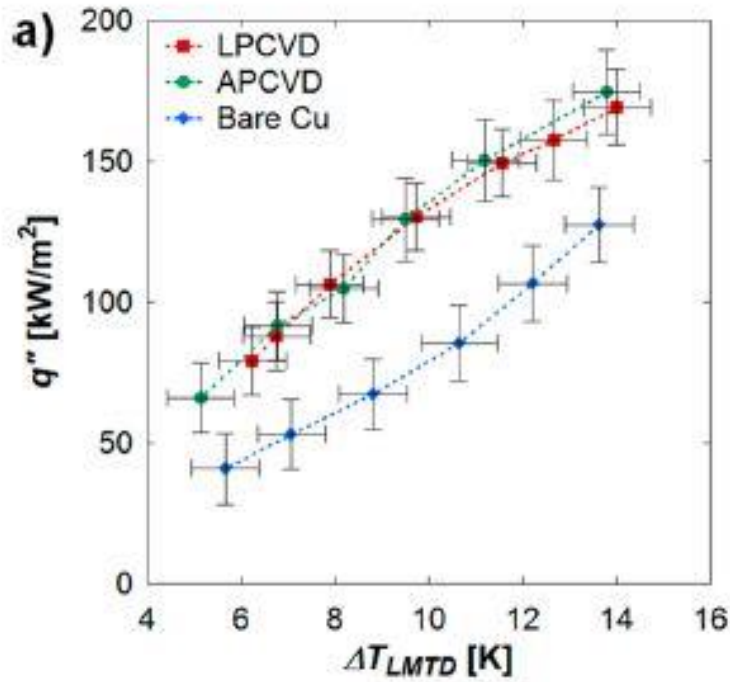
Figure 6.13: Overall surface heat flux as a function of r log mean temperature difference (ΔTLMTD) for bare copper, LPCVD and APCVD graphene coatings. [127].

6.1.5 Ion implantation method

Another method to reduce the surface energy and the surface wettability of the condensing surface and achieve dropwise condensation is using plasma ion implantation method. The basic concept of the ion implantation method is fabricating alloys which have low surface energy in a metallic surface layer of 1-2 μm by utilizing magnetron sputtering ion plating or dynamic mixing ion implantation technology [164]. The reduction in the free surface energy of the implanted surface can be explained based on the fundamental equation of the free surface energy, which is given by;

$$E_b = U_b - TS_b \tag{6.1}$$

Where E_b is the free surface energy, U_b is the internal energy, T is the surface temperature, and S_b is the surface entropy. It can be noticed from the above equation that the free surface energy can be reduced by decreasing the internal surface energy (U_b) and by increasing the surface entropy (S_b). The implantation of foreign elements, which have high surface energy, into the surface leads to an increase in the surface entropy. This is because that the implanted elements cause an increased disorder in the surface. In addition, if the implanted elements have enough ion energy, the interatomic bond energy in the surface will be decreased, and hence the internal energy will be considerably reduced. Consequently, increasing the ion energy of the implanted elements leads to more decreasing in the surface free energy of the implanted surface.

The ion implantation method was first discovered by Zhang et al. [164, 186] and Qi et al. [163]. They have investigated the effects of various surface processing methods, including ion plating, and ion-beam mixing technology to reduce the surface energy of the condensing surface and promote dropwise condensation. They found that the dropwise condensation heat transfer is considerably affected by the processing condition for different implanted elements. Their experiments showed that using ion implantation of N, Ar, He, H, and Cr in copper tubes can achieve excellent dropwise condensation. The Cu–Cr alloy layer, which is prepared on the copper substrate by using ion plating and ion-beam mixing combination technique, sustained dropwise condensation for about 8500 h of experimentation [163, 186]. Another study was also introduced by Zhao and Burnside [164]. They have fabricated a PTFE-coated surface with implanted Cr^+ on a single horizontal tube. They found that a pure PTFE-coated surface provides a DWC heat

85

transfer coefficient for steam 1.8 times as large as that on the untreated tube filmwise value. However, the implanted PTFE-coated surface provides heat transfer coefficients five times more than that in filmwise condensation on the unimplanted tubes. For this reason, researchers have paid considerable attention to implement this novel technology in promoting dropwise condensation on different condensing surfaces by developing different alloy composites, having low surface energy, on condensing surfaces such as titanium, stainless steel, aluminum, etc. The influence of various parameters including the number of ion dose, the implantation energy, macroscopic surface roughness, and oxidation effects on the condensation performance were investigated [163, 164, 187-189].
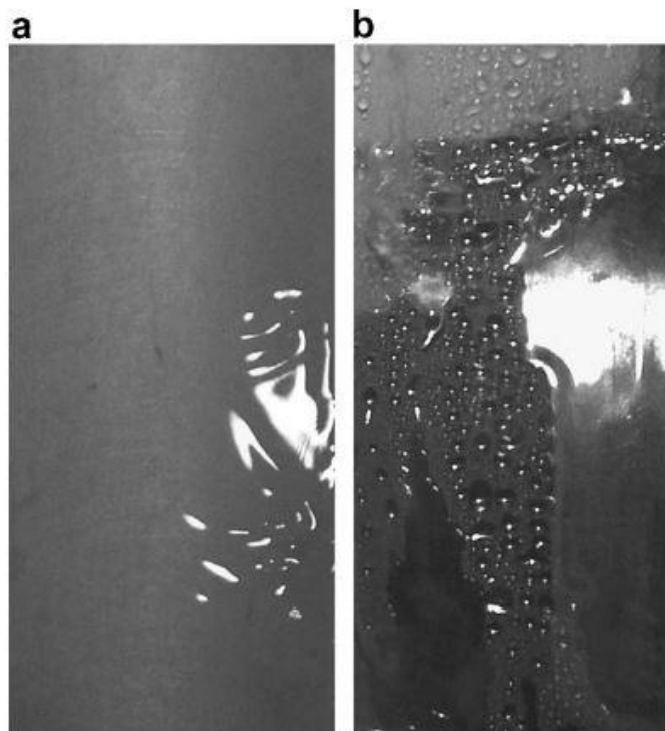
Figure 6.14: The condensation phenomena on the the aluminum surface (a) FWC on unimplanted surface (b) and mixed FWC and DWC on implanted polished Al 6951 plates [188].
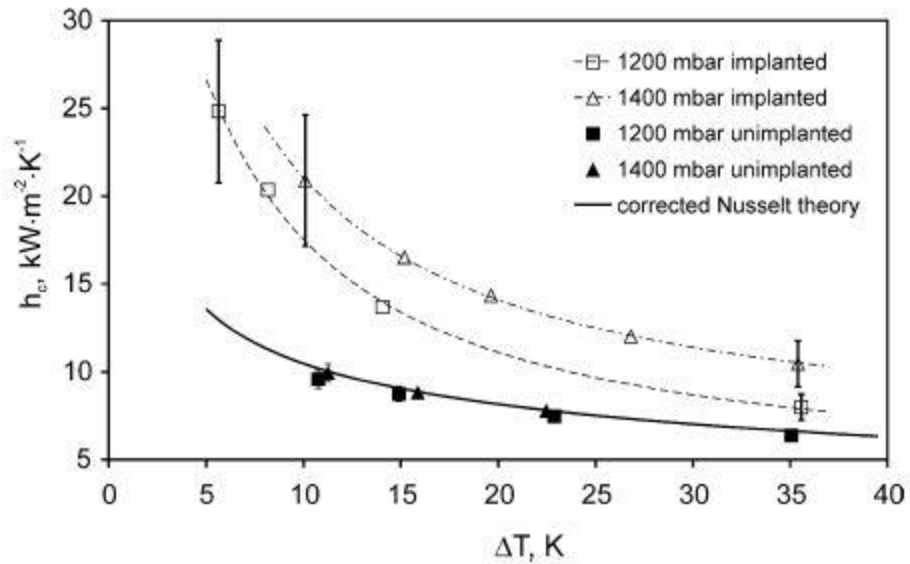
Figure 6.15: **T**he heat transfer coefficient as a function of surface subcooling on unimplanted and implanted polished Al 6951 plates at different steam pressure [188].

Rausch et al. [188] have investigated the effect of two aluminum alloys of Al 3003 and Al 6951, which are prepared by using ion beam implantation technology, on promoting Stable dropwise condensation (DWC) of saturated steam. The first part of this study was carried out using aluminum alloy discs of Al 3003 and Al 6951 with changing ion dose and implantation energy. The results showed that DWC could be promoted on Al 6951, but there was a mixture of FWC and DWC on Al 3003 as shown in Figure 6.14. The second part of this work was conducted at steam pressures of 1200 and 1400 mbar on vertical plates of the same materials to measure the condensation heat transfer coefficients as a function of surface subcooling. As shown in Figure 6.15, the heat transfer coefficient increases while the steam pressure increases and the surface subcooling decreases. It was also observed that if the ion implantation does not induce DWC on the implanted surfaces, the condensation heat transfer coefficient cannot be improved. The aluminum alloys are very sensitive to the implantation parameters

87

including ion dose and the implantation energy. Therefore, it was found that owing to the inhomogeneity of the alloy compositions, DWC was achieved only on about 50% of the vertical plate with an enhancement factor of 2.0 compared to complete FWC value. It was also observed that the surface roughness for the aluminum alloys has a crucial effect on the obtained DWC form. The smooth surfaces are preferred for the improvement of DWC. Furthermore, the endurance of the dropwise condensation of saturated steam was continually sustained on the polished Al 6951 sample for about 8 months of experimentation. However, after exposing the sample to ambient air for 2 months, the surface was oxidized, and when the sample reinstalled into the condenser, the condensation form on the surface changed to FWC.
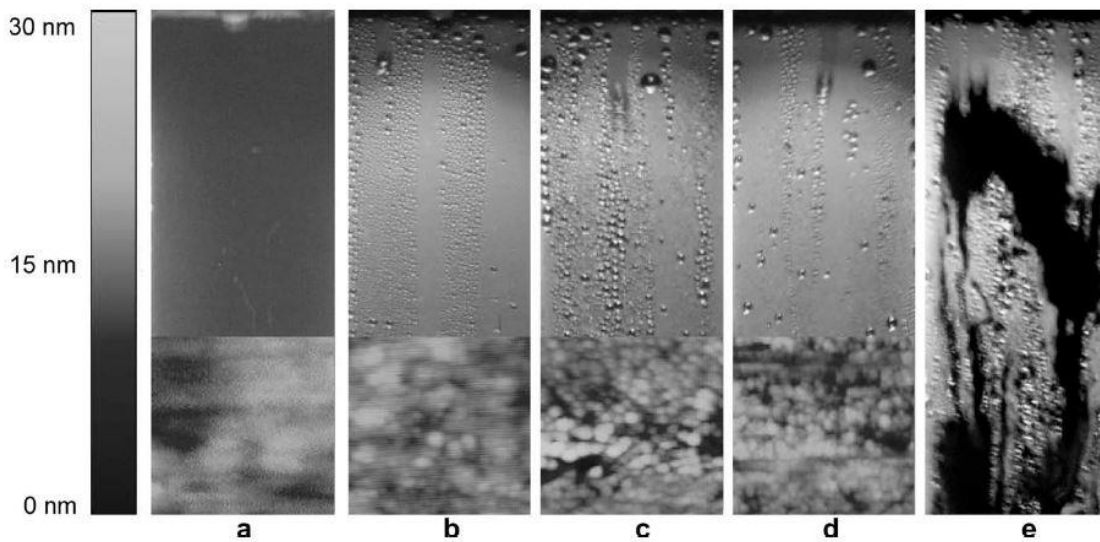
Figure 6.16: Condensation observation on polished titanium surfaces (a) Pure unimplanted titanium (b) $10^{16}N^+cm^{-2}$ ion dose and 20 Kev implantation energy (c) $10^{16}N^+cm^{-2}$ ion dose at 60 Kev (d) $10^{15}N^+cm^{-2}$ ion dose at 20 Kev (e) $10^{15}N^+cm^{-2}$ ion dose at 20 Kev [189].

Dropwise condensation of steam at atmospheric pressure was achieved on rough and polished titanium surfaces using ion beam implantation of N^+ [189]. It was observed that in spite of the high wettability characterized by low contact angle and high surface

www.manaraa.com

free energy, dropwise condensation can be promoted by ion implantation method. The effect of ion implantation method parameters, such as the number of ion doses and the implantation energy, on condensation heat transfer performance, was investigated. Figure 6.16 shows the visual observation for condensation on the unimplanted and implanted samples at different numbers of ion doses and implantation energy. It was also noticed that the applied ion implantation parameters did not significantly affect the condensation heat transfer coefficient as shown in Figure 6.17. In addition, the heat transfer measurements showed that the condensation heat transfer coefficient for the ion-implanted titanium plates is 5.5 times larger than those values in the complete filmwise condensation.
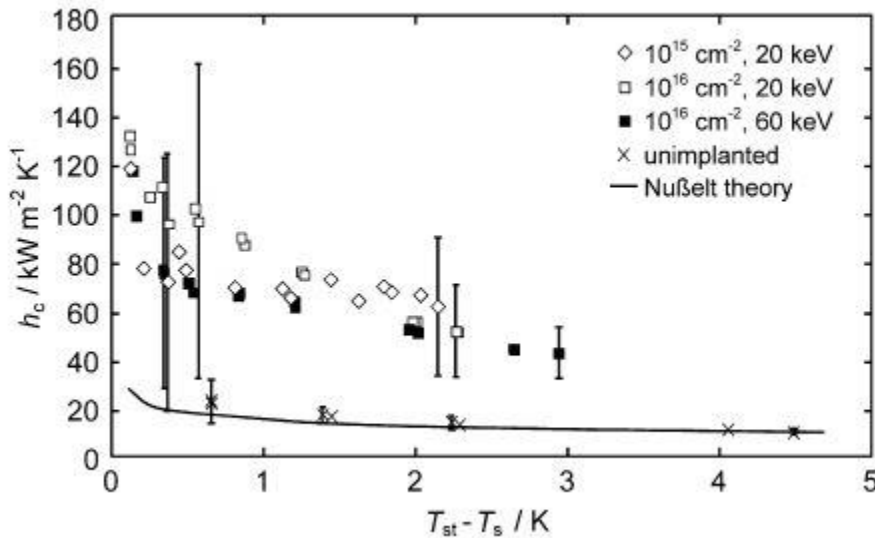
Figure 6.17: The effect of the number of ion dose and implantation energy on condensation heat transfer coefficient on titanium surfaces.

Kananeh et al. [187] have applied the Plasma-ion implantation method to promote stable dropwise condensation of saturated steam on horizontal stainless steel tubes. Figure 6.18 exhibits the condensation phenomena on the bare unimplanted and implanted stainless steel tubes using the ion beam method. The effect of the number of ion doses on

89

the condensation heat transfer performance has been investigated. The results showed that increasing the ion dose increases the condensation heat transfer coefficients and the heat flux density. This is because of the decrease in the free energy and the wettability of the implanted surface.
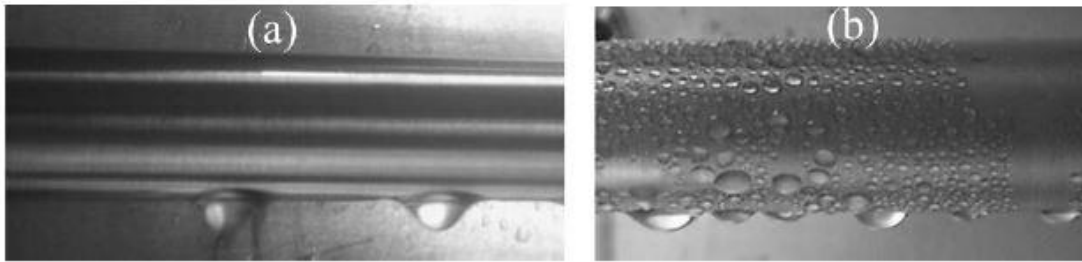
Figure 6.18: (a) Filmwise condensation (FWC) on an unimplanted stainless steel tube (b) dropwise condensation (DWC) on an implanted stainless steel tube [187].
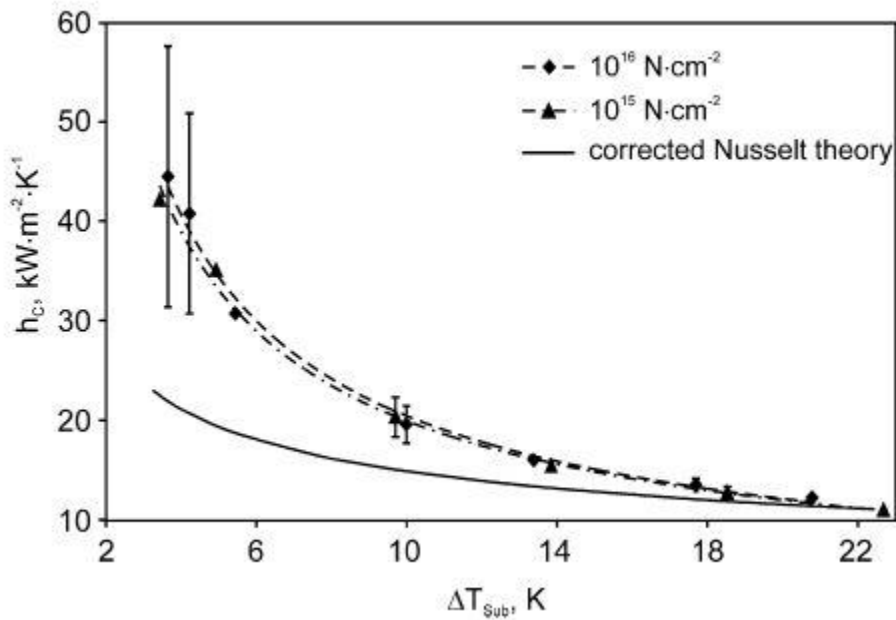
Figure 6.19: Heat transfer coefficient on implanted stainless tube versus the degree of subcooling, with different ion doses at a steam pressure of 1050 mbar and compared with FWC values calculated by corrected Nusselt theory [187].

Figure 6.19 shows the heat transfer coefficient as a function of subcooling temperature at a steam pressure of 1050 mbar for implanted stainless steel tubes with

www.manaraa.com

different ion doses, and a comparison with FWC values calculated by corrected Nusselt theory. It was also found that, for stainless steel tubes implanted with a nitrogen ion dose of 1016 and 1015 N cm^2, the heat transfer coefficient for DWC was enhanced by a factor of 3.2 and 2.2, respectively compared with complete filmwise condensation values calculated by the corrected Nusselt film theory. In addition, it was observed that as the subcooling increases the heat transfer coefficient decreases. This is due to the increase in the amount of condensate on the tube surface, resulting in additional heat transfer thermal resistance. It was also noticed that the heat flux density and the heat transfer coefficient increase with increasing steam pressure at constant subcooling as shown in Figure 6.20. This is due to the decrease of the interfacial resistance to mass transfer at the liquid-vapor interface, and the increase in the steam temperature, leading to reduce the surface tension of the condensate and the droplet diameter which rolls off the condensing surface.
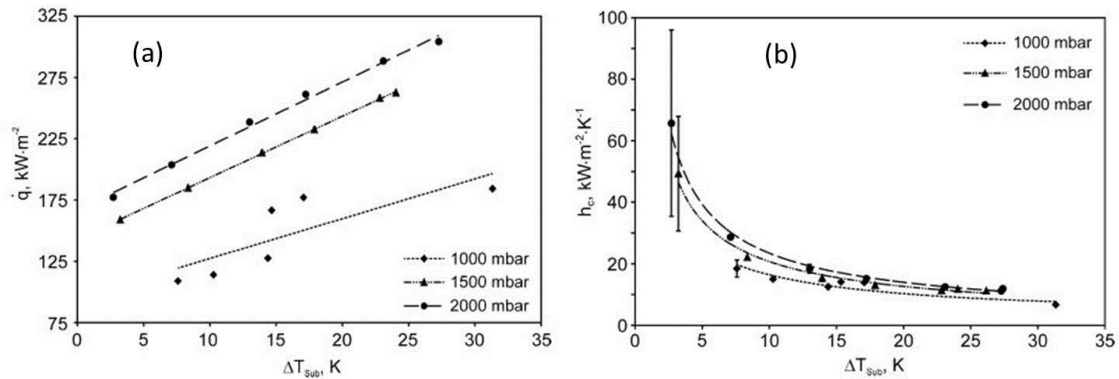
Figure 6.20: (a) Measured heat flux density (b) Measured heat transfer coefficient, on an implanted tube with an ion dose of 1016 N cm^{-2} as a function of subcooling, for different steam pressures [187].

6.2 Effects of surface modifications on promoting dropwise condensation

6.2.1 Superhydrophobic surfaces

The combination of nano/microstructures and low-surface-energy coatings to fabricate superhydrophobic surfaces, with an apparent contact angle larger than 150∘ and

91

a contact angle hysteresis approaches to 0, results in achieving extreme nonwetting properties and allowing droplets to form in a Cassie wetting state [81]. These surfaces can be developed by reducing the surface energy and modifying the surface structure by producing superficial micro/nano-roughness using, for example, chemical etching or other developed techniques. Recently, fabricating such surfaces to promote dropwise condensation had drawn significant attention [126, 140, 155, 190-192]. Although the superhydrophobic surface can achieve dropwise condensation, it is sensitive to some crucial issues. First, the droplet nucleation density on the superhydrophobic surface is much lower than that on a hydrophilic surface. This is because of the higher nucleation energy barrier on a superhydrophobic compared to that on the hydrophilic surface [193, 194]. Second, the high apparent contact angles of liquid droplets on superhydrophobic surfaces results in increasing the conduction resistance through the condensing droplet and thereby reducing the overall heat transfer performance [155, 195]. Third, although the vapor layer within the superhydrophobic surface causes the condensate droplet to be in the Cassie state, it also leads to increase the thermal resistance [155] . Moreover, a transition from the suspended Cassie state to the undesired sticky Wenzel state can happen for the condensed droplets on the superhydrophobic surface due to the Laplace pressure instability mechanism [192, 196, 197], resulting in reducing the droplet departure frequency. Furthermore, under high supersaturation conditions, liquid flooding within the nanostructures can be induced due to the increased droplet nucleation density, resulting in reducing the dropwise condensation efficiency [126, 198]. Therefore, according to the above discussion, an efficient designed superhydrophobic is required to enable increasing droplet nucleation density, reducing droplet departure size, and

www.manaraa.com

minimizing thermal barrier [199]. It was reported that a superhydrophobic surface with a roughness less than the capillary length scale, where Bond number much smaller than unity, can improve droplet mobility and reduce the departure radii, resulting in continuous shedding of liquid droplets in condensation [198, 200, 201]. However, it was found that not all the superhydrophobic surfaces can shed off condensing droplets away under condensation. The Bond number and liquid-solid fraction should be less than 0.1 and 0.3, respectively to achieve efficient shedding of condensate [202]. Recently, it was found that the condensation heat transfer performance was enhanced on some of the Superhydrophobic surfaces [167, 203-205]. However, it was observed inefficacy in enhancing heat transfer rates on other superhydrophobic surfaces [154, 199, 206, 207]. Also, a low droplet departure frequency and flooding were recognized on some of the superhydrophobic surfaces [154, 207], resulting in inefficient heat and mass transfer. Accordingly, the effect of superhydrophobic surfaces in improving condensation is controversy in the literature.
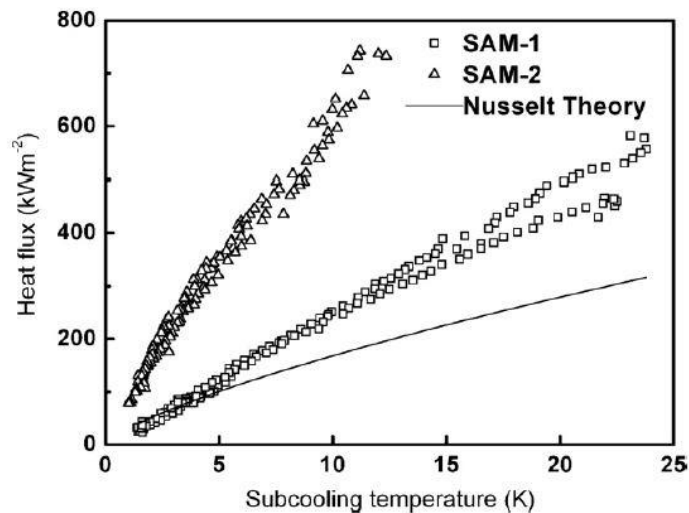
Figure 6.21: Heat flux as function of surface subcooling for nanostructures (SAM-1) and smooth (SAM-2) coated surfaces, during dropwise condensation (DWC) [207].

93
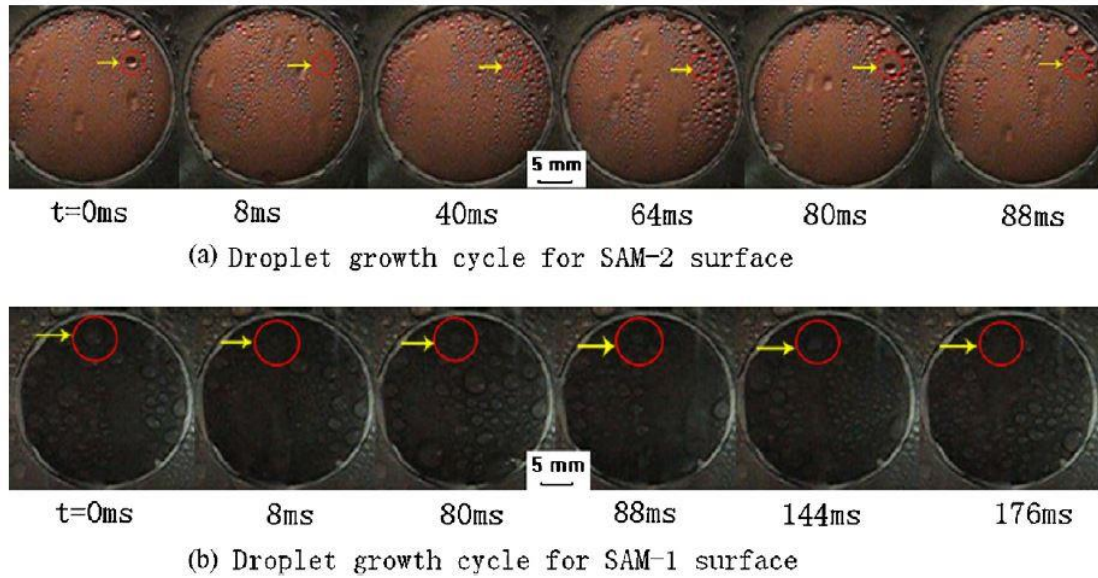
Figure 6.22: Droplet growth cycle during dropwise condensation for nanostructures (SAM-1) and smooth (SAM-2) coated surfaces, at atmospheric pressure and surface subcooling (ΔT = 3-5K) [207].

Zhong et al. [207] have experimentally investigated the influence of the surface free energy and nanostructures on steam dropwise condensation performance on vertical copper surfaces. Self-assembled monolayers coatings of n-octadecyl mercaptan were implemented to prepare a hydrophobic surface on a mirror-polished copper substrate (SAM-2). On the other hand, nanostructures on a copper substrate were prepared by oxidation and chemical etching methods, and then the prepared surface was treated with the SAM coating to form a superhydrophobic surface (SAM-1). The experimental results showed that even though the condensing surface area and the apparent contact angle of the superhydrophobic nanostructure (SAM-1) are higher than those on the mirror-polished surface (SAM-2), the latter has higher dropwise condensation performance. The condensation heat transfer is improved by a factor of 3 for the mirror-polished surface (SAM-2) and by a factor of 1.8 for the superhydrophobic nanostructure surface (SAM-1), compared to filmwise condensation values predicted by Nusselt's model, as shown in

94

Figure 6.21. This is because the apparent surface free energy of the nanostructure surface (SAM-1) is greater than that of the mirror-polished surface (SAM-2), which indicates that the surface free energy difference between the condensate and the condensing surface of SAM-2 is higher than that of SAM-1. Moreover, the droplet departure diameter on the nanostructured surface during dropwise condensation is greater than that on the (SAM-2) surface as shown in Figure 6.22. This is due to the larger contact angle hysteresis for the nanostructured (SAM- 1) surface and the adhesion effect when the condensate fills the nanostructure surface, which results in reducing the droplet departure frequency. Consequently, the dropwise condensation heat transfer coefficients for (SAM-2) surface are greater than those of (SAM-1) surface.
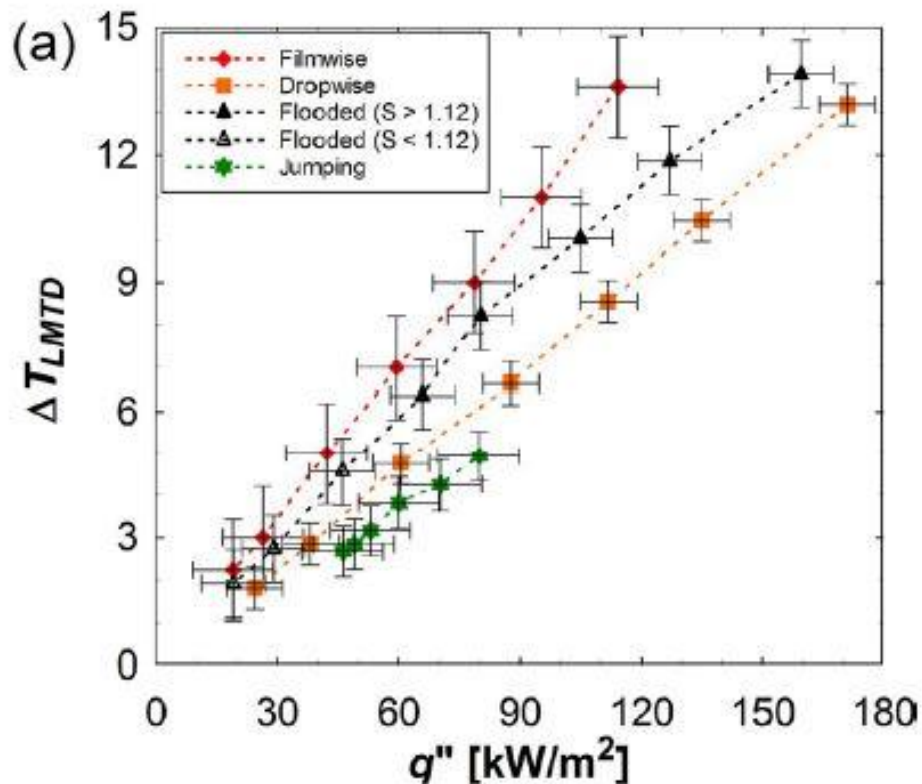
Figure 6.23: Overall surface heat flux (q″) as a function of state log mean water to vapor temperature difference (ΔTLMTD) for tube surfaces undergoing filmwise, dropwise, flooded, and jumping condensation [154].

95
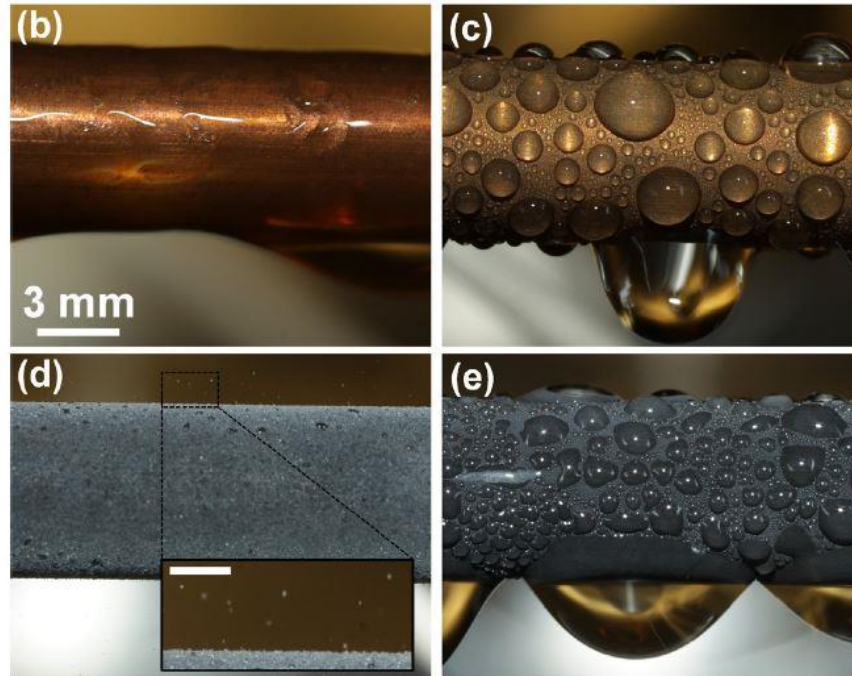
Figure 6.24: Images of the condensation on (b) a smooth hydrophilic Copper tube, FWC, (c) a silane coated smooth Copper tube, DWC (d) jumping-droplet superhydrophobic condensation on a nanostructured CuO tube at low subcooling, and (e) flooded condensation on a nanostructured CuO tube at high subcooling [154].

Miljkovic et al. [154] have experimentally studied the effect of superhydrophobic copper oxide (CuO) nanostructures surfaces on promoting steam dropwise condensation on horizontal copper tubes. A wet chemical etching method was first used to develop the nanostructured copper oxide (CuO) coating, and then the surface was deposited in fluorinated silane (trichloro(1H,1H,2H,2H-perfluorooctyl) to decrease the surface free energy and achieve the superhydrophobic surface. The oxide thickness of the silanized copper oxide surface was about 1 μm, which promises a low conduction thermal resistance to the heat transfer. It was demonstrated that at low surface subcooling, droplet self-propelled jumping phenomenon could be induced when droplets coalesce on such superhydrophobic nanostructured surfaces, resulting in enhancing the dropwise condensation heat transfer by increasing the removal of condensate formed on such low-energy surfaces. The experimental results showed that when using silanized copper oxide

www.manaraa.com

(CuO) superhydrophobic surfaces, the overall heat flux and the condensation heat transfer coefficient could be enhanced by 25% and 30%, respectively compared to that on smooth hydrophobic surfaces at low supersaturations ($S < 1.12$). On the other hand, the coalescence-induced droplet jumping phenomena on the superhydrophobic copper oxide surface was not observed at higher surface subcooling. It was found that at high supersaturations ($S > 1.12$), the condensation heat transfer coefficient was reduced by 40% compared to the smooth hydrophobic condensing surface as shown in Figure 6.23. This is because that the nanostructured surface was flooded with the condensate and then more condensation on the flooded surface led to form highly pinned Wenzel droplets with irregular shapes and large droplet shedding sizes. Figure 6.24 shows Images of the condensation on a smooth hydrophilic Copper tube, a silane coated smooth Copper tube, jumping-droplet superhydrophobic condensation on a nanostructured CuO tube at low subcooling, and flooded condensation on a nanostructured CuO tube at high subcooling.

Parin et al. [208] have investigated the ability of four different superhydrophobic aluminum samples in achieving steam dropwise condensation. The four samples were modified via four wet-chemical etching techniques to achieve nanoscale roughness, and then to reduce the surface free energy, a fluorosilane film was deposited on these different samples using two different methods (pin coating and immersion). The contact angle measurements showed that three samples have advancing contact angles higher than 150° and contact angles hysteresis lower than 10° at room temperature, while the fourth sample, which was modified using another etching technique, has high advancing contact angle ($\theta_a = 151°$) but low receding contact angle ($\theta_r \approx 10°$). The experimental results showed a successful dropwise condensation could be achieved on

97

superhydrophobic surfaces (Sample #1, #2 and #3), but the fourth sample, which has high contact angle hysteresis, revealed filmwise condensation. However, the dropwise condensation on the other three surfaces changed to a hybrid and filmwise condensation after some time of experimentation. Furthermore, it was also found that the fabrication chemical process has a significant effect on the dropwise condensation enhancement. Sample 1, which has the highest roughness, showed the highest value of condensation heat transfer coefficient and it is approximately 8 times larger than that values of filmwise condensation on the untreated aluminum sample as shown in Figure 6.25.
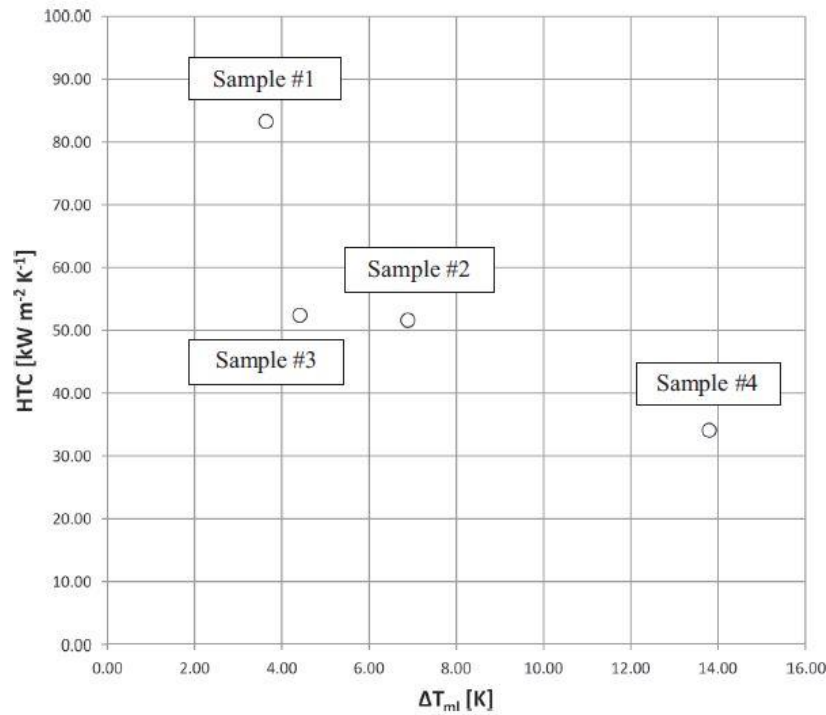
Figure 6.25: Maximum values of heat transfer coefficient (HTC) as a function of mean logarithmic temperature difference between steam and wall for Sample #1, Sample #2, Sample #3 and Sample #4 during pure steam condensation. [208].

Chang Lu et al. [209] have developed a superhydrophobic silicon nanowire (SiNW) array-coated surface on a vertical silicon wafer to promote steam dropwise condensation. A chemical etching method was first used to form the silicon nanowire

arrays with diameters and spacings ranging from 50 to 300 nm, and a height of 10 μm approximately as shown in Figure 6.26. A thin layer of Teflon was coated on the silicon nanowire surface with a thickness of 20 nm using the inductive coupled plasma reactive ion etching method to obtain the superhydrophobic SiNW nanowire surface. The surface has a large number of microscale cavities, which can promote heterogeneous nucleation and enhance the droplet departure frequency. Moreover, a large capillary force can be achieved due to the nanowire surface, resulting in effective condensate shedding and preventing the condensate from penetrating into the nanostructured surface. Figure 6.27 shows the obtained condensation heat transfer coefficients and heat fluxes versus the surface subcooling on the plain hydrophilic, plain hydrophobic and superhydrophobic (SiNW) silicon surfaces. The experimental results showed that at low surface subcooling approximately 1 K, the jumping of liquid droplets phenomena with a high droplet departure frequency was observed, which led to a high heat transfer coefficient (HTC) of 88 ± 16 kW/m^2 K on the superhydrophobic surface. This value is 155% and 87% greater than those on the plain hydrophilic and hydrophobic silicon surfaces, respectively. Furthermore, even though the heat transfer reduces with increasing the subcooling due to the increase in the condensate surface coverage ratio, there was no flooding observed on the superhydrophobic silicon nanowire surface at high subcooling, and the liquid droplets can shed off the surface efficiently. For instance, at a high surface subcooling of 15 K, a heat transfer coefficient (HTC) of 19 ± 2.0 kW/m^2 K was achieved. This value is higher than those obtained on the plain hydrophilic and hydrophobic silicon surfaces by 100% and 42%, respectively.

99
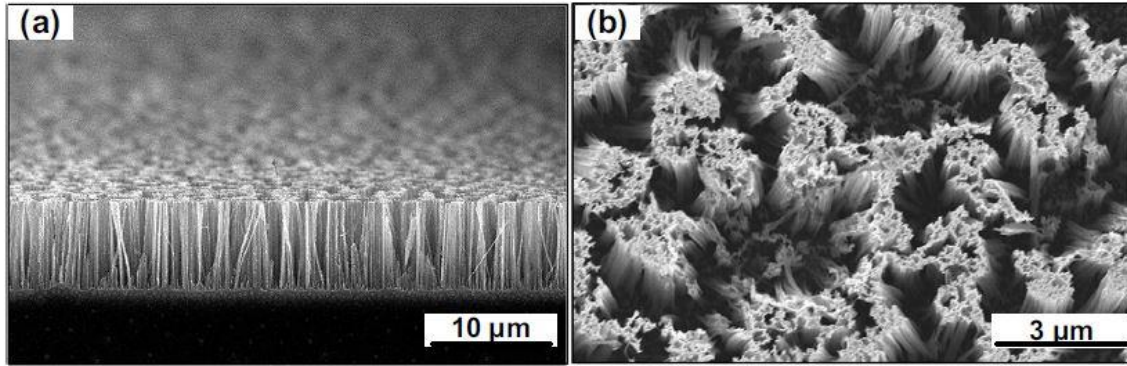
Figure 6.26: SEM images of silicon nanowire (SiNW) array-coated surface: (a) cross-sectional view; (b) top view [209].
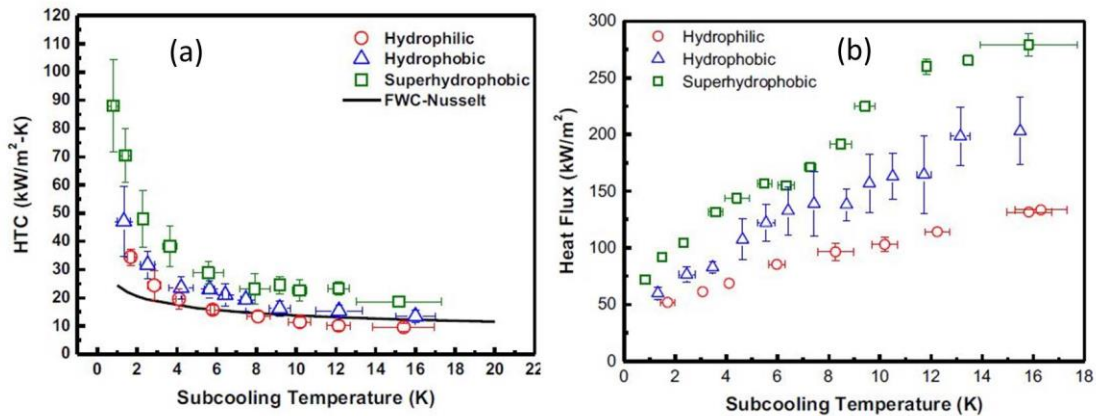
Figure 6.27: (a) Condensation heat transfer coefficients (HTC); and (b) heat fluxes as function of surface subcooling for the plain hydrophilic surface, plain hydrophobic surface, and the superhydrophobic silicon nanowire (SiNW) surface [209].

Hoenig and Bonner [210] have fabricated superhydrophobic microporous copper wick structures on copper substrates to promote steam dropwise condensation. The microporous copper powder was first sintered on the copper substrate at 975 ℃ in a hydrogen furnace and then coated with a thiol-based self-assembled monolayer to obtain the superhydrophobic surface. The effect of the sintered copper powder diameters ranging from 4 μm to 119 μm on the heat transfer performance was experimentally investigated. The experimental results showed that the thermal performance improved with decreasing the copper powder diameter as shown in Figure 6.28 and Figure 6.29.

100
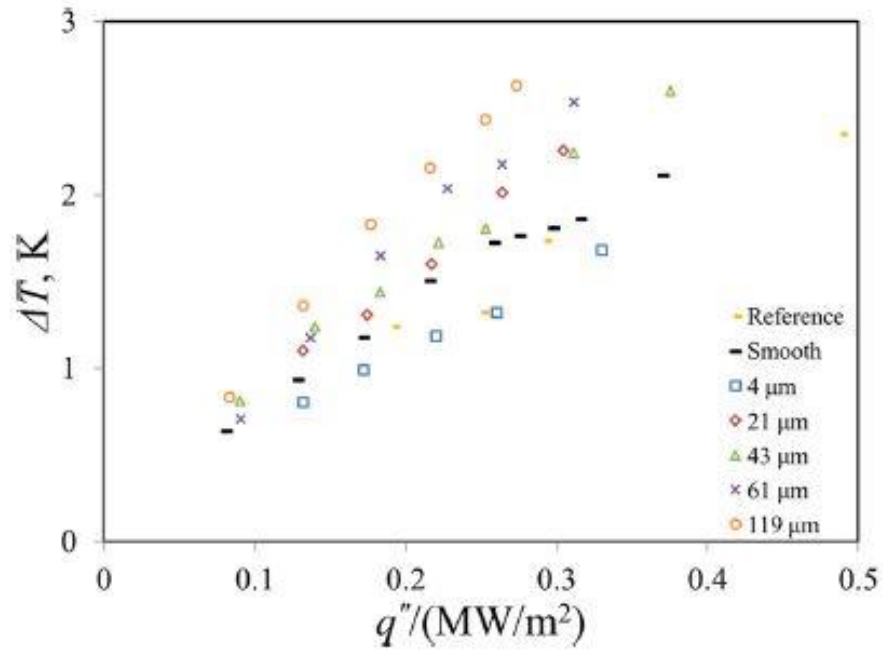
Figure 6.28: local condensation heat flux as a function of surface subcooling on the superhydrophobic microporous wick structures compared with hydrophobic plain copper surface [210].
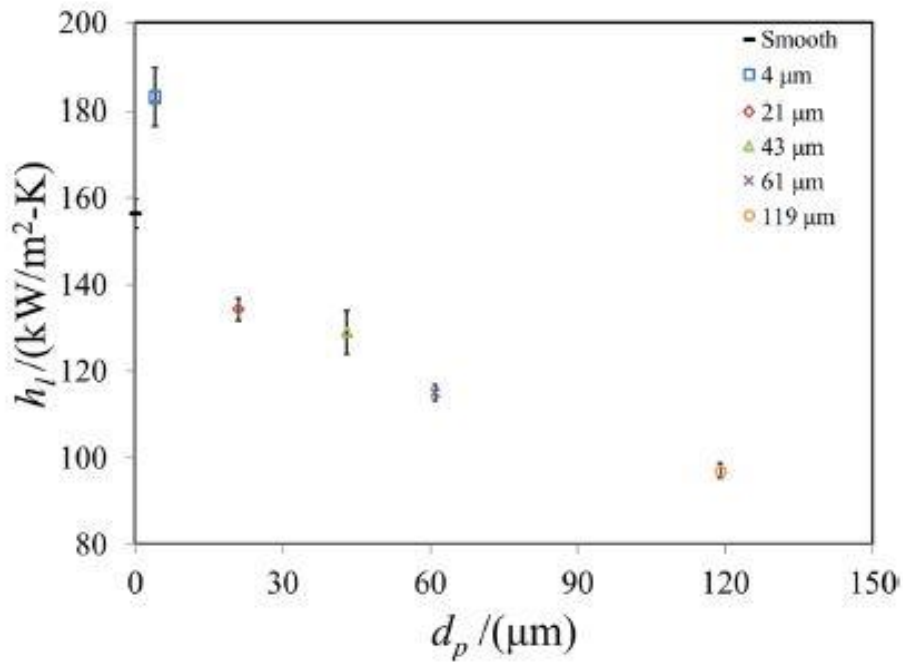
Figure 6.29: condensation heat transfer coefficient as a function of the copper powder diameter [210].

101
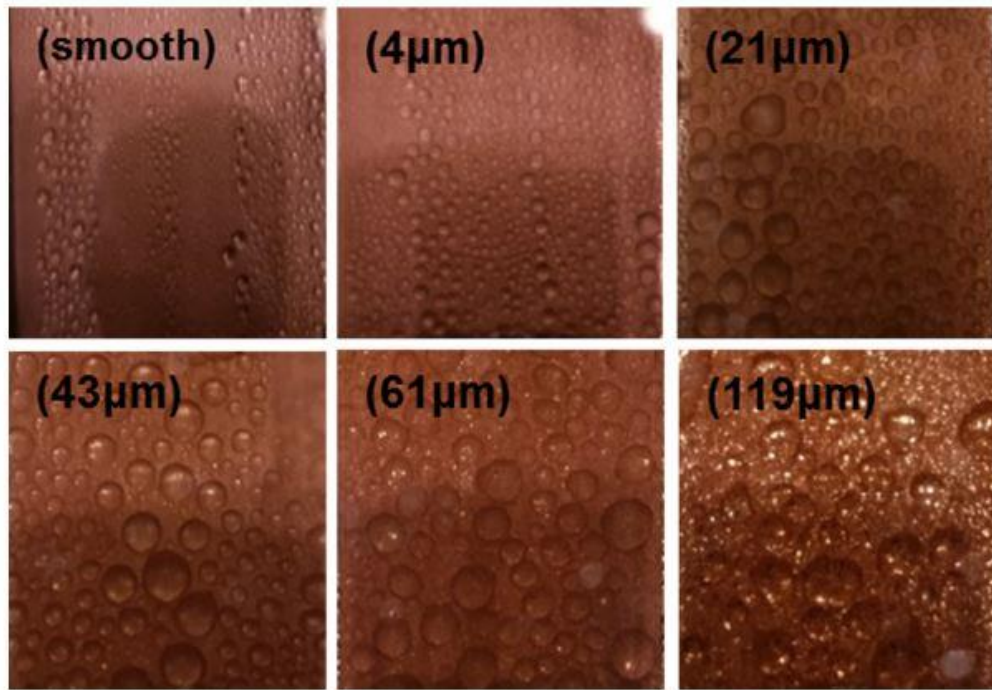
Figure 6.30: Droplet growth and coalescence on a plain copper surface and the superhydrophobic microporous wick structures prepared with different copper powder diameters [210].

It was obtained a 23% improvement in the local condensation heat transfer coefficient for the superhydrophobic microporous surface having the smallest copper powder diameter of 4 μm compared to the plain hydrophobic copper surface. This enhancement was due to the lower contact angle hysteresis for the smallest powder dimeters as proven by the reduction in the departing droplet size. On the other hand, it was found that the local heat transfer coefficients for the surfaces having the copper powder diameters of 21 μm and more were less than the local heat transfer coefficients obtained on the plain hydrophobic copper surface. This is because the pinned droplets, which were penetrated in the wick structure, led to change the departing droplet size distribution to larger sizes as shown in Figure 6.30. Consequently, the reduction in the thermal performance was due to the additional conduction resistance of the large

102

departing droplet radii and the lower departure frequency. The same outcome was observed by Dietz et al. [211]. They have reported that the potential for higher dropwise condensation heat transfer performance on the textured superhydrophobic nanostructures is achieved when the size of departing droplets is less than 10 μm.
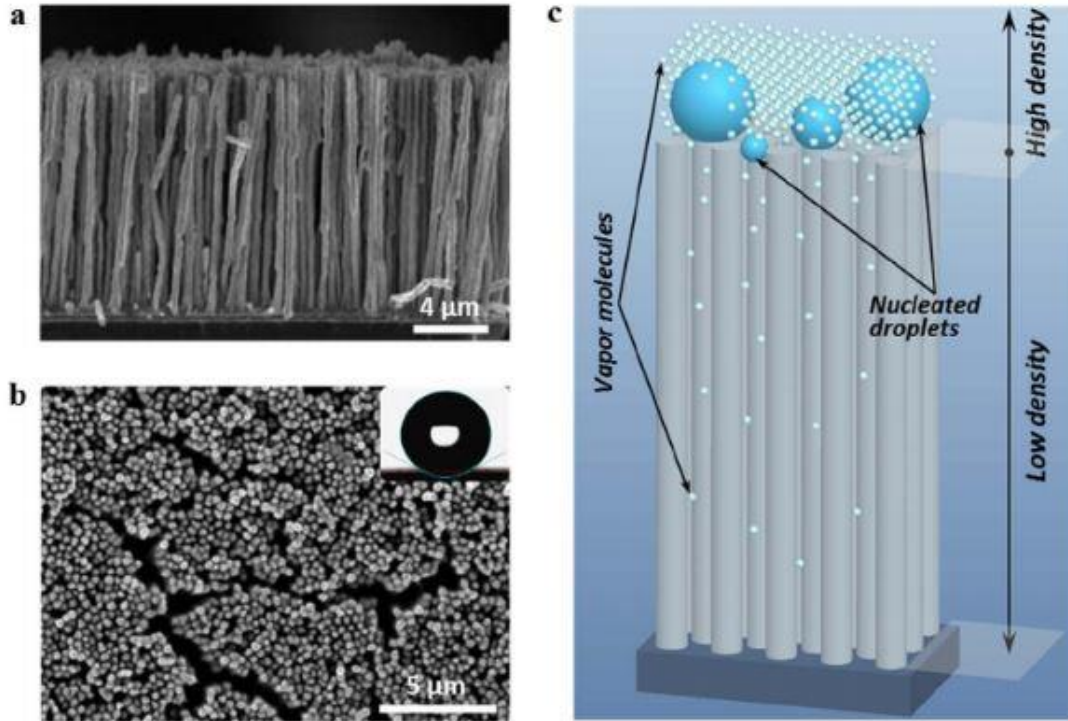
Figure 6.31: SEM pictures of the hydrophobic copper nanowires: (a) cross-sectional and (b) top view; (c) Schematic illustrating the density difference of water vapor inside and outside of the nanowires separations, the spatial confinement effect could control the droplet nucleation to happen at the top of the nanowires [212].

Feng et al. [212] have demonstrated that the spontaneous motion of the condensate droplets on superhydrophobic copper surfaces is highly affected by the surface roughness and surface energy. The nanostructures with higher perpendicularity abundantly narrow spacing and lower surface energy can result in lower pinning of condensate droplets and thus enhance the droplets mobility. The same behavior was observed by Wen et al. [143]. They have developed hydrophobic copper nanowires on

103

copper surfaces to investigate the steam dropwise condensation enhancement. Porous alumina (PAA) templates were bonded on the copper substrates so that the copper nanowires can be fabricated using the electrodeposition method. The nanowires were with a height of 20 μm and 30 μm diameters ranging from 200 to 240 nm and separations ranging from 100 to 140 nm. The fabricated surfaces were then coated with a thiol-based self-assembled monolayer to reduce the surface free energy. The measured apparent contact angle on the surfaces was about $139.2 \pm 3.5°$.
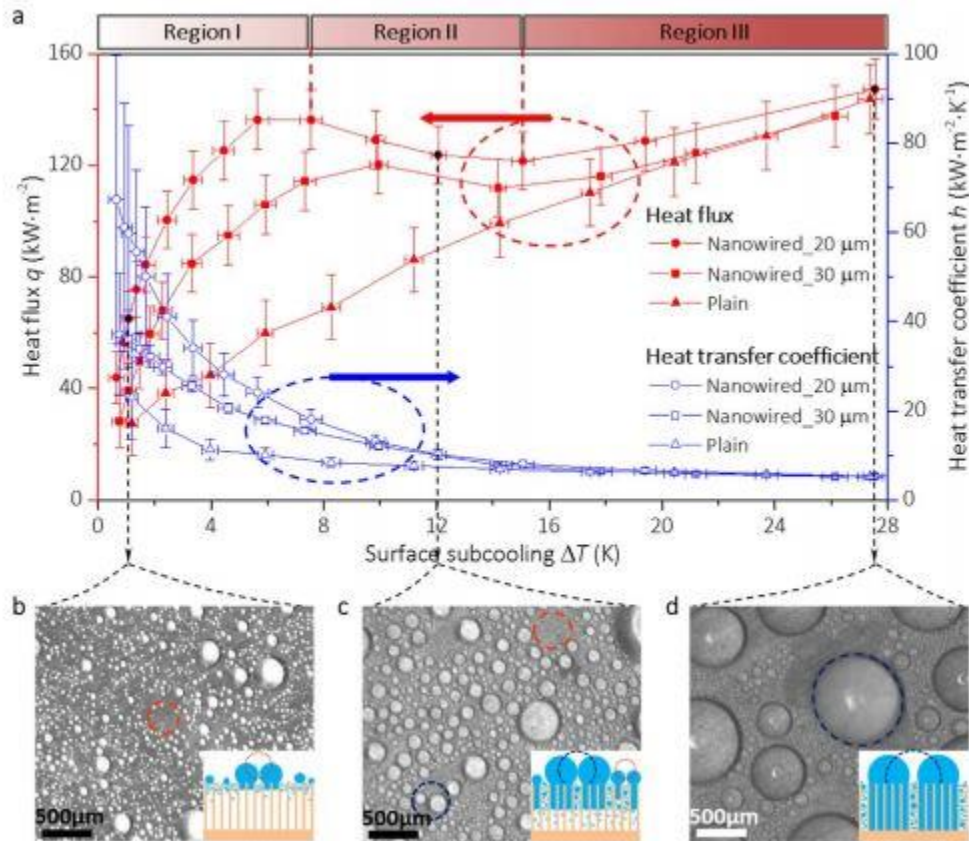
Figure 6.32: (a) heat flux and HTC as a function of surface subcooling on hydrophobic nanowired surfaces; and the condensation modes under different surface subcooling: (b) jumping condensation; (c) mixing condensation; (d) dropwise condensation [212].

It was observed that due to the high aspect ratio (height/separation) of the nanowires, which led to the density difference of water vapor inside and outside of the

104

nanowires separations, the spatial confinement effect could control the droplet nucleation to happen at the top of the nanowires as shown in Figure 6.31. Consequently, the penetration of the liquid droplets inside the nanowires was reduced, resulting in enhancing the droplets mobility and thus the dropwise condensation heat transfer over a wide range of surface subcooling. In this study, the experimental and theoretical results showed that the overall heat flux on the hydrophobic nanowired surface with the height of 20 μm and 30 μm was enhanced by 100% higher than those on the plain hydrophobic surface over a surface subcooling ranging up to 24 K as shown in Figure 6.32. This enhancement was due to the highly efficient coalescence-induced droplet jumping at low and high surface subcooling, which is in contrast with the previously reported enhancement that achieved only at a low surface subcooling ($\Delta T < 5$ K).

6.2.2 Hierarchical Superhydrophobic Surfaces

Previous research [201, 213] have reported that there was no heat transfer enhancement on superhydrophobic surfaces with only microscale roughness. This is because of the formation of greatly sticky droplets in Wenzel state [80] in the cavities between the microstructures. Cheng et al. [198] have studied steam condensation on a two-tier superhydrophobic surface. A continuous dropwise condensation was observed on this textured surface. However, during the experimentation and under high heat flux conditions, the surface was flooded on the multiscale texture, leading to a lower condensation heat transfer coefficient in comparison with a flat hydrophobic surface. To overcome this situation and allow the formation of condensate droplets in the Cassie state, Researchers have developed superhydrophobic surfaces with hybrid micro/nanoscale roughness [100, 198, 214-217]. It was first demonstrated by Chen and

105

coworkers [140, 218] that surfaces with hierarchical microscale and nanoscale topologies are superhydrophobic during steam condensation and promote high-frequency droplet departure.
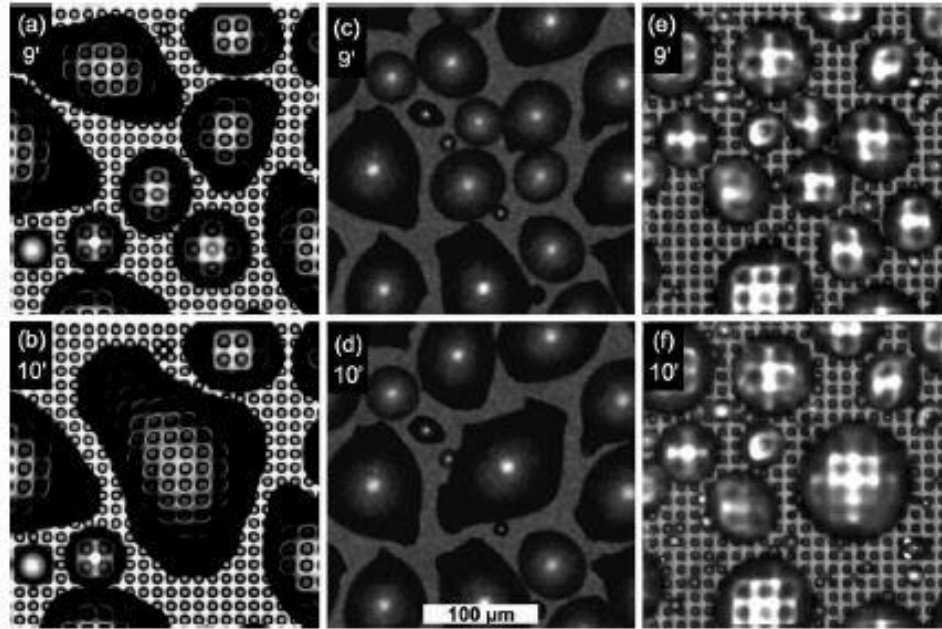
Figure 6.33: Coalescence of droplets on parylene-coated textures: (a-b) one tier with only micropillars; (c-d) one tier with only nanopillars; (e-f) two-tier roughness [218].

Chen et al. [218] have demonstrated continuous dropwise condensation of steam on a superhydrophobic surface with two-tier roughness. The two-tier texture, which mimicked lotus leaves, was prepared on the silicon substrate by depositing short carbon nanotubes (CNTs) with an average height of 400 nm on micromachined silicon pillars using plasma enhanced chemical vapor deposition method. The textured surface was then coated by either a parylene or a hexadecanethiol self-assembled monolayers to reduce the surface free energy. The comparison between the two-tier texture and one-tier texture including either microtexture of Si micropillars or nanotextures of CNT nanopillars was carried out to investigate the condensate droplets behavior on these different texture

106

designs. It was observed that on a one-tier texture with only micropillars or nanopillars, the condensate droplets penetrated into the cavities of these textures and formed sticky droplets in Wenzel state, and that observation was consistent with the literature. However, on the two-tier texture, the condensate droplets tend to stay in the Cassie state as shown in Figure 6.33. Besides, it was demonstrated that the hexadecanethiol-coated two-tier surface retained superhydrophobic during and after condensation and enabled higher drop removal compared to the parylene-coated surface. This is because the condensate droplets were tended to stick to the parylenecoated surface and the drop removal was due to the large size of droplets or momentum, which is similar to the behavior of condensation observed on lotus leaves [88]. Thus, the enhancement of the hexadecanethiol coating was due to the lower surface energy compared to the wax coating of lotus leaves.

Chen et al. [100] have demonstrated continuous dropwise condensation of steam on hierarchical nanograssed micropyramid architecture on silicon substrate. They showed that by spatial controlling of the surface roughness to achieve a global superhydrophobicity and locally wettable patches, both the drop nucleation and drop departure could be significantly enhanced on the condensing surface. The wettable patches could promote droplet nucleation whereas the global superhydrophobicity yielded efficient drop departure without sticking to the substrate. Furthermore, it was experimentally demonstrated that the dropwise condensation heat transfer was enhanced due to the increase in the surface coverage of small droplets, the droplet number density, droplet growth rate and droplet departure rate. It was found that the droplet number

107

density and the droplet departure rate on the hierarchical surface increased by approximately 65% and 450% compared to a superhydrophobic nanostructures surface.

Chen et al. [219] have developed hierarchical superhydrophobic micro/nano-structured surfaces on copper substrates to study the effect of the microscale roughness on the steam dropwise condensation dynamics. The patterned microstructured surface was fabricated on the copper substrate using lithographical and electroplating methods. Then nanostructures were developed on the electroplated microstructured surface using a chemical etching method to form the hierarchical patterned micro/nano-structured surface. The surface was then coated by a silane-based self-assembled monolayer to provide the superhydrophobicity on the surface. The comparison between the hierarchical superhydrophobic surface and only a microstructured and nanostructured surfaces was investigated to illustrate the effect of such surfaces on the droplet growth rate and the droplet departure frequency. The measured apparent contact angles of the superhydrophobic hierarchical surface, micro-structured surface, and nano-structured surface were approximately 165°, 150°, and 160° respectively. In this work, it was observed that the condensate droplets were strongly pinned to the microstructured surface and over time a filmwise condensation mode occurred on the condensing surface. On the other hand, the hierarchical and nanostructured surfaces exhibited dropwise condensation mode, but the droplet departure frequency was much higher for the hierarchical surface compared to that on the nanostructured surface. This is due to the smaller average surface coverage by condensate droplets on the hierarchical surface in comparison with the nanostructured surface. Consequently, it was obtained a 40% greater droplet growth rate

108

and a 300% higher droplet departure rate for the hierarchical surface compared to the superhydrophobic nanostructured surface.

6.2.3 Hybrid surfaces

Another efficient method to enhance the dropwise condensation heat transfer performance is fabricating a hybrid surface by combining both hydrophobic and hydrophilic regions on the condensation surface. This approach can result in reducing the thermal barrier for vapor condensation while raising droplet shedding [155, 220], increasing the droplet nucleation density [221, 222] and decreasing the droplet departure size [193, 223]. Kumagai et al. [224] have studied first the effects of hybrid surfaces on condensation heat transfer performance by patterning alternating hydrophilic and hydrophobic stripes in horizontal and vertical orientations on the condensation surface. The dimensions of the hydrophobic and hydrophilic stripes were at and above the capillary length scale. In their study, they showed that there was an optimum width for the hydrophobic and hydrophilic stripes for enhancing condensation heat transfer in the filmwise regions. Their results showed higher heat transfer enhancement on the hybrid surface compared to that on a surface with complete filmwise condensation, but below that values on a surface with complete dropwise condensation.
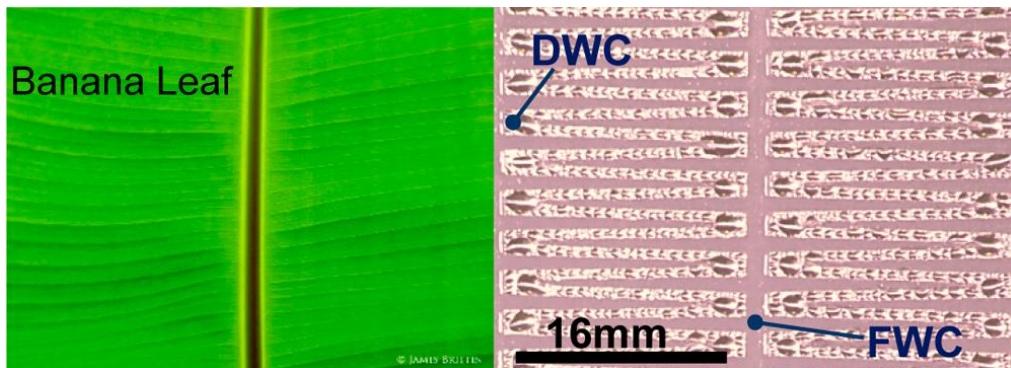
Figure 6.34: The design of the bioinspired interdigitated wettability patterns on the aluminum surface [121].

109
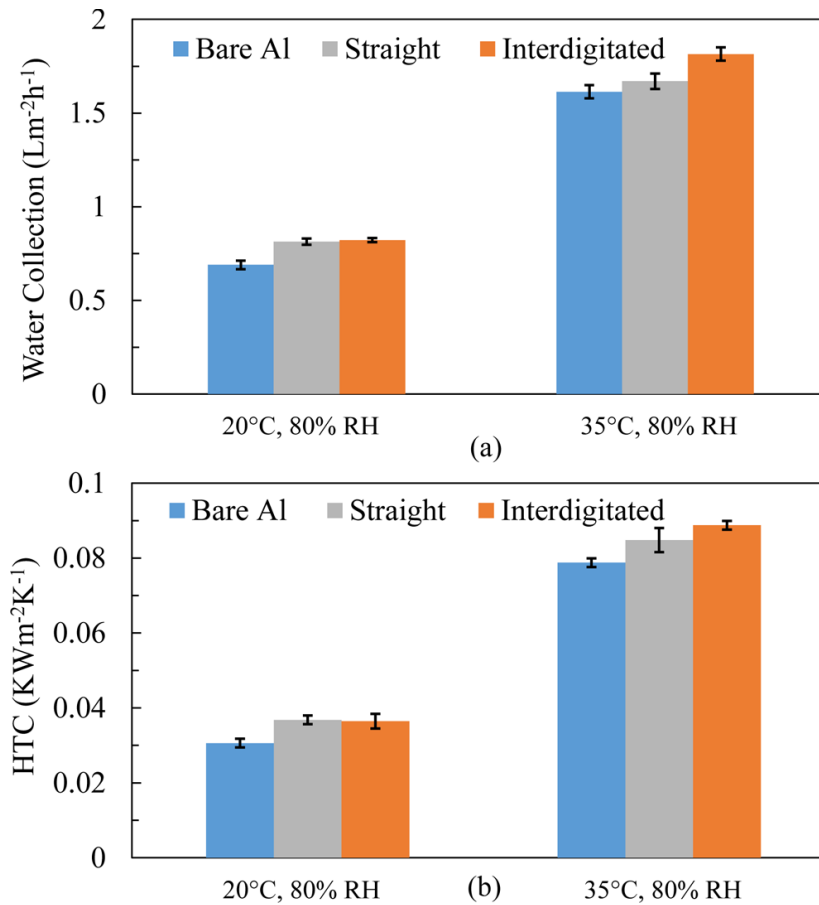
Figure 6.35: The overall enhancement in (a) the condensation collection rate and (b) the heat transfer coefficient (HTC), on the bioinspired interdigitated wettability pattern design and the unpatterned bare and the straight-line patterned aluminum surfaces at two different condensation conditions [121].

Ghosh et al. [121] have developed a hybrid surface combining alternating hydrophilic straight parallel strips and interdigitated super-hydrophilic tracks like wedge-shaped patterns inspired by the vein network that found in the banana leaves on the aluminum surface to spatially control the droplet nucleation density, the maximum droplet size and to enhance the droplet drainage rate. The hybrid surface was fabricated using Laser-patterned masking and chemical etching methods without applying any hydrophobizing coating. Figure 6.34 shows the design of the bioinspired interdigitated wettability patterns on the aluminum surface. The condensation experiment was carried

out at different saturation temperatures and relative humidity and in the presence of non-condensable gases. The condensation heat transfer performance on the hybrid surface was improved due to the increase in the condensation collection rates and reducing the droplet diameters departing from the condensing surface. It was found that on the regions with the lower wettability, the average maximum droplet size was about 42% of the width of the corresponding strips. An overall enhancement in the condensation collection rate and heat transfer coefficient (HTC) up to 19% and 20%, respectively were achieved on the bioinspired interdigitated wettability pattern design compared to that on the unpatterned bare and the straight-line patterned aluminum surfaces as shown in Figure 6.35 at different condensation conditions.
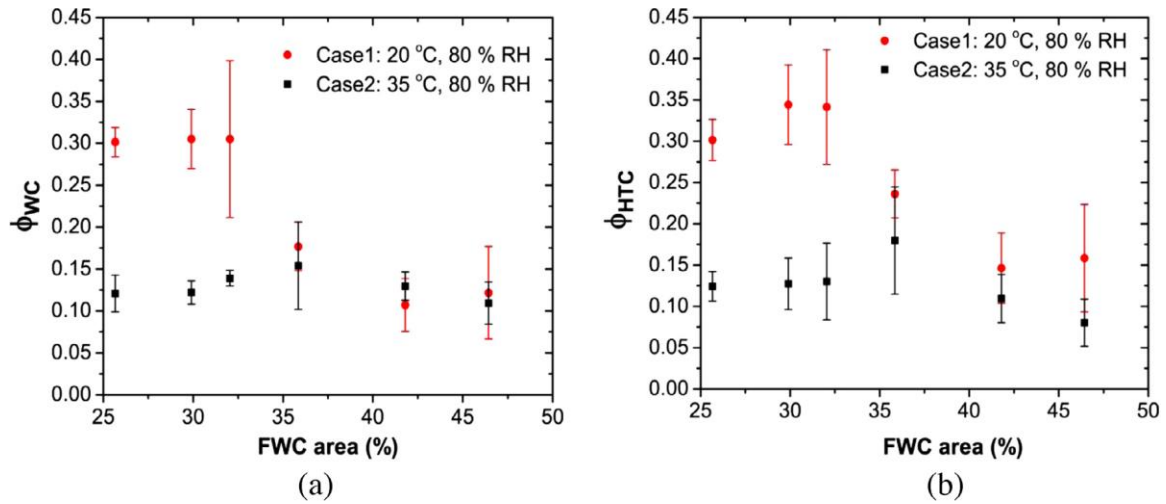
Figure 6.36: The improvement in (a) water collection rate (WC), and (b) heat transfer coefficient (HTC) for different FWC fractional areas under two different environmental conditions [225].

Mahapatra et al. [225] have demonstrated the effectiveness of a hybrid surface combining superhydrophilic staggered interdigitated patterns on a hydrophilic aluminum surface to promote the overall condensation heat transfer performance by improving the droplets removal from the condensing surface in the presence of non-condensable gases.

111

The steam condensation experiments were conducted on vertical surfaces and at different dry bulb temperatures and humidity ratios. The area percentage of the superhydrophilic staggered interdigitated patterns regard to the overall condensing surface has been changed until achieving the optimum fractional area that maximizes the water drainage rate and condensation heat transfer rate. The enhancement in the heat transfer coefficient and the water collection rate were up to 34.4% and 30.5%, respectively in comparison with the values for a bare hydrophobic aluminum surface when the hydrophilic fractional area is about 29.9% of the total surface area as shown in Figure 6.36. In addition, the enhancement of 18% in the heat transfer coefficient and 15.4% in the water collection rate was achieved compared to the bare hydrophobic aluminum surface when the hydrophilic fractional area was about 35.9% of the total plate area.

Leu et al. [226] have developed hybrid surfaces including hydrophilic and hydrophobic strips patterns on vertical silicon surfaces to study their effects on producing self-driving force for droplet movement and thus improving the vapor condensation efficiency. Figure 6.37 shows the condensation phenomena on hydrophilic, hydrophobic, and hybrid surfaces. It was observed that the droplets velocity was faster on the hybrid surface than those surfaces without surface modification. During the condensation, it was seen that the droplets nucleate and grow on the hydrophobic strips to reach a certain size and then migrate with high momentum toward the more hydrophilic regions. In this study, it was found that the condensation surface with a strip pattern of 1.0 mm for both hydrophobic and hydrophilic strips could achieve higher condensation efficiency than the ordinary surface without the surface energy patterns. The experimental results showed a

112

maximum enhancement of 20% in the heat transfer rate for the hybrid surface compared

to a surface with complete dropwise condensation as shown in Figure 6.38.
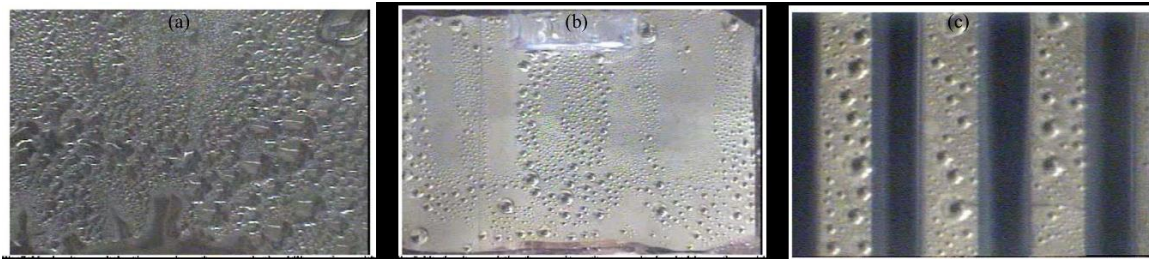
Figure 6.37: The condensation behavior on (a) hydrophilic, (b) hydrophobic, and
(c) hybrid surfaces on vertical silicon surfaces [226].
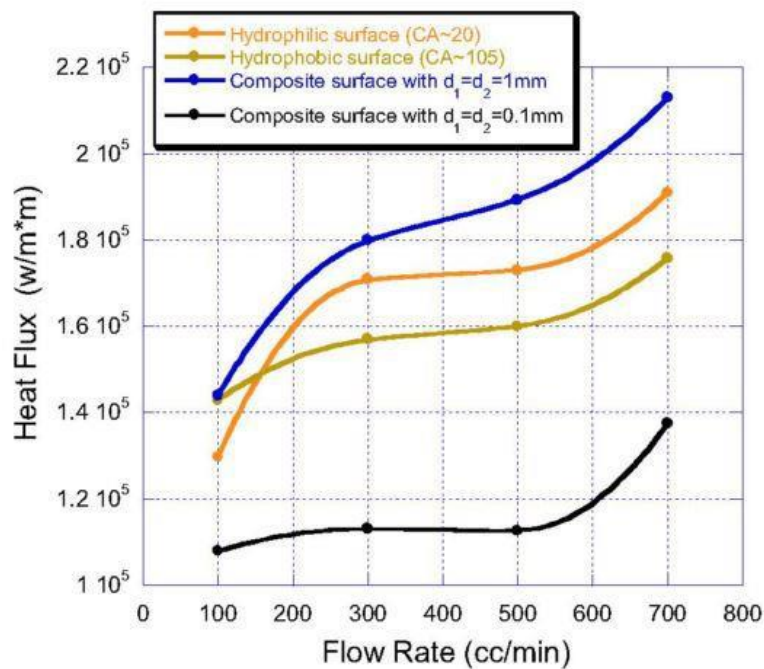
Figure 6.38: Heat flux at different flow rates of cooling water for various hybrid surface
designs [226].

Lee et al. [227] have experimentally investigated the influence of a hybrid surface

consisted of superhydrophobic and hydrophilic strips on the condensation heat transfer

performance. The superhydrophobic surface was fabricated by spinning silica

nanoparticles coating on a copper substrate using the sol-gel method, and then the surface

was treated chemically by a silane base self-assembled monolayer to reduce the surface free energy.
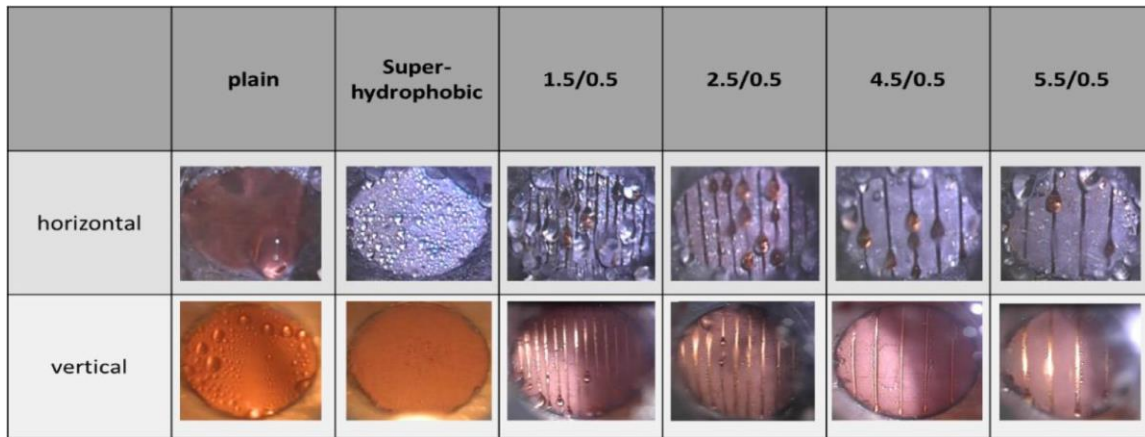
Figure 6.39: Images of dropwise condensation behavior for different orientations on plain, superhydrophobic surfaces and hybrid surfaces with various hydrophobic strips width [227].

Experiments were conducted on different types of surfaces including the hybrid surface, plain hydrophobic surface, and the superhydrophobic surface under horizontal and vertical surface orientations as shown in Figure 6.39. The width of the superhydrophobic strips was changed from 1.5 to 5.5 mm, while the width of the hydrophilic strips was maintained at a 0.5 mm. The experimental results showed that higher heat transfer coefficients were obtained on vertically oriented surfaces of plain and superhydrophobic surfaces due to the condensates sweeping effects which helped the smaller droplets to shed off the condensing surface. Moreover, it was found that in the case of the horizontal orientation, the heat transfer rate could be improved with increasing the width of the hydrophobic strips. The condensation heat transfer coefficient was enhanced 1.2 times compared to that of the superhydrophobic surface. On the other hand, it was observed for the vertically oriented surfaces that due to the droplets sweeping effects, the heat transfer coefficients increased efficiently with decreasing the width of

the hydrophobic strips while increasing the strip's width led to flooding the surface and reducing the heat transfer performance. Figure 6.40 shows the effect of changing the width of the hydrophobic strips on the condensation heat transfer rate under horizontal and vertical orientations.
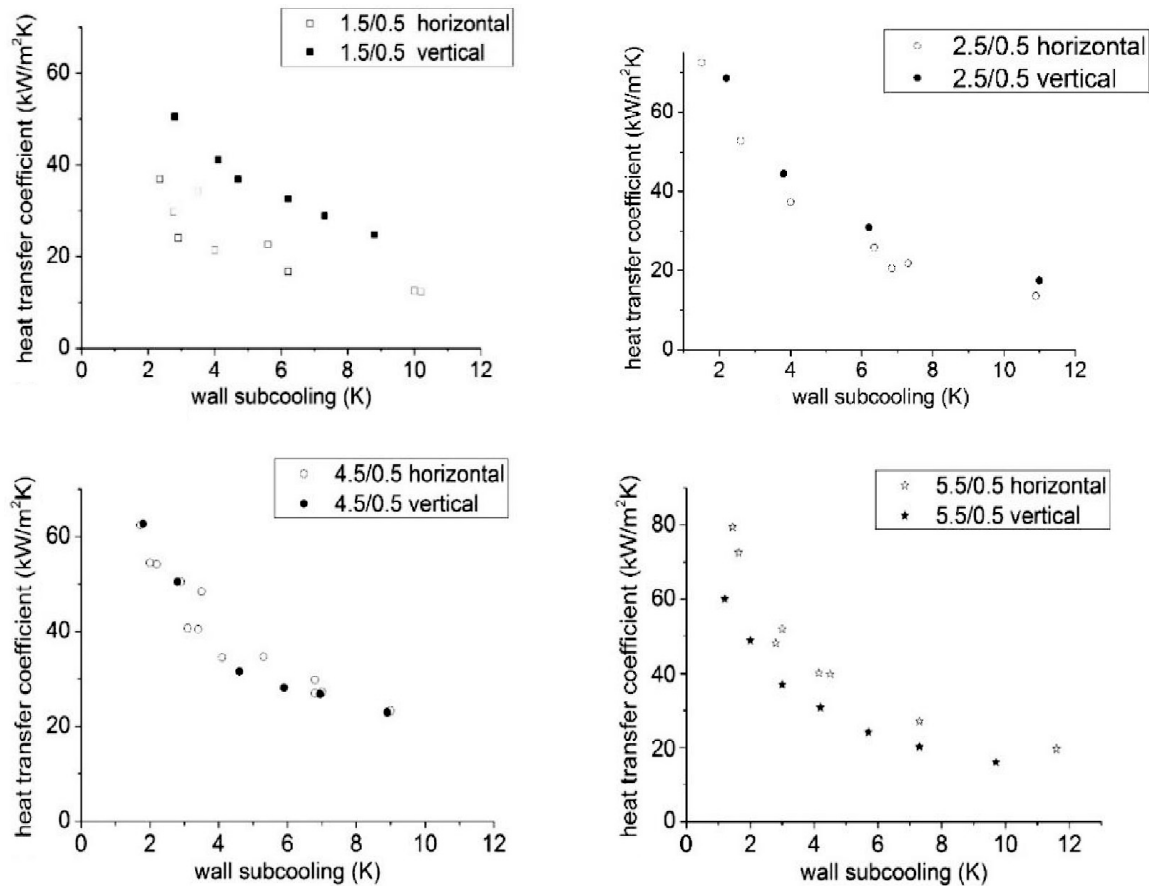
Figure 6.40: Condensation heat transfer coefficient (HTC) as a function of surface subcooling for hybrid surfaces with various hydrophobic strips width and under horizontal and vertical orientations [227].

Peng et al. [228, 229] have experimentally and theoretically investigated the influence of hybrid surfaces consisted of hydrophilic-hydrophobic straight stripes on promoting the steam condensation heat transfer performance at atmospheric pressure on vertical copper discs as shown in Figure 6.41. The results revealed that the condensation heat transfer performance increases with decreasing the width of the hydrophilic strips

115

while increasing the hydrophobic region width led to increase the maximum droplet radius and reduce the droplet population density resulting to the existence of an optimum hydrophobic region width. A steam condensation heat transfer enhancement factor was found, and it rises first with increasing the hydrophobic region width and then reduces with more increasing. In this study, the heat transfer rate for the optimum hydrophobic region width of 0.55 mm, which is corresponding to the maximum droplet radius of 0.25 mm, was enhanced by 23 % compared to complete dropwise condensation. Figure 6 42 shows the condensation heat transfer enhancement on different hydrophobic–hydrophilic hybrid surfaces compared to the complete hydrophobic surface. In addition, it was found that the condensation heat transfer enhancement factor reduces with increasing the surface subcooling and the optimum enhancement factor is mainly affected by the surface subcooling. At the surface subcoolings of 2.0 K, 4.0 K, and 6.0 K, the optimum enhancement factors were about 1.23, 1.11 and 1.07, respectively.
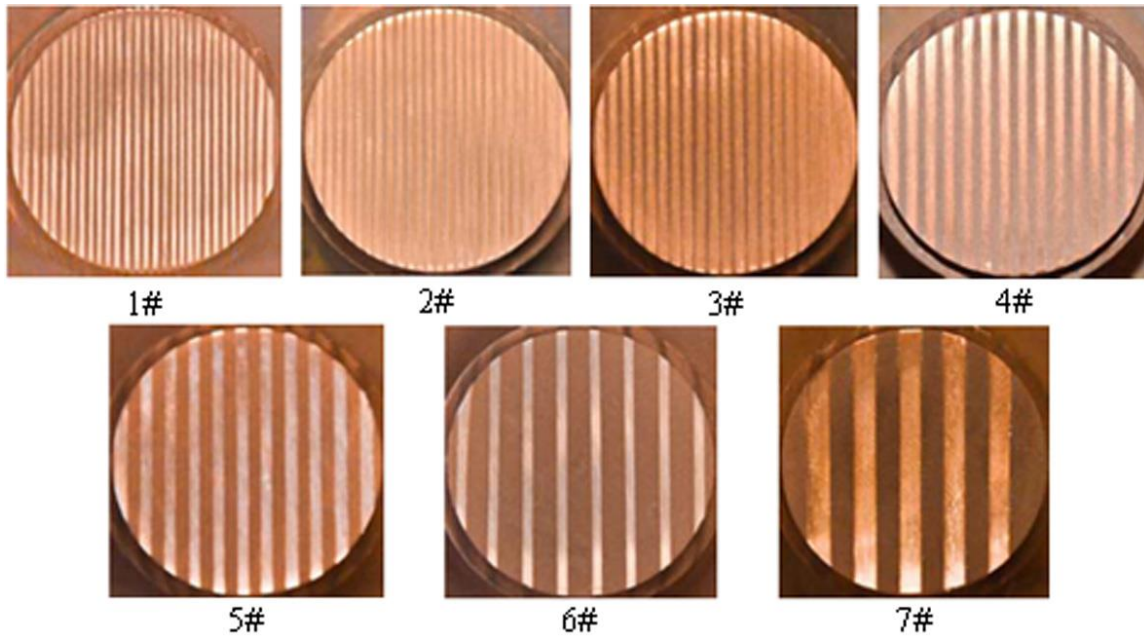
Figure 6.41: Images of the prepared hybrid surface with different hydrophobic and hydrophilic regions (gray: hydrophilic region, light: hydrophobic region) [229].

116
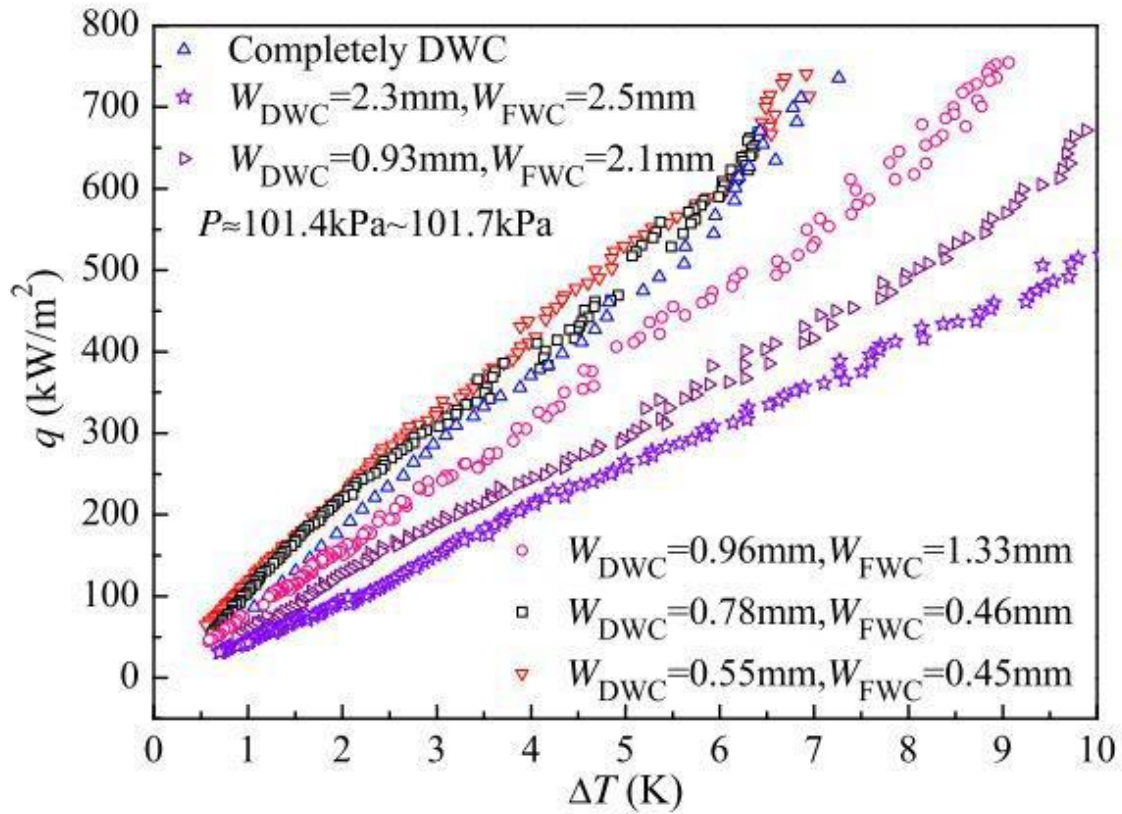
Figure 6 42: Effect of the hybrid surfaces in condensation the heat transfer enhancement compared to that of complete hydrophobic surface [229].
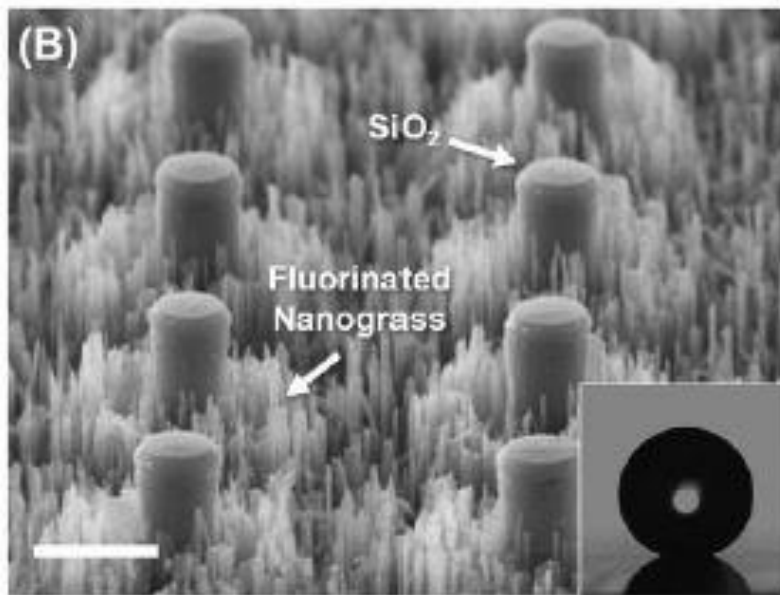
Figure 6.43: The SEM image of the hybrid design inspired by the natural beetle shell [199].

117
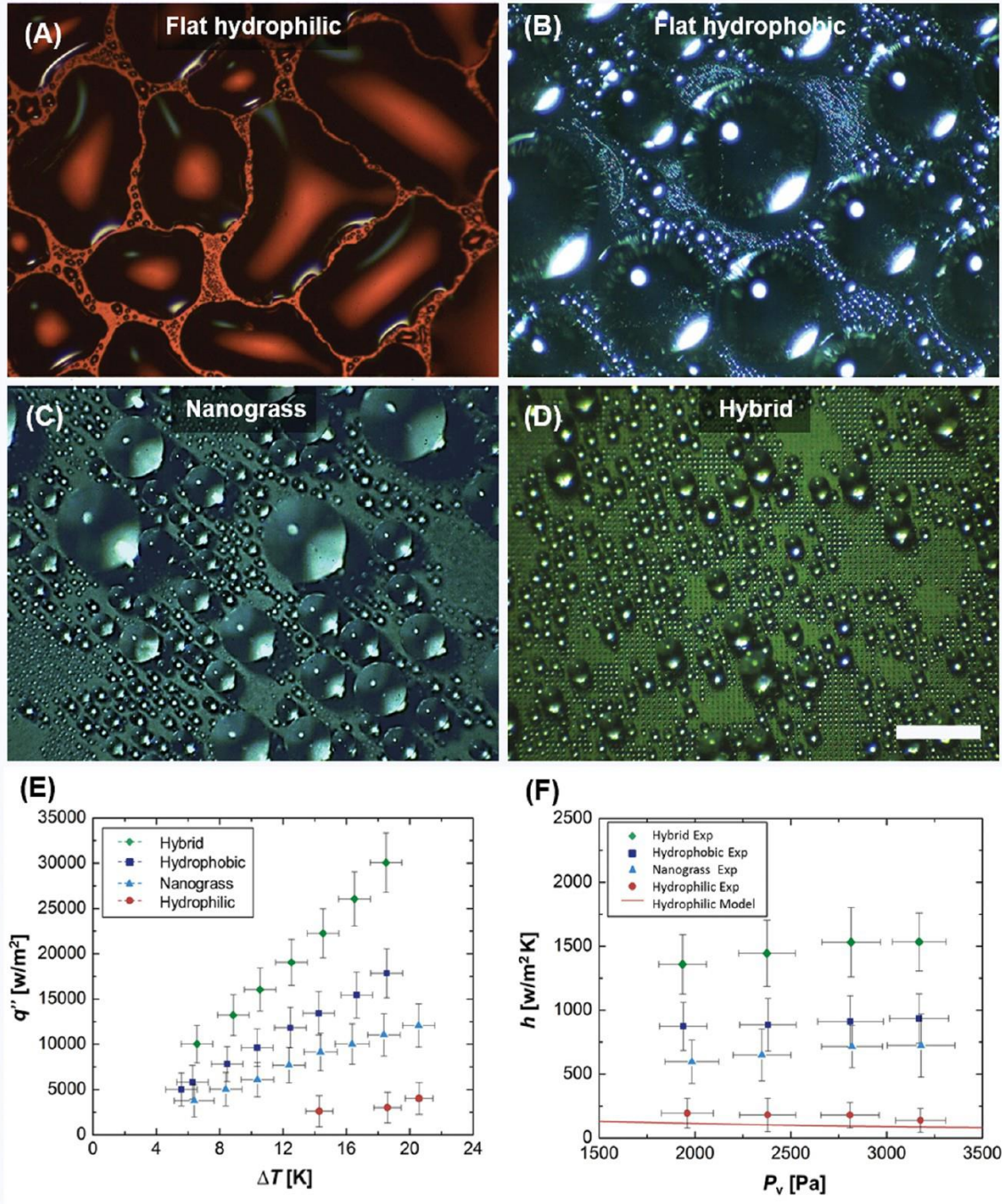
Figure 6.44: The condensation phenomena on (a) flat hydrophilic, (b) flat hydrophobic, (c) Nanograss, and (c) hybrid surface; (E,F) The comparison between the different surfaces on the condensation heat transfer enhancement [199].

Hou et al. [199] have developed a hybrid surface inspired by the natural beetle shell with a high contrast wettability to promote the steam condensation performance. The bioinspired hybrid surface as shown in Figure 6.43 consists of micropillar patterns

118

which are covered by hydrophilic silicon dioxide on the top to facilitate faster droplet nucleation and droplet depinning on the hydrophilic region. The area surrounded the micropillars was coated by a conformal nanograssed superhydrophobic surface to achieve the dropwise condensation and promote the droplet self-removal. The fractional area of the hydrophilic SiO_2 patches to the total surface area was controlled to achieve a repeated condensation mode transition from the filmwise to the dropwise condensation. It was found that the droplet nucleation density and the initial droplet growth rate on the bioinspired hybrid surface were much greater than that of the unpatterned superhydrophobic surfaces. Moreover, the optimized hybrid surface showed approximately 63% enhancement in the heat transfer coefficient as compared to the plain hydrophobic silicon surface. Figure 6.44 shows the condensation phenomena and the heat transfer measurements as a function of the surface subcooling and the partial pressure of the saturated pressure for flat hydrophilic, flat hydrophobic, nanograssed superhydrophobic, and the hybrid surfaces. The maximum heat transfer enhancement was achieved on the hybrid surface as compared to that on the other surfaces.

Alwazzan et al. [230] have developed hybrid surfaces combining hydrophobic and hydrophilic parallel straight stripes on horizontal copper tubes to promote the condensation heat transfer performance and the droplet dynamics. The hydrophobic region of the hybrid surface was fabricated using the self-assembled monolayer (SAM) coating on the bare copper tube, while the hydrophilic region was first sandblasted by using 50 microns silicon carbide and then treated with the self-assembled monolayer coating. Experiments were conducted, at steam saturation conditions, atmospheric

119

pressure and in the presence of non-condensable gases (air), to investigate the effect of the hydrophobic to hydrophilic width ratio on the heat transfer enhancement.
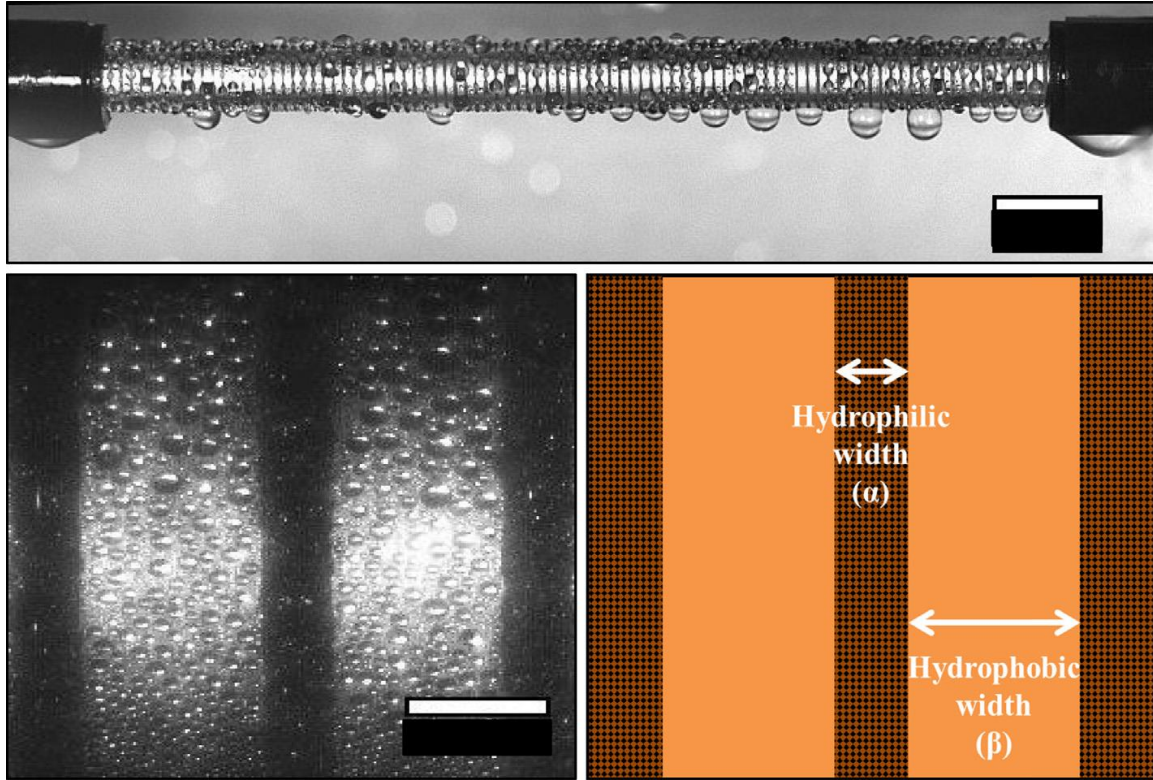
Figure 6.45: Images of the design and the condensation phenomena on the developed hybrid surface [230].

Figure 6.45 exhibits the condensation phenomena on the horizontal copper tube with the hybrid surface. The experimental results showed that the hybrid surfaces have higher heat transfer coefficients and heat fluxes in comparison with those surfaces with complete filmwise, complete sandblasted and complete dropwise condensation as shown in Figure 6.46. Furthermore, in this study, it was found an optimum hydrophobic to hydrophilic width ratio corresponding to a hydrophobic and hydrophilic width of 0.6 mm and 0.3 mm, respectively. With this optimum ratio, a maximum condensation heat transfer coefficient was achieved with a value of 85.0 kW/m^{2}K, at a subcooling temperature of 9 ℃. This enhancement is about 4.8 and 1.8 times higher than those of

120

complete filmwise and dropwise condensation, respectively. Moreover, it was demonstrated that increasing the hydrophilic region can result in a filmwise condensation mode, while droplets bridging phenomena was observed with decreasing the width of the hydrophilic strips, resulting in reducing the condensation rate.
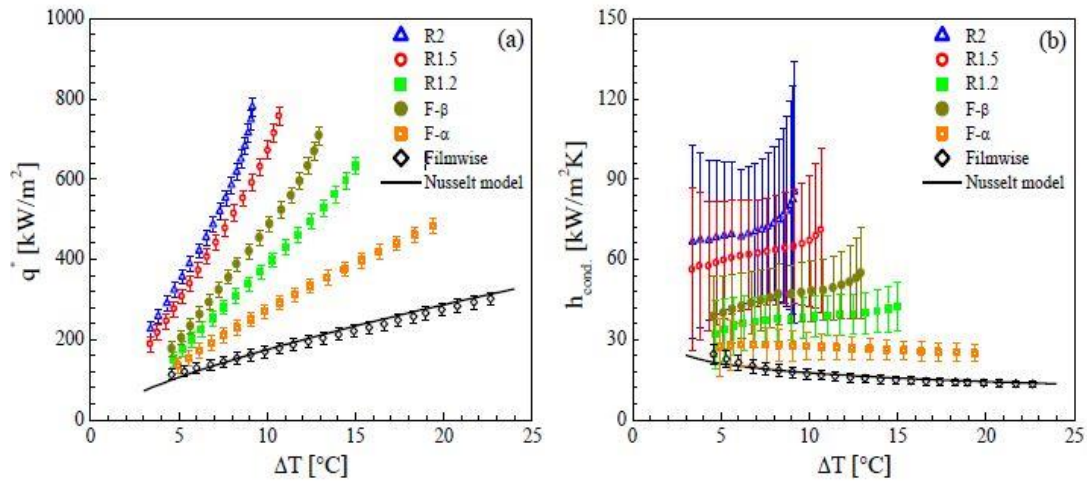
Figure 6.46: The condensation heat transfer enhancement for the hybrid surface in comparison with those surfaces with complete filmwise, complete sandblasted and complete dropwise condensation [230].

The same group [230] have then investigated the influence of hybrid surfaces with different configurations on the condensation heat transfer enhancement. Egab et al. [231] have first developed a hybrid surface consisted of hydrophobic circular patterns and a hydrophilic background on a horizontal copper tube. They found that the heat transfer coefficients were lower than those on a surface with a complete dropwise condensation. Then they changed the hybrid pattern design to a hydrophobic background with hydrophilic patterns. They have investigated the effect of the pattern shape (circular, ellipse, and diamond), size and the gap between two adjacent patterns on the heat transfer performance and the droplets dynamics. Figure 6.47 shows the design and the condensation phenomena on the circular hybrid surface. The comparison between hybrid

121

surfaces with circular hydrophobic patterns of different sizes and gaps and the complete filmwise, complete dropwise and complete sandblasted surfaces is shown in Figure 6 48.
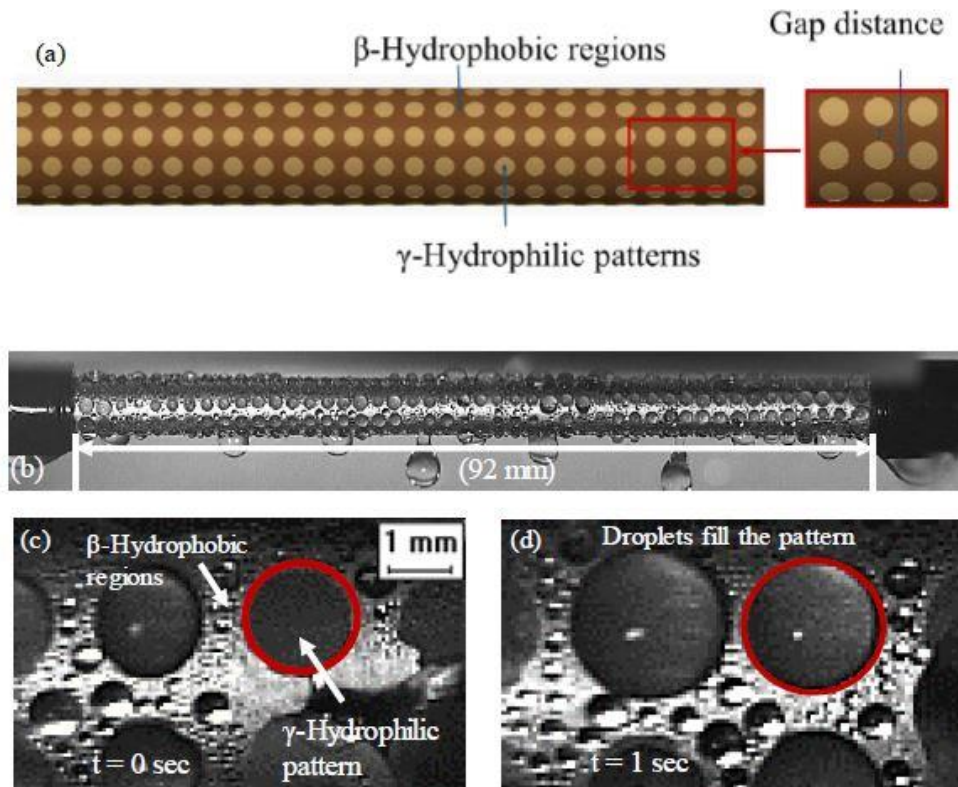
Figure 6.47: The design and the condensation behavior on the circular hybrid surface [231].

With the hydrophilic circular patterns, a maximum enhancement in the condensation heat transfer rate up to 12% was achieved compared to that on the surface with a complete dropwise condensation at an optimum diameter of 1.5 mm and a gap of 0.5 mm. In this study, a similar bridging droplets phenomena as Ref [230] was observed with decreasing the gap between the two neighboring patterns, resulting in reducing the condensation rate. Thus they found that changing the gap is more effective than the pattern size on promoting the condensation heat transfer performance. They have demonstrated that when the gap between the two circular patterns was 1.5 mm, the

droplet departure frequency was about 1.37 times higher than that hybrid surface with a gap of 0.5 mm. Then, with the same pattern area and the gap of 1.5 mm, the comparison between the hybrid surfaces with hydrophobic circular, elliptical and diamond patterns was investigated. The results showed that the hybrid surface with hydrophobic diamond patterns has the higher condensation heat transfer performance compared with the hybrid surfaces having elliptical and circular patterns. However, at the gap of 1.5 mm, the condensation heat transfer performance on the hybrid surfaces with elliptical and circular patterns was lower than the surface with complete dropwise condensation. Furthermore, for the hybrid surface with diamond patterns, a maximum enhancement in the heat transfer rate up to 40% was achieved compared to a complete dropwise surface when the gap between the two adjacent patterns was 1.0 mm as shown in Figure 6.49.
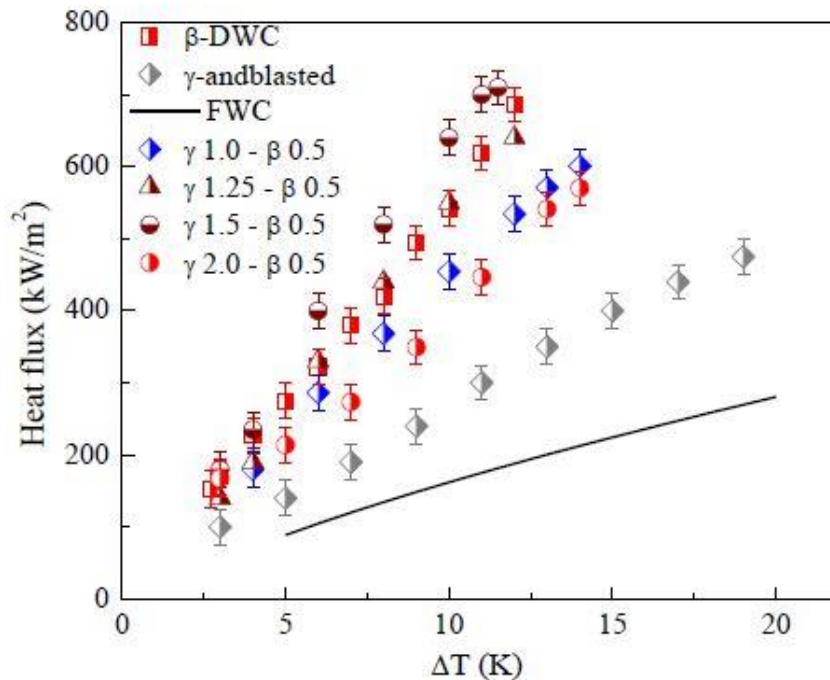
Figure 6 48: The comparison between hybrid surfaces with circular hydrophobic patterns of different sizes and gaps and the complete filmwise, complete dropwise and complete sandblasted surfaces on the condensation heat transfer enhancement [231].

123
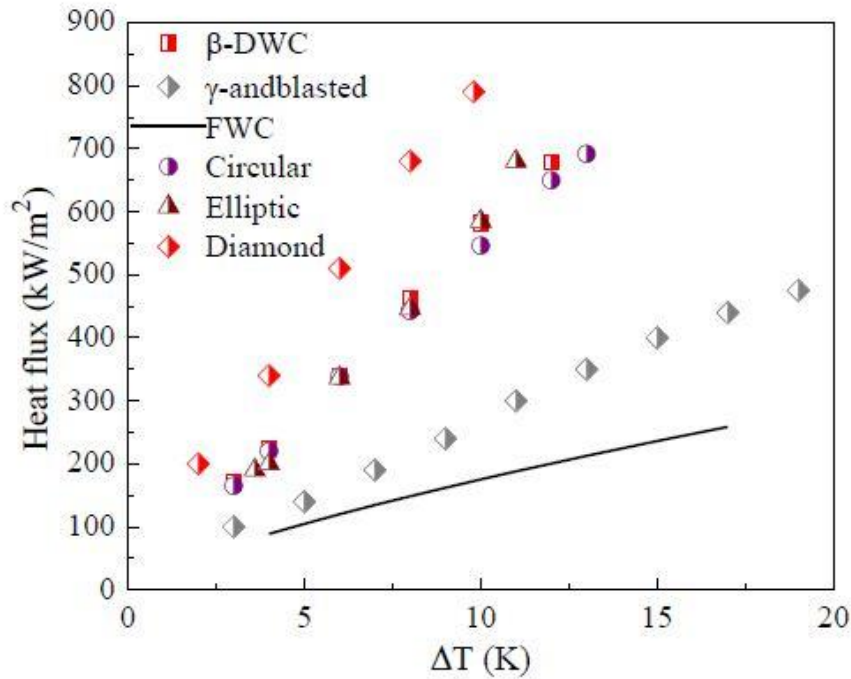
Figure 6.49: Heat flux as a function of surface subcooling for the circular, elliptical and diamond hybrid surfaces (The gap = 1 mm), and the complete filmwise, complete dropwise and complete sandblasted surfaces [231].

6.2.4 Lubricant-infused surfaces

Due to its self-cleaning [232], self-healing [233], and antifouling [234] characteristics, lubricant-infused surfaces, which consist of hydrophobic micro-/nanostructures infused with a low-surface energy lubricant (oil), have been recently proposed for dropwise condensation enhancement [108, 125, 233, 235, 236] . Anand et al. [125] have developed lubricant-impregnated surfaces to reduce the pinning of condensate droplets within the texture of the hierarchical micro/nano-textured superhydrophobic surface. Their results demonstrated that the condensate droplets mobility for sizes as small as 100 μm on such surfaces was highly enhanced compared to those identical textured superhydrophobic surfaces developed without lubricating. This is because the condensate droplets on the lubricant-infused surface stay floating on the

124

lubricant with minimum pinning to the surface compared with superhydrophobic surfaces in which the droplets grow and become highly pinned within their textures. Consequently, the enhancement of the water droplets mobility led to a continuous sweeping effect which results in clearing the surface for fresh nucleation and thereby enhancing condensation heat transfer performance. Figure 6.50 shows the condensation concept on the lubricant-impregnated surface.
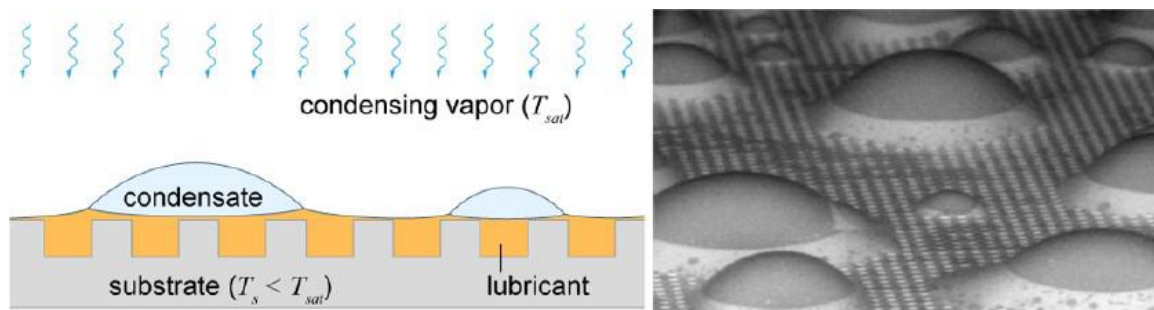
Figure 6.50: The condensation concept on the lubricant-impregnated surface [125].

Xiao et al. [108] have developed a lubricant-infused surface consisted of oil-infused micro and nanostructured surfaces with heterogeneous surface chemistry to enhance condensation heat transfer performance. They have first developed an oil-infused heterogeneous coating on a flat silicon surface with micropillar arrays to investigate the physics of condensation behavior. Then they have studied the effect of the oil-infused heterogeneous nanostructured copper oxide surface, which is coated on a horizontal copper tube, on the condensation heat transfer enhancement. They have demonstrated that the immersion of water droplets within the lubricant (oil) in the presence of the biphilic functional coating is essential to drastically achieve high nucleation densities while sustaining easy water droplets removal with low contact angle and contact angle hysteresis as shown in Figure 6.51. The increase in the nucleation

125

density of droplets was due to the decrease in the interfacial energy between the condensate droplet and the lubricant. The experimental results showed that a maximum enhancement of approximately 100% in condensation heat transfer coefficient was achieved on oil-infused heterogeneous nanostructured copper oxide surfaces in comparison with the complete dropwise condensing surfaces, in the presence of non-condensable gases (air) as shown in Figure 6.52.
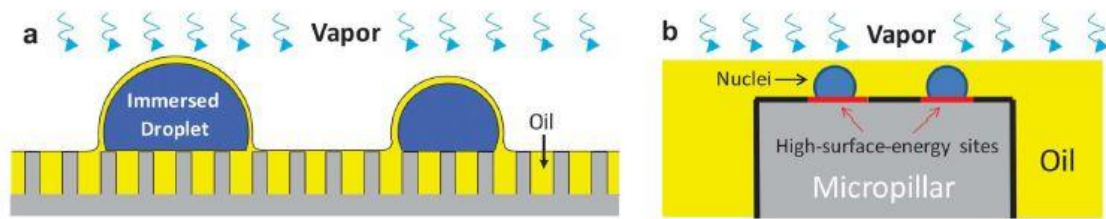
Figure 6.51: (a) Schematic image to show the concept of diffusing of water vapor through the thin oil film and forming immersed water droplets on the micropillars tips. (b) The nucleation formation on sites having high surface energy on the tips of micropillar [108].
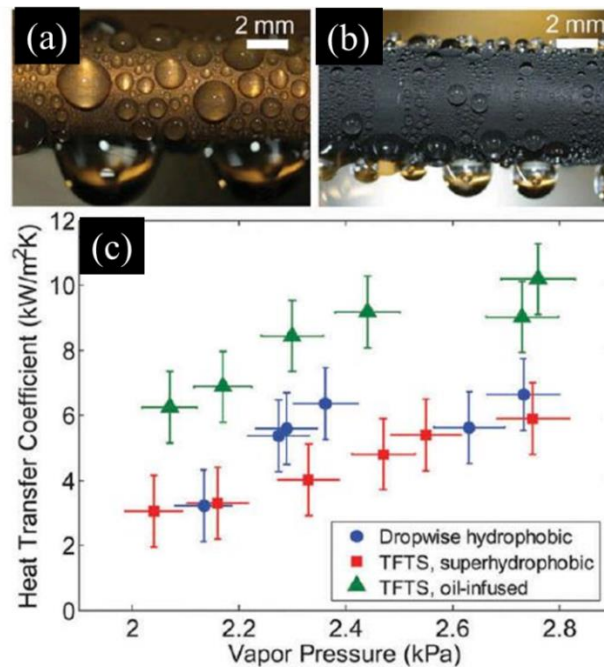
Figure 6.52: (a) dropwise condensation of steam on a hydrophobic horizontal copper tube and (b) condensation on a copper tube coated with an oil infused TFTS-coated copper oxide (CuO) surface (c) Over all heat transfer coefficient as a function of the vapor pressure for the lubricant infused surface compared with hydrophobic and superhydrophobic surfaces [108].

126
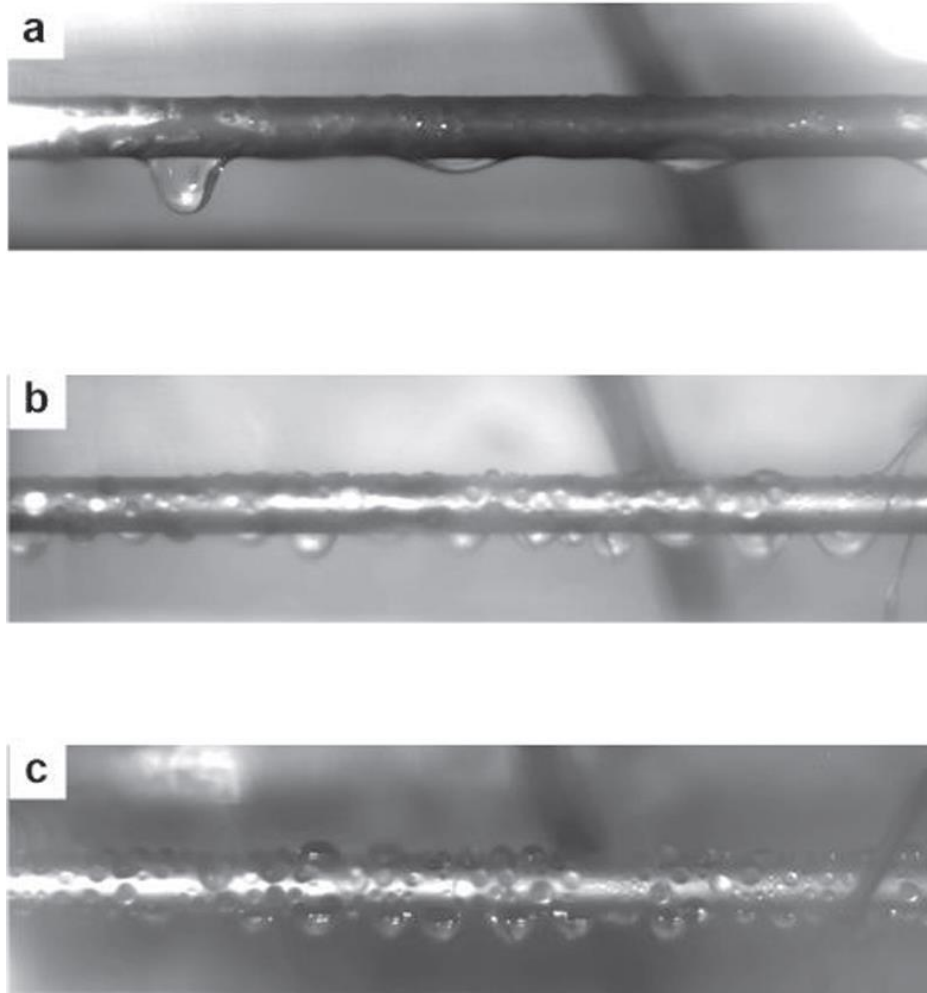
Figure 6.53: Steam condensation on (a) a raw copper tube (b) 500 mPa-s oil-infused nanograss tube (c) 100 cSt oil-infused nanograss tube, with a coolant inlet temperature at 15 ℃ [236].

Quan et al. [236] have fabricated thin hydrophobic films of oil infused nanograss on horizontal copper tubes to investigate the steam condensation heat transfer enhancement at the saturation condition. The oil-infused hybrid nanograss film was fabricated by modifying the cleaned substrate with the silane self-assembled monolayer (vinyltrimethoxysilane) and then the silane treated surface was grafted by polydimethylsiloxane (PDMS) chains. After that silicon oil with either low or high viscosity was infused into the grafted PDMS thin films. Figure 6.53 shows the steam

127

condensation phenomena on a raw copper tube and tubes coated with the oil-infused nanograss film. It was demonstrated that the droplet removal rate was considerably increased after conducting droplet sliding experiments on an inclined surface coated with the oil-infused nanograss film. Furthermore, it was determined that the condensation heat transfer coefficient was enhanced up to about 50% on a horizontal copper tube coated with the oil-infused nanograss film in comparison with a raw copper surface as shown in Figure 6.54.
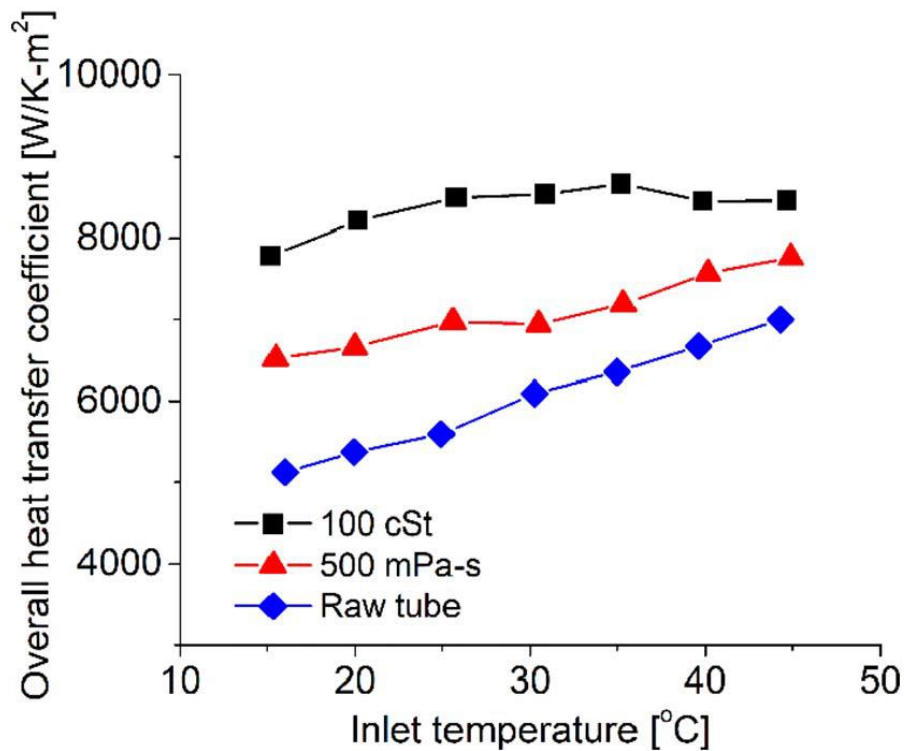
Figure 6.54: Over all heat transfer coefficient as a function of coolant inlet temperature for raw copper tubes and copper tubes coated by oil-infused nanograss [236].

6.3 Summary and conclusions from the literature review

Based on the literature review, numerous methods have been developed to achieve and sustain the dropwise condensation. These methods depend upon reducing the free surface energy of the condensing surface by using such as self-assembled monolayer

coatings, polymer coatings, noble metals and graphene coatings, or ion implantation method. Other methods depend upon the combination of nano/microstructures and low-surface-energy coatings to fabricate superhydrophobic surfaces with either nanostructures or microstructures or both (Hierarchical surface), or to fabricate hierarchical surfaces infused with lubricants (oils). Another method was also introduced to enhance the condensation performance efficiently by fabricating hybrid surfaces combining hydrophobic and hydrophilic regions on the condensation surface. The advantage and the disadvantage of these different methods for enhancing and sustaining the dropwise condensation can be concluded as follow;

Self-assembled monolayers (SAMs) have negligible heat transfer resistance due to the low thermal resistance of molecular film thickness (~1 nm).[149]. However, the chemical stability and the endurance of this coating have not well-understood for the two types of SAM coatings including the alkylthiol (sulfur-based ligand), and alkylsilane (silicon-based ligand).

The thicker polymer coating (>1 μm) on the condensing surface can maintain durable dropwise condensation, but with lower enhancement due to the increase in the thermal resistance of the polymer film compared to the SAM coating [131]. The ultra-thin polymer coatings (with a polymer film thickness less than 1 μm) were not able to chemically protect the substrates from oxidation when they were exposed to a steam/ water environment [160]. Therefore, robust ultrathin polymer coatings are required.

Noble metals (i.e gold and silver), which have a little additional thermal resistance to heat transfer, can promote dropwise condensation due to the presence of hydrocarbon physisorbed contamination on the condensing surface [179]. The fabrication of noble

129

metals coatings on the condensing surfaces is highly expensive compared with the other method and in order to maintain dropwise condensation, a contaminant source is required. It was proven that a critical minimum thickness is required to achieve dropwise condensation, while a smaller thickness than the minimum value leads to film or mixed condensation. It was verified that the promotion of DWC on the electroplated gold and silver surfaces was related to the carbon-to-(gold/silver) and oxygen ratio [182].

The graphene layer consisting of a two-dimensional hexagonal lattice of carbon atoms has hydrophilicity behavior, which is similar to the noble metals behavior during condensation, and it can promote dropwise condensation with robust chemical stability and lower thermal resistance on some metals [127]. However, the chemical stability and the durability of the ultrathin graphene coating on some metals (i.e., copper, Aluminum, etc) need to be investigated and compared to the ultrathin polymer coating prepared by the plasma-enhanced chemical vapor deposition method. Moreover, the graphene coating so far cannot be originated on the rough or the metal oxidized surfaces so that can lead to develop superhydrophobic surfaces with higher chemical stability compared to the metal surfaces.

The dropwise condensation can be achieved by implanting foreign elements, which have high surface energy, into a metallic surface layer of 1-2 μm surface using magnetron sputtering ion plating or dynamic mixing ion implantation technology [164]. This technique results in increasing the surface entropy, reducing the internal energy and thereby reducing the free surface energy, and that depends on the ion energy of the implanted elements. This method showed good condensation heat transfer at low subcooling temperatures. However, flooding occurred at high surface subcooling,

130

resulting in reducing the condensation heat transfer performance [187]. Also, this technique is highly expensive and the scalability needs to be demonstrated.

The influence of superhydrophobic micro/nanostructured surfaces in enhancing dropwise condensation is controversy in the literature. It was reported that the condensation heat transfer performance was enhanced on some of the superhydrophobic surfaces at low surface subcooling, since coalescence-induced droplet jumping phenomena was observed [154]. On the other hand, it was demonstrated inefficacy in enhancing heat transfer rates on other surfaces at high subcooling, since a low droplet departure frequency and surface flooding were recognized [154, 207]. However, It was reported that a superhydrophobic surface with a roughness less than the capillary length scale, where Bond number much smaller than unity (0.1), can improve droplet mobility, decrease the departure droplet diameter, and results in continuous shedding of liquid droplets in condensation [198, 200, 201]. It was also demonstrated that the dropwise condensation could be enhanced on the superhydrophobic nanostructured surfaces having higher perpendicularity and narrow spacing, which results in lower pinning of condensate droplets and thus enhancing the droplets mobility [212].

Furthermore, it was demonstrated by some researchers that there was no heat transfer enhancement on superhydrophobic surfaces with only microscale roughness [201, 213]. This is because of the formation of greatly pinned droplets in Wenzel state in the cavities between the microstructured surface, resulting in flooding the surface and reducing the condensation performance. However, at low supersaturations, the hierarchical and nanostructured surfaces showed dropwise condensation mode due to the formation of condensate droplets in the Cassie state [219]. The droplet departure

131

frequency was much higher on the hierarchical surface in comparison with that on the nanostructured surface. This is due to the smaller average surface coverage by condensate droplets on the hierarchical surface compared to the nanostructured surface. On the other hand, at high supersaturations, the condensation enhancement was degraded due to the surface flooding [219].

The superhydrophobic hierarchical surfaces infused with a low energy lubricant (oil) were implemented to reduce the pinning of condensate droplets within the micro/nano-textured and thereby enhancing the droplet removal rate [108, 125, 233, 235, 236]. The enhancement of the condensate droplets mobility can lead to continuous droplets sweeping which can help to clear the condensing surface for fresh nucleation and thereby enhancing condensation heat transfer performance much higher compared with the hierarchical surface without lubrication. On the lubricant infused surface, controlling the nucleation density, low contact angles and low contact angles hysteresis can be achieved, but more research is needed to investigate the effect of lubricant drainage on the heat transfer performance.

The hybrid surfaces consisting of hydrophobic and hydrophilic regions exhibited high condensation heat transfer enhancement. This approach helps to increase the droplet nucleation density, decrease the droplet departure size and increase the droplet removal rate. It was determined that an optimum width is required between two adjacent hydrophobic and hydrophilic patterns in order to avoid the droplets bridging phenomena, which results in reducing the condensation heat transfer performance [230]. Additionally, even though the hybrid surfaces showed higher condensation performance recently, but

132

they lack to the chemical stability, which is essential to maintain dropwise condensation for long-term durability.

6.4 Research objectives

The objective of the current research is to experimentally investigate the condensation heat transfer characteristics of steam on horizontal copper tubes at the saturation condition and in the presence of the non-condensable gases. The horizontal copper tube would be coated with hydrophobic and superhydrophobic coatings with different morphologies such as a smooth copper surface, cuprite surface (Cu_2O) with sub-microscale porous structures and nanoscale pores size, rough copper surface with microscale porous structures and microgrooves, and micro/nanostructures of copper oxide (CuO) and green patina ($Cu_4SO_4(OH)_6$ surfaces in order to study the influence of such coatings on promoting the steam dropwise condensation performance. A thiol-based self-assembly monolayer coating is used to reduce the surface energy of the developed surfaces. The effects of the coating thickness and the role of oxygen and carbon on the condenser surface on the DWC condensation enhancement would be studied. Therefore, a test setup was constructed to experimentally investigate the condensation heat transfer characteristics. The contact angle measurements, Scanning electron microscopy (SEM), Energy dispersive spectroscopy (EDS) and X-ray photoelectron spectroscopy (XPS) tests were carried out to characterize the morphology, and the surface chemical compositions of the different surfaces. Moreover, a high-speed camera was implemented to visualize the dropwise condensation behavior and analyze the droplet dynamics on the different surfaces in order to compare between the droplets dynamics analysis results and the results obtained experimentally during the condensation experiment. Furthermore, based

133

on the droplets dynamics analysis method, the influence of the droplet departure frequency and droplet departure diameter on the DWC performance would be investigated on the different coatings.

CHAPTER 7

EXPERIMENTAL INVESTIGATION

7.1 Experimental Setup

In order to evaluate the condensation heat transfer performance on horizontal tubes at saturation conditions and in the presence of non-condensable gases (air), a condensation experiment setup was built. The experimental apparatus system as shown in Figure 7.1 and Figure 7.2 consists of four major parts: a steam generation system, a water coolant circulating system, a condensing chamber, and a data acquisition system. A water reservoir (10 L capacities) made of stainless steel was equipped with two controlled electric heaters to generate steam inside the condensing chamber. The main (AVANTCO) and auxiliary (Brisk Heat) heaters, which have total output powers of 3500W and 550 W, respectively, were used to control the steam generation rate and provide sufficient steam at the saturation conditions. A flexible stainless steel tube with a 19.05 mm diameter and 1524 mm long was used to deliver the generated steam to the condensing chamber. Also, in order to make sure dry steam can be delivered to the chamber, a cord heater (Brisk Heat HTC451003) with a diameter of 4.7 mm and 3657 mm long was wrapped around the flexible tube and controlled by a proportional-integral-derivative (PID) temperature controller (BriskHeat-SDC120KC-A SDC). Both the flexible tube and the cord heater were wrapped with a flexible thermal insulation material.

The aluminum condensation chamber, with dimensions of 20 cm (length) x 10 cm (width) x 24 cm (height), was provided with four cartridge heaters embedded from the

135

bottom of the chamber's corners and controlled by a temperature controller (PID) to prevent condensation on the chamber walls during the condensation process. In addition, the outside walls of the chamber were wrapped by a thermal insulation material to reduce the heat losses to the surroundings during the experimentation. The chamber was provided with two openings at the upper and lower sides to maintain the atmospheric pressure inside the condensing chamber and to drain out the condensed steam. Three calibrated T type thermocouples with an accuracy of 0.1%, and a calibrated pressure transducer (Omega PX01C1-050A5T) were placed at the top of the condensing chamber to measure the steam temperature and pressure, respectively. The chamber was also equipped with a 6-inch-diameter circular glass window made of heat-resistant borosilicate glass for condensing observation. Also, two flexible polyimide- etched-foil-heaters (Briskheat-ENP-R-775-01) were mounted on the glass window to prevent the condensation from occurring on the inner wall of the window and allow for clear observation and visualization. A high-speed camera (Phantom v7.3) and LED light source (light-emitting-diode) were used to take visualization and photography during the condensation process.

The water coolant system consists of a galvanized-steel water tank with a capacity of 56 liters, a gear pump, and flow meter. The water tank is equipped with a stainless steel immersion-heater with a heat capacity of 2000 W, a T-type thermocouple and a temperature controller to adjust and change the water temperature in the tank. The gear pump (SHURflo –GMBN4VA53 – 9.7 GPM – 125 Psi) was used to circulate water from the water tank to the test section, which is placed inside the condensing chamber. At the pump discharge line, two valves were installed to control the water coolant flow rate,

136

which was measured by a flow meter (OMEGA-FMG-92, 0.26–6.6 GPM, with an accuracy of ±1%) integrated along the coolant line. Before the test section, a controlled cord heater (BriskHeat- HWC1240) with 7315 mm long and a heat capacity of 1440 W was wrapped around the delivered coolant line to yield additional temperature control before the test section. The testing sample was assembled with the coolant line by using two push-to-connect branch tee adapters connected at the inlet and outlet of the test section. In order to measure the inlet and outlet temperatures of the water coolant, two calibrated K type thermocouples were connected and inserted into the tee adapters to the center of the coolant flow. All the experimental measuring data are directed to a data acquisition unit (34972A, Agilent) and recorded with a LabVIEW program built-in PC.
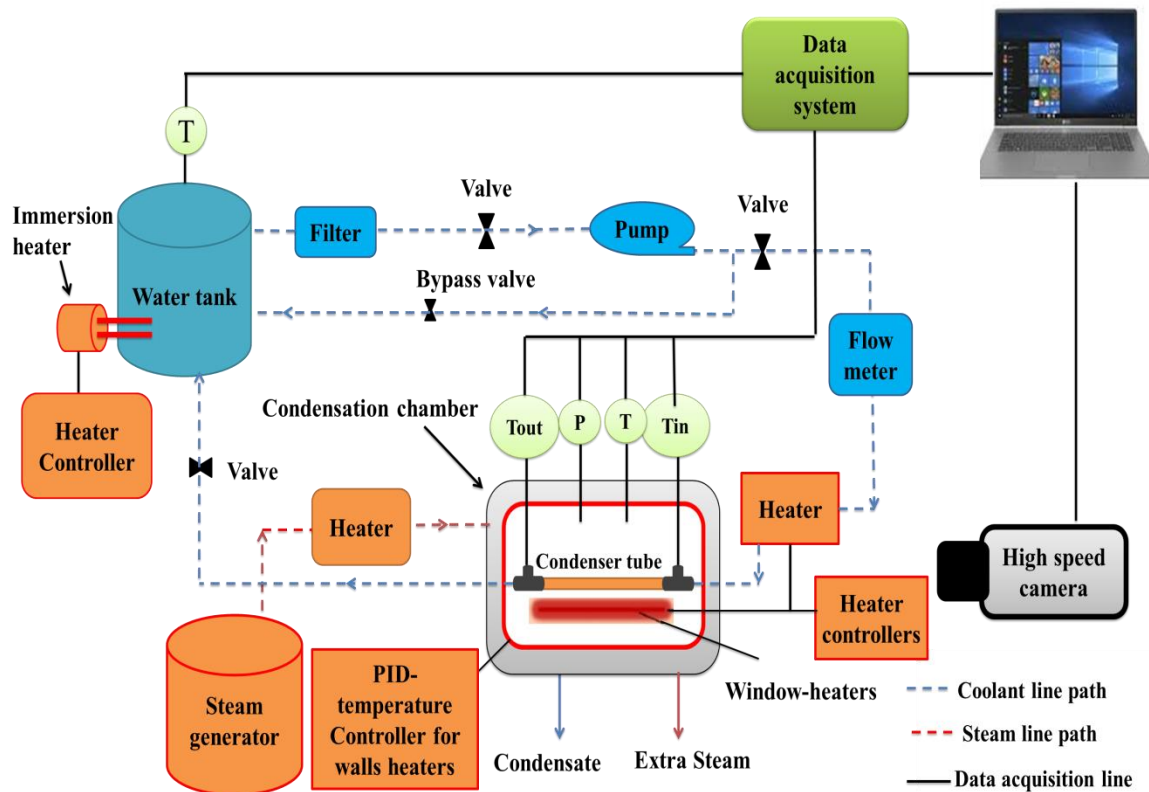
Figure 7.1: A schematic diagram of the condensation setup on a horizontal tube at the saturation conditions.

137
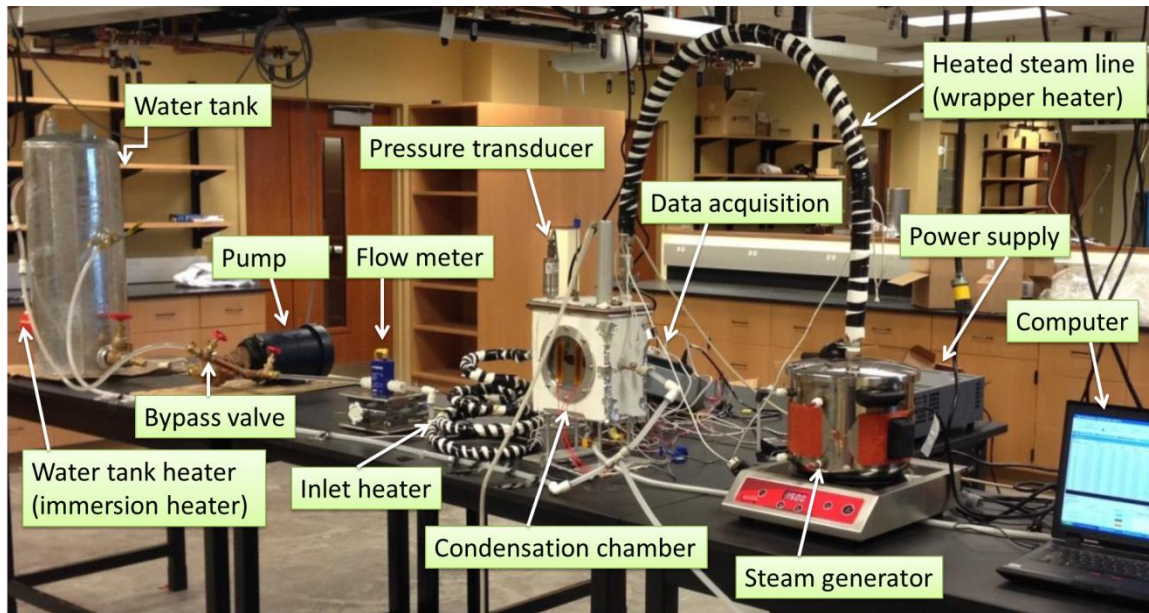
Figure 7.2: A photograph of the condensation setup on a horizontal tube at the saturation conditions.

7.2 Experimental procedure

The main heater related to the steam generator system was adjusted to operate with a full heat capacity of 3500 W to increase the water temperature inside the water reservoir. When the water temperature reached about 70 ºC, the condensation occurred on the window's glass of the condensation chamber. In order to prevent condensation on the window and to reduce the non-condensable gases inside the condensing chamber, the window's heaters were operated from the beginning, and the temperature of the water reservoir was maintained at 98±1 ºC by controlling the output power of the main heater for about 30 min. Then, when the window's glass became clear, the temperature of the water reservoir was maintained at 100 ºC by operating the main heater with full heat capacity. The steam was then delivered to the condensation chamber for about 10 min before pumping the coolant water inside the coolant line to assure a steady state saturation condition was reached, and dry steam was delivered. After that, to start the

138

condensation experiment and collect the data, the coolant water was pumped into the coolant side and maintained at 3±2% L/min, and all the additional heaters were operated. The inlet temperature of the coolant was gradually increased during the experiment from about 28ºC to 85ºC, corresponding to the Reynolds number changing from 18,000 to 40,000, respectively. The continuous increase of the inlet temperature of the coolant was due to the circulation of coolant water from the water tank and the testing section and the three heating sources including the water tank's immersion heater, the preheater installed before the test section and the heat transfer from the vapor condensation. In order to confirm the steady-state saturation condition, the steam temperature and pressure inside the condensation chamber, as well as the chamber wall temperatures were monitored. For all experiments, the near atmosphere pressure measured inside the condensation chamber was ranging from about 0.106 to 0.112 ± 0.002 MPa. Condensation experiments were conducted for each testing sample for the visualization study and heat transfer characterizations. In order to avoid the errors resulting from the radiation effect on the heat transfer measurements, the window's heaters and LED light source were not operated during the condensation experiment. However, for the visualization study, they were operated for clear observation and to prevent condensation from occurring on the window.

7.3 Data Reduction

The overall heat transfer coefficient U_o of the condenser tube is determined by;

$$U_O = \frac{Q}{\Delta T_{LMTD} A_o} \tag{7.1}$$

Where Q is the total heat transfer rate, ΔT_{LMTD} is the log mean temperature difference, and A_o is the outer surface area of the tube. The ΔT_{LMTD} can be determined by

139

$$\Delta T_{LMTD} = \frac{(T_{sat}-T_{in,c}) - (T_{sat}-T_{out,c})}{\ln\left(\frac{T_{sat}-T_{in,c}}{T_{sat}-T_{out,c}}\right)} \tag{7.2}$$

Where T_{sat} is the saturated steam temperature, and $T_{in,c}$ and $T_{out,c}$ are the inlet and outlet temperatures of the cooling water, respectively. The total heat transfer rate Q can be determined by

$$Q = \dot{m}_C \, C_{P,C} \left(T_{out,c} - T_{in,c}\right) - Q_{loss} \tag{7.3}$$

Where $\dot{m}_C$ is the mass flow rate of the coolant, $C_{P,C}$ is the coolant specific heat capacity and Q_{loss} is the heat losses, which was computed by calibration experiment as will be explained in detail in section 7.4.

By considering all the thermal resistances in the system (the condenser tube), the overall heat transfer coefficient (U_O) can be determined as follow;

$$\frac{1}{U_O A_O} = \frac{1}{h_C A_i} + \frac{\ln(D_O/D_i)}{2\pi L K_{tube}} + \frac{1}{h_{cond} A_O} \tag{7.4}$$

Where K_{tube} is the thermal conductivity of the condenser tube, h_C is the inner (coolant) heat transfer coefficient, h_{cond} is the outer (condensate) heat transfer coefficient, $D_i \; and \; D_O$ are the inner and the outer diameters of the tube, respectively, A_i is the inner surface area of the tube and L is its length. Now, by arranging equation (7.4), the condensation heat transfer coefficient (h_{cond}) can be calculated by

$$h_{cond} = \left(\frac{1}{U_O} - \frac{1}{h_C(D_i/D_O)} - \frac{\ln(D_O/D_i)}{2K_{tube}/D_O}\right)^{-1} \tag{7.5}$$

The convective heat transfer coefficient for cooling water inside the tube (h_C) is given by

$$h_C = \frac{Nu_C K_C}{D_i} \tag{7.6}$$

140

Where Nu_C is the coolant Nusselt number inside the tube, and K_C is the thermal conductivity of the coolant (water). The Nusselts number (Nu_C) can be calculated by using a Sieder-Tate correlation for turbulent flow [237]

$$Nu_C = C \, Re_C^{0.8} \, Pr^{\frac{1}{3}} \left(\mu_C / \mu_{C,W} \right)^{0.14} \tag{7.7}$$

Where C is a constant coefficient, and it equals 0.035 in this study [238], Re is Reynolds number, Pr is the Prandtl number, μ_C is the water viscosity computed at the average bulk temperature, and $\mu_{C,W}$ is the water viscosity computed at the wall temperature. To determine the mean values of the fluid properties at the reference temperature, which is related to the fluid bulk and wall temperature, an iterative scheme was carried out by assuming the surface temperature until reaching the convergence in the calculation.

In this study, it was difficult to measure the local tube's surface temperature which is affected by the unsteady of the droplet's size, growth, and removal with time on the condensing surface. However, the definition of the heat transfer coefficient can be used to determine the surface subcooling (ΔT_{sub}), which is defined by the temperature difference between the tube's outer surface and the steam inside the chamber, and then the outer tube's surface temperature (T_S) as follow

$$\Delta T_{sub} = (T_{Sat} - T_S) = \frac{Q}{h_{cond} A_O} \tag{7.8}$$

$$T_S = \Delta T_{Sub} - T_{Sat} \tag{7.9}$$

Also, the condensation heat flux can be determined by

$$q'' = \frac{Q}{A_O} \tag{7.10}$$

141

7.4 Heat loss calculation

To determine the effective heat transfer rate through only the outer surface of the condenser tube, a calibration experiment was performed to compute the heat added to the system by other sources, such as the heat transfer by conduction or condensation through the tube fittings and connections or the heat transfer by radiation from the heated chamber's walls. For the calibration test, a copper tube, which has the same dimensions as the testing tubes, was thermally insulated with moisture resistance silicon foam and then installed in the testing section. The condensation experiment was then conducted to determine the inner and outer temperatures of the isolated tube and then to calculate the heat transfer rate by using equation (7.3) but without the second term in the right hand side. In this case, the computed heat transfer rate represents the heat loss, which is determined by

$$\left[Q_{losses} = \dot{m}_C \, C_{P,C} \left(T_{out,c} - T_{in,c} \right)_{isulated \; tube} \right] \tag{7.11}$$
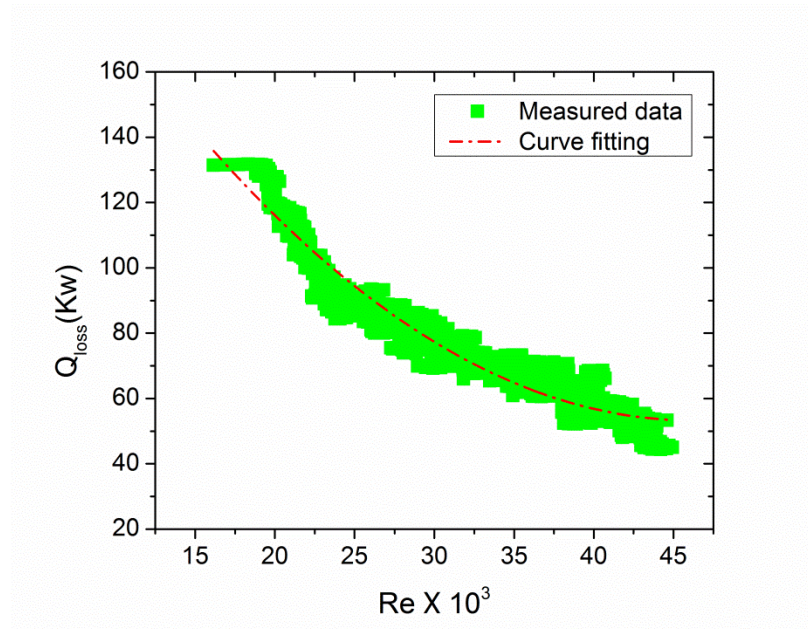
Figure 7.3: An example of the measured heat loss as a function of Reynolds number (Re) for the condensation experiment.

142

The heat losses for the insulated tube was then plotted as a function of Reynolds number as shown in Figure 7.3 and the curve fitting equation of the date was used to calculate the heat losses as a function of Reynolds number during the condensation experiments.

Figure 7.4: Image of filmwise condensation at saturation conditions, on a smooth copper tube (92 mm length) treated with hydrogen peroxide (H_2O_2).

7.5 Calibration and validation of the experimental setup

In order to calibrate the experimental setup and validate between the experimental and the theoretical results, a condensation experiment was conducted on a horizontal copper tube, which is treated with 30 % hydrogen peroxide (H_2O_2) for about 1 hour to achieve complete filmwise condensation. The experimental results were then compared with the classical Nusselt model for filmwise condensation on the horizontal tube, which is given by [239].

$$h_{FWC} = \left[\frac{\rho_C \, (\rho_C - \rho_v) \, g \, h'_{fg} \, K_C^3}{\mu_C D_O (T_{Sat} - T_S)} \right]^{\frac{1}{4}} \tag{7.12}$$

Where ρ_C, ρ_v, g, and h'_{fg} are the coolant density, vapor density, gravity, and the corrected enthalpy of vaporization, which is determined by [239]

$$h'_{fg} = h_{fg} \left[1 + 0.68 \left(\frac{C_{P,l} \, (T_{Sat} - T_S)}{h_{fg}} \right) \right] \tag{7.13}$$

143

All the liquid properties in equations (7.12) and (7, 13) were computed at the average fluid temperature related to the fluid bulk and wall temperatures except ρ_v and h_{fg} which were computed at the vapor saturation temperature (T_{Sat}).
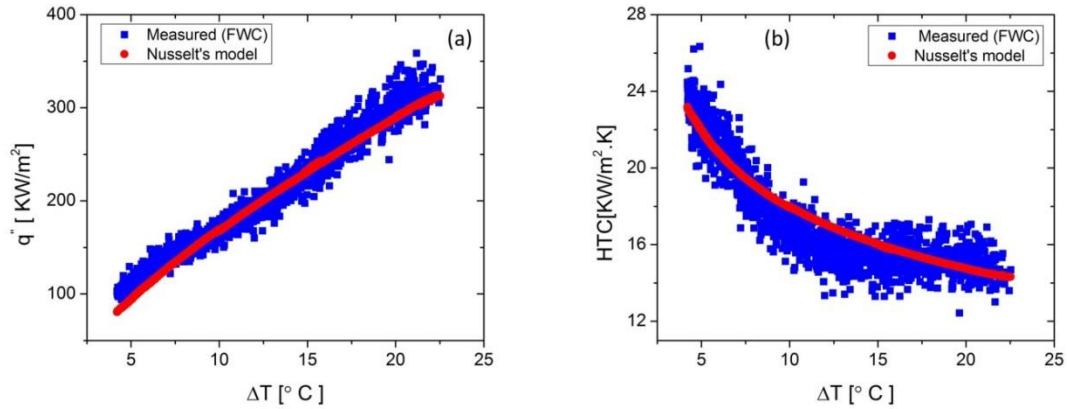
Figure 7.5: Experimental results of condensation (a) Heat flux (b) heat transfer coefficient as a function of surface subcooling, compared with Nusselt model for filmwise condensation.
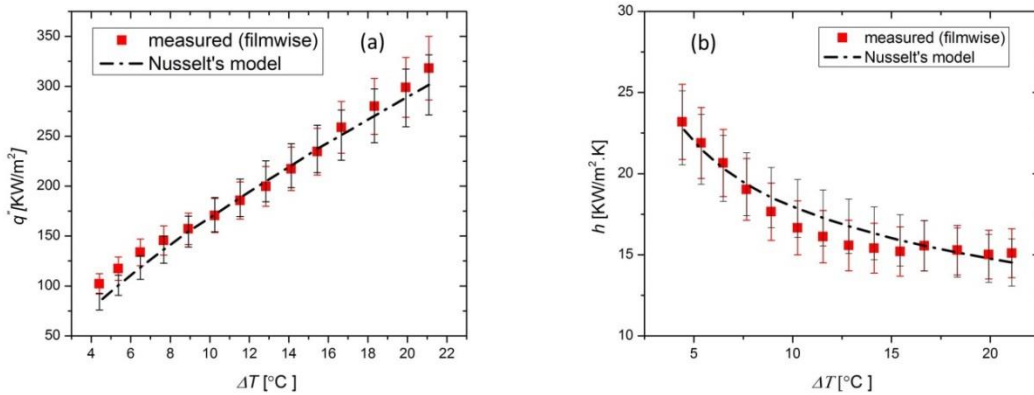
Figure 7.6: Experimental results of condensation (a) Heat flux (b) heat transfer coefficient as a function of surface subcooling, compared with Nusselt model for filmwise condensation, after the refining process.

Figure 7.4 shows the complete filmwise condensation behavior on the horizontal copper tube treated with the hydrogen peroxide at the saturation conditions. With considering the heat losses in the system, the measured data of the heat flux (HF) and the heat transfer coefficient (HTC) as a function of surface subcooling was compared with

144

theoretical results calculated by the Nusselt model of filmwise condensation (FWC), and a great agreement was achieved between the experimental and theoretical results as shown in Figure 7.5, indicating accurate measurements of the heat flux and heat transfer coefficient. Furthermore, due to the fluctuation in the readings of mass flow rate, the inlet and outlet temperatures of the coolant, the data was reduced and refined for all the experimental data by taking the average for every 20-50 readings. Figure 7.6 presents the final results of the heat flux and heat transfer coefficient as a function of the surface subcooling after applying the refining process.

In addition, in order to confirm the experimental validation, a calibrated T type thermocouple with a diameter of 0.508mm was used to measure the local surface temperature of the tube during the condensation experiment as described by Alwazzan et al [230]. The thermocouple was inserted in a hole with a 0.5 mm depth at the center of the tube wall and then fixed using a soldering process. A good agreement was achieved between the theoretical results presented by the Nusselt model for the complete filmwise condensation (FWC) and the experimental results obtained by the direct measurement of the surface temperature and the calculating method that explained in section (7.3).

7.6 Non-condensable gases measurement

The percentage of the non-condensable gases (NCG %) during the condensation experiment was computing by Alwazzan et al. [230] as follow;

$$NCC \% = \frac{P_1 - P_2}{P_1} \times 100 \tag{7.14}$$

Where P_1 is the saturated pressure measured by the pressure transducer, which is installed inside the condensation chamber, and P_2 is the calculated pressure at the saturated temperature measured by the thermocouples. It was found that the percentage of the non-

145

condensable gasses (air) for all the condensation experiments was in the range between 3.56% and 6.84%.

7.7 Droplet dynamics analysis method (DA)

A high-speed camera (Phantom v7.3) and LED light source (light-emitting-diode) were utilized to visualize the droplets dynamics on the condenser surfaces. For each testing sample, video clips were recorded at 100 frames per second with a recording duration of about 20 seconds containing 2000 frames. The videos were recorded at inlet coolant temperatures within a range of 30-85℃ and an increment of 10℃ except for the inlet temperature of 85℃. The image processing software (Image J) was implemented to determine the droplet departure frequency and the droplet departure diameter. The droplet departure frequency was found based on counting the total number of droplets departed the condenser surface and the recording duration of the video clip. The droplet departure diameter was measured at the different inlet coolant temperatures to determine the volume of the departure droplets. The heat transfer rate based on the droplets dynamics analysis method (DA) explained above was computed as follows;

$$Q_{DA} = \dot{m}_c h_{fg} = \rho_v \bar{V} f h_{fg} \tag{7.15}$$

Where, $\dot{m}_c$ is the condensation rate, ρ_v is the density of the saturated vapor, $\bar{V}$ is the average volume of the departure droplets, f is the droplets departure frequency, and is h_{fg} the latent heat.

The heat flux was also computed as follow;

$$q_{DA}'' = {Q_{DA}}/{A_o} \tag{7.16}$$

146

7.8 Uncertainty analysis

The uncertainties in the measurements (R_Z) for the temperatures, pressures, mass flow rate, heat flux, convective heat transfer coefficient, condensation heat transfer coefficient, and overall heat transfer coefficient were considered in the data reduction analysis. The estimation of uncertainty was derived based on the error propagation method presented by Kline and McClintock [240], as follow;

$$R_Z = \left[\left(\frac{\partial R}{\partial r_1} \right)^2 Z_1 + \left(\frac{\partial R}{\partial r_2} \right)^2 Z_2 + \cdots + \left(\frac{\partial R}{\partial r_n} \right)^2 Z_n \right]^{\frac{1}{2}} \tag{7.17}$$

Where ($R = R(r_1, r_2, \ldots, r_n)$) is a function of independent variables (n), Z_i is the uncertainty in the variable (r_i). The uncertainties of propagation in the calculated values of the experimental parameters are listed in **Table 7. 1**.

Table 7. 1: Uncertainties of the experimental measurements

Experimental measurements	Uncertainty
Condensing surface area (A)	2 %
Coolant inlet and outlet temperatures ($T_{in,c}, T_{out,c}$)	0.5 K
Saturated vapor temperature (T_{Sat})	0.2 K
Saturated vapor pressure (P_{Sat})	2 %
Mass flow rate of the coolant ($\dot{m}_C$)	1 %
Heat flux ($q^{''}$)	4-9 %
The convective heat transfer coefficient (h_C)	10 %
The condensation heat transfer coefficient (h_{cond})	13-57 %

147

7.9 Surface preparation and characterization

7.9.1 Green patina samples

In order to fabricate a green patina coating on the copper tube surface, the tube sample (Cu-101, 99.99% purity, McMaster-Carr) with an outer diameter of 6.35 mm, a wall thickness of 0.9 mm and a length of 92 mm was first polished by 220, 1000 and 2000 grit sandpapers, respectively. Second, the sample was dipped in 10 wt. % of the sulfuric acid solution (H_2SO_4) and cleaned in an ultrasonic bath for 10 min to remove the native oxides formed on the surface. The sample was then ultrasonically cleaned in acetone, ethanol and distilled water for 10 min, respectively. After completing the cleaning process, the sample was immersed in a 0.04 M $KClO_3$ solution at 60 °C for 12 h to be oxidized and form a red cuprite film (Cu_2O) on the tube surface. The pH value of the solution was measured by using PH meter (PHH222, OMEGA) and adjusted at a value of 3 by adding drops of Sulfuric acid (10 % wt) to the solution to speed up the chemical reaction and develop a uniform coating. After that, a second reaction was started by adding 0.1 M copper sulfate pentahydrate ($CuSO_4.5H_2O$) to the solution. Then after 60 h of the second reaction, the cuprite film was coated with a green layer called brochantite ($Cu_4SO_4(OH)_6$). The as-prepared patina coating was then washed with distilled water and dried in air. In order to reduce the surface energy and convert the superhydrophilic properties of the patina surface to superhydrophobic ones, the surface was immersed in 0.0025 mol/L solution of n-octadecyl mercaptan in ethanol for 90 min at 75°C and then washed with ethanol and dried in air. Figure 7 7 shows the polished copper tube, the coated cuprite film, the brochantite coating and the patina surface treated with the self-assembled monolayer coating (SAM).

148
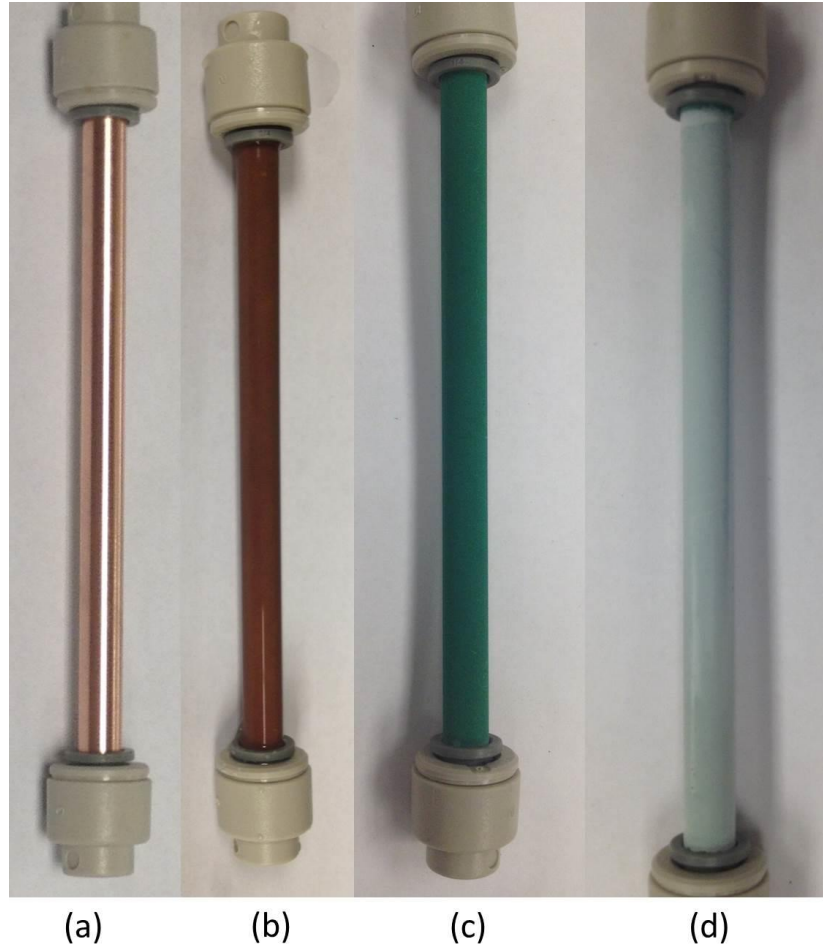
Figure 7 7: Photograph images of (a) the polished copper tube, (b) the coated cuprite film, (c) the brochantite coating and (d) the patina surface treated with the self-assembled monolayer coating (SAM).

It was observed that if the second reaction was treated with or without stirring at 60 rpm, the thickness of the brochantite layer could be controlled. It was noted that the steering of the solution leads to an increase in the brochantite thickness for about 200.0 μm compared to about 50.0 μm without stirring as shown in Figure 7.8b and Figure 7.8c. Furthermore, it was remarked that the patina thickness could be reduced for about 1.0 μm when the preparation time was about 6 hours at the room temperature. The thickness of the coating was measured by taking a side view image by a field-emission scanning

149

electron microscopy (SEM, TESCAN Vega-3 SBU, USA), which was taken at 10 KV SEM HV.
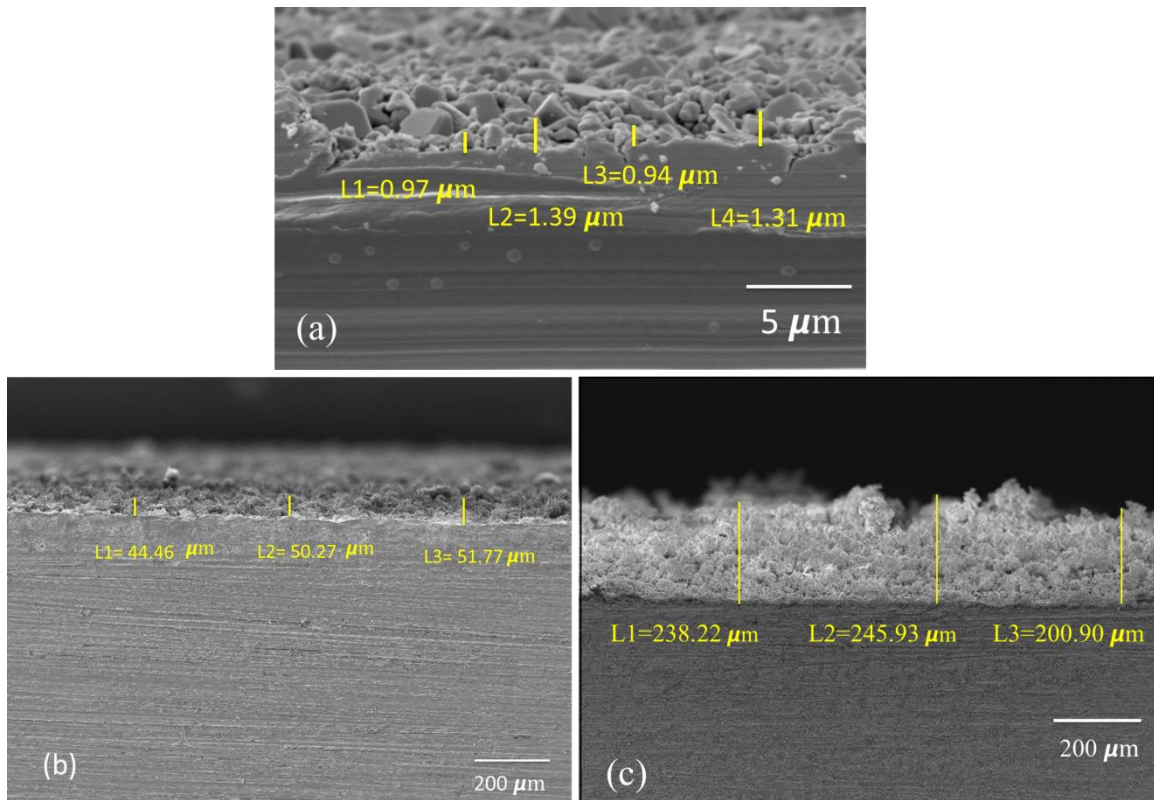
Figure 7.8: Scanning electronic microscopy (SEM) images to show (a) the measured thickness of the cuprite coating, (b) the measured thickness of brochantite coating without stirring process during the second reaction and (c) the measured thickness of brochantite coating with stirring process at 60 rpm during the second reaction.

The surface morphology of the as-prepared cuprite (Cu_2O), green patina and the treated patina with SAM surfaces is characterized by a field-emission scanning electron microscopy (SEM). As shown in Figure 7.8a and Figure 7.9a, the SAM images reveal that after the first reaction a reddish crystal film of Cuprite (Cu_2O) with cubic microstructures (300 nm-1.6 μm) was formed on the copper substrate. Then after completing the second reaction, a greenish 3D crystalline dandelion-like (flower-like) microstructures of brochantite ($Cu_4SO_4(OH)_6$) with dimensions between 10 μm and 20

150

μm is developed on the copper substrate as shown in Figure 7.9c. However, as shown in Figure 7.9d, the SEM image reveals that the surface morphology of the patina surface was changed after the SEM treatment. The color of the 3D crystalline dandelion-like structured changed from green to white and they became unsharpened and shorter.
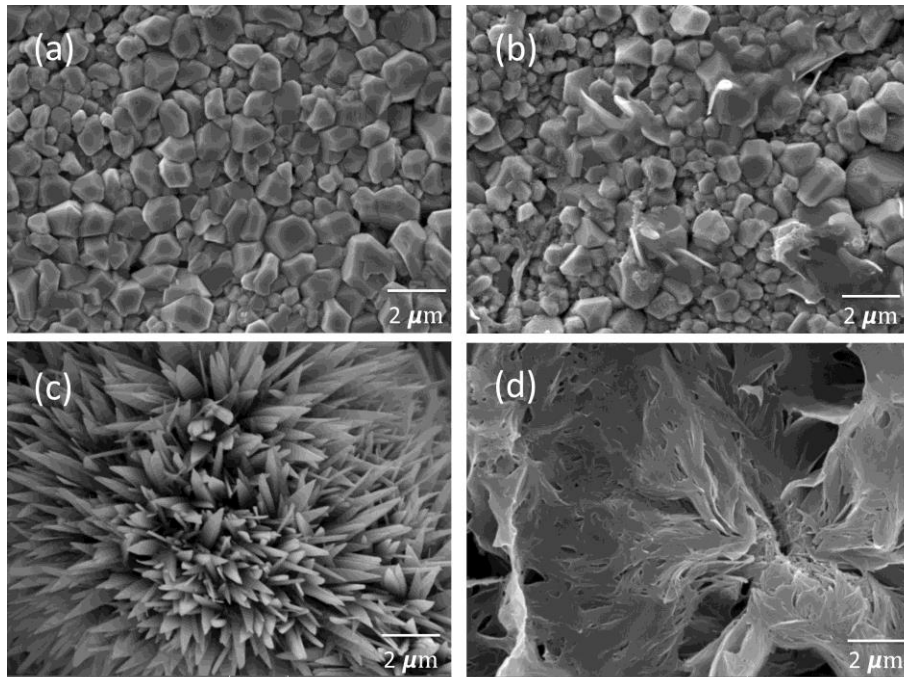
Figure 7.9: The SEM images of (a) the as-prepared cuprite (Cu_2O) coating, (b) the cuprite surface treated with SAM, (c) the green patina coating and (d) the treated patina with SAM.

The chemical compositions of the cuprite, patina and the treated patina with SAM were analyzed using energy dispersive spectroscopy (EDS), which was performed with the same field-emission scanning electron microscope. As shown in Figure 7.10, the (EDS) spectrum results recorded at 20 KV reveals that the as-prepared cuprite surface is mainly composed of Cu and O elements. Moreover, the EDS spectrum result for the brochantite surface reveals that the surface consists of Cu, O, and S elements. It is clear that according to the (EDS) characterization, carbon contamination was formed on the oxide layer of the cuprite and brochantite due to the environmental or the vacuum

151

chambers contamination. The other ratio of the gold introduced on the surfaces was due to the layer coated using sputter cleaning to achieve high resolution of SEM images. On the other hand, the EDS spectrum showed that the treated patina surface with SAM consisted of copper and high values of carbon and sulfur since the oxygen value was decreased highly and replaced by the carbon and sulfur after the chemical etching using the self-assembled monolayer.
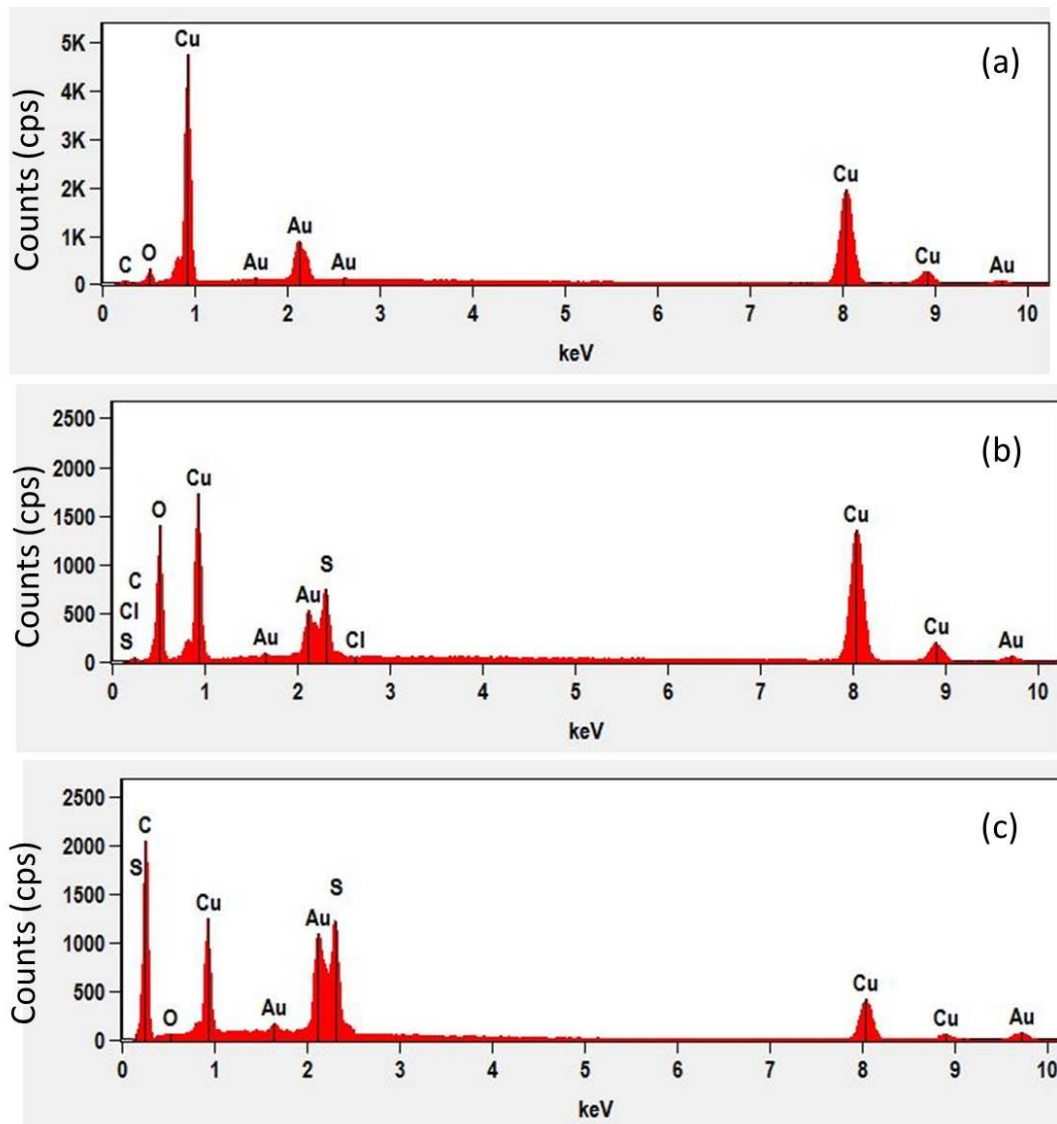
Figure 7.10: The energy dispersive spectroscopy (EDS) spectrum results recorded at 20 KV for the (a) cuprite (Cu_2O) coating, (b) the patina coating and (c) the patina surface treated with SAM.

152
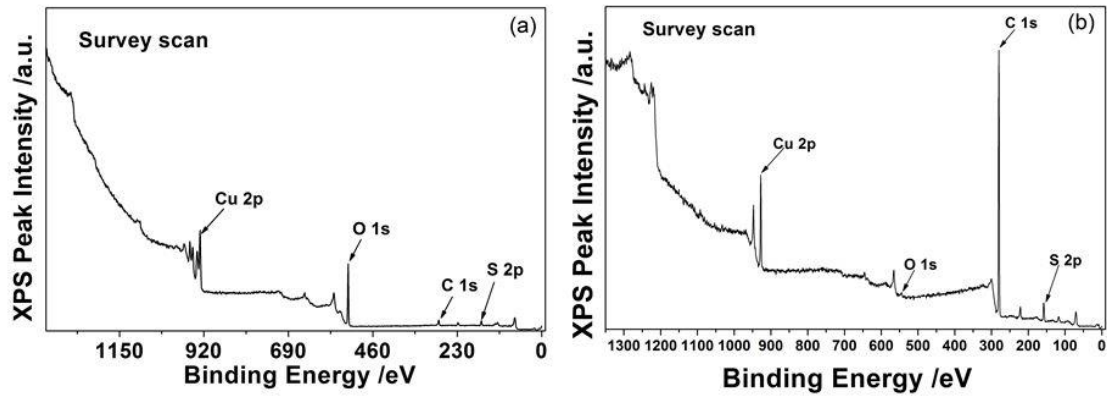
Figure 7.11: The X-ray photoelectron spectroscopy (XPS) survey scan of (a) the patina surface and (b) the treated patina with SAM.
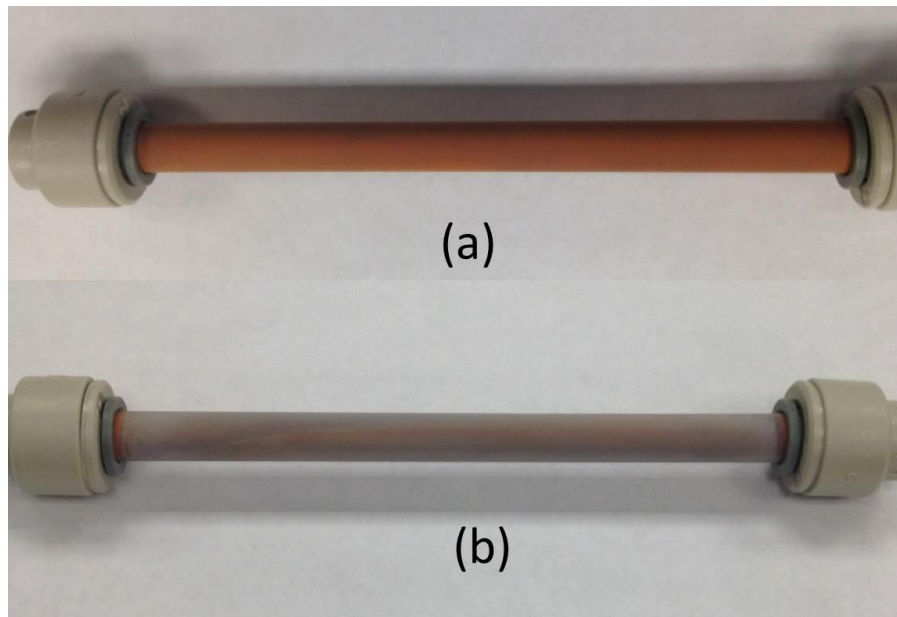
Figure 7.12: Photograph images of (a) the polished patina surface treated with SAM and (b) the treated surface with SAM for about 30 min after the polishing process.

The chemical composition of the patina surface was also analyzed using X-ray photoelectron spectroscopy (AXIS Ultra DLD XPS, Kratos Analytical Ltd., U.K). As shown in Figure 7.11, the XPS analysis of the brochantite surface shows the presence of Cu (2p) peak at 934.3eV, O (1s) peak at 530.9eV, C (1s) peak at 284.6 eV and S (2p) peak at 168.2 eV, referring to the brochantite components on the surface. However, after

153

the SAM treatment, the amount of oxygen was reduced considerably, and a high value of carbon was developed on the surface. The results of the XPS and EDS analysis were consistent.
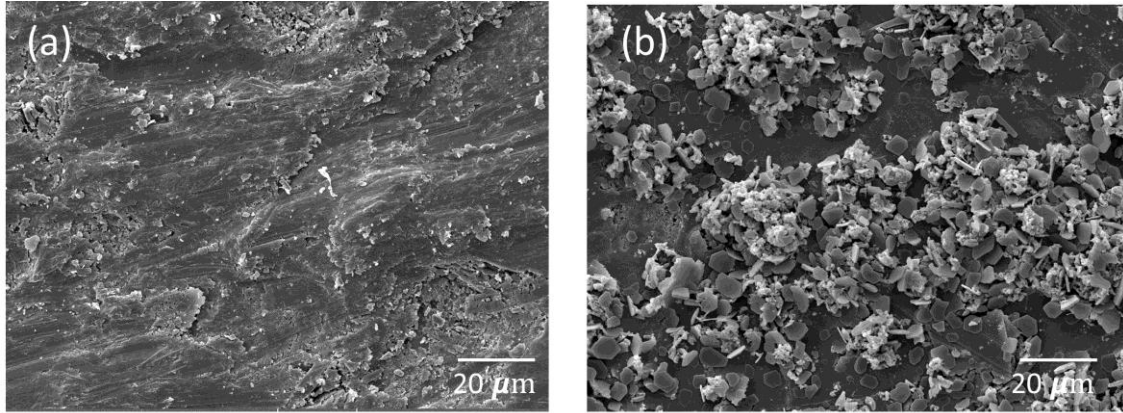
Figure 7.13: The SEM images of (a) the polished patina surface treated with SAM and (b) the treated surface with SAM for about 12 min after the polishing process.

In this work, in order to improve the dropwise condensation performance and reduce the effect of the water penetration into the cavity of the microstructures of the patina surface as well as reduce the patina thickness to decrease the conductive thermal resistance, the treated patina surface with SAM was polished using a fine white paper. Figure 7.12a shows the surface with a dark orange color after the polishing process. The surface was then treated with the SAM for about 12 to 15 min. to reduce the white (carbon) layer on the surface. It was observed that after the SAM treatment for about 30 to 60 min, a thick uniform white layer covered the polished surface even though the microstructures were removed and a smooth surface was created as shown in Figure 7.12b. Figure 7.13 shows the SEM images of the polished patina surface treated with SAM and the treated surface with SAM for about 12 min after the polishing process. It can be seen that the white carbon is still formed on the polished smooth surface and then its value increased after the SAM treatment leading to create a rough surface.

154
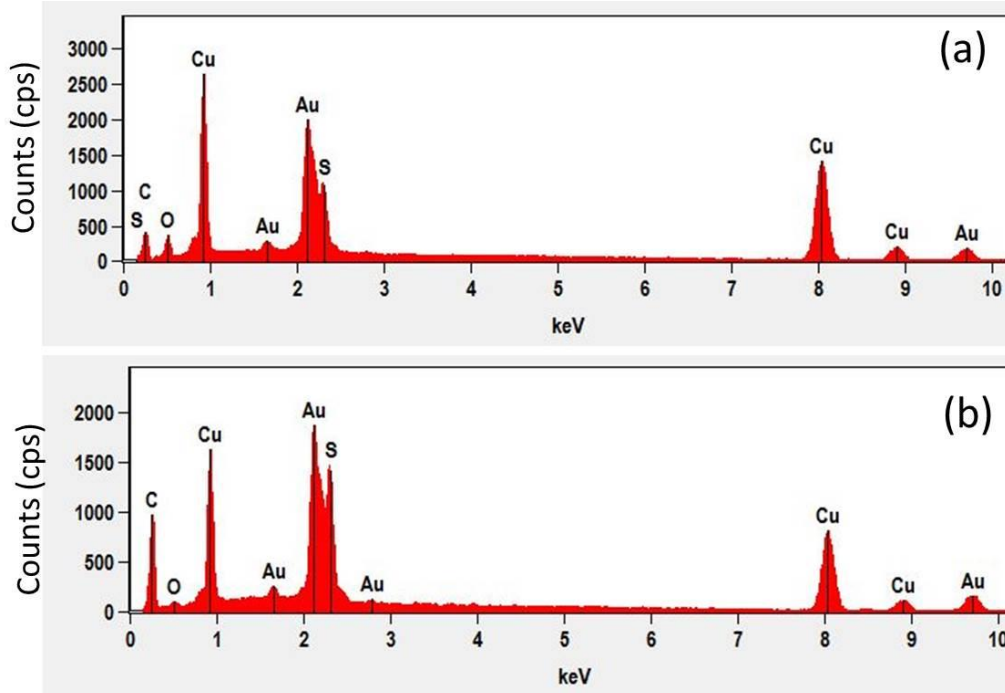
Figure 7.14: The EDS spectrum results recorded at 20 KV for (a) the polished patina surface treated with SAM and (b) the treated surface with SAM for about 12 min after the polishing process.

Furthermore, as shown in Figure 7.14, the EDS spectrum result for the polished brochantite surface reveals that the surface consists of Cu, O, S and C elements. Then the value of oxygen was reduced, and the values of carbon and sulfur increased after the SAM treatment. The comparison between the patina surface (Patina1), the treated patina with SAM (Patina2), the polished Patina2 (Patina3), and the treated patina3 with SAM (Patina4) is shown in Figure 7.15. It can be observed that the atomic weight percentages of copper and oxygen are high for Patina1, and then the oxygen was completely reduced while the carbon was highly increased for Patina2. The values of the copper and oxygen then increased, and the value of carbon decreased after the polishing process for Patina3. Then the opposite happened for Patina4 after the SAM treatment for Patina3. As a result, it can be concluded that as the amount of oxygen on the oxidized surface increases the

155

amount of carbon could be increased considerably after the SAM treatment, resulting in reducing the wettability of the surface and increasing its hydrophobicity.

In this study, the effect of the patina surfaces, which include the treated patina with SAM (Patina2) with thicknesses of about 1.0 μm, 50.0 μm, and 200.0 μm, the polished patina (patina3) and the treated patina with SAM (patina4), on the condensation heat transfer enhancement was experimentally investigated.
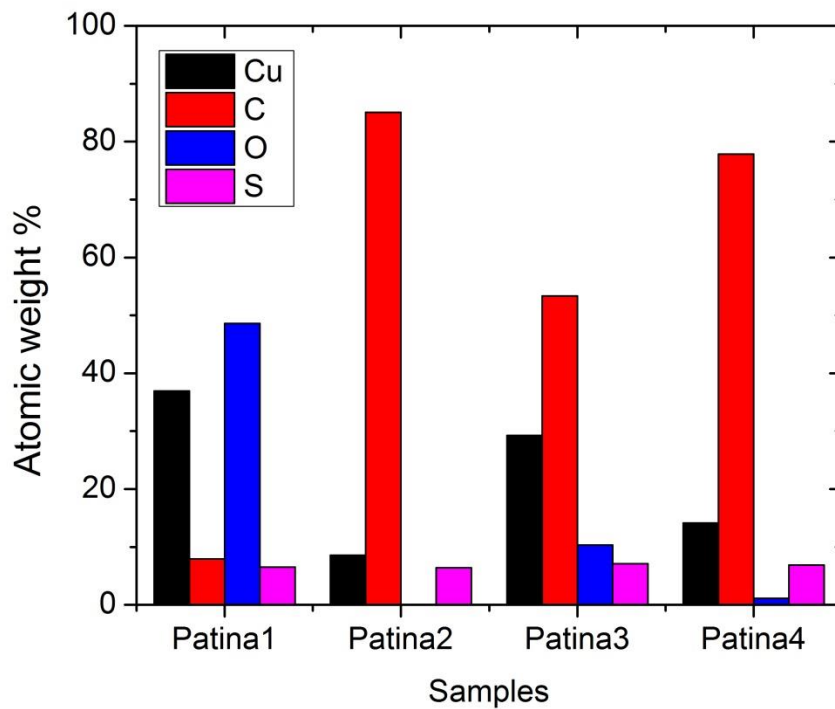
Figure 7.15: The atomic weight percentage of copper (Cu), oxygen (O), carbon (C) and sulfur (S), on (a) the patina surface (Patina1), (b) the treated patina with SAM (Patina2), (c) the polished Patina2 (Patina3), and (d) the treated patina3 with SAM (Patina4).

7.9.2 Copper oxide (CuO) samples

The polished and cleaned copper tube was immersed into an alkaline solution consisted of 3.75 g of NaClO$_2$, 5 g of NaOH, 100 g of Na$_3$PO$_4$·12H$_2$O, and distilled water (100 ml) at 95 °C [30, 241]. Then after 30 min, the nanostructured copper oxide (CuO)

156

coating was developed on the surface. During the chemical oxidation process, a brown cuprite film was initially coated on the surface and then it was oxidized to form a black film of copper oxide (CuO) on the surface according to the following two chemical reactions;

$$2Cu + 2OH^- \rightarrow Cu_2O + H_2O + 2e^- \tag{7.18}$$

$$Cu_2O + 2OH^- \rightarrow 2CuO + H_2O + 2e^- \tag{7.19}$$
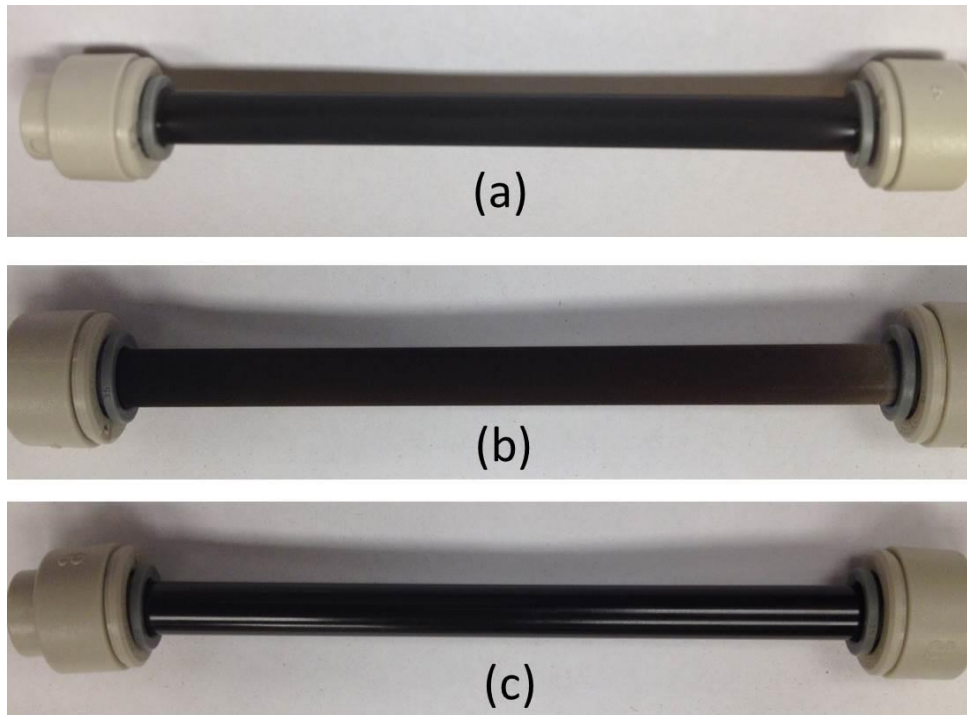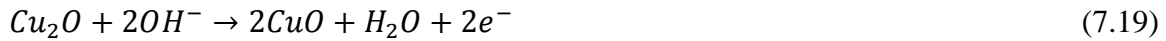
Figure 7.16: Photograph images of (a) the as-prepared nanostructured copper oxide (CuO) on the copper tube, (b) the copper oxide surface treated with SAM and (c) the polished copper oxide surface treated with SAM.

Furthermore, for hydrophobic functionalization, the copper oxide surface was treated with the self-assembled monolayer as explained before. Figure 7.16 shows the copper tube coated with the copper oxide coating and the surface treated with the SAM coating. As shown in Figure 7.17, the SEM images reveal that the as-prepared copper oxide nanostructures consisted of sharp blade-like morphology with approximately 1.0

157

μm height. However, the SEM image of the copper oxide surface treated with the SAM shows that the 3D sharp blade-like structured became shorter and blunter. The surface was also coated with the white carbon layer which led to increasing the roughness of the surface.
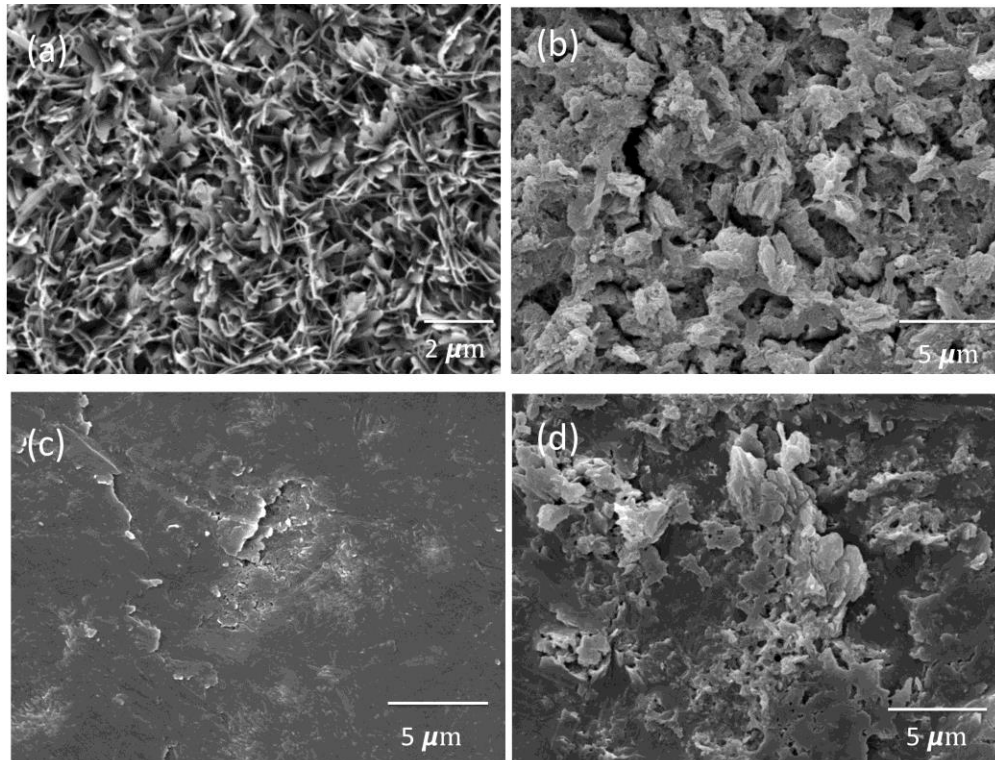
Figure 7.17: The SEM images of (a) the as-prepared nanostructured copper oxide (CuO), (b) the copper oxide surface treated with SAM, (c) the polished copper oxide surface treated with SAM and (d) the treated surface with SAM for about 12 min after the polishing process.

The EDS spectrum result for the CuO surface, as shown in Figure 7.18a, reveals that the surface consists of Cu, O, and C elements. The small amount of carbon was originated due to the environmental contamination. However, after the SAM treatment as shown in Figure 7.18b, the amount of oxygen was reduced on the surface and high values of sulfur and carbon were formed on the surface, referring to the same behavior observed for the treated patina surface with SAM. This indicates that as the oxygen increase on the

158

surface, it could be highly decreased after the SAM treatment and a high value of carbon could be formed on the surface.
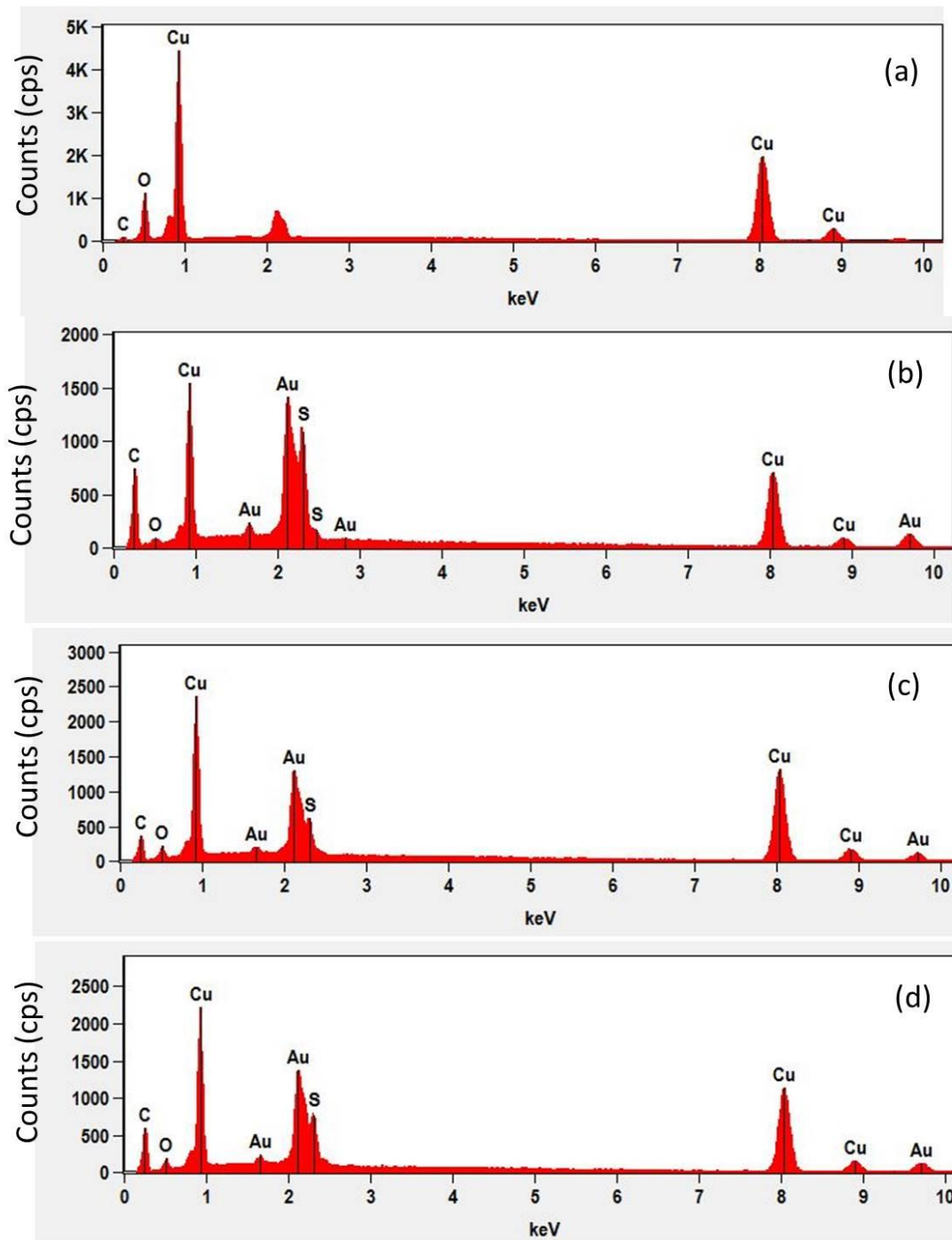
Figure 7.18: The EDS spectrum results recorded at 20 KV for of (a) the as-prepared CuO surface, (b) the treated CuO with SAM, (c) the polished CuO surface treated with SAM and (d) the treated surface with SAM for about 12 min after the polishing process.

159

Figure 7.19: The atomic weight percentage of copper (Cu), oxygen (O), carbon (C) and sulfur (S), on the nanostructured CuO surface (CuO)1, the treated with SAM (CuO)2, the polished surface treated with SAM (CuO)3, and the treated with SAM after the polishing process (CuO)4.

The same polishing process used to remove the microstructured patina surface was implemented herein for the nanostructured CuO surface treated with SAM. Figure 7.16c shows a brilliant black CuO coating on the copper tube after the polishing with a fine white paper. As shown in Figure 7.17c, the SEM image shows a smooth surface and white carbon atoms are still formed on the surface. Also, as shown in Figure 7.18c, the EDS spectrum result exhibits the existence of carbon and sulfur on the surface after the polishing process. In order to reduce the white carbon layer which can be thicker based on the treatment time, the surface was treated with SAM for about 12 to 15 min. As

160

shown in Figure 7.17d, the SEM image reveals to increasing the surface roughness and carbon on the surface. Furthermore, as shown in Figure 7.18d, the EDS analysis result shows the increase in the values of carbon and sulfur and the decrease in the value of oxygen on the surface after the SAM treatment. Figure 7.19 shows the comparison between the nanostructured CuO surface (CuO)1, the treated with SAM (CuO)2, the polished surface treated with SAM (CuO)3, and the treated with SAM after the polishing process (CuO)4. The same behavior for the patina surfaces was observed here. After the SAM treatment, the atomic weight of oxygen was reduced while the carbon was considerably increased. Then the opposite occurred after the polishing process. However, after the second and shorter SAM treatment, the value of carbon increased, whereas the copper and oxygen decreased on the surface. The four different copper oxide surfaces were tested during the condensation experiment to investigate their effects on the heat transfer condensation enhancement.

7.9.3 Cuprous oxide (Cu_2O) samples

During the first oxidation process in fabricating the cuprite coating on the copper tube, it was observed that the color of the surface changed from red to orange according to the preparation time. Moreover, the color of the surface was converted to a dark orange color during the second oxidation process at the room temperature as shown in Figure 7.20. Therefore, in this study, the different cuprite surfaces were characterized and treated with the SAM coating to investigate the condensation heat transfer enhancement on these surfaces. The comparison between the SEM images for the red and orange cuprite films, as shown in Figure 7.9a and Figure 7.21a, reveals that a uniform sub microscale porous structure with nanoscale pores size was deposited with a red color after about two hours

161

of the first oxidization process and then the particles became smaller and broken when the color changed to orange after about 12 hours. However, as shown in Figure 7.10a and Figure 7.22a, the EDS analysis results show the presence of Cu, O elements on both surfaces, referring to the composition of cuprite surface. Moreover, the results exhibit a higher value of oxygen on the orange cuprite film, which led to a higher value of carbon after the SAM treatment compared to the red cuprite film treated with SAM, as shown in Figure 7.22b and Figure 7.22c. The SEM images for the two treated surfaces shows the presence of white carbon on the surfaces as shown in Figures Figure 7.9b and Figure 7.21b.

(a)   (b)   (c)   (d)
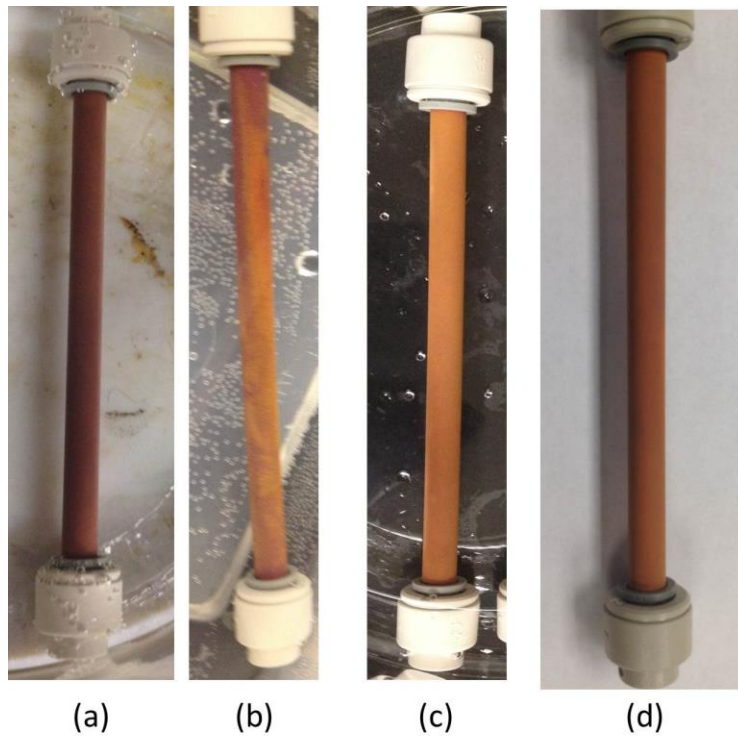
Figure 7.20: Photograph images of cuprite coating on the copper tube, (a) a red coating was developed on the surface after about 2 hours of the first oxidation process, (b) the red coating was changed partially to orange with increasing the time of the first oxidation process, (c) the color of the surface was completely changed to orange after 12 hours of the preparation time and finally (d) the orange color became more orangish when the surface treated with the second oxidation process for about 6 hours at the room temperature.
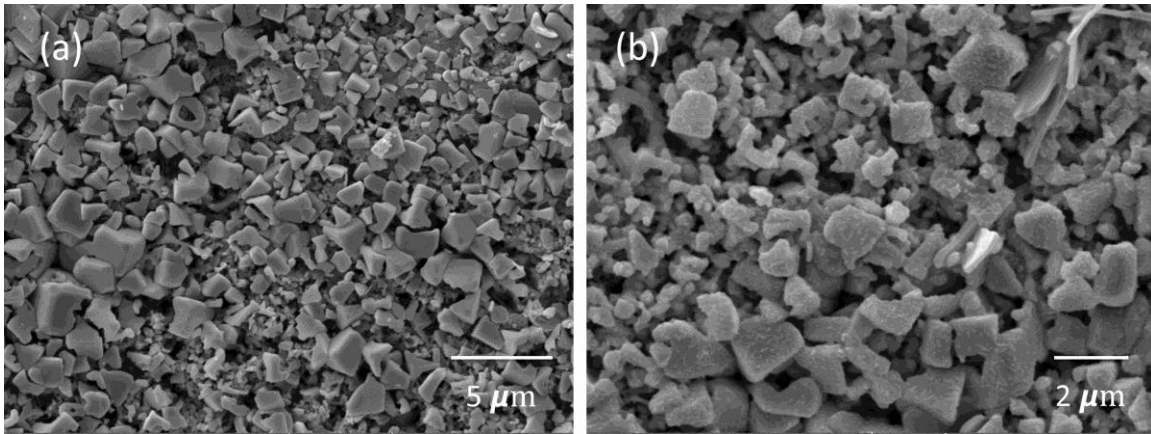
Figure 7.21: The SEM images of (a) the as-prepared cuprite (Cu_2O) coating with orange color and (b) the orange cuprite surface treated with SAM.

In this part of the study, in order to enhance the chemical stability of the cuprite film, it was oxidized using hydrogen peroxide to increase the oxygen ratio and make the chemical composition of Cu_2O close to the copper oxide surface. Therefore, the as-prepared cuprite film was immersed in 30 % of H_2O_2 at room temperature for 24 hours. Figure 7.23 shows that the color of the surface changed from a red color to reddish or black based on the treatment time. The thickness of the oxidized cuprite surface was measured and compared with the copper oxide and the polished copper oxides surfaces as shown in Figure 7.24. The measured thicknesses were about 5mm, 17.0 mm and 50.0 mm for the oxidized cuprite surface (Cu_2O)3, the nanostructures copper oxide surface (CuO)2, and the polished copper oxide surface (CuO)4, respectively.

The oxidized cuprite surface was then treated with SAM for about 2 hours. It was observed that the surface was coated with a thick white layer of carbon, referring to the high oxygen content which is formed on the surface after the H_2O_2 treatment. Thus the surface was coated with a high content of carbon after the SAM treatment. To reduce the amount of carbon, the surface was polished with a fine white paper. After this process, the surface was treated with SAM for 12 to 15 min. to achieve a thinner white layer of

163

carbon on the surface. Figure 7.22d presents the EDS spectrum results for the as-prepared surface. It can be seen that the carbon content was increased after the above surface preparation. Furthermore, as shown in Figure 7.25, the SEM image shows that the surface morphology of cuprite surface treated with H_2O_2 and SAM with different magnifications. In the case of the H_2O_2 treatment, the copper content is higher and the carbon content is lower for the treated surface with H_2O_2 compared with the nanostructured CuO prepared using the alkaline solution as shown in Figures Figure 7.19 and Figure 7.26.
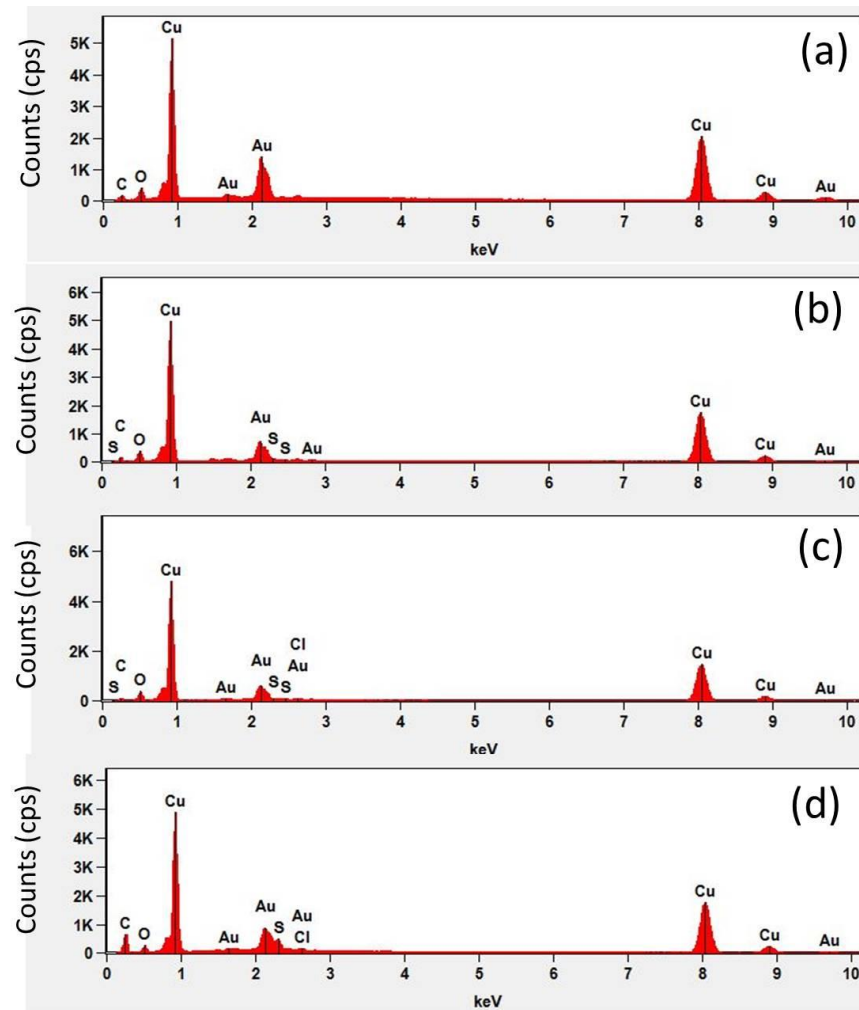
Figure 7.22: The EDS spectrum results recorded at 20 KV for (a) the cuprite (Cu_2O) coating with orange color (b) the orange cuprite surface treated with SAM, (c) the red cuprite surface treated with SAM and (d) the cuprite surface (red) treated with H_2O_2/SAM, polished and then treated secondly with SAM for about 15 min.

164

Figure 7.26 shows the contents of copper, oxygen, carbon, and sulfur on the red cuprite surface $(Cu_2O)1$, the treated Cu_2O with SAM $(Cu_2O)2$, the treated Cu_2O with H_2O_2 and SAM $(Cu_2O)3$, the orange cuprite surface $(Cu_2O)4$, and the treated orange cuprite surface with SAM $(Cu_2O)5$. As shown in this figure, as the oxygen content increased due to the oxidation process, the content of carbon was highly increased on the treated surfaces with SAM.

Figure 7.23: A photograph image of cuprite coating treated with H_2O_2/ SAM , polished and then treated secondly with SAM for about 15 min. The color changed from red to more reddish and then to black after the H_2O_2 treatment, which is similar to the color of the copper oxide surface.
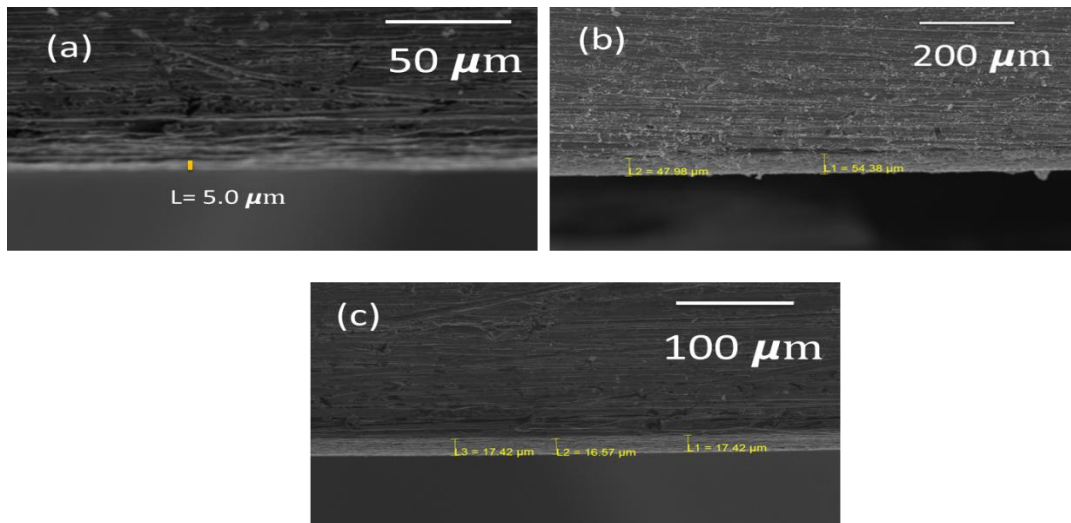
Figure 7.24: The coating thickness of (a) the oxidized cuprite surface $(Cu_2O)3$, (b) the CuO surface and (c) the polished CuO surface after the SAM treatment
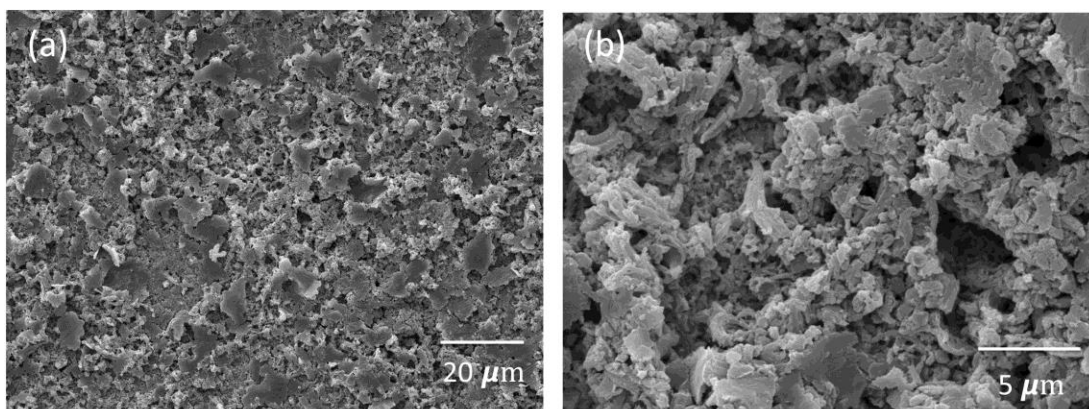
Figure 7.25: The SEM images of the as-prepared red cuprite (Cu_2O) coating treated with H_2O_2/ SAM, polished and then treated secondly with SAM for about 15 min, at (a) 20 $\boldsymbol{\mu}$m length scale and (b) 5 $\boldsymbol{\mu}$m length scale.
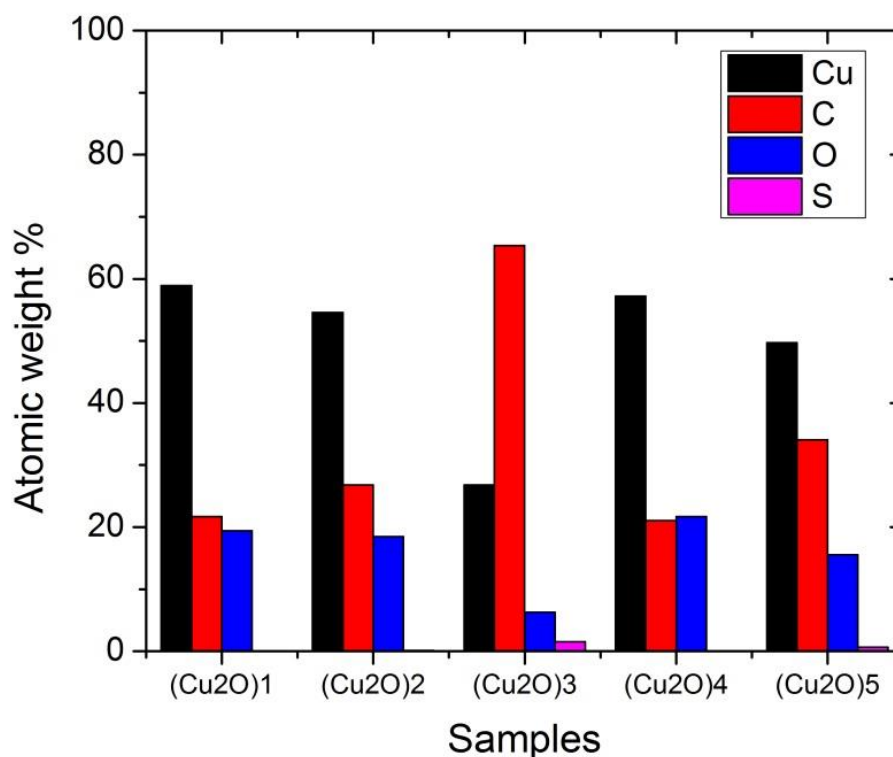
Figure 7.26: The atomic weight percentage of copper (Cu), oxygen (O), carbon (C) and sulfur (S), on the red cuprite surface (Cu_2O)1, the treated red Cu_2O surface with SAM (Cu_2O)2, the treated Cu_2O with H_2O_2 and SAM (Cu_2O)3, the orange cuprite surface (Cu_2O)4, and the treated orange cuprite surface with SAM (Cu_2O)5.

166

Figure 7.27: A photograph image of the yellow copper surface prepared by cleaning the cuprite coating ultrasonically in sulfuric acid, acetone, and ethanol, respectively.
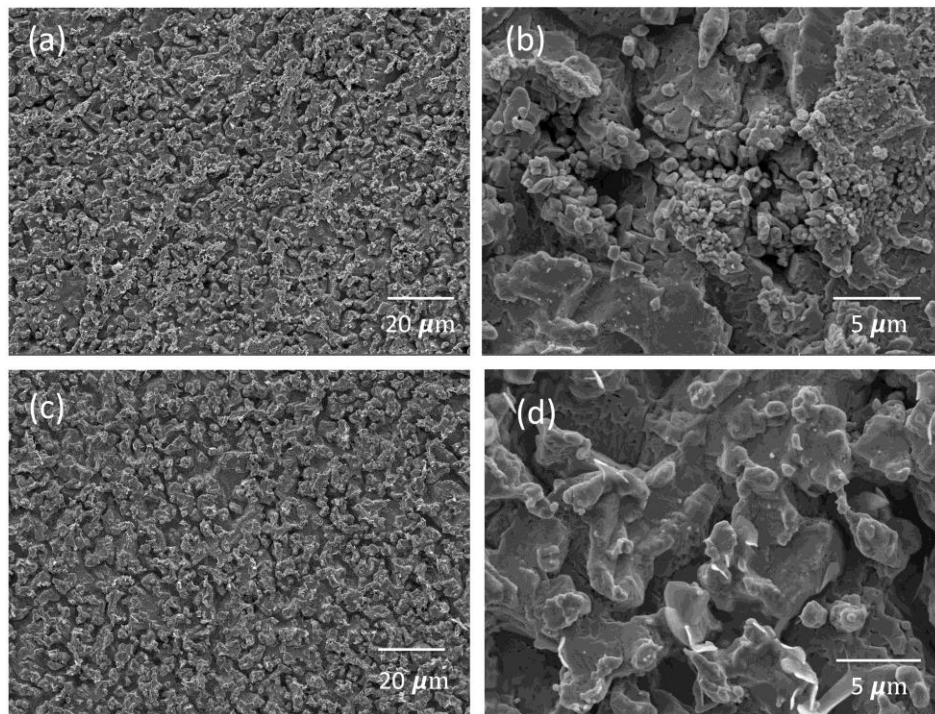
Figure 7.28: The SEM images of the yellow copper surface at (a) a length scale of 20 μm and (b) a length scale of 5.0 μm. Also, the SEM images of the yellow copper surface treated with SAM at (c) a length scale of 20 μm and (d) a length scale of 5 μm.

167

7.9.4 Copper (Cu) samples

A novel copper surface with a yellow color, as shown in Figure 7.27, was prepared by the ultrasonic cleaning of the copper tube coated with a red cuprite film. The latter was ultrasonically cleaned in 10 wt. % of the sulfuric acid solution (H_2SO_4), acetone and ethanol, respectively to remove the cuprite film completely from the surface. Then the as-prepared sample was washed in distilled water and dried in air. The sample was then treated with the SAM coating for hydrophobic functionalization.

Figure 7.28 shows the SEM images with different magnifications for the new copper surface with and without the SAM treatment. It can be seen that a rough surface with microscale porous structure and microgrooves (1.0-2.0 μm) was developed after removing the porous cuprite film. Increasing the surface roughness could increase the hydrophobicity on the surface after the SAM treatment compared to the smooth copper surface. Furthermore, the EDS spectrum results as shown in Figure 7.299 reveal that the novel copper surface consists of copper and a small amount of carbon due to the environmental contamination. Then the carbon content was increased after the SAM treatment.
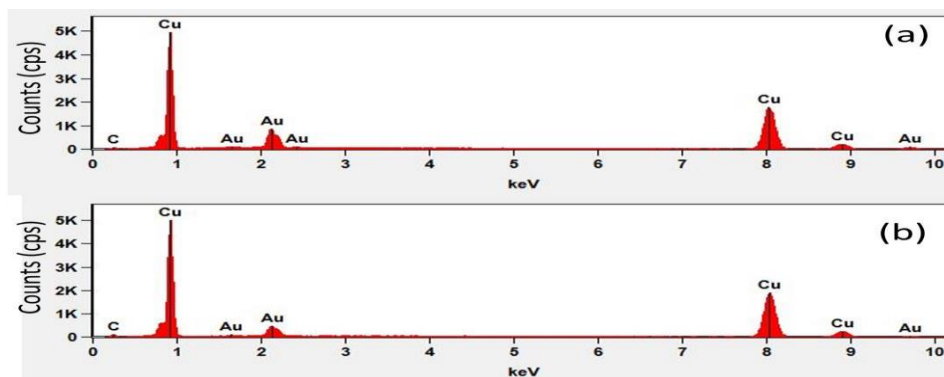
Figure 7.29: The EDS spectrum results recorded at 20 KV for (a) the yellow copper surface prepared by removing the cuprite coating and (b) the yellow copper surface treated with SAM.

The novel copper surface was also immersed in 30 % of hydrogen peroxide (H_2O_2) for 24 hours at room temperature to enhance the chemical stability and increase the oxygen ratio on the surface. Also, the latter process could increase the carbon content on the surface and promote the chemical bonding between the substrate and the SAM coating. It was also observed a thick white film of carbon was formed on the surface when the SAM treatment was more than 30 min. Therefore, the surface was polished by a fine white paper to remove the white carbon film and then treated with SAM for about 12 to 15 min.
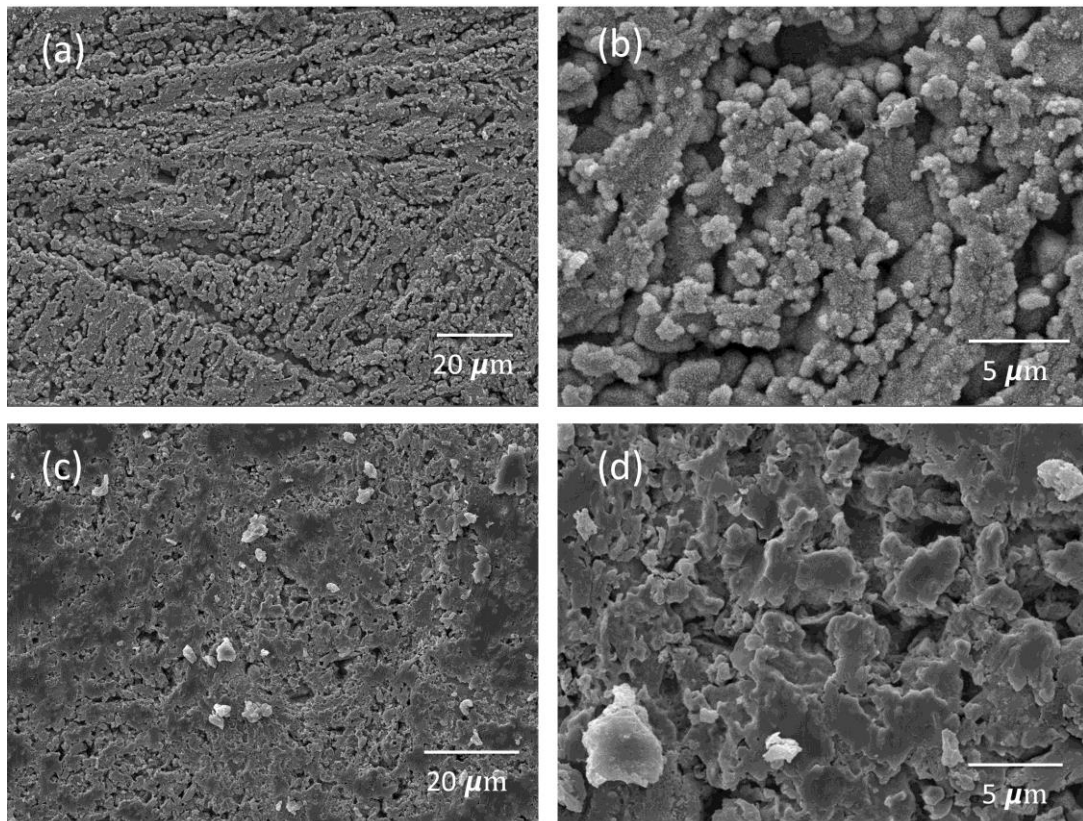
Figure 7.30: The SEM images of the yellow copper surface treated with H_2O_2 (a) a length scale of 20 μm and (b) a length scale of 5 μm. Also, the SEM images of the yellow copper surface treated with H_2O_2 /SAM, polished and then treated with SAM for about 12 min at (c) a length scale of 20 μm and (d) a length scale of 5 μm.

Figure 7.3030 shows the SEM images at different magnifications for the yellow copper surface treated with H_2O_2 and the surface treated with H_2O_2 /SAM, polished and then treated with SAM for about 12 min. It can be noticed that there is no change in the surface morphology after the hydrogen peroxide or the SAM treatment. However, the oxygen content on the surface was increased after the H_2O_2 treatment, and the carbon content was increased with decreasing the amount of copper and oxygen after the SAM treatment as shown in Figure 7.311a and Figure 7.311b.
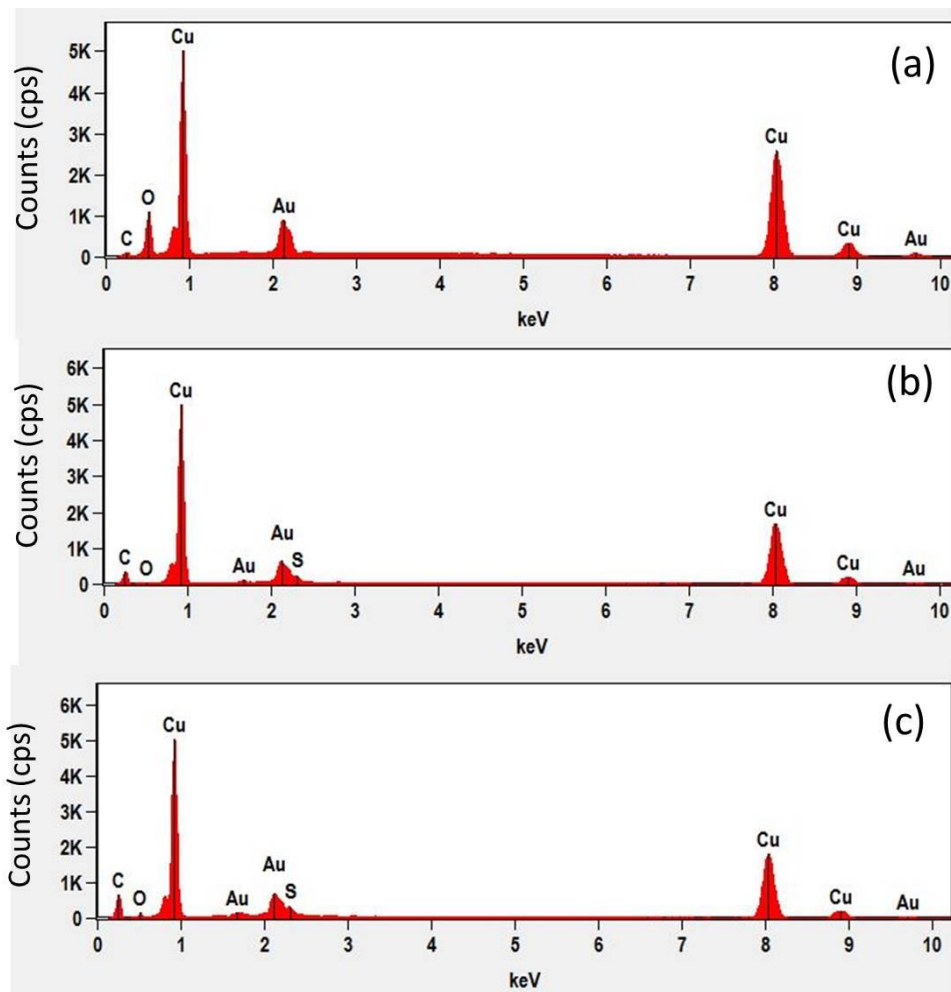
Figure 7.31: The EDS spectrum results recorded at 20 KV for (a) the yellow copper surface treated with H_2O_2, (b) the yellow copper surface treated with H_2O_2 /SAM, polished and then treated with SAM for about 12 min and (c) the plain copper surface treated with H_2O_2 /SAM.

In this study, the novel copper treated with SAM (Cu)1 and the treated with H_2O_2/SAM, polished and then treated with SAM for about 12 to 15 min (Cu)2 were compared with the plain copper surface treated with SAM and the plain surface treated with H_2O_2/SAM. Figure 7.322 shows the images of the plain copper tube, the treated with H_2O_2 , and the treated with SAM after the H_2O_2 treatment.
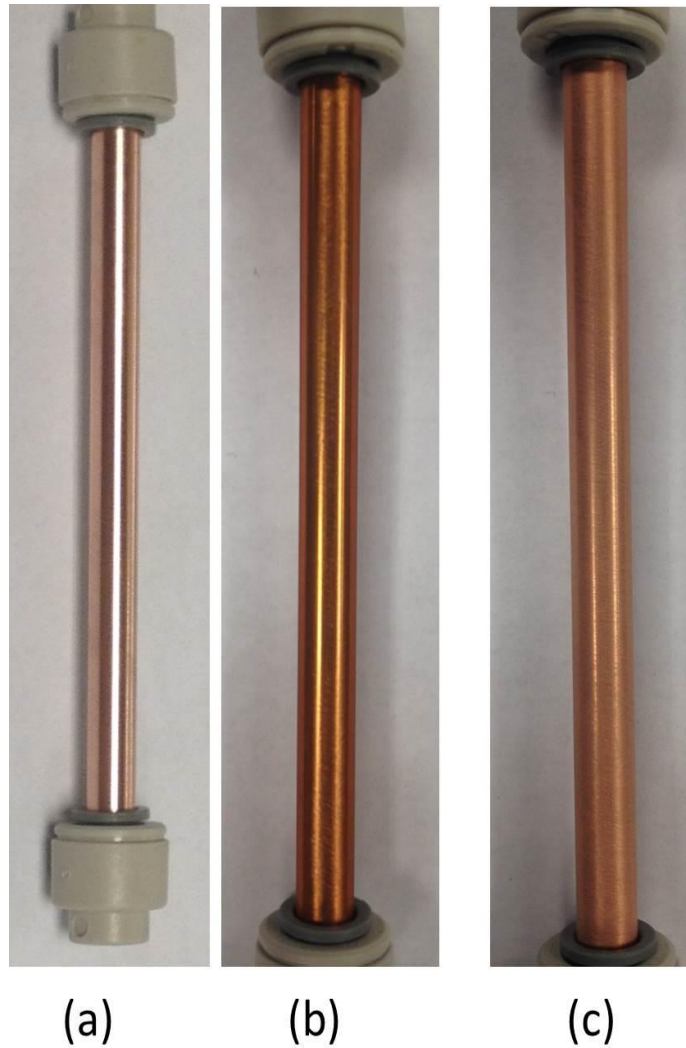
Figure 7.32: Photograph images of (a) the plain copper tube, (b) the plain surface treated with H_2O_2 and (c) the treated with SAM after the H_2O_2 treatment.
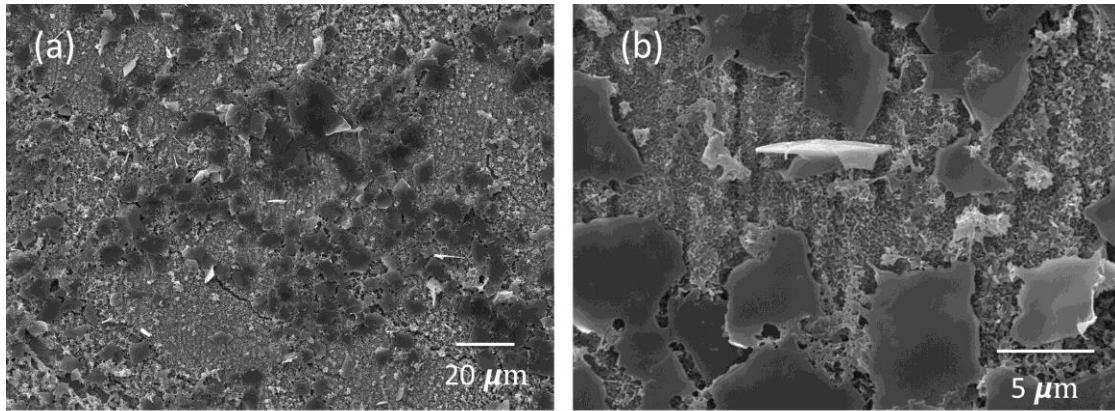
Figure 7.33: The SEM images of the plain copper surface treated with H_2O_2 /SAM at (a) a length scale of 20 μm and (b) a length scale of 5 μm.
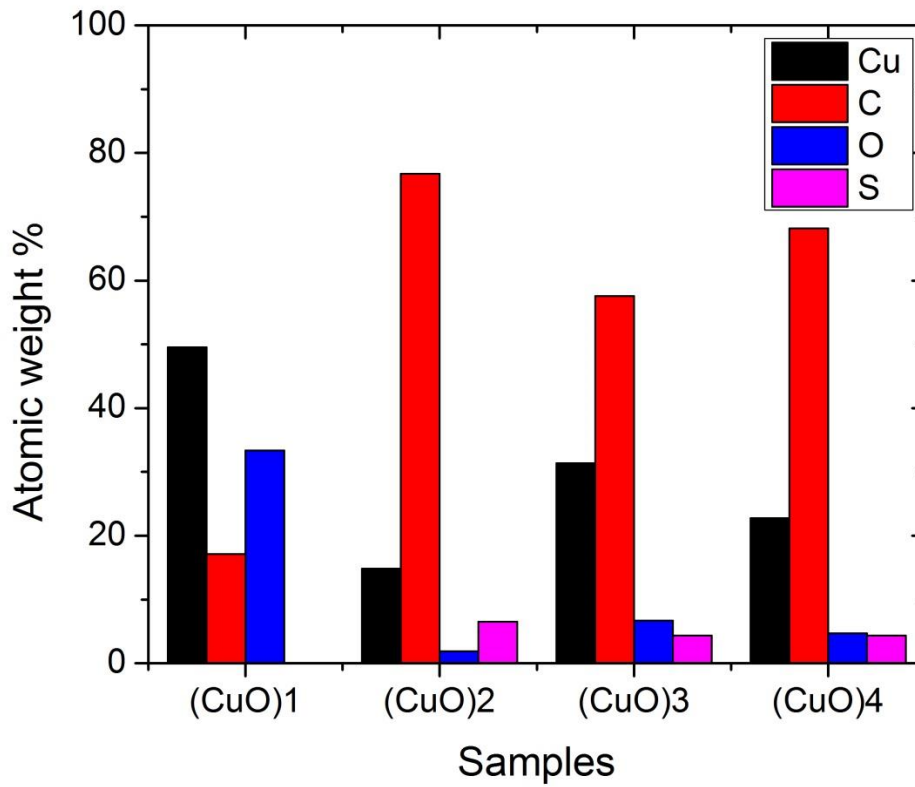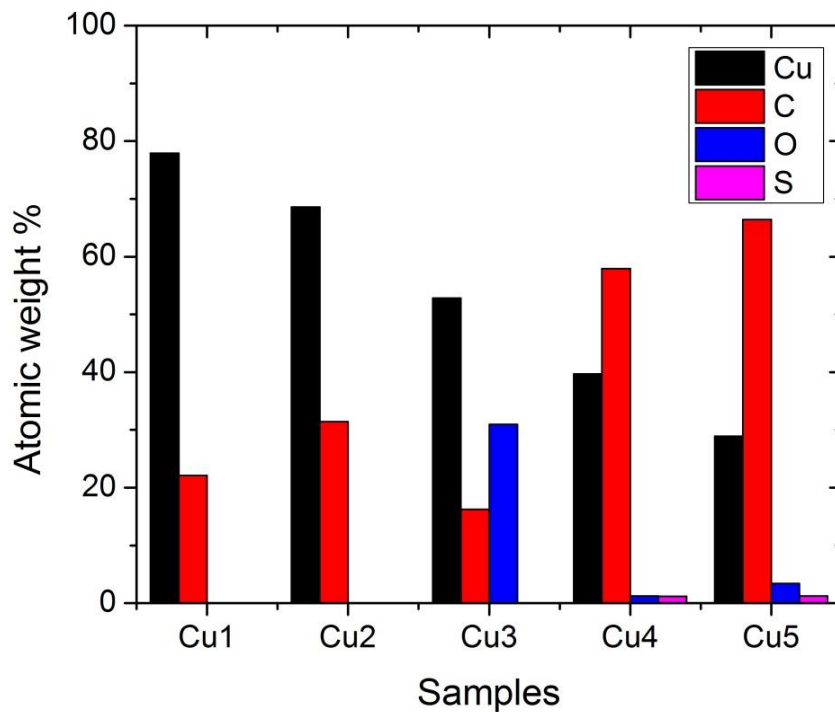

Figure 7.34: The atomic weight percentage of copper (Cu), oxygen (O), carbon (C) and sulfur (S), on the yellow copper surface (Cu1), (b) the yellow surface treated with SAM (Cu2), the yellow surface treated with H_2O_2 (Cu3), the yellow surface treated with H_2O_2/SAM, polished and then treated with SAM for about 12 min (Cu4) and the plain copper surface treated with H_2O_2/SAM (Cu5).

172

Figure 7.333 shows the SEM image of the plain copper surface treated with H_2O_2 and SAM with different magnifications. It can be noticed that the surface morphology and the surface roughness are different than the yellow copper surface. Moreover, the carbon content is higher on the plain copper surface treated with H_2O_2/SAM compared to the treated yellow surface with H_2O_2/SAM as shown in Figure 7.311 and Figure 7.344. Figure 7.344 shows the atomic weight percentage for the yellow copper surface (Cu1), the yellow surface treated with SAM (Cu2), the yellow surface treated with H_2O_2 (Cu3), the surface treated with H_2O_2/SAM, polished and then treated with SAM for about 12 to 15 min (Cu4) and the plain copper surface treated with H_2O_2/SAM (Cu5). It can be seen there is no oxygen content on the yellow surface before and after the SAM treatment. Then the atomic weight percentage of oxygen was increased after the H_2O_2 treatment. After the SAM treatment, the oxygen content was highly decreased while the carbon content was increased. Also, there is a small value of sulfur was originated on the surface due to the chemical composition of the SAM coating. Furthermore, it can be observed that the contents of carbon and oxygen are a little higher on the plain copper surface treated with H_2O_2/SAM compared to the yellow surface treated with H_2O_2/SAM.

7.9.5 The contact angle measurements

The surface wettability on the different prepared coatings was characterized by measuring the static contact angle of water on those coatings. The contact angle was measured by a contact angle system at the room temperature and in the air conditions. The size of the individual water droplet was about 5 μl. The value of the contact angle was obtained by averaging different measurements on different positions and samples. The average contact angle on the plain copper surface coated with SAM was about

173

125.6° $\pm$ 0.6° . **Error! Reference source not found.**5 shows the static contact angle on

he hydrophobic plain copper surface (Cu/SAM)

Angles: (123.90°,125.90°)
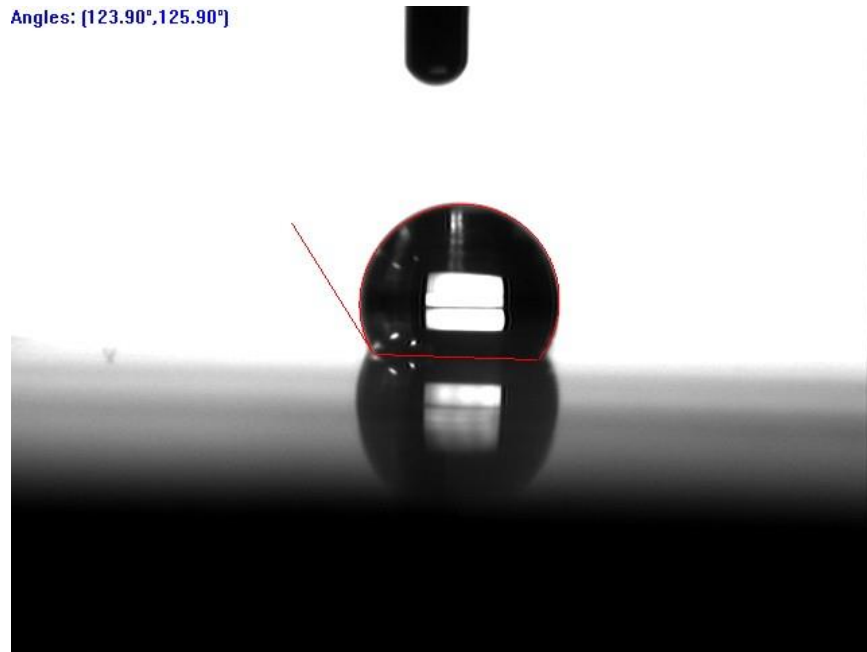
Figure 7. 35: The contact angle measurements on Cu/SAM.sample

Angles: (154.30°,154.40°)
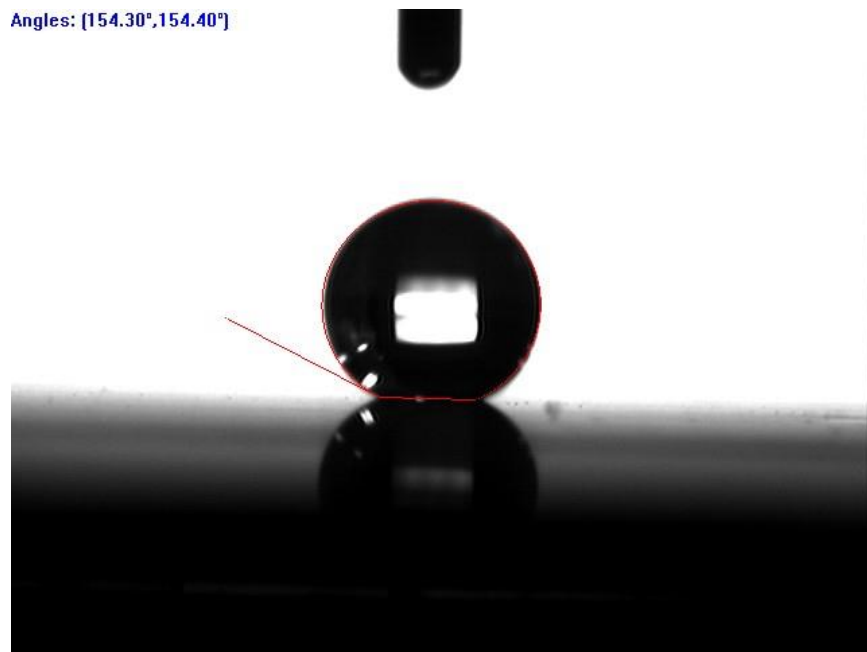
Figure 7.36: The contact angle measurements on the Cu2 sample.

Furthermore, the average contact angle on the yellow copper surface coated with SAM (Cu2) was about 150° ± 4°. Figure 7.366 reveals the static contact angle on this surface. From this figure, it can be seen that the surface is superhydrophobic since the contact angle is higher than 150°, but it was a little lower by 4 degrees on some samples. The contact angle on the hydrophobic yellow copper (Cu2) is higher than the plain copper surface (Cu/SAM) due to the existence of the nanoporous structure on the first surface as demonstrated by the SEM tests. This nanoporous structure led to increasing the roughness and the hydrophobicity on this surface. The same behavior was observed on the cuprite coating $(Cu_2O)2$ with the microporous structure. The average contact angle on this surface was about 150° ± 5°. Figure 7.377 exhibits the contact angle on the hydrophobic cuprite surface
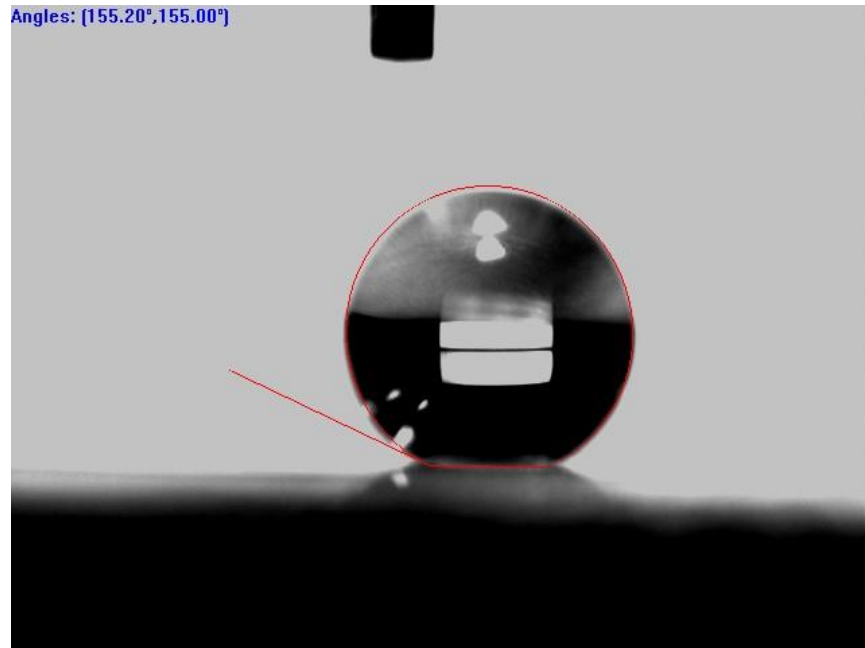
Figure 7.37: The contact angle measurements on the hydrophobic cuprite sample $(Cu_2O)2$.

Additionally, it was hard to measure the static contact angle on the hydrophobic oxidized plain copper surface (Cu5), the yellow copper (Cu4), the cuprite surface

175

(Cu_2O)3, the copper oxide (CuO)2, and the green patina (patina2) surfaces. This is because of the droplet jumping phenomena observed on those coatings as shown in Figure 7.388 to Figure 7.422. When the droplet felt down and touched the surface, it started to jump and then left the surface. This indicates to the low surface wettability and the high contact angle which is about $168° \pm 2°$ on these surface. Moreover, Figure 7.433 exhibits the low surface wettability for instance for the hydrophobic yellow copper surface oxidized by H_2O_2 (Cu4).The droplet cannot wet and sustain on the surface during the contact angle measurement test. The surface was moved up to touch the droplet and then moved down so that the droplet can wet the surface but the droplet moved up and left the surface, referring to the low surface energy and wettability on this surface.
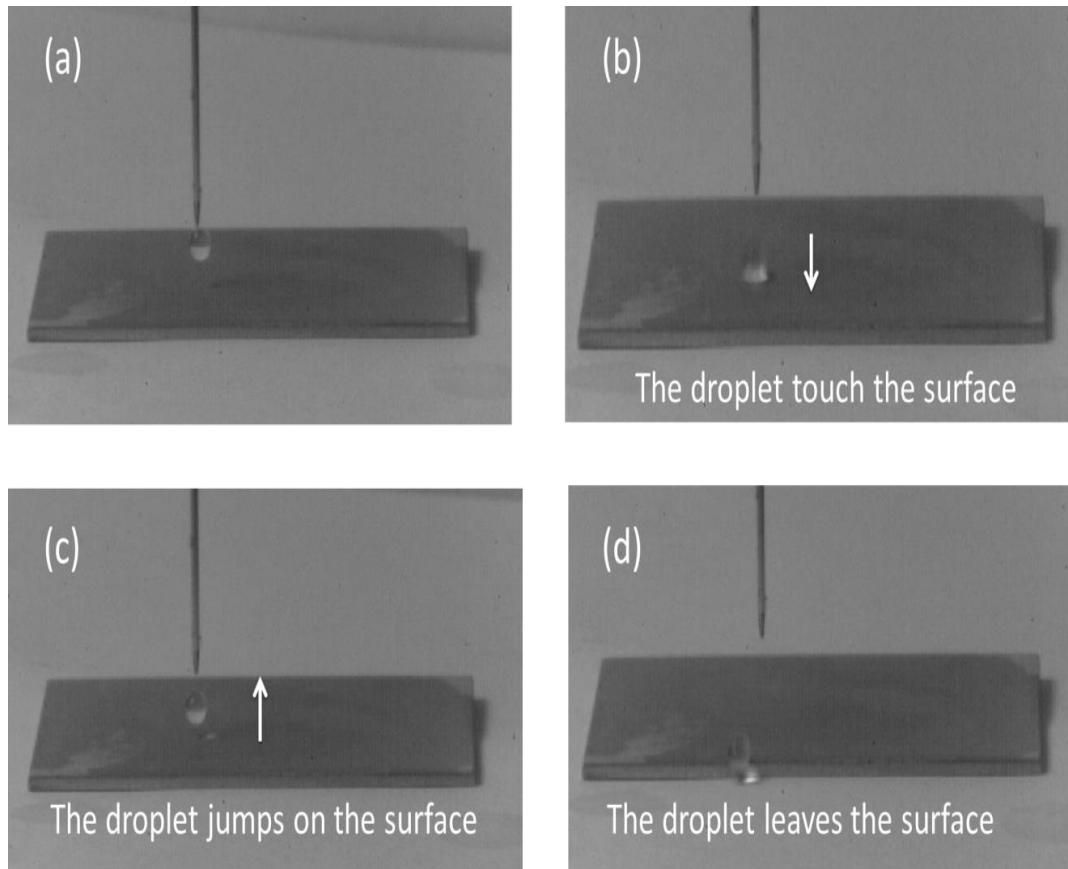
Figure 7.38: The droplet jumping phenomena on Cu/SAM sample.

176
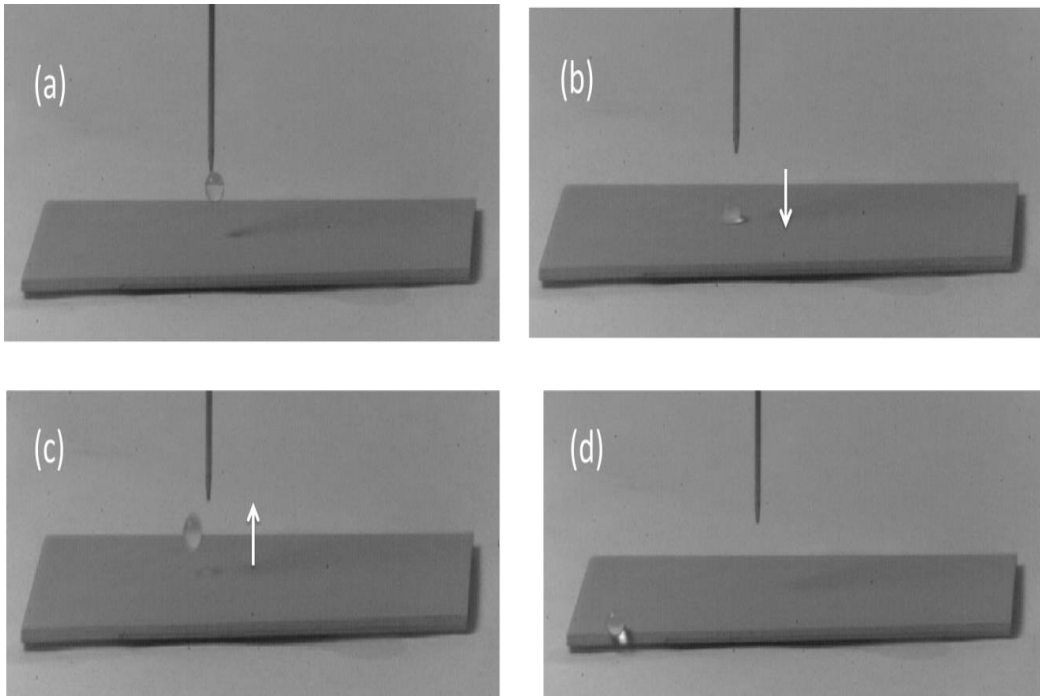
Figure 7.39: The droplet jumping phenomena on Cu4 sample.
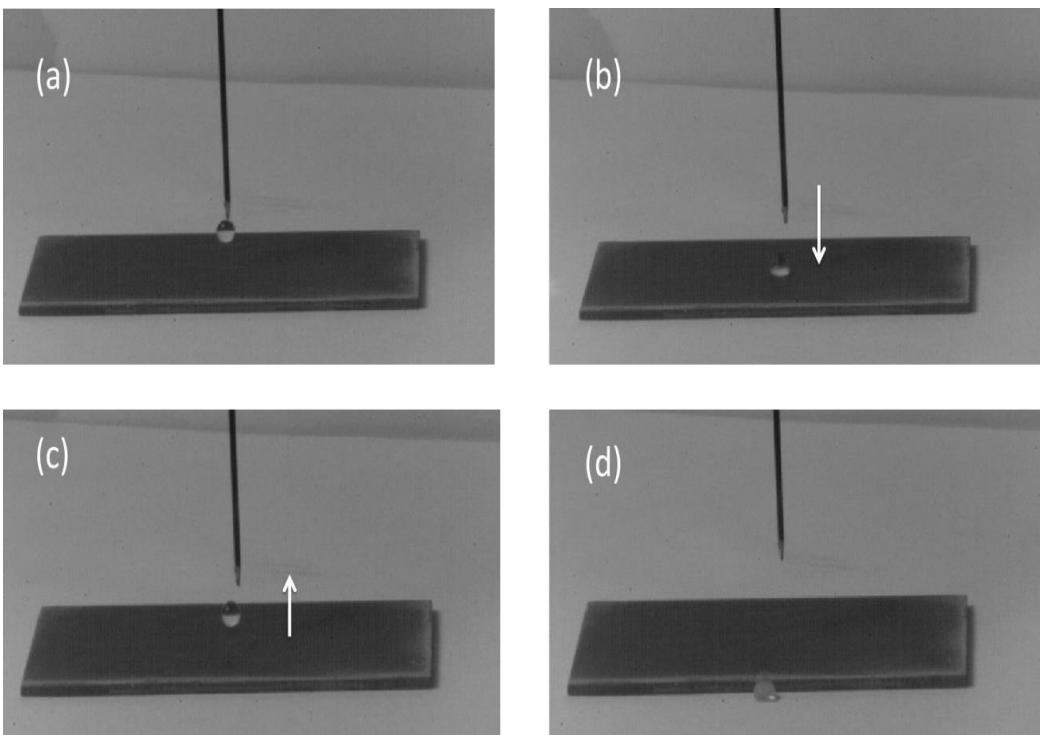
Figure 7.40: The droplet jumping phenomena on (Cu_2O) 3 sample

177
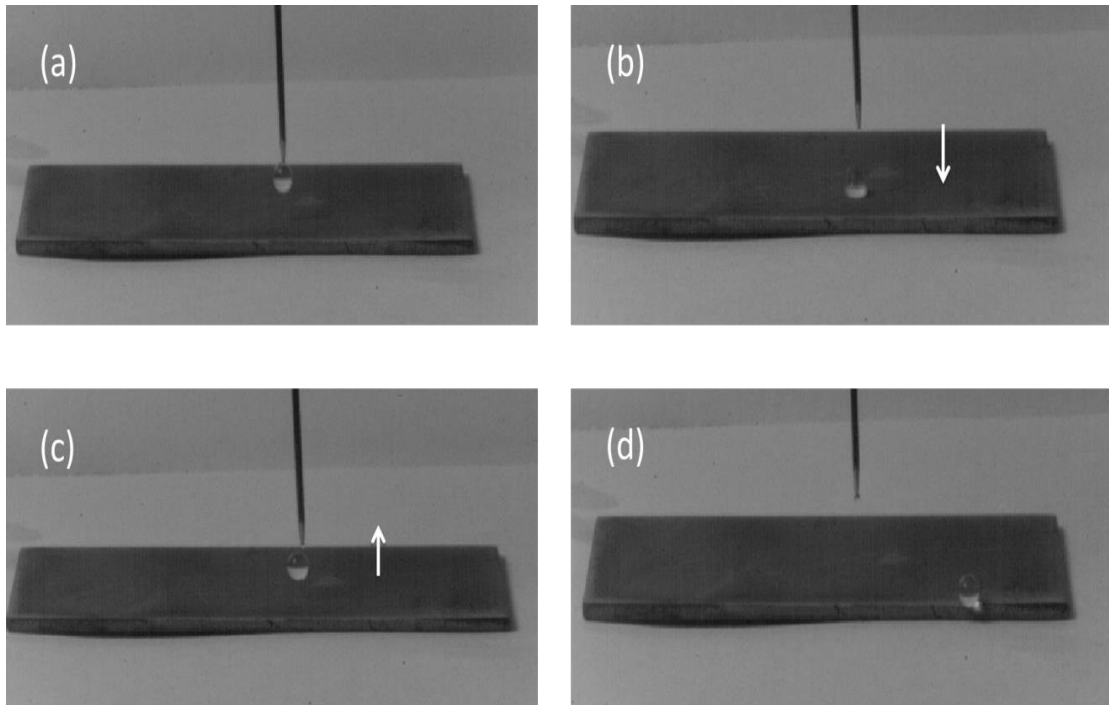
Figure 7.41: The droplet jumping phenomena on (CuO)2 sample
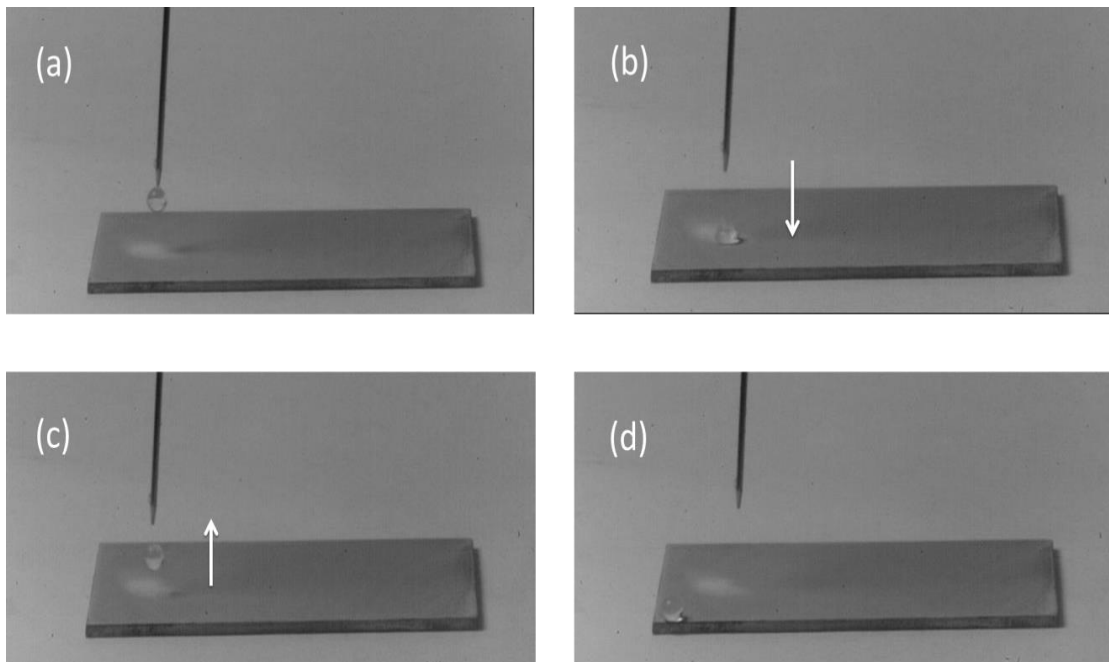
Figure 7.42: The droplet jumping phenomena on patina2 sample.

178
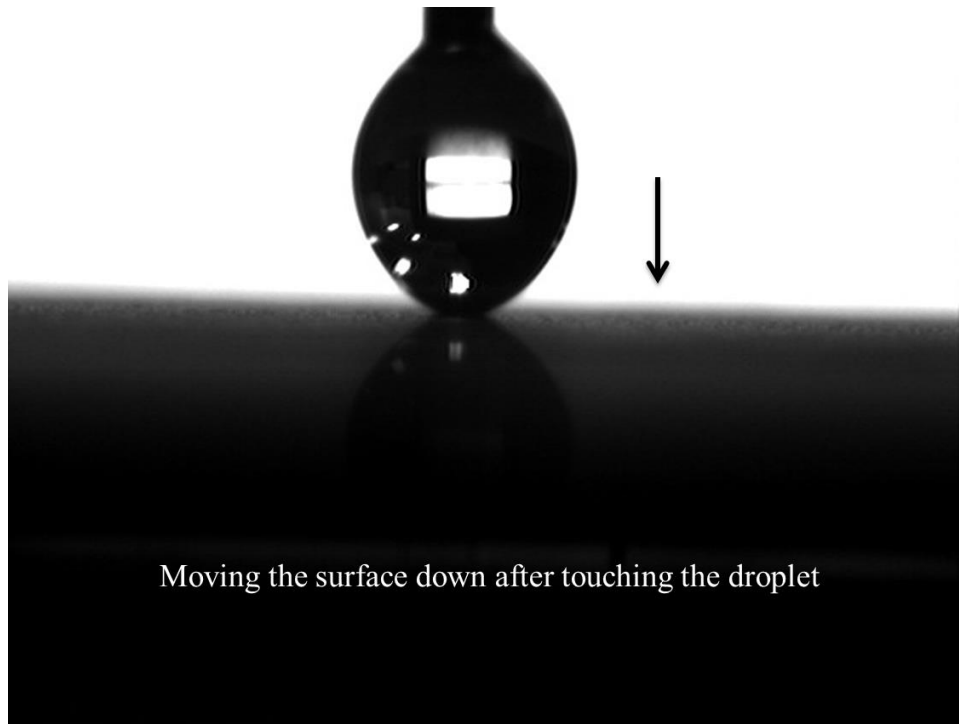
Figure 7.43: The hydrophobic oxidized yellow copper surface (Cu4) was moved up to touch the droplet and then moved down but the droplet left the surface showing the low surface energy on this surface

CHAPTER 8

RESULTS AND DISCUSSIONS

In this study, a series of condensation experimentations were carried out on horizontal tubes, at the saturation conditions and in the presence of the non-condensable gases, to investigate the effect of hydrophobic copper and copper oxides coatings with different morphologies (smooth, porous with nanoscale pores size or microgrooves, micro/nanostructures) on the steam condensation heat transfer performance. All the samples prepared and tested in this study are listed and labeled in **Table 8.1**,**Table 8.2** and **Table 8.3**. The samples include the copper, cuprite (Cu_2O), copper oxide (CuO) and the green patina surfaces with their modifications as explained in chapter 7. The results obtained for these samples were also compared with those for complete filmwise and dropwise condensation on the plain copper surface and with Nusselt's model of FWC.

Table 8.1: Specifications and labeling of the patina and copper oxide samples

	Labeled Sample	Samples specifications
1	patina1	Hydrophilic patina surface
2	patina2	The patina surface (patina1) treated with SAM
3	patina3	The polished patina2 surface after the SAM treatment
4	patina4	The treated patina3 surface with SAM
5	(CuO)1	Hydrophilic copper oxide surface
6	(CuO)2	The copper oxide surface (CuO)1 treated with SAM

180

7	(CuO)3	The polished (CuO)2 surface after the SAM treatment
8	(CuO)4	The treated (CuO)3 surface with SAM

Table 8.2: Specifications and labeling of the cuprite samples.

	Labeled Sample	Samples specifications
1	$(Cu_2O)1$	The hydrophilic cuprite surface with red color
2	$(Cu_2O)2$	The treated red cuprite surface $(Cu_2O)1$ with SAM
3	$(Cu_2O)3$	The treated red cuprite surface $(Cu_2O)1$ with H_2O_2/ SAM
4	$(Cu_2O)4$	The hydrophilic cuprite surface with orange color
5	$(Cu_2O)5$	The treated orange cuprite surface $(Cu_2O)4$ with SAM
6	$(Cu_2O)6$	The mixed red/orange cuprite surface treated with SAM
7	$(Cu_2O)7$	The dark orange cuprite surface treated with SAM

Table 8.3: Specifications and labeling of the copper samples

	Labeled Sample	Samples specifications
1	Cu/SAM or (Cu/SAM)_S1	The plain copper sample one treated with SAM
2	(Cu/SAM)_S2	The plain copper sample two treated with SAM
3	Cu1	The yellow- rough copper sample
4	Cu2	The yellow- rough copper sample treated with SAM
5	Cu3	The yellow- rough copper sample treated with H_2O_2
6	Cu4	The treated yellow surface (Cu3) with SAM
7	Cu5	The treated plain copper surface with H_2O_2 /SAM
8	Cu or FWC	The hydrophilic plain copper surface

181

8.1 Condensation heat transfer characterization on green patina and copper oxide coatings.

8.1.1 Effect of the micro/nanostructructures of the patina and copper oxide coatings on the condensation performance

The influence of green patina and copper oxide surfaces, with the micro/nanostructures, on the condensation heat transfer performance was investigated. Figure 8.1 shows the photographic images of the dropwise condensation behavior on the superhydrophobic green patina and copper oxide surfaces. It can be seen that the white carbon layer on the patina surface is much higher than that on the copper oxide surface. This is related to the high content of oxygen and sulfur on the brochantite surface, resulting in increasing the carbon content on the surface after the self-assembled monolayer treatment as explained in chapter 7. Although the increase of the carbon on the brochantite surface led to reducing the surface wettability which represented by increasing the apparent contact angle and decreasing hysteresis contact angle, the conductive thermal resistance increased highly on this surface compared to the copper oxide surface with the lower coating thickness. In order to demonstrate the condensation heat transfer characterization on green patina and copper oxide samples, the measured heat flux and the heat transfer coefficient were plotted as a function of subcooling temperature.

The effect of the patina thickness on the condensation heat transfer enhancement was investigated. Figure 8.2 shows the effect of three different patina thicknesses on the condensation heat transfer performance. At the low and high subcooling temperatures, it was found that the condensation heat transfer performance was below the values of the

182

filmwise condensation by about (12.08-29.6) % and (44.5-49.05) % for the patina surfaces (patina2) with coating thicknesses of about 50.0 ml and 200.0 ml, respectively .However, the condensation heat transfer was enhanced by (40.1-87.1) % on the patina surface with a coating thickness less than or about 1.0 μm. From Figure 8.2, it can be seen that, for the patina surface (patina2) with a 1.0 ml coating thickness, a maximum heat flux of 460.0 KW/m^2.K and a maximum condensation heat transfer coefficient of 29.46 kW/m^2.K were obtained at a subcooling temperature of 15.62 ℃. This indicates that the enhancement in the heat transfer performance is about 1.87 times higher than that for the complete filmwise condensation surface. It can be inferred from above that as the thickness of the patina surface increased the condensation performance was decreased due to the increase in the conductive thermal resistance of the coating as well as to the highly sticky of the condensate droplets in cavities of the microstructures, leading to reduce the droplets drainage rate.
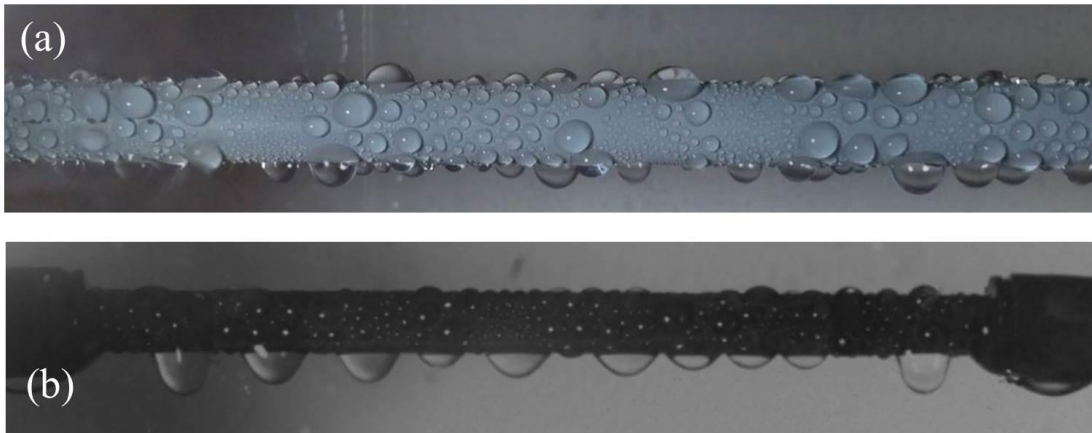
Figure 8.1: The photographic images of the dropwise condensation behavior on the superhydrophobic surfaces: (a) the microstructured green patina surface with ~50.0 μm and (b) the nanostructured copper oxide surface.

Furthermore, from Figure 8.2, it can be noticed that the condensation performance on the superhydrophobic patina surface is less than that of the complete dropwise

183

condensation on the hydrophobic plain copper surface. This is attributed to some important factors affecting the dropwise characteristics, including the substrate thermal conductivity, the thermal resistance associated with SAM coating and the coating thickness, the thermal resistance of the condensate droplet, the interfacial interaction between the condensate droplet and the condensing surface, as well as the roughness of the condensing surface. The thermal resistance of the hydrophobic plain copper surface is much lower than the patina surface due to the high thermal conductivity of the copper substrate and the negligible thermal resistance of the ultra-thin SAM coating. Moreover, the interfacial interaction between the condensate droplets and the condensing surfaces with different structures such as smooth, porous and micro/nanostructures plays an important factor influencing the dropwise condensation characteristics. During the dropwise condensation, the steam begins to condense on the surface as individual droplets at the atomic scale. When the small droplet starts to grow and then to shed off the surface, it will be affected by four forces, namely, the gravitational force of the condensate droplet, the drag forces related to the steam motion inside the condensing chamber, and the adhesion forces represented by the surface drag force and the surface tension. Consequently, the droplet grows until reaching a critical size so that the gravitational and the steam motion forces can overcome the adhesion forces which are highly affected by the surface structure. As a result, the droplet diameter departure increases as the adhesion forces increases, resulting in increasing the thermal resistance of the condensate droplet and thereby reducing the condensation heat transfer performance. Another factor for the reduction in the dropwise condensation performance is the surface roughness. When the droplet starts to roll off and sweep on the condensing

184

surface, it undergoes higher drag force on the rough surface compared to smooth one, resulting in decreasing the sweeping cycle of the droplets.

Meanwhile, the effect of the patina thickness on the condensation performance was demonstrated. However, it was hard to control the thickness of the nanostructured copper oxide surface (CuO). The oxidation process takes about 5.0 minutes to develop the wick structures with a coating thickness of about 50.0 μm on the copper surface treated with the alkaline solution as mention before. Therefore, in this section, the effect of the nanostructured copper oxide surface with and without the self-assembled monolayer coating (SAM) on the condensation heat transfer enhancement was investigated. Figure 8.3 shows the heat fluxes and heat transfer coefficients as a function of surface subcooling for the hydrophilic and hydrophobic copper oxide surfaces. The heat transfer performance for the hydrophilic copper oxide surface (CuO)1 was less than that on the filmwise condensation (FWC). This is due to the higher thermal resistance of the substrate and the coating thickness of the hydrophilic copper oxide surface (CuO)1 compared to the smooth hydrophilic copper surface . On the other hand, the condensation enhancement was increased for the hydrophobic copper oxide surface (CuO)2 compared to that of the filmwise condensation. The maximum enhancement was about 48.7 % at a surface subcooling of 20.3 ℃. However, the results were then decreased to be close to the FWC after testing the sample the next day. The SAM coating was degraded to form a flooded surface with large and irregular shapes. Miljkovic et al. [154] were also reported the reduction in the condensation heat transfer performance on the wick structured copper oxide surface due to the surface flooding at the high surface subcooling.
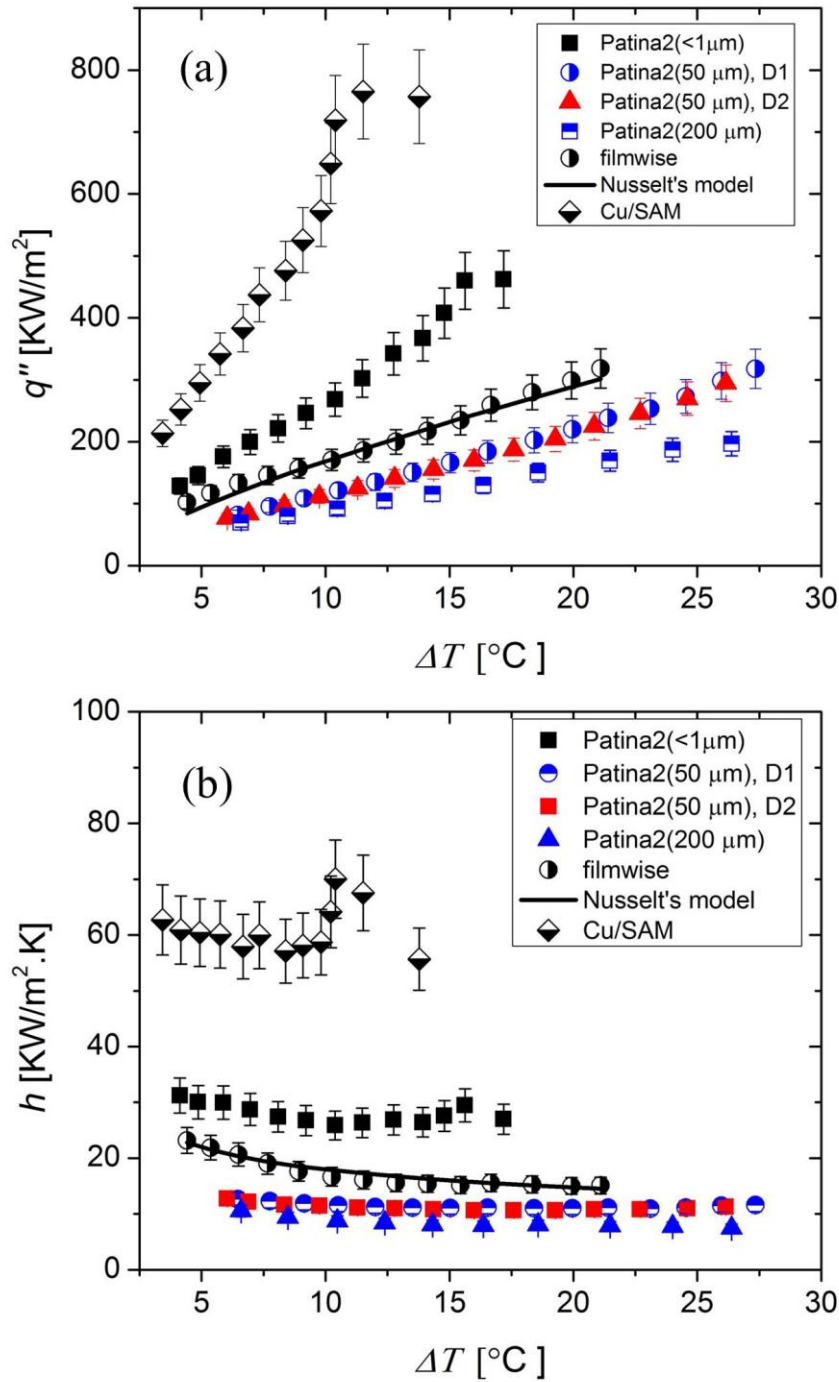
Figure 8.2: The condensation heat flux and heat transfer coefficient as a function of the surface subcooling on the the superhydrophobic patina surface with three different coatings thicknesses.The results are also compared with the complete filmwise and dropwise condensation as well as the Nusselt's model for the plain copper surface.
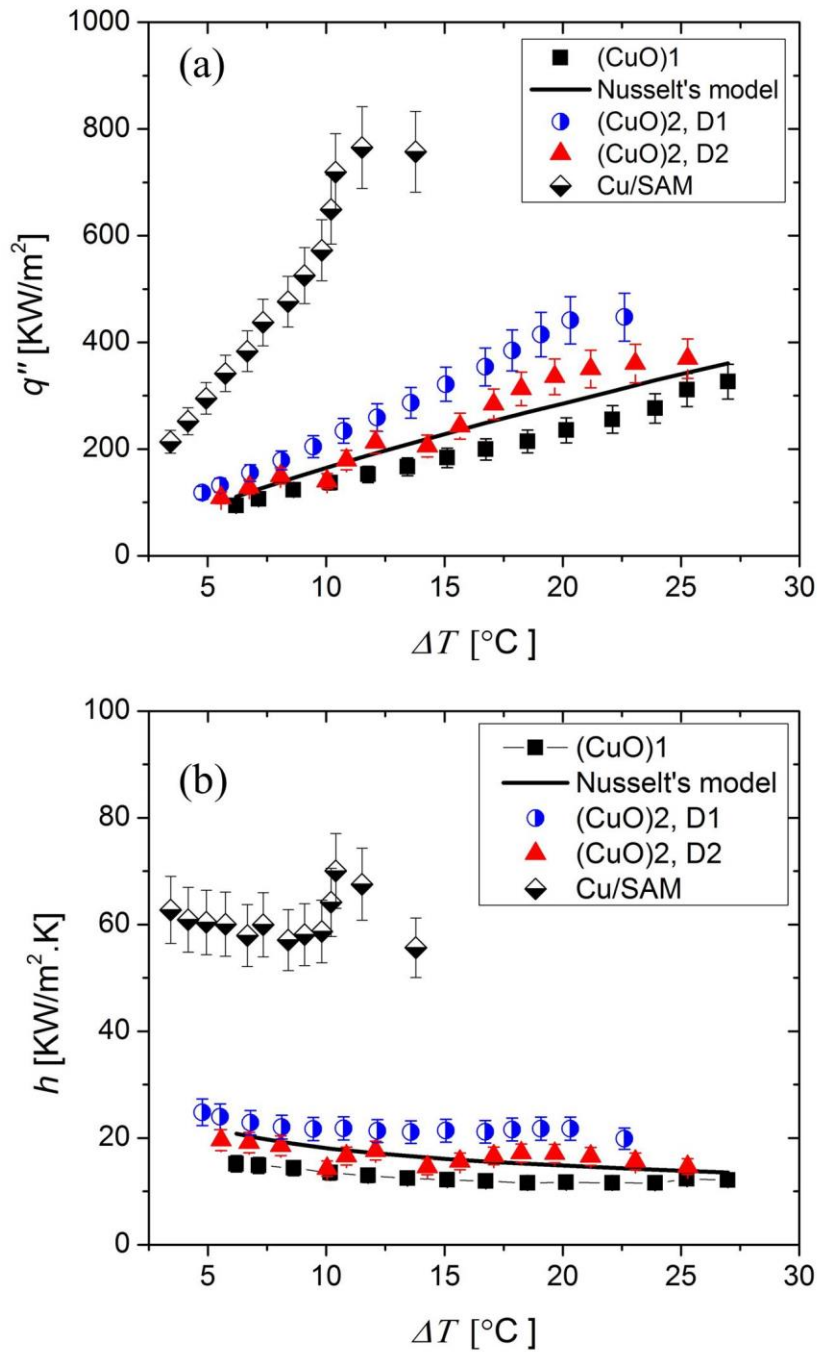
Figure 8.3: The condensation heat flux and heat transfer coefficient as a function of surface subcooling for the superhydrophilic and superhydrophobic copper oxide surfaces, with comparison with the complete filmwise and dropwise condensation as well as the Nusselt's model for the plain copper surface. The superhydrophobic surface was tested two times in two days. The label D1 means the first day, whereas D2 refers to the second day.

187

8.1.2 Effect of removing the micro/nanostructructures of the patina and copper oxide coatings on the condensation performance

In order to enhance the condensation heat transfer for the patina and copper oxide surfaces, the micro/nanostructures were removed by polishing the surface after the SAM treatment as explained in chapter 7. This process can keep the chemical stability of the oxides surfaces, reduce the influence of the pinned droplets in the cavities of the structure as well as the high thermal resistance of the coating and thereby increasing the condensation performance. Figure 8.4 demonstrates the dropwise condensation on the polished patina and copper oxide surfaces. From Figure 8.4a, it can be seen that the green coating of the patina was removed and a coating with a dark orange color was maintained after the polishing process. This refers to the chemical composition of the cuprite surface and the sulfate formed from the second oxidation process as explained in chapter 7 as well as to the formation of the carbon on the surface after the SAM treatment. The dark orange color makes the surface more chemically stable compared to the red cuprite surface due to the existence of the sulfate on the surface. Furthermore, from Figure 8.4b, it can be noticed that the color of the copper oxide changed to a brilliant black color without affecting the chemical composition of the surface. In this study, the polished patina surface (patina4) was tested 12 times for 31 days. Figure 8.4a shows the sustainable dropwise condensation on the polished patina surface (patina4) after 31 days (Test 12) of testing and the exposure to the air environment. The same behavior was observed on the polished copper oxide surface (CuO)4 as shown in Figure 8.4b. This figure reveals the sustainable dropwise condensation after three weeks of testing (Test 8). More interestingly is that after the polishing process, the chemical bonding between the

188

coating and the copper substrate is highly strong for the patina and copper oxide surface. In the case of the patina coating, this is attributed to the strong bonding between the cuprite coating and the copper surface. The mechanical properties of the cuprite surface were investigated by measuring the surface hardness and modulus using a Nanoindentation test at a maximum load of 1.0 mN. It was great of interest to detect that the cuprite coating has superior mechanical properties and higher than that of the copper substrate. The measured values of the modulus and hardness of the cuprite surface were 24.0189 ± 4.6 GPa and 732.967 ± 292.75MPa, respectively. Thus, after the polishing process, the cuprite coating was strongly bonded to the copper substrate. The same behavior was observed for the copper oxide coating after the polishing process.
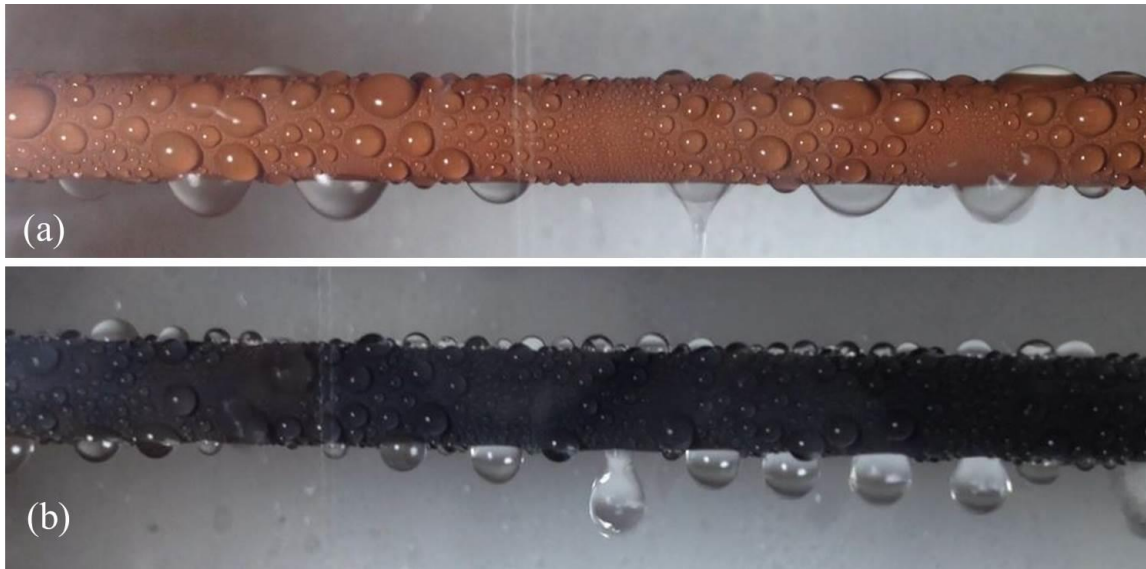
Figure 8.4: Photographic images of the dropwise condensation behavior on (a) the polished patina surface and (b) the copper oxide surface treated with SAM after the polishing process. The images were taken after one month and three weeks for the polished patina and Copper oxide surfaces, respectively.

The heat flux and the heat transfer coefficient as a function of subcooling temperature were plotted to demonstrate the condensation heat transfer performance for the polished patina and copper oxide surfaces. Figure 8.5 shows the heat transfer

performance for the polished copper oxide surface (CuO)4 compared to the complete filmwise and dropwise condensation on the plain copper surface. The polished copper oxide surface (CuO)4 was first tested 6 times for 6 days. Each test was conducted after 24 hours of the last test. The same surface was then polished (CuO)3 and tested without the SAM treatment after 7 and 21 days.
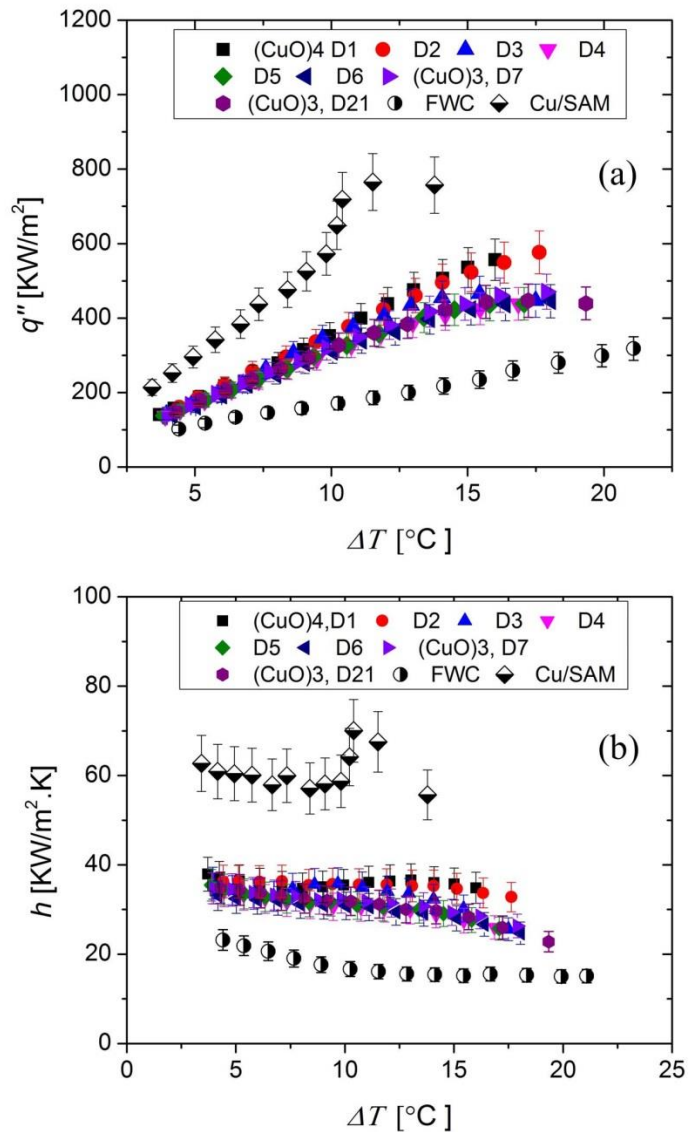
Figure 8.5: The condensation heat transfer performance on the polished copper oxide surface (CuO)4 tested six times in six days and then polished (CuO)3 and tested two times in two weeks without the SAM treatment.

190
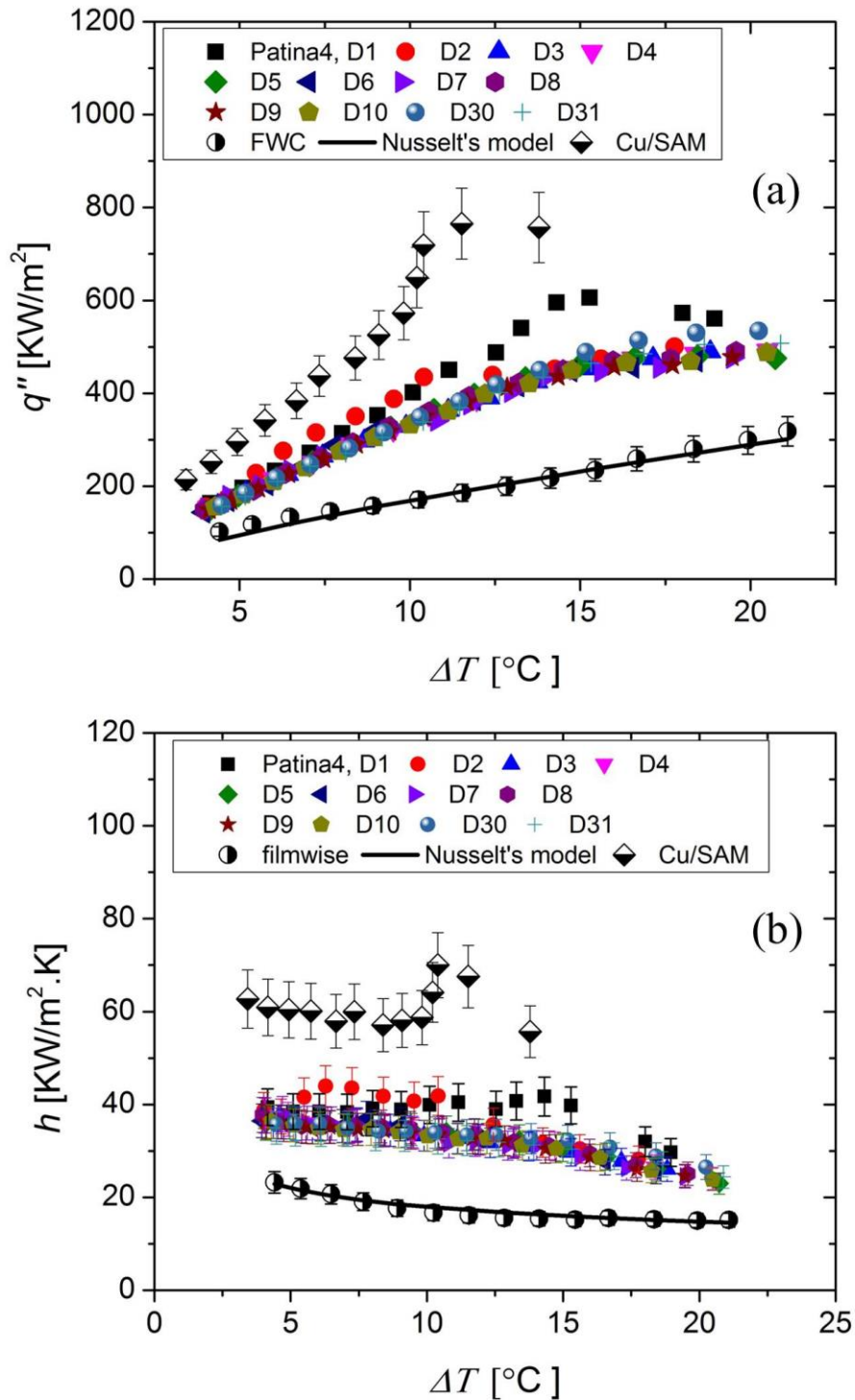
Figure 8.6: The condensation heat transfer performance on the polished patina surface (patina4) tested 12 times in 31 days, in comparison with the hydrophobic plain copper surface (Cu/SAM), the hydrophilic plain surface (FWC) and the Nusselt's model

191
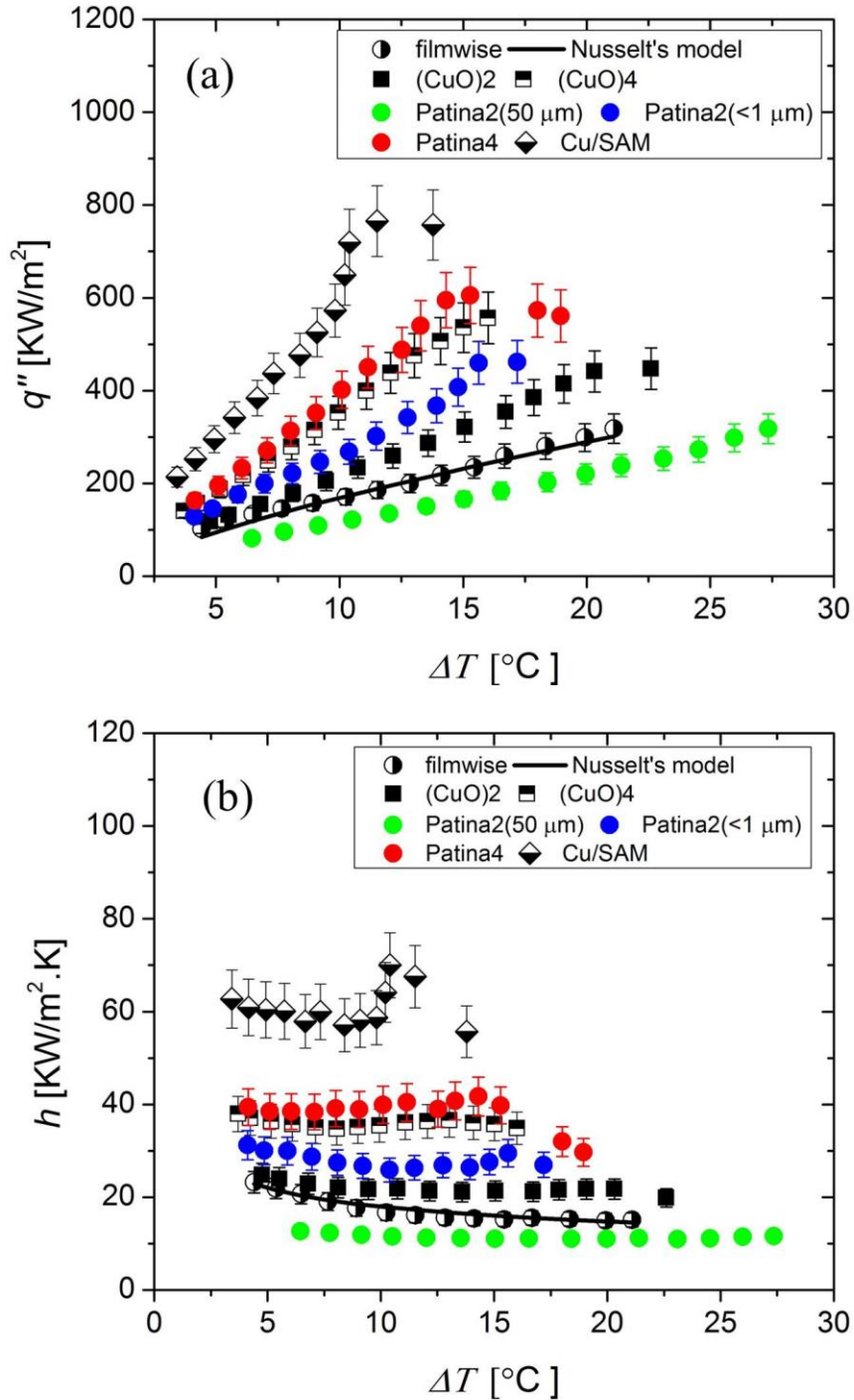
Figure 8.7: The heat flux and heat transfer coefficient as a function of surface subcooling for the patina and copper oxide surfaces before and after the polishing process, with comparison with the complete filmwise and dropwise condensation as well as the Nusselt's model for the plain copper surface.

Figure 8.5 exhibits that the results obtained are almost constant for the first two tests, but they degraded for the third test and then maintained approximately constant for the other tests even for the polished surface without SAM treatment (CuO)3. This refers to the high bonding between the copper oxide surface and the carbon originated from the SAM coating even after the polishing process. From Figure 8.5, the heat flux and the heat transfer coefficient for the polished copper oxide surface (CuO)4 were enhanced by 122.7 % and 122.64 % with maximum values of 556.47 (KW/m^2) and 36.0 (KW/m^2.K), at subcooling temperatures of 16.0 ℃ and 14.08 ℃ , respectively compared to that on the filmwise condensation surface. However, the enhancement in the heat flux and heat transfer coefficient were then reduced after the first two tests to be 103.0 % and 103.7 % with maximum values of 453.95 (KW/m^2) and 33.61 (KW/m^2.K), respectively at a subcooling temperature of 14.06 ℃. The fresh testing sample showed a high enhancement at the high subcooling temperatures for the first two days of testing, but then the enhancement was decreased and maintained constant referring to the stability of the nucleation density and the droplet removal rate on the SAM coating.

The condensation performance was also demonstrated on the polished patina surface (patina4). The same behavior on the polished copper oxide surface was observed herein. Figure 8.6 shows the results for the sample that tested 12 times for 31 days. It can be seen that the performance was higher for the first test and then it decreased and became stable for the other tests. For the first test, the enhancements in the heat flux and the heat transfer coefficient were about 158.62 % and 159.29 % corresponding to maximum values of 594.94 (KW/m^2) and 41.71 (KW/m^2.K), respectively achieved at a subcooling temperature of 14.3 ℃. Then, for test 12 after 31 days, the enhancements in

193

the heat flux and the heat transfer coefficient were reduced to 103.4 % and 103.8 % corresponding to maximum values of 488.7 (KW/m^2) and 32.32 (KW/m^2.K) obtained at a subcooling temperature 15.16 ℃, respectively. From the above results, it is clear that the polished copper oxide and patina surfaces showed higher and reliable condensation performance compared to that on the surfaces with micro/nanostructures.

Figure 8.7 shows the condensation heat transfer performance on the nanostructured copper oxide surface (CuO)2, the polished copper oxide surface (CuO)4, the microstructured patina surface with different thicknesses (patina2), and the polished patina surface (patina4), in comparison with those of the filmwise and dropwise condensation on the plain copper surface. The Figure reveals that the condensation performance on the polished surfaces is higher than those on the copper oxide and patina surfaces with micro/nanostructures even on the patina surface with a thickness coating about or less 1.0 ml. This is because the latter coatings have higher carbon layer resulting in increasing the thermal resistance and thereby decreasing the heat transfer performance. Moreover, from Figure 8.7, it can be noticed that the heat fluxes and the heat transfer coefficients are slightly higher than those for the polished copper oxide surface (CuO)4. This is also attributed to the lower thermal resistance of the substrate and the coating thickness. Furthermore, the condensation enhancements on the polished copper oxide and patina surfaces are still less than that on the hydrophobic plain copper surface (Cu/SAM) even after the polishing process. This is due to the lower thermal resistance of the latter compared to the high thermal resistance of the polished copper oxide and patina surfaces related to the substrate material, coating thickness, and the SAM thickness represented by the carbon layer on the surface. As a result, the condensation heat transfer performance

194

was improved by 1.87, 1.48, 2.2, and 2.59 times for the fresh samples of the patina surface (patina2) with about 1.0 ml, nanostructured copper oxide surface $(CuO)2$, the polished copper oxide surface (CuO)4, the polished patina surface (patina4), respectively compared to that on the filmwise condensation surface.
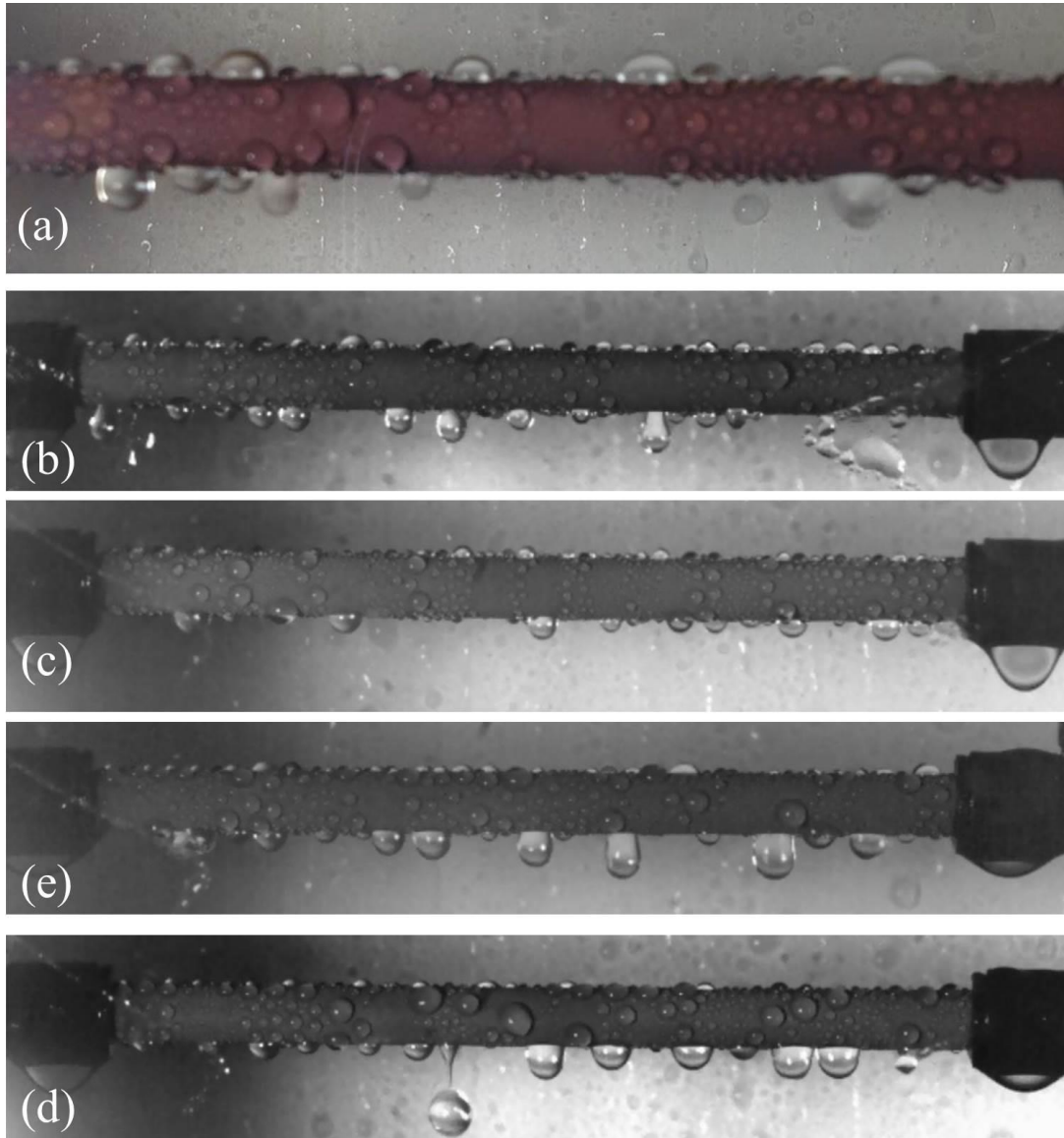
Figure 8.8: Images of the dropwise condensation behavior on the hydrophobic cuprite surface (Cu_2O) with (a,b) red , (c) orange , (d) mixed red/orange and (e) dark orange colors.

195
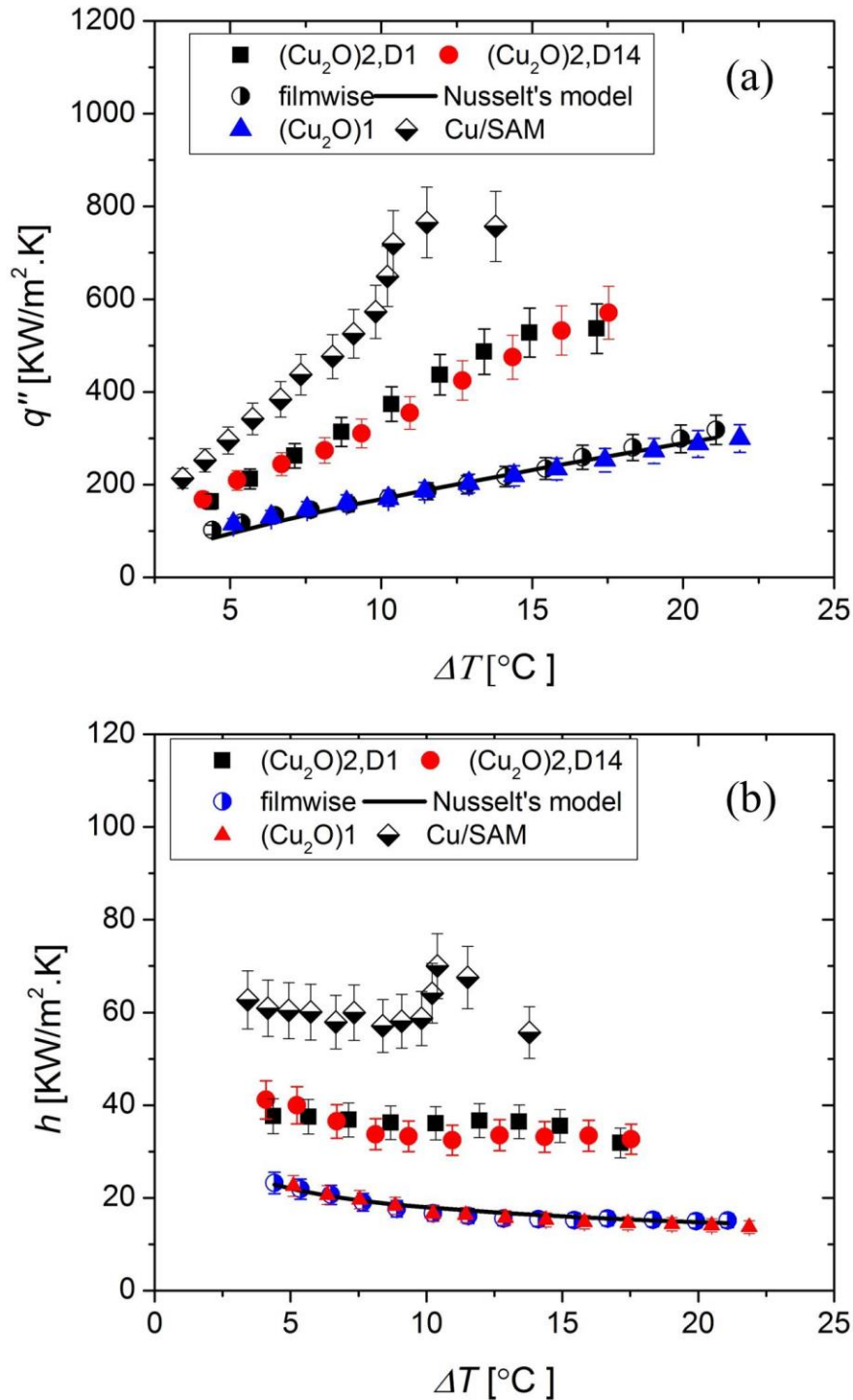
Figure 8.9: The condensation heat transfer performance for the not fresh-red cuprite surface $(Cu_2O)2$ prepared and then tested after about one month. The sample was tested two times in two weeks.

196
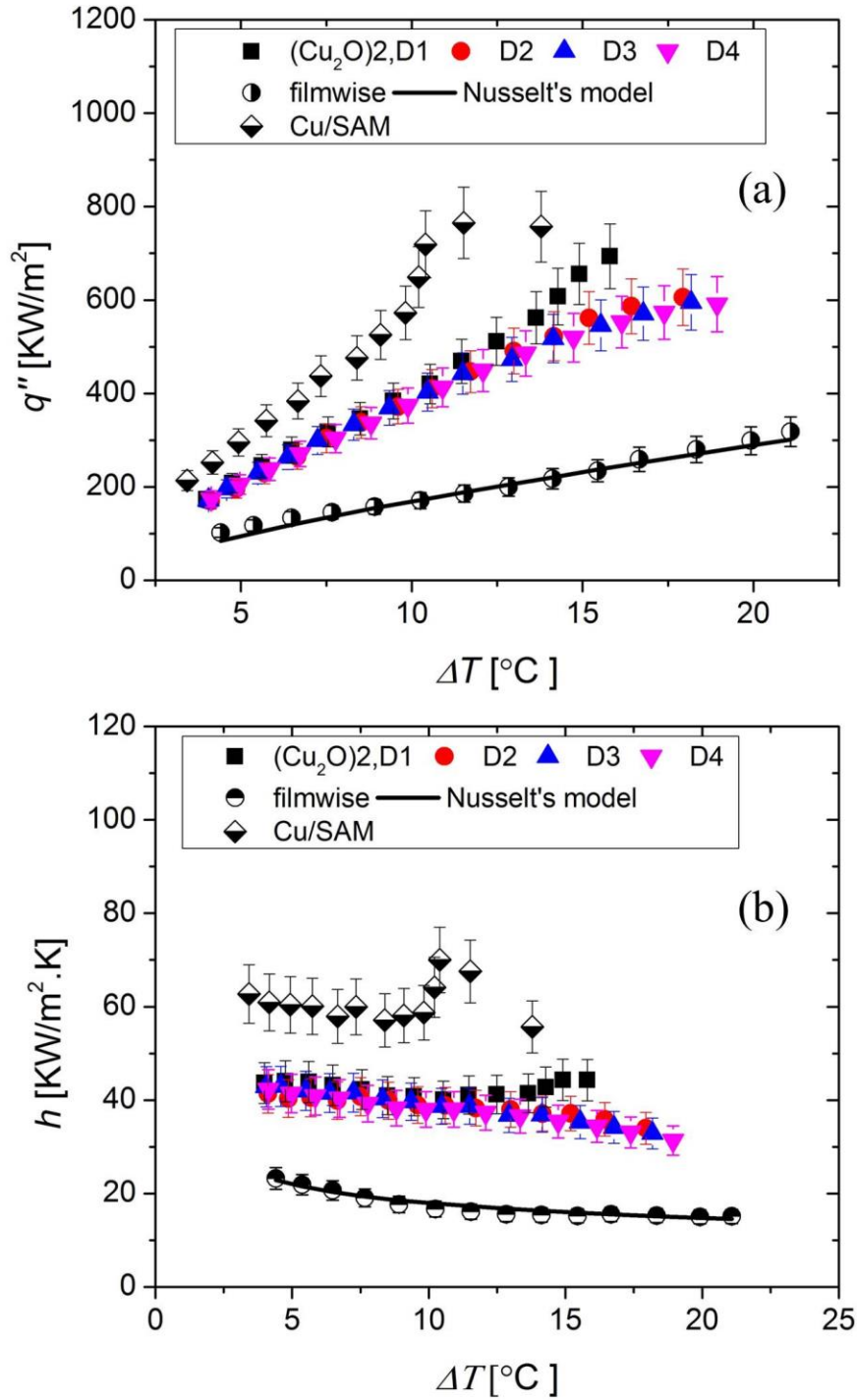
Figure 8.10: The condensation heat transfer performance for the fresh-red cuprite surface $(Cu_2O)2$ prepared and then tested four times in four days.
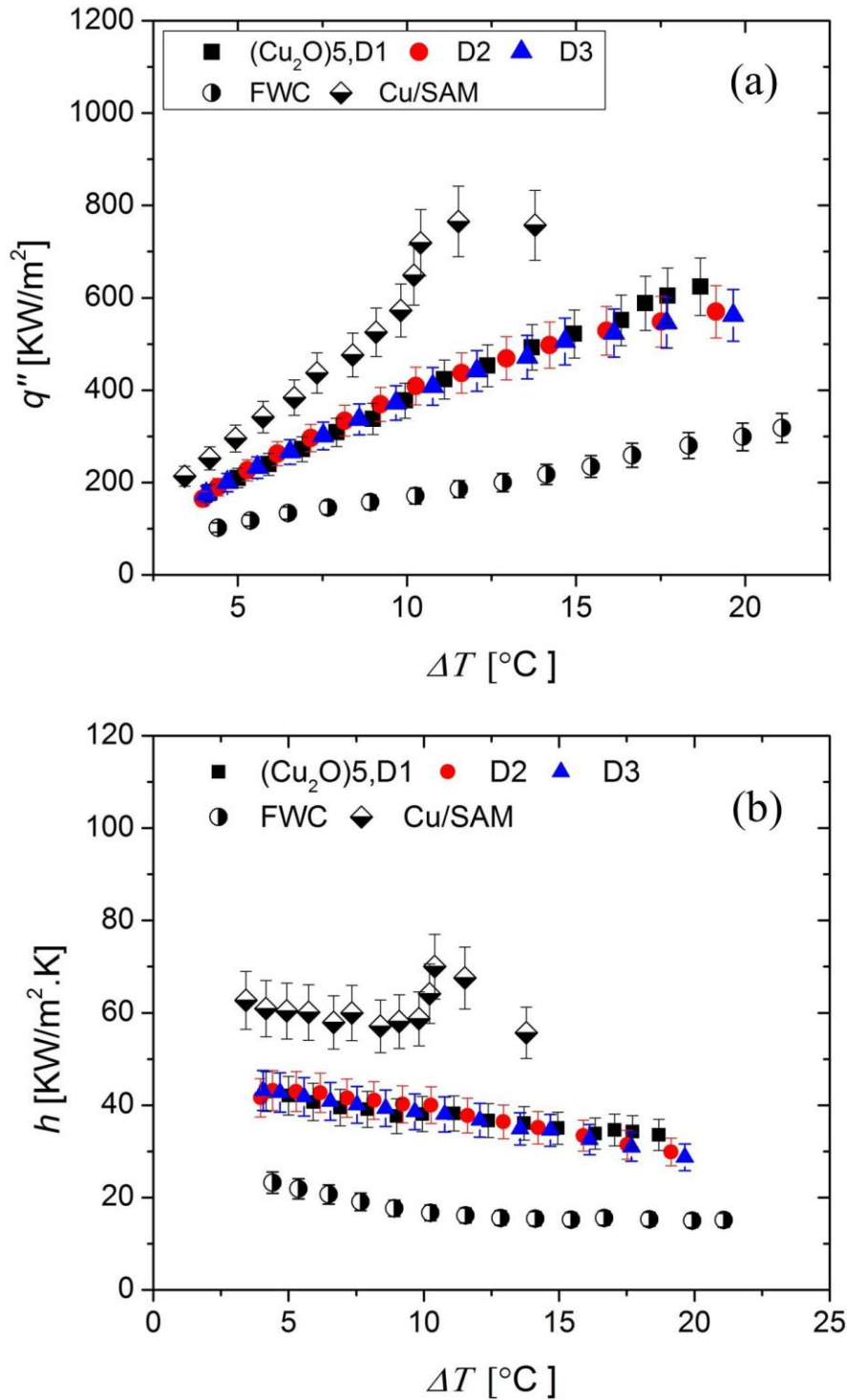
Figure 8.11: The condensation heat transfer performance for the fresh-orange cuprite surface $(Cu_2O)5$ tested three times in three days.
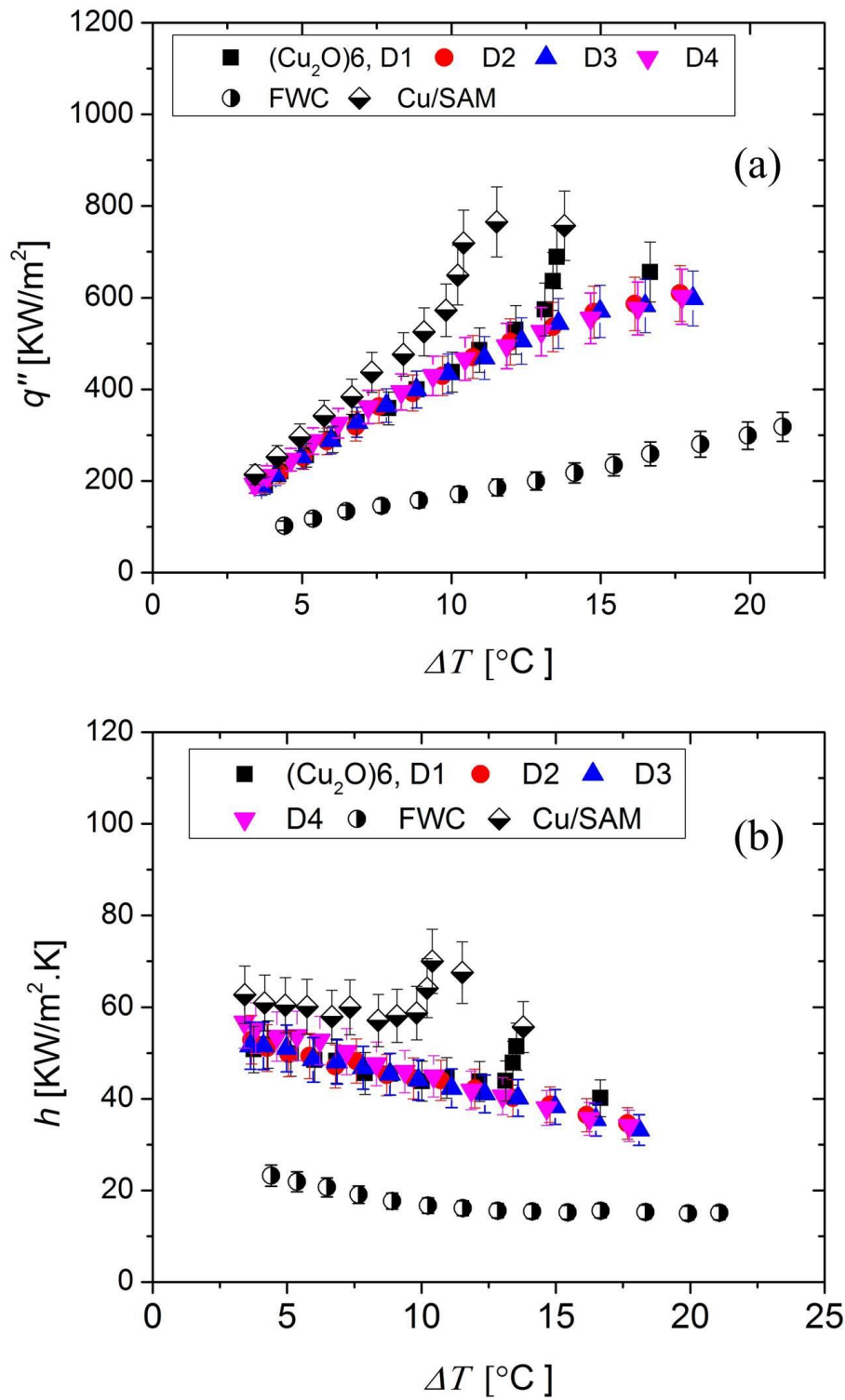
Figure 8.12: The condensation heat transfer performance for the mixed red/orange cuprite surface $(Cu_2O)6$ tested four times in four days.
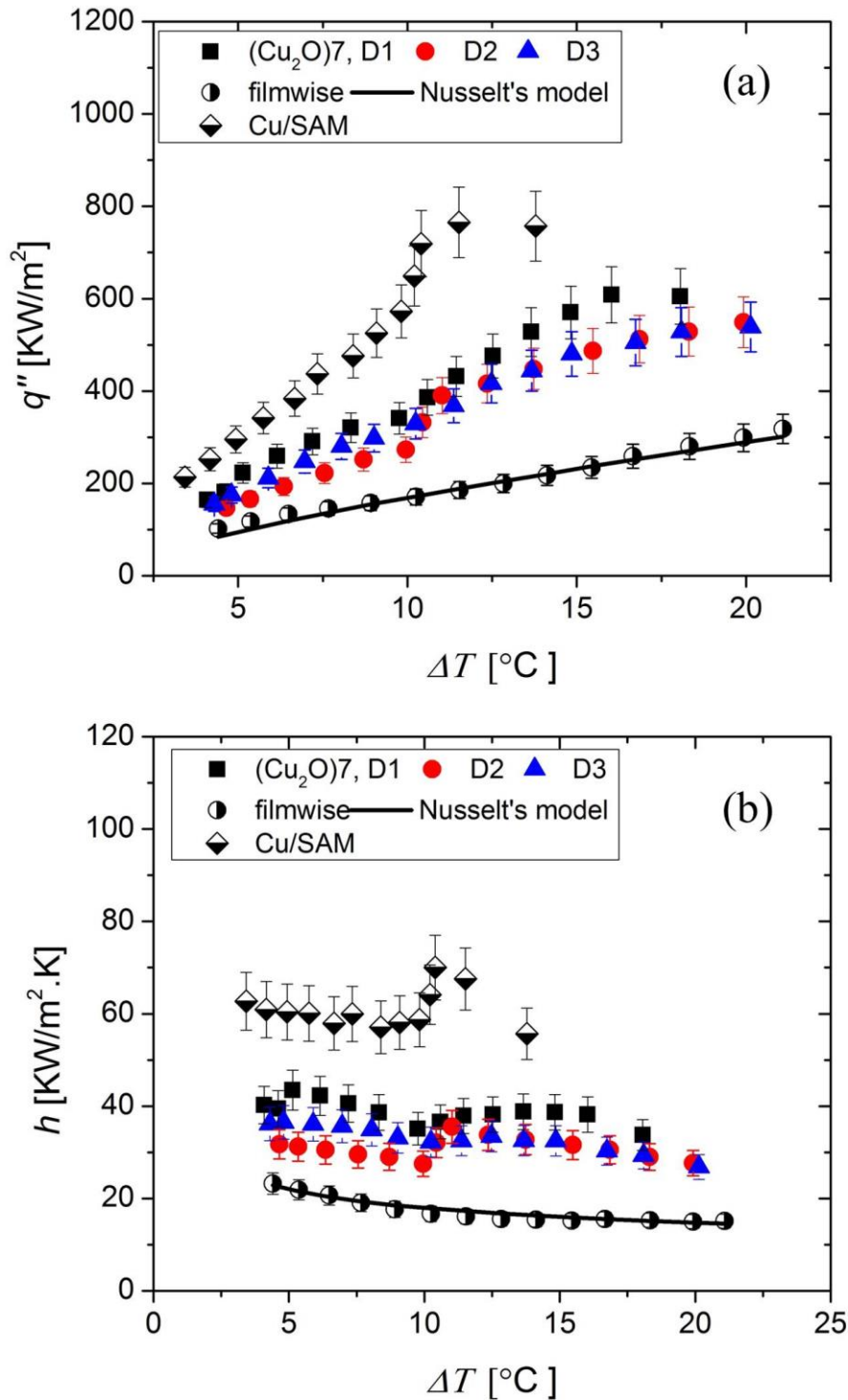
Figure 8.13: The condensation heat transfer performance for the dark orange cuprite surface $(Cu_2O)7$ tested three times in three days.

8.2 Condensation heat transfer characterization on the porous structured cuprite coatings.

8.2.1 Effect of the cuprite coatings with different colors on the dropwise condensation performance

The influence of the porous structure of the cuprite coating with the different colors (red, orange, mixed red/orange, and dark orange) on improving the dropwise condensation efficiency was investigated. The cuprite surface has sub microscale porous structure with a nanoscale pores size less than 500 nm. Figure 8.8 demonstrates the dropwise condensation on the different cuprite surfaces. Furthermore, Figure 8.9 shows the condensation heat transfer performance for the not fresh-red cuprite surface $(Cu_2O)2$. The surface was prepared and treated with the SAM coating and then tested during the condensation experiment after approximately one month of the surface preparation. Two experimentations were then conducted for the testing sample in two weeks. From Figure 8.9, it can be seen that the results of the two tests are approximately consistent. As shown in the figure, the enhancements in the heat flux and the heat transfer coefficient were promoted by 128.29 % and 121.2 %, demonstrating to enhancements of 2.28 and 2.2 times, respectively over that of the FWC model. The maximum values of the heat flux and heat transfer coefficient were 536.4 (KW/m^2) and 35.02 $(KW/m^2.K)$, respectively and they had been achieved at a subcooling temperature of 13.4 ℃. Condensation experiments were then conducted on a fresh sample as shown in Figure 8.10. The sample was tested four times in four days. The enhancement in condensation heat transfer performance was higher for the first test at the high subcooling temperatures, but then the results became stable for the other experimentations. From Figure 8.9 and Figure 8.10, it

201

can be noticed that the experimental results are approximately consistent for both the unfresh and fresh samples except the results of the first test for the fresh sample. For this sample, the condensation heat transfer enhancement was about 2.8 times higher than that for the filmwise condensation model as shown in Figure 8.10. The maximum enhancements in the heat flux and heat transfer coefficient were about 180.41% and 182.51 %, corresponding to maximum values of 693.3 (KW/m^2) and 44.28 ($KW/m^2.K$), which had been obtained at a subcooling temperature of 15.8 ℃, respectively, Then, the enhancements were degraded to about 133.68% and 134.57 % for the heat flux and the heat transfer coefficient with maximum values of 561.48 (KW/m^2) and 37.13 ($KW/m^2.K$), respectively at a subcooling temperature of 15.19 ℃.

A series of experimentations had been then conducted to demonstrate the dropwise condensation enhancement on the cuprite surface with orange (Cu_2O)5, mixed red/orange (Cu_2O)6, and dark orange colors (Cu_2O)7. Figure 8.11 clarifies the consistent results obtained on the cuprite surface with the orange color (Cu_2O)5. The sample was tested three times in three days. The figure reveals that the maximum enhancements in the heat flux and the heat transfer coefficient were about 124.65% and 125.58%, corresponding to the maximum values of 604.22 and 34.29, respectively obtained at the subcooling temperature of 17.7 ℃.

Figure 8.12 demonstrates the dropwise condensation enhancement on the cuprite surface with the mixed red/orange colors (Cu_2O)6. The sample was tested four times in four days. Each test was performed in 24 hours from the last one. From Figure 8.12, the condensation heat transfer enhancement was greater for the first test than those for the other tests. This is as explained before due to the high hydrophobicity of the fresh

202

sample, which was then degraded and became stable during the condensation tests, referring to the stability of the surface wettability, the nucleation density and the droplet removal rate. For the fresh sample, the maximum values of the heat flux and the heat transfer coefficient, which are achieved at a subcooling temperature of 13.53 ℃, were approximately 588.53 (KW/m^2) and 51.39 (KW/m^2.K), respectively. This demonstrates maximum improvements of 212.04% and 214.68% in the heat flux and heat transfer coefficient, respectively, in comparison with that achieved for the FWC model.

Figure 8.13 shows the condensation heat transfer performance on the cuprite surface with the dark orange color (Cu_2O)7, referring to the existence of the sulfate on the surface as explained before. The sample was tested three times in three days. It can be seen from Figure 8.13, higher condensation results were first obtained with the fresh sample, and then the performance decreased and maintained approximately constant for the other tests according to the same reason mentioned previously. For this sample, the improvements in the heat flux and heat transfer coefficient were about 143.58% and 144.61%, respectively compared to that for the filmwise condensation surface. These improvements are corresponding to maximum values of 608.74 (KW/m^2) and 38.17 (KW/m^2.K) for the heat flux and heat transfer coefficient, which were achieved at a surface temperatures of 16.02 ℃.

According to the above results, it is clear that the dropwise condensation promotion on the cuprite coating with the porous structure is more reliable and higher compared to that on the micro/nanostructured copper oxide and green patina surfaces. This is mainly attributed to the lower thermal resistance of the substrate and coating thickness of the cuprite surface, as well as to the lower adhesion forces related to the

203

interfacial interaction between the droplets condensate and the porous condensation surface compared to those on the micro/nanostructured surfaces. Another important reason is that a large capillary force can be achieved on the condensate droplets due to the narrow nanoscale cavities of the porous structure with the microscale thickness (300 nm-1.6 μm), resulting in preventing the droplets from penetrating into the cavities of the porous structured surface. Accordingly, this can promote the droplets nucleation, droplets shedding and the droplets departure frequency. However, the droplets departure diameter will be with a larger size compared to those droplets achieved on the hydrophobic plain copper surface, resulting in lower dropwise condensation compared to the latter besides the other reasons mentioned previously. The above explanation for the efficient dropwise condensation on the cuprite coating can be first proven based on the research presented by Wen et al [143] and Feng et al. [212]. They have reported that the droplets mobility on the nanostructures can be promoted by lowering the pinning of the condensate droplets into the cavities of the nanostructures having higher perpendicularity, narrow spacing and lower surface energy. Secondly, Miljkovic et al. [242] have numerically investigated the dropwise condensation on the superhydrophobic surfaces with different pillar heights. They have reported that the dropwise condensation on these surfaces increases as the height of the pillar decreases due to the lower thermal resistance of the lower pillar heights. They have also demonstrated a good dropwise condensation for the pillar heights ranging between 1.0 to 2.0 μm. Thus, because of the thickness of the presented cuprite coating is within this range, the dropwise condensation might be promoted. Another effective reason for this promotion can be clarified based on the research presented by Xu et al. [243]. They have investigated experimentally and analytically the droplet motion

204

within the superhydrophobic surface with a V-shaped grooved structure. They have demonstrated that as the cross-sectional angle of the V-shaped groove decreases, the droplet can transform from the immersed state to the suspended state. The droplet with the suspended state can depart from the groove bottom with increasing the droplet volume size. The spontaneous motion of the droplet with the rising of the droplet volume depends upon the influence of the capillary force and the cross-sectional angle of the V-shaped groove structure. Consequently, the droplet removal rate was improved on the cuprite coating with the narrow cavities and thin coating thickness, resulting in improving the heat transfer performance during the dropwise condensation.

Figure 8.14: Photographic images of (a) the cuprite surface coated partially with irregular copper oxide coating and (b) the behavior of the dropwise condensation on the damaged surface when starting the condensation experiment with steam temperature and pressure higher than the saturation conditions.

8.2.2 Effect of oxidizing the cuprite surface to the copper oxide using the hydrogen peroxide treatment on the condensation performance

During the condensation experiments, it was observed that when the steam was supplied to the condensation chamber for a long time, the steam temperature increased

more than the saturation temperature. The measured temperature using the thermocouples was about 103 ℃, referring to the high amount of steam inside the chamber. Therefore, when just get starting the condensation test on the cuprite surface with the red color $(Cu_2O)2$, the color on some spots of the surface was directly changed to a black one, referring to the formation of the copper oxide coating on the surface. This action occurred after the third experimentation for the testing sample at the condition mention above. Figure 8.14 demonstrates the condensation behavior on the cuprite surface coated partially with the irregular shapes of the copper oxide coating. Furthermore, Figure 8.15 exhibits the condensation heat transfer performance on this testing sample which was tested 10 times in ten days. It can be seen from this figure that the condensation performance was degraded compared to the other samples tested before at the saturation conditions. The reduction in the condensation performance is due to the irregular shapes of the condensate droplets which were approximately flooded on the regions coated with the copper oxide coating with the higher surface energy compared to the undamaged parts of the surface. However, the dropwise condensation enhancement is still higher than that on the FWC model. For instance, for test 10 (Day 10), the heat flux and the heat transfer coefficient were enhanced by 71.06% and 63.94%, respectively compared to the FWC model. The maximum values of the heat flux and heat transfer coefficient were 419.5 (KW/m^2) and 25.73 ($KW/m^2.K$), and they had been achieved at a subcooling temperature of 16.3 ℃, respectively.

In order to deal with the above problem by improving the chemical stability of the surface, the cuprite surface with the red color $(Cu_2O)1$ was treated with the hydrogen peroxide to be oxidized and changed to the copper oxide coating. During this treatment, it

206

was observed that the red cuprite surface was first changed to a dark red color and then to a black one depending on the treatment time. This indicates that the coating thickness of the copper oxide surface based on hydrogen peroxide treatment can be controlled better than that surface prepared using the alkaline solution as mentioned before. The coating thickness of the oxidized cuprite surface as reported in chapter 7 was about 5.0 μm and it is less than the copper oxide and the polished one with the coating thickness of about 50.0 μm and 17.0 μm, respectively. Figure 8.16 shows the dropwise condensation behavior on the treated sample $(Cu_2O)3$ which was tested three times in three days. As shown in Figure 8.17, the improvements in the heat flux and the heat transfer coefficient were about 116.7% and 117.2%, respectively, referring to maximum values of 591.37 (KW/m^2) and 32.8 $(KW/m^2.K)$ obtained at a subcooling temperature of 18.07 ℃, respectively. From Figure 8.17, it can be noticed that the condensation results are reliable and consistent for the three experimentations tests.

The comparison between the results of the dropwise condensation heat transfer enhancements obtained for the cuprite surfaces with different colors (red, mixed red/ orange, orange, dark orange), and the transformed one to the copper oxide surface are shown in Figure 8.18. It can be seen that the condensation results are approximately consistent even for the red cuprite surface transformed to the copper oxide one $(Cu_2O)3$. The figure also reveals the higher condensation heat transfer performance for the cuprite surface with the mixed red/ orange color $(Cu_2O)6$ at the high subcooling temperatures. Moreover, the condensation efficiency on these surfaces is still lower than that on the plain hydrophobic surface. This is related to the reasons mentioned before including the conductive thermal resistance of the substrate material and the coating thickness as well

207

the different interfacial interaction between the condensate droplets and the condensation surface with porous structure, resulting in higher adhesion forces on the condensate droplets, and larger droplet departure diameters compared to that on the plain hydrophobic surface.
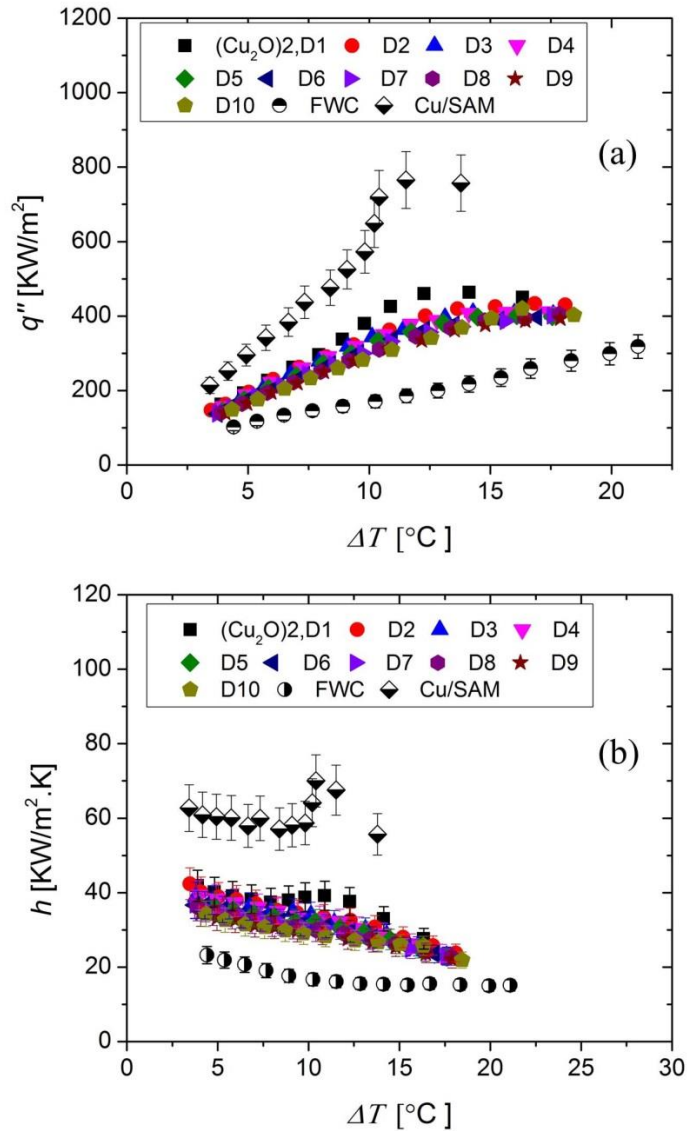
Figure 8.15: The condensation heat transfer performance for the damaged cuprite surface $(Cu_2O)2$ exposed to steam temperature and pressure higher than the saturation conditions. The sample was tested ten times in ten days.
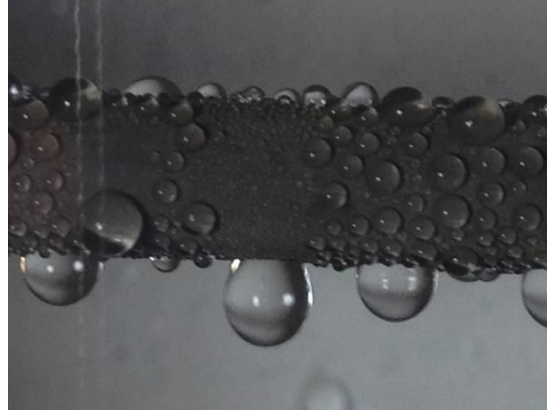
Figure 8.16: A photographic image of the dropwise condensation behavior on the cuprite surface $(Cu_2O)3$, which was oxidized by the hydrogen pyroxide for 24 hours and then treated with the SAM coating.
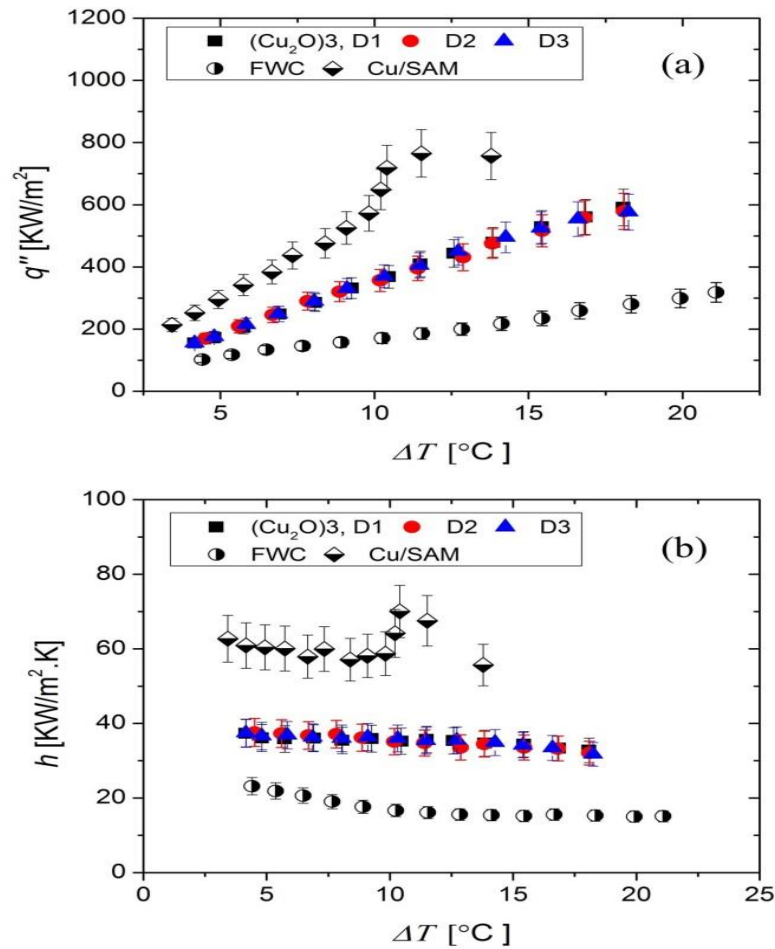
Figure 8.17: The condensation heat transfer performance for the superhydrophobic cuprite surface $(Cu_2O)3$.

209
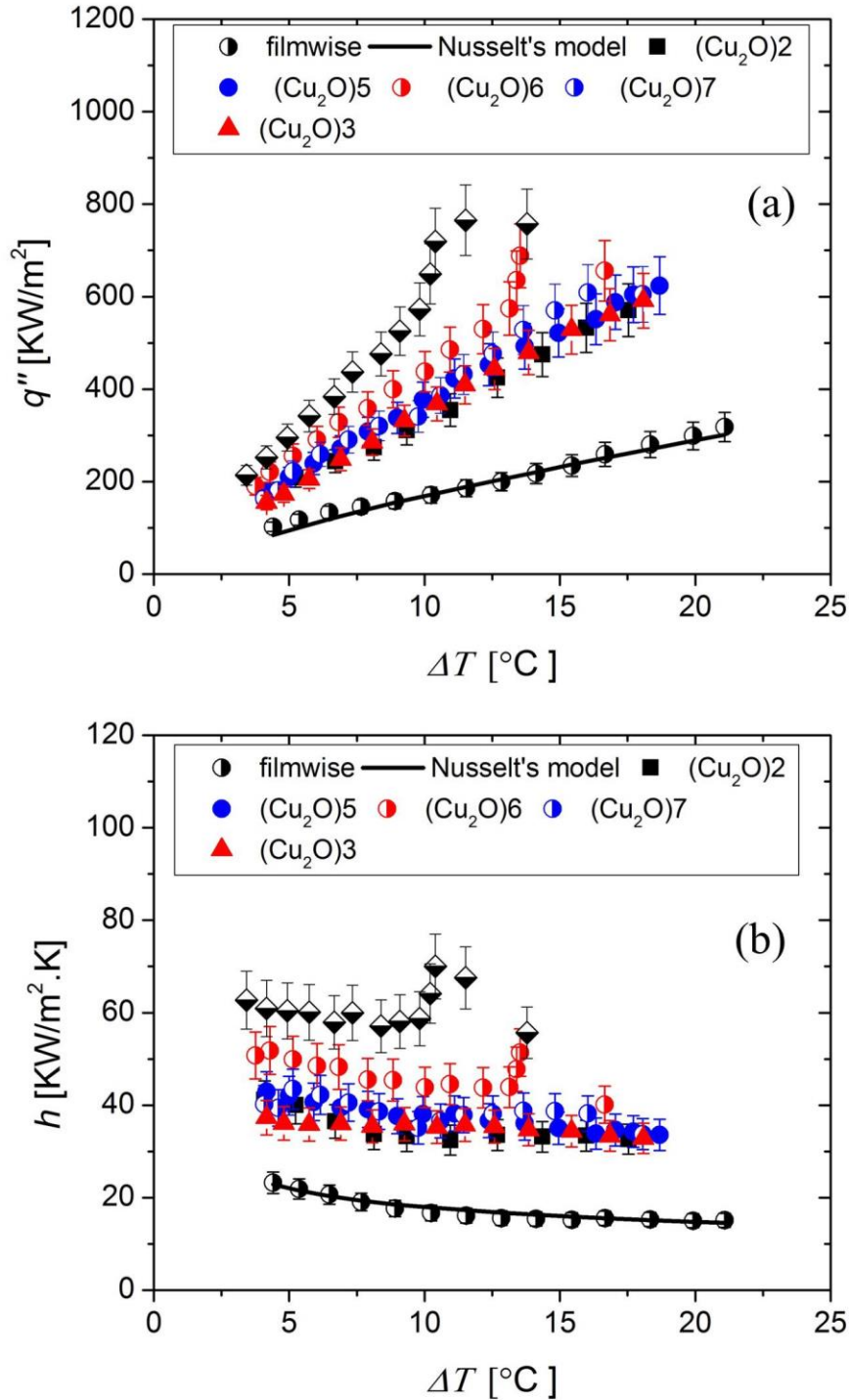
Figure 8.18: The comparison between the dropwise condensation heat transfer enhancements on the cuprite surfaces with different colors ($(Cu_2O)2$, $(Cu_2O)5$, $(Cu_2O)6$, $(Cu_2O)7$), and the transformed one to the copper oxide surface using hydrogen pyroxide $(Cu_2O)3$.
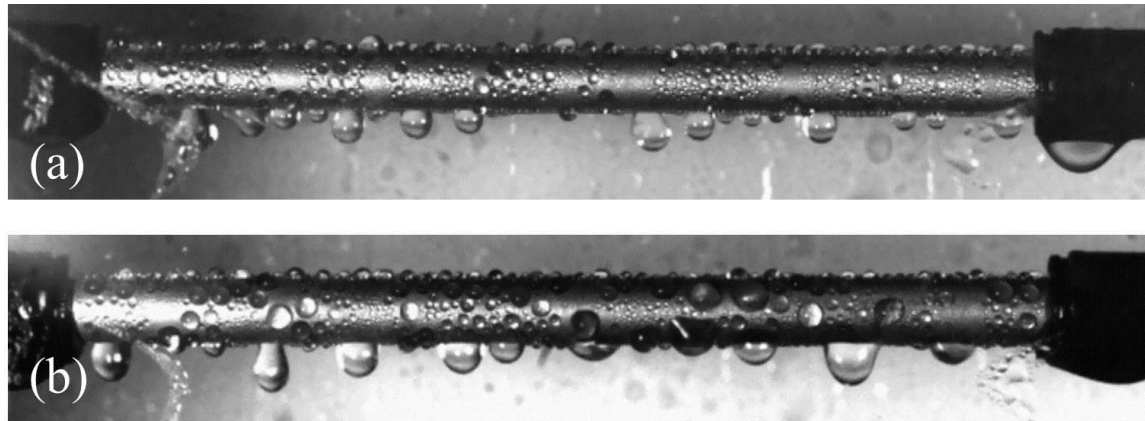
Figure 8.19: Images of the dropwise condensation behavior on the two prepared hydrophobic plain copper surfaces, (a) the surface washed with water and dried before the SAM treatment, and (b) the surface washed in acid and ethanol and then treated with the SAM coating.

8.3 Condensation heat transfer characterization on the copper surface with different structures and with oxidization processing

In this section, the dropwise condensation performance on hydrophobic copper surfaces with smooth and rough structures as well as with the treatment with the hydrogen peroxide to improve the chemical stability of these surfaces was investigated. First, two plain hydrophobic copper surfaces were prepared in different ways to demonstrate the influence of the surface preparation on the condensation heat transfer performance. The first sample (Cu/SAM_S1) was polished and then immersed in 10 wt. % of the sulfuric acid solution for 10 min to remove the native oxides from the surface and then cleaned ultrasonically in a bath of acetone, ethanol and distilled water for 10 min, respectively. The sample was then dried in the air and treated with the SAM solution. On the other hand, the second sample (Cu/SAM_S2) was treated with the same polishing and cleaning processes as explained above, but before the treatment with the SAM solution, the surface was cleaned ultrasonically in the sulfuric acid solution and ethanol, respectively. Then, the surface was directly immersed in the SAM solution. After

211

this treatment, it was observed some white layers formed on the surface and led to decrease the condensation heat transfer performance due to the increase in the thermal resistance of the SAM coating compared to that formed on the other prepared sample (Cu/SAM_S1). Figure 8.19 exhibits the dropwise condensation behavior on the two different plain hydrophobic surfaces. It can be observed that the condensate droplets on the second sample (Cu/SAM_S2) shed off the surface with larger size compared to the other sample, resulting to lower condensation heat transfer performance.

Figure 8.20 shows the dropwise condensation enhancements on those two surfaces. The first sample (Cu/SAM_S1) was tested one time, whereas the second one (Cu/SAM_S2) was tested four times in one week. For the first sample (Cu/SAM_S1), the heat flux and the heat transfer coefficient were enhanced by 295.42% (3.95 times) and 299.69% (4.0 times), respectively compared to that on the FWC model. The maximum values of the heat and the heat transfer coefficient were 719.18 (KW/m^2) and 70.02 ($KW/m^2.K$), and they had been obtained at a subcooling temperatures of 10.4 ℃, respectively. However, for the second sample (Cu/SAM_S2), the maximum values of the heat flux and the heat transfer coefficient were 677.25 (KW/m^2) and 48.58 ($KW/m^2.K$) at a subcooling temperatures of 14.02 ℃, respectively. The enhancements were about 199.01% (3 times) and 200.47% (3 times) for the heat flux and the heat transfer coefficient, respectively compared to that on the filmwise condensation surface. From Figure 8.20, it can be seen that for the first test on the fresh sample, a higher condensation enhancement was achieved compared to the other tests. However, the condensation performance became then stable and reliable for the other experimentations with

212

maximum enhancements of 150.48% (2.5 times) and 151.62% (2.51 times) for the heat

flux and the heat transfer coefficient, respectively at a degree subcooling of 13.88 ℃.
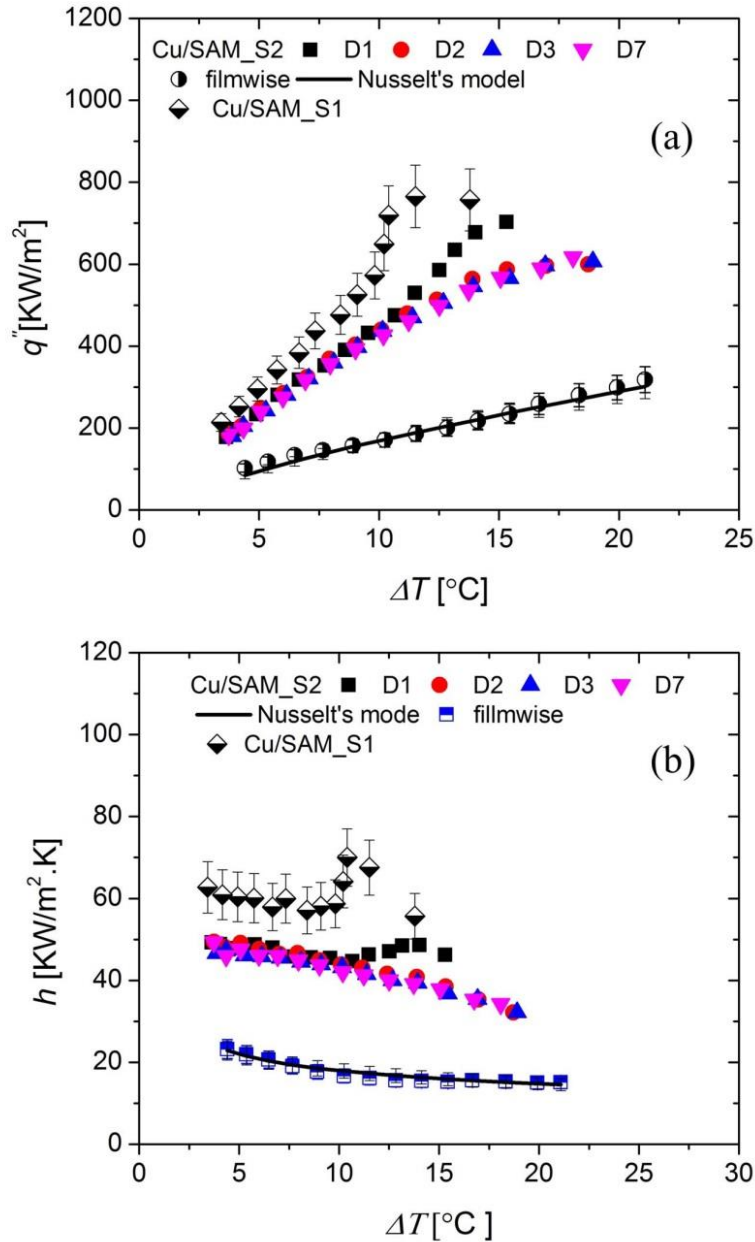
Figure 8.20: The condensation heat transfer performance on the two hydrophobic plain copper surfaces, (a) the surface washed with water and dried before the SAM treatment (Cu/SAM_S1), and ,(b) the surface washed in acid and ethanol and then treated with the SAM coating (Cu/SAM_S2), in comparison with the complete filmwise condensation surface and the Nusselt's model. The sample (Cu/SAM_S2) was tested four times in one week.

213
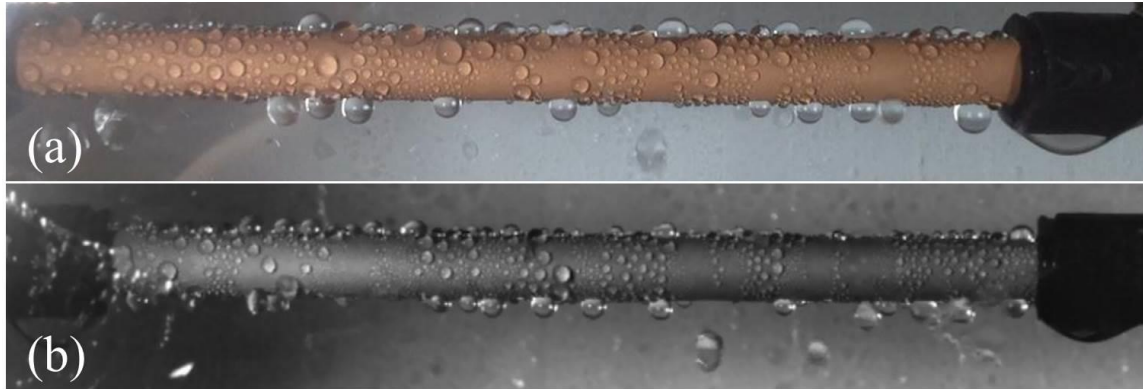
Figure 8.21: (a,b) Photograph images of the dropwise condensation behavior on the rough superhydrophobic copper surface with yellow color. (a) is a colorful picture, whereas (b) is a picture captured from the high speed camera video.

The condensation heat transfer performance on the novel superhydrophobic copper surface with the microscale porous structure with microgrooves (Cu2) was then demonstrated. As explained in chapter 7, the new copper surface with the yellow/or orange color was prepared by removing the porous-structured cuprite coating. The cuprite surface was first cleaned ultrasonically in sulfuric acid, acetone, and ethanol, respectively and then rinsed with distilled water. After that, the as-prepared sample was dried in the air or by heating in the furnace at 75.0 ℃. Figure 8.21 shows the dropwise condensation behavior on the superhydrophobic copper surface with the yellow color (Cu2). From the contact angle measurements as explained in chapter 7, the new copper surface with the rough surface shows more hydrophobicity compared to that for the smooth copper surface (Cu/SAM). For this reason, the condensation heat transfer enhancement was a little higher for the rough hydrophobic copper surface compared to the smooth one, as shown in Figure 8.22. The improvements in the heat flux and the heat transfer coefficient were about 332.8 % and 339.96 %, respectively compared to the filmwise condensation model, and they were about 12.65 % and 13.43 %, respectively compared to the plain

214

hydrophobic surface (Cu/SAM). The maximum values of the heat flux and heat transfer coefficient were 797.05 (KW/m^2) and 76.72 (KW/m^2.K), and they had been achieved at a subcooling temperature of 10.6 ℃, respectively. Furthermore, the condensation experiments for the rough copper surface (Cu2) were conducted three times in three days, showing the highest enhancement for the fresh sample and the reliability and stability in the results for the other experimentations.
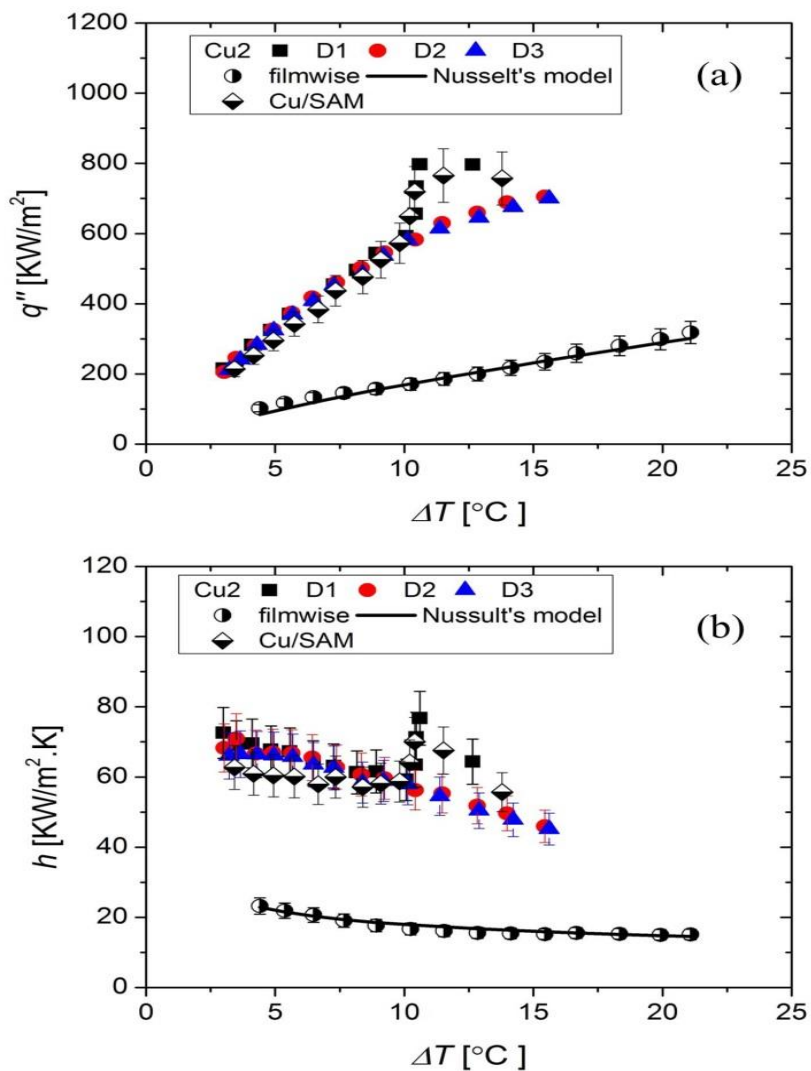
Figure 8.22: The condensation heat flux and heat transfer coefficient as a function of the surface subcooling for the rough superhydrophobic copper surface (Cu2) tested three times in three days.

215
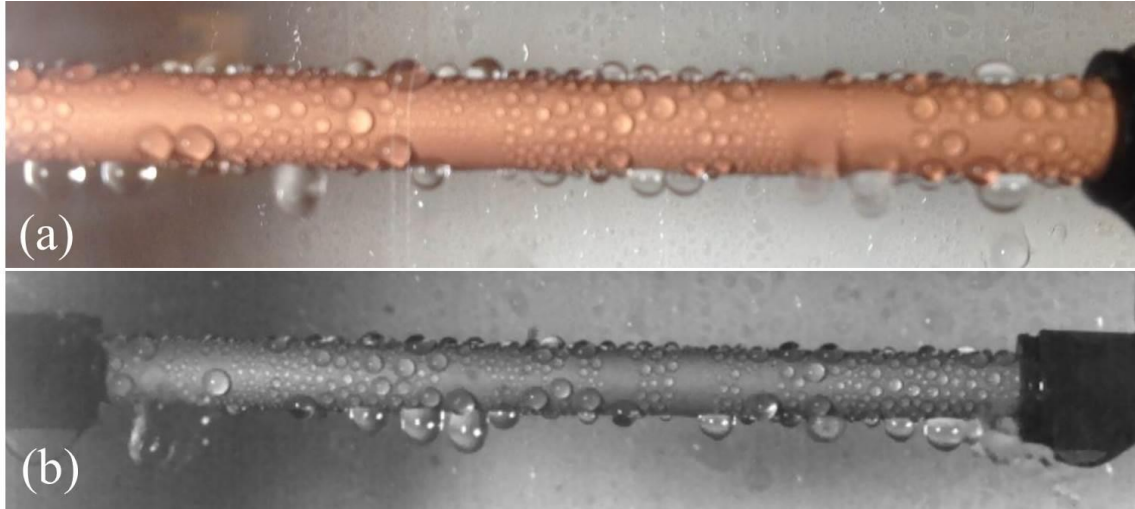
Figure 8.23: (a,b) Photograph images of the dropwise condensation behavior on the rough-oxidized copper surface with yellow color, (a) is a colorful picture, whereas (b) is a picture captured from the high speed camera video.

In order to improve the chemical stability of the copper surfaces with smooth and rough structures and sustain the dropwise condensation on such surfaces for long-term durability, they have immersed in the hydrogen peroxide solution to be oxidized and to increase the content of oxygen on the surface. As the chemical treatment time increases, the oxygen content increases on the surface, and thereby the surface changes from cuprite or copper oxide one. In this study, the surfaces were treated in the hydrogen peroxide for 24 hours, and that led to forming a red coating on the surface, referring to the cuprite coating as explained in chapter 7. The dropwise condensation behavior on the plain hydrophobic copper surface treated with the hydrogen peroxide (Cu5) and that on the superhydrophobic rough surface (Cu4) is shown in Figure 8.23. Furthermore, Figure 8.24 and Figure 8.25 show the dropwise condensation heat transfer performance on the two surfaces. The rough-oxidized surface (Cu4) was tested seven times in seven days, whereas the smooth-oxidized surface (Cu5) was tested three times in three days. From Figure 8.24, the improvements in the heat flux and the heat transfer coefficient were

about 235.72% (3.35 times) and 238.18% (3.38 times), respectively for the rough-oxidized surface (Cu4) compared to that for the FWC model. The greatest values of the heat flux and heat transfer coefficient, corresponding to the subcooling temperature of 13.73 ℃, were 749.13 (KW/m^2) and 55.0 ($KW/m^2.K$), respectively. On the other hand, for the smooth-oxidized surface (Cu5), the improvements were approximately 124.56% (2.24 times) and 125.32% (2.25 times) for the heat flux and heat transfer coefficient, respectively, referring to maximum values of 582.24 (KW/m^2) and 34.73 ($KW/m^2.K$) obtained at a degree subcooling of 16.83 ℃, respectively.

The comparison between the dropwise condensation results before and after the oxidization processing for the smooth and rough (microscale porous structures with microgrooves) copper surfaces is presented in Figure 8.26. The figure clarifies that the condensation heat transfer performance for the rough-oxidized superhydrophobic surface (Cu4) is still reliable, stable and similar to that for the superhydrophobic surface without oxidization treatment (Cu2). On the other hand, the enhancement was degraded for the smooth-oxidized hydrophobic surface (Cu5) compared to that for the smooth surface without the oxidization processing (Cu/SAM). The highest condensation enhancement for the rough-oxidized superhydrophobic surface (Cu4) compared to the oxidized plain surface (Cu5) is due to the higher oxygen content on the latter, resulting to the higher carbon content on the surface after the SAM treatment as shown in Figure 7.34. As a result, the increase in the amount of carbon on the surface results in increasing the conductive thermal resistance, reducing the nucleation density and increasing the droplet departure diameter, and thereby reducing the droplet departure frequency which affects the condensation performance efficiency.

217
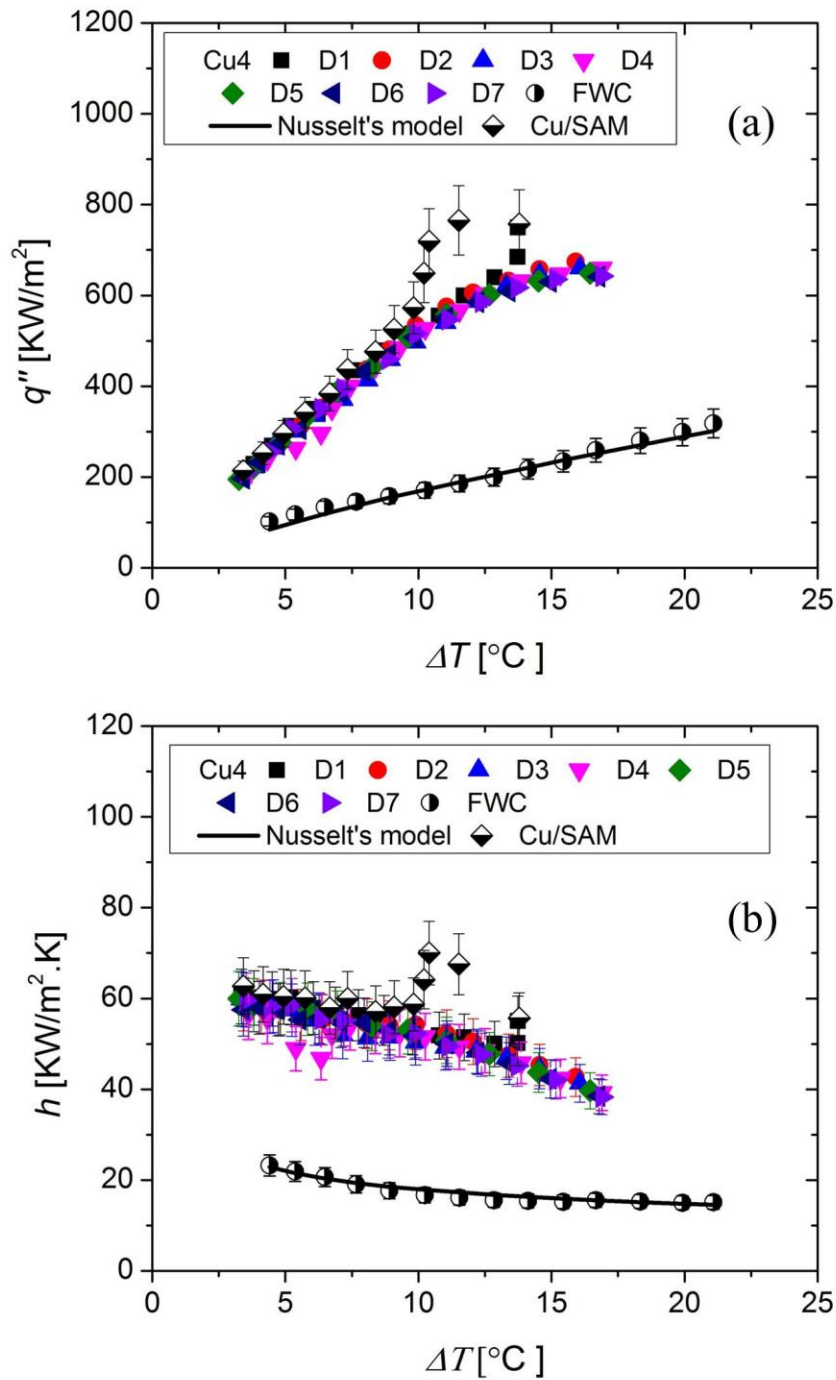
Figure 8.24: The condensation heat flux and heat transfer coefficient as a function of the surface subcooling on the rough-oxidized copper surface (Cu4), the plain hydrophobic copper surface (Cu/SAM), the plain hydrophilic copper surface (FWC) and the Nusselt's model. The superhydrophobic surface (Cu4) was tested seven times in seven days.
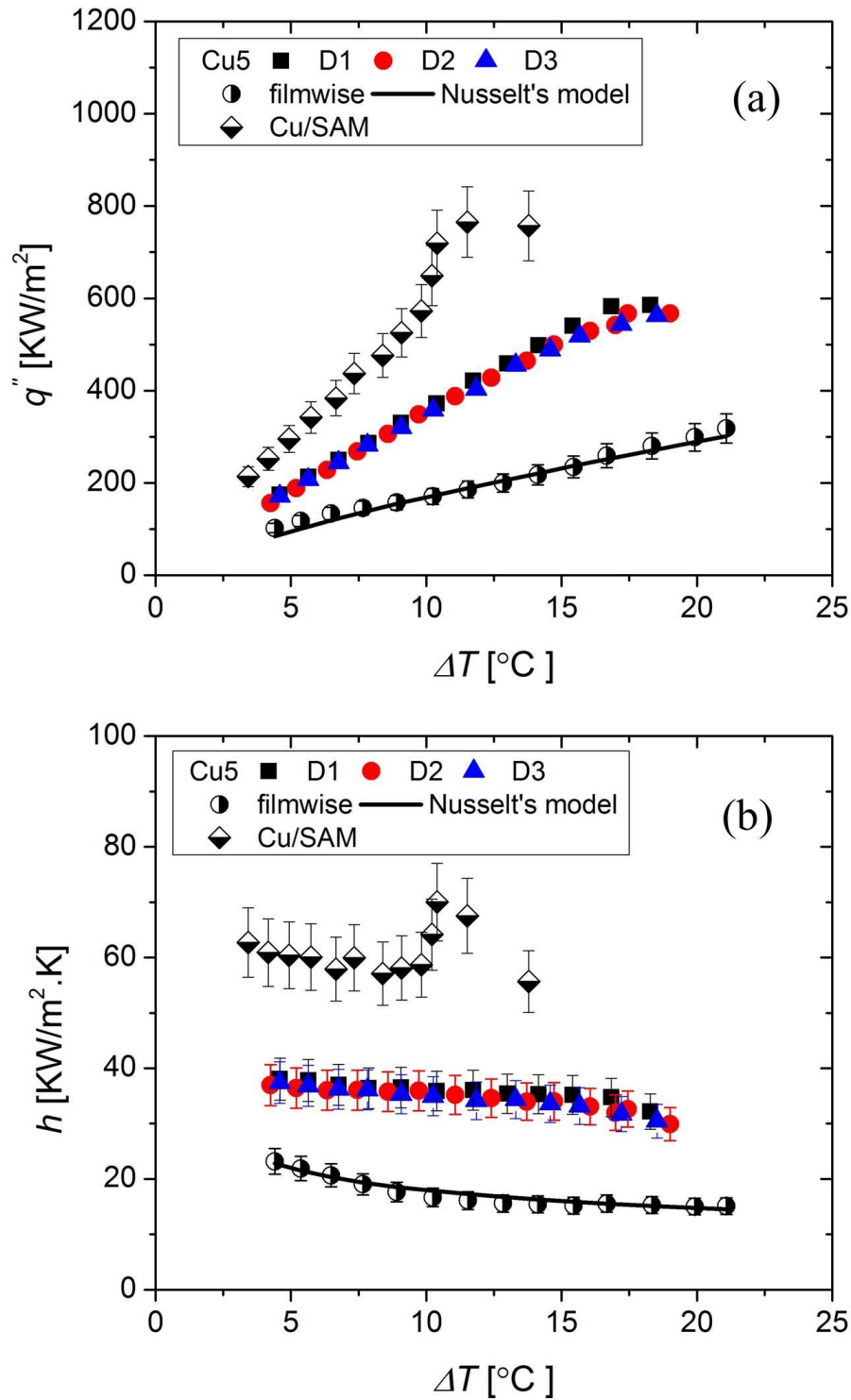
Figure 8.25: The condensation heat flux and heat transfer coefficient as a function of the surface subcooling for the plain-oxidized hydrophobic copper surface (Cu5) was tested three times in three days.

In addition to the above, the comparison between the condensation results for the smooth/rough-oxidized copper surfaces (Cu5/Cu4), the cuprite surface $(Cu_2O)2$, the oxidized cuprite surface $(Cu_2O)3$, the polished copper oxide surface $(CuO)4$, and the polished patina surface (patina4) is shown in Figure 8.27. From the figure, it can be seen that compared to the FWC model, the condensation enhancements for most the oxidized surfaces are approximately consistent except for the polished patina surface which showed a little more enhancement and the rough-oxidized copper surface with the highest performance. Consequently, it can be concluded from the presented condensation results for the different surfaces with different structures and modification that the dropwise condensation performance is mainly affected by some parameters. One parameter is the thermal resistance associated with the thermal conductivity of the substrate material, the coating thickness, the SAM coating thickness, and the amount of carbon, oxygen, and metal on the surface, which also affect the hydrophobicity of the surface, the nucleating density, and the droplets removal rate. Since for efficient droplet nucleation, a hydrophilic surface is required, whereas a superhydrophobic surface is needed for effective droplets removal rate. The latter was significantly improved on the rough (microscale porous structure with microgrooves) superhydrophobic copper surface in this study. Another important parameter on the dropwise condensation performance is the interfacial interaction between the condensate droplet and the condensation surface. This parameter is highly different on surface structures, such as the smooth, porous, micro/nanostructures due to the difference in the adhesion forces affecting the condensate droplet on such surfaces. From the presented results, it was observed that as the surface roughness and the coating thickness increased, for instance, for the micro/nanostructured

220

surface, the adhesion forces affecting the condensate droplet increased, resulting in increasing the droplet departure diameter and reducing the droplet departure frequency.
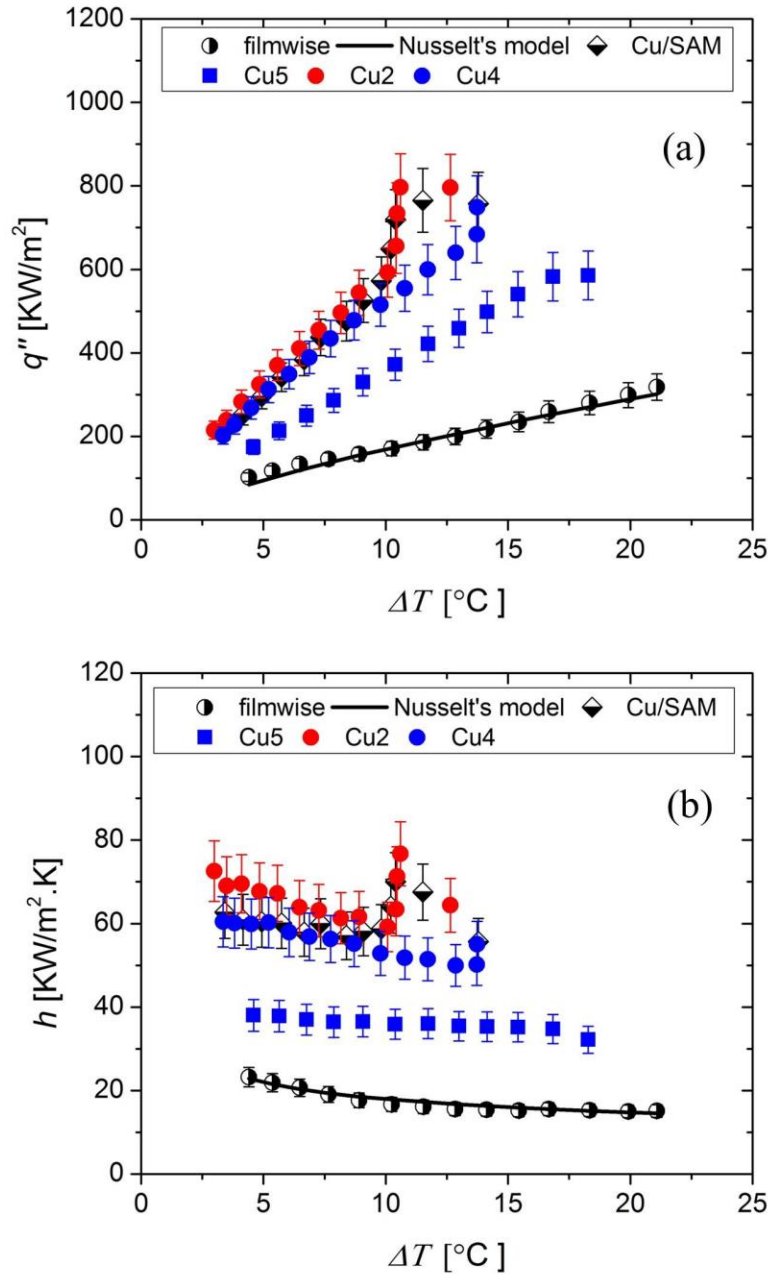
Figure 8.26: The condensation heat flux and heat transfer coefficient as a function of the surface subcooling for the rough superhydrophobic copper surface (Cu2), the rough-oxidized copper surface (Cu4), the plain-oxidized hydrophobic copper surface (Cu5), the plain hydrophobic copper surface (Cu/SAM), the plain hydrophilic copper surface (FWC) and the Nusselt's model.

221
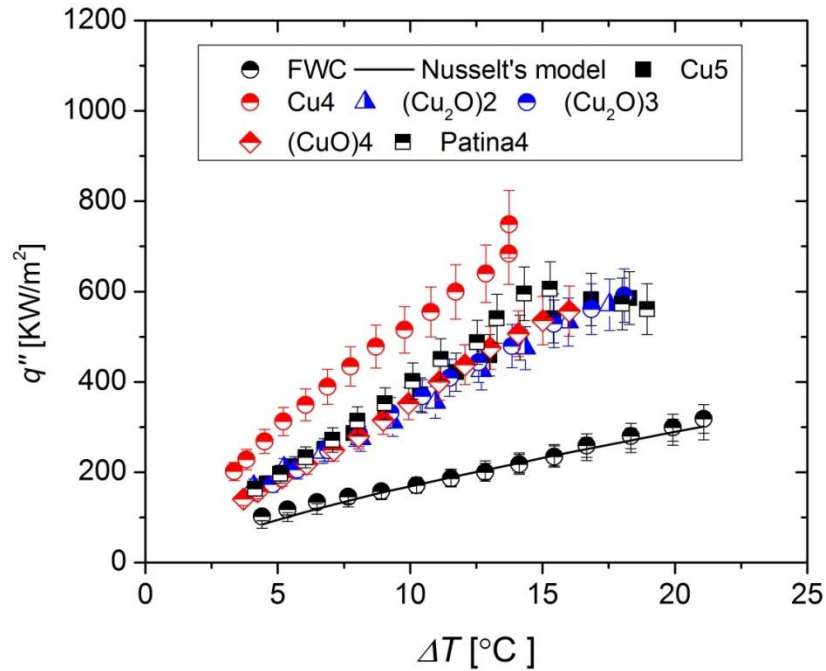
Figure 8.27: The comparison between the condensation heat transfer performance results for the Smooth-oxidized copper surface (Cu5), the rough-oxidized copper surface (Cu4), the cuprite surface $(Cu_2O)2$, the oxidized cuprite surface by the hydrogen pyroxide $(Cu_2O)3$, the polished copper oxide surface $(CuO)4$, and the polished patina surface (patina4), the plain hydrophobic copper surface (Cu/SAM), the plain hydrophilic copper surface (FWC) and the Nusselt's model.

8.4 Droplets dynamics analysis results

For all the developed coatings in this study, the measured heat flux based on the experimental measurement method (Exp.) was plotted as a function of the subcooling temperatures and compared with the heat flux computed based on the droplets analysis method (DA). The effects of the droplet departure frequency and the average droplet departure diameter on the dropwise condensation enhancement were also investigated.

8.4 1 Green patina and copper oxide coatings

Figure 8.28 and Figure 8.29 show the comparison between the heat flux measured experimentally (Exp.) and that computed based on the droplets dynamics analysis method (DA) as a function of the surface subcooling for the green patina and CuO surfaces. It can

222

be seen that a good agreement was achieved based on the two different methods. This indicates that the droplets analysis method is a good technique to validate the experimental results. Additionally, from the two figures, it can be concluded that after removing the microstructure the heat flux on the patina4 and (CuO)4 was highly enhanced compared to patina2 and (CuO)2 with the microstructure surfaces. This is due to the enhancement in the droplet departure frequency after the polishing process as shown in Figure 8.30. Besides, Figure 8.31 exhibits that the average droplet departure diameter was decreased for the patina4 and (CuO)4 compared to patina2 and (CuO)2 with the higher thickness and thermal resistance as well as due to the effect of the microstructure on the droplet mobility as explained previously. Moreover, it can be noticed that the patina4 surface has slightly higher droplet departure diameter and lower droplet departure frequency compared to the (CuO)4. Additionally, from Figure 8.30 and Figure 8.31, it can be drawn that the droplet departure frequency increases with decreasing the droplet departure diameter. However, for the condensation rate enhancement, the increase in the volume of the departure droplets and the droplet departure frequency are highly required.

8.4 2 Cuprite coatings (Cu_2O)

Also, herein a good agreement was achieved between the results obtained based on the experimental measurement method (Exp.) and the droplet dynamics analysis method (DA) for the different (Cu_2O) coatings. Figure 8.32 and Figure 8.33 show the heat flux as a function of the surface subcooling based on the two methods for cuprite surface (Cu_2O)2 with the red color, the cuprite surfaces treated with H_2O_2/ SAM (Cu_2O)3, cuprite surface with orange color (Cu_2O)5, the cuprite surface with red/orange

223

color $(Cu_2O)6$ and the cuprite surface with the dark orange color $(Cu_2O)7$. Furthermore, Figure 8.34 reveals the droplet departure frequency on those different coatings. It can be seen that the droplet departure frequency is higher for the $(Cu_2O)2$ and $(Cu_2O)3$ compared to the other surfaces but that doesn't mean the condensation heat transfer on those would be higher. As shown in Figure 8.35, the average droplet departure diameters on those surfaces were less than that on the other coatings. That led to slightly lower heat flux values as shown in Figure 8.32 and Figure 8.33. The maximum enhancement was on the $(Cu_2O)6$ with the highest average droplet departure diameter.

8.4 3 Copper coatings

The results based on the two different methods mentioned before were also plotted for the plain hydrophobic copper surface (Cu/SAM), the copper surface with the yellow color (Cu2), the oxidized plain surface with H_2O_2/ SAM (Cu5) and the oxidized yellow surface with H_2O_2/ SAM (Cu4) as shown in Figure 8.36 and Figure 8.37. The same trend was observed between the results obtained based on the experimental measurements method (Exp.) and the droplet analysis method (DA). From the two figures, it can be noticed that the maximum heat transfer enhancement was achieved on the yellow copper surface. This is because of the highest droplet departure frequency as shown in Figure 8.38. The departure frequency is much higher on the yellow surface compared on the plain copper surface. This increase in the departure frequency was because of the smaller size of the droplet departure diameter as shown in Figure 8.39. The droplet size decreases with decreasing the subcooling temperature. The maximum droplet size was about 3.37 mm at a subcooling temperature of 10.2 ℃ and the minimum size was about 2.3 mm at a subcooling temperature of 3.0 ℃. Even though the yellow

224

copper surface has the highest departure frequency and the smallest size of droplet departure diameter compared to the plain copper surface the heat transfer rate was slightly enhanced. This is due to the effect of the large droplet size on the condensation rate enhancement. Furthermore, it was great of interest that the oxidized yellow surface has higher enhancement compared to the oxidized plain copper surface as well as to the Cu_2O coatings. This is due to the lower amount of oxygen on the surface which led to a less amount of carbon after the SAM coating as explained before, resulting in lower thermal resistance compared to the other coatings. As shown in Figure 8.39, the oxidized yellow surface has higher departure frequency and droplet departure diameter compared to the oxidized plain copper surface,
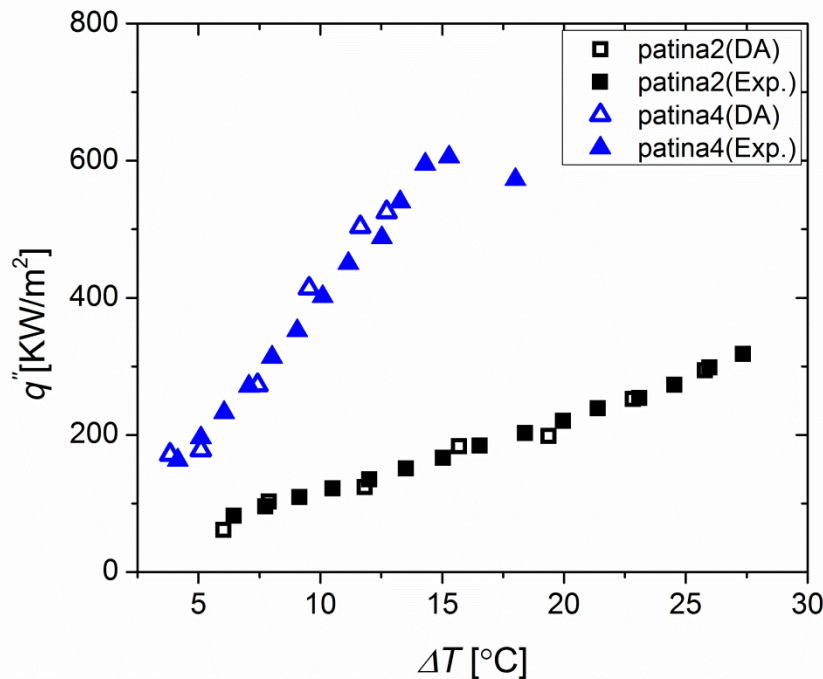
Figure 8.28: The heat flux (determined based on the experimental measurement {Exp.) and the droplets dynamics analysis (DA) methods) as a function of the subcooling temperature for the samples patina2 and patina4 surfaces.
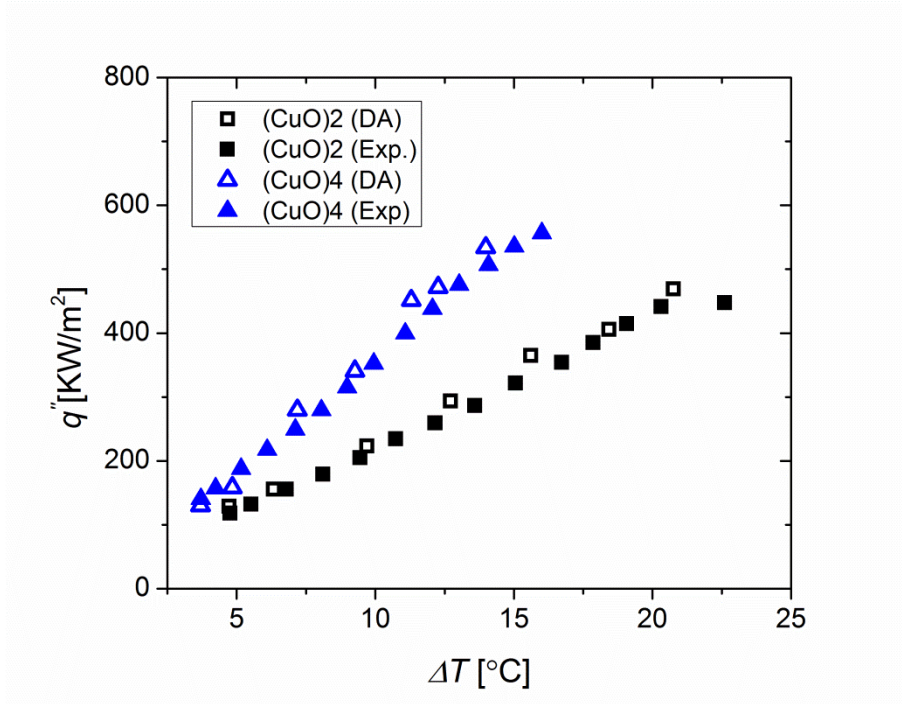
Figure 8.29: The heat flux (determined based on the experimental measurement {Exp.) and the droplets dynamics analysis (DA) methods) as a function of the subcooling temperature for the samples (CuO)2 and (CuO)4 surfaces.
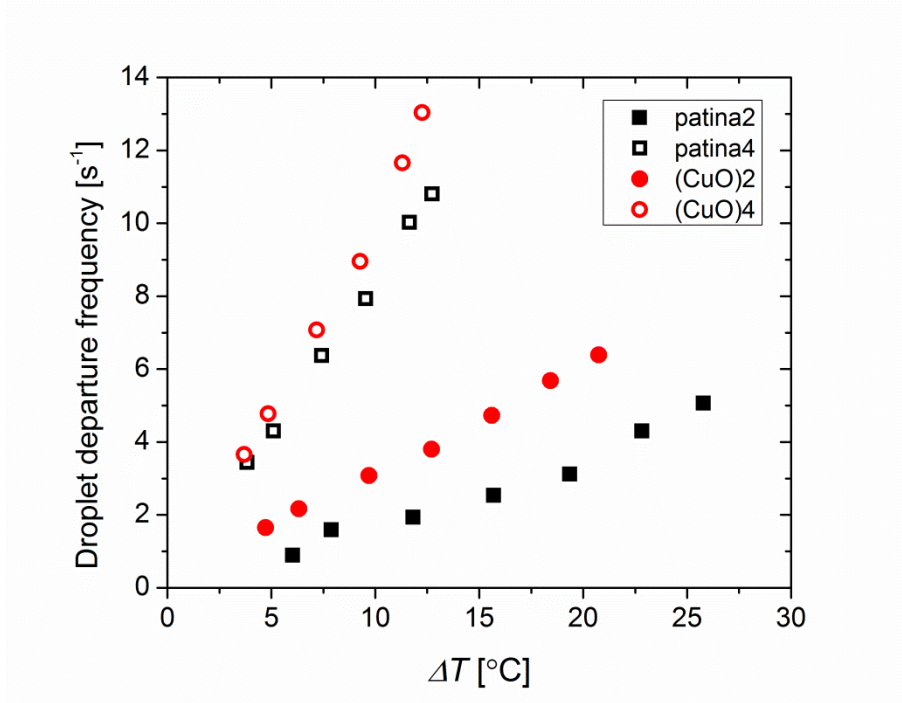
Figure 8.30: The droplet departure frequency (computed based on the DA method) as a function of the subcooling temperature for samples patina2, patina4, (CuO)2 and (CuO)4.

226
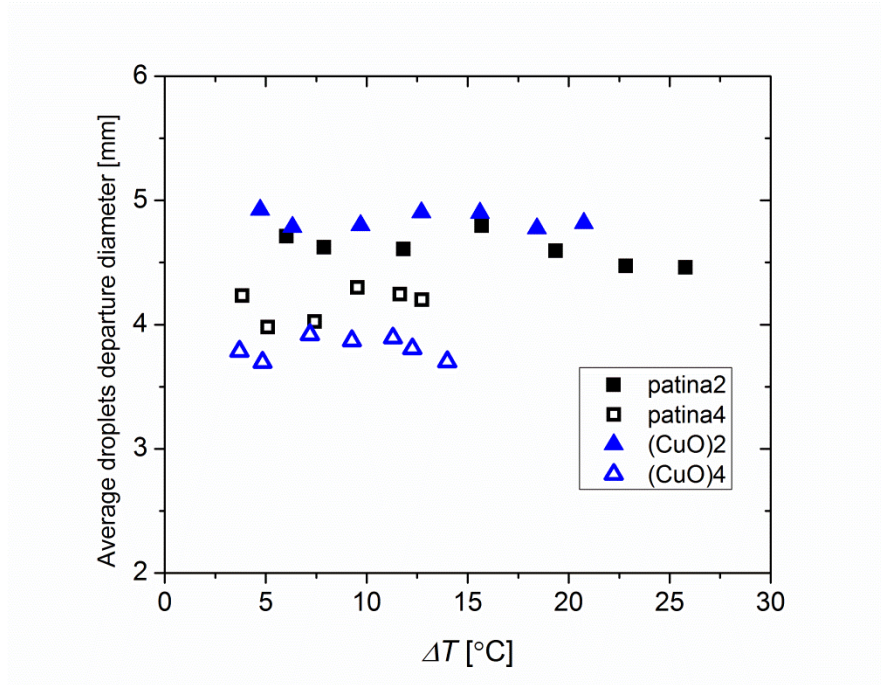
Figure 8.31: The average droplet departure diameter (computed based on the DA method) as a function of the subcooling temperature for samples patina2, patina4, (CuO)2 and (CuO)4.
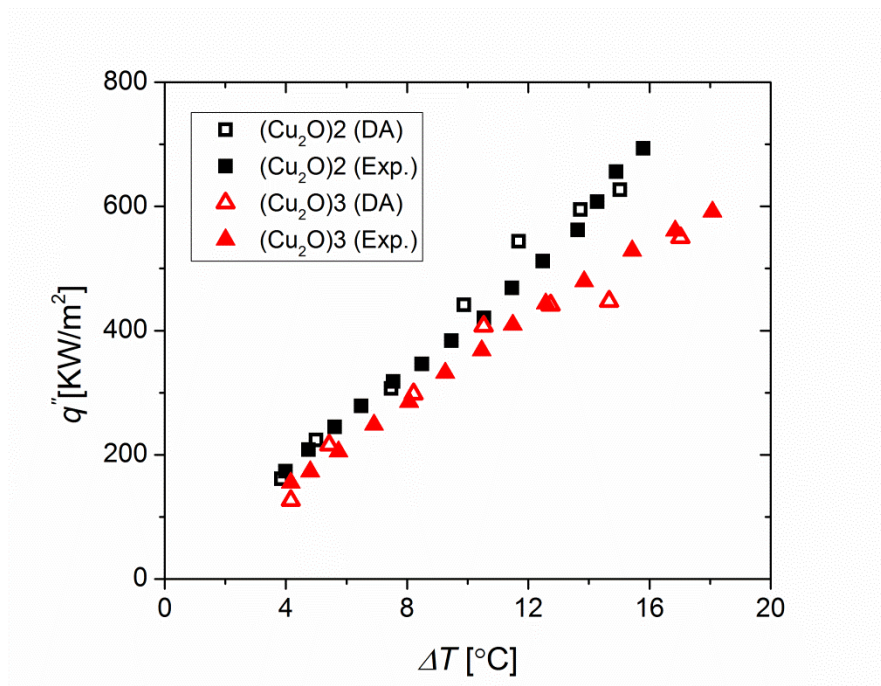
Figure 8.32: The heat flux (determined based on the experimental measurement {Exp.) and the droplets dynamics analysis (DA) methods) as a function of the subcooling temperature for samples $(Cu_2O)2$ and $(Cu_2O)3$.

227
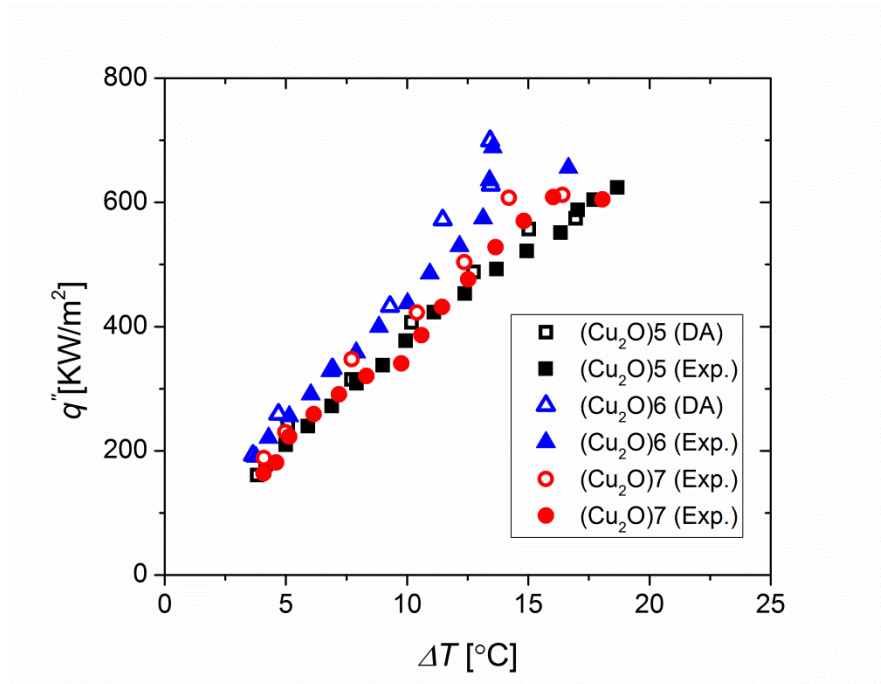
Figure 8.33: The heat flux (determined based on the experimental measurement {Exp.} and the droplets dynamics analysis (DA) methods) as a function of the subcooling temperature for samples $(Cu_2O)5$, $(Cu_2O)6$ and $(Cu_2O)7$.
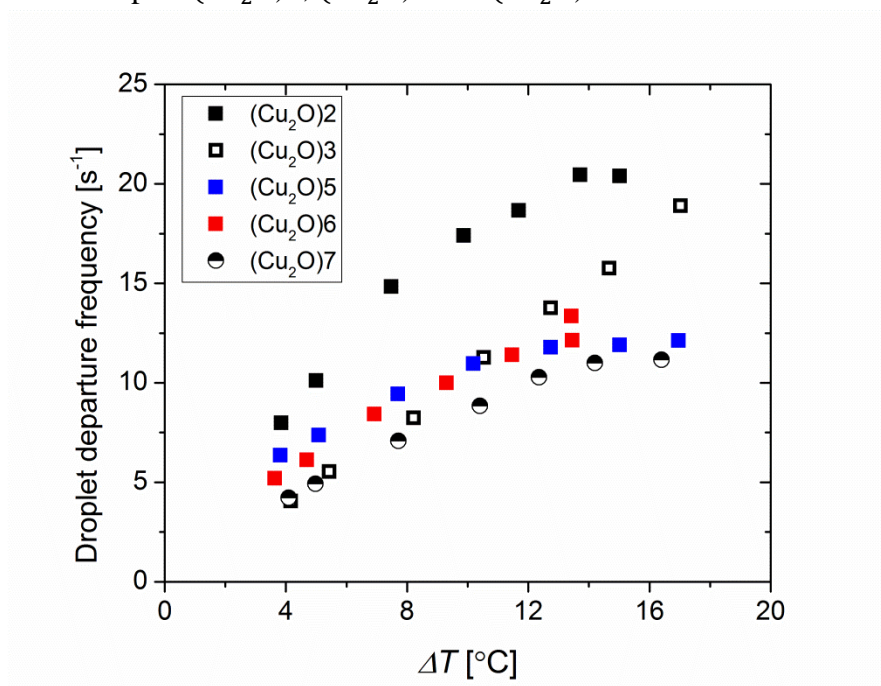
Figure 8.34: The droplet departure frequency (computed based on the DA method) as a function of the subcooling temperature for samples $(Cu_2O)2$, $(Cu_2O)3$, $(Cu_2O)5$, $(Cu_2O)6$ and $(Cu_2O)7$.

228
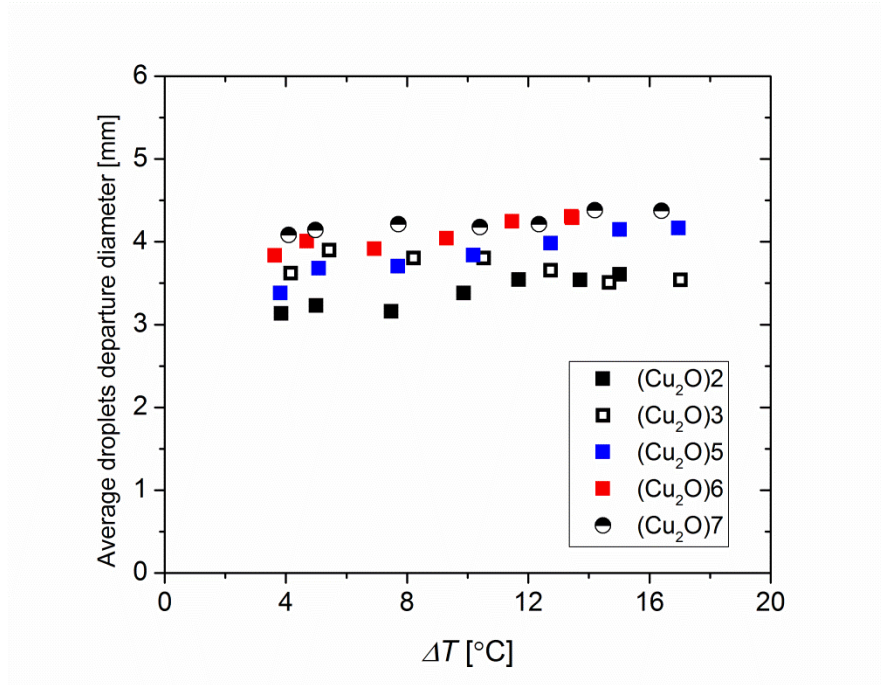
Figure 8.35: The average droplet departure diameter (computed based on the DA method) as a function of the subcooling temperature for samples $(Cu_2O)2$, $(Cu_2O)3$, $(Cu_2O)5$, $(Cu_2O)6$ and $(Cu_2O)7$.
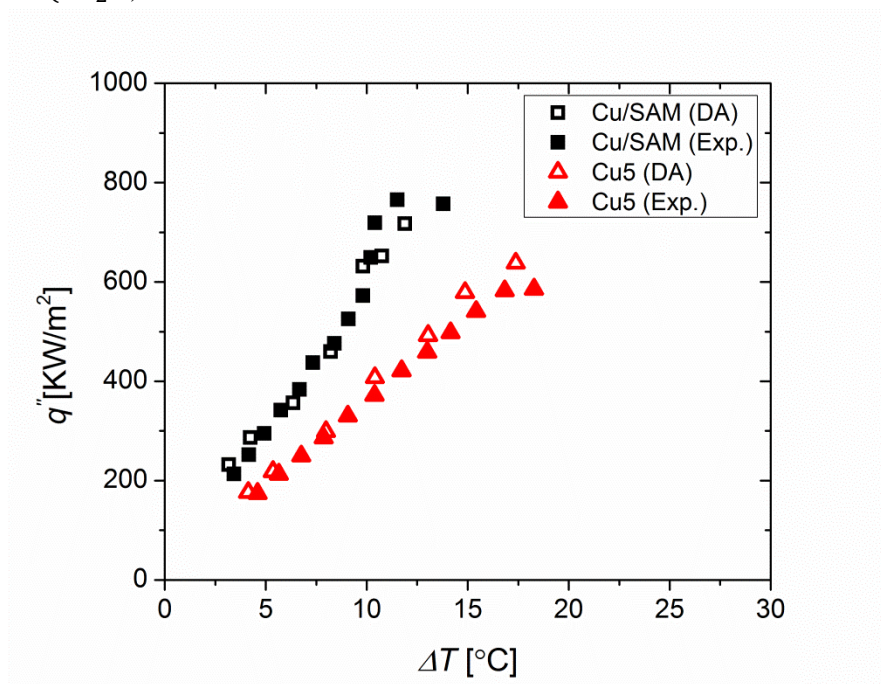
Figure 8.36: The heat flux (determined based on the experimental measurement {Exp.) and the droplets dynamics analysis (DA) methods) as a function of the subcooling temperature for samples Cu/SAM and Cu5.

229
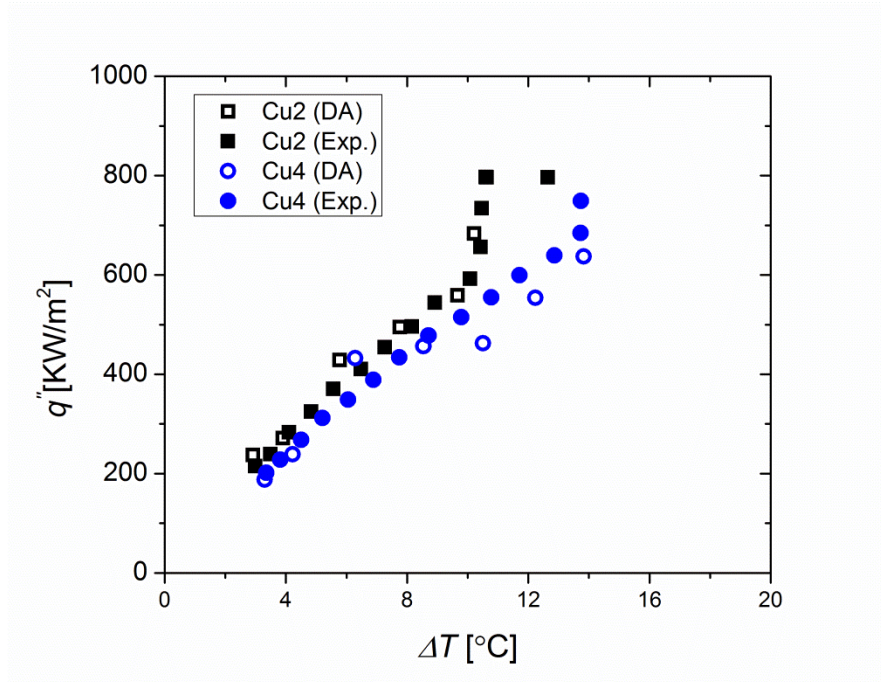
Figure 8.37: The heat flux (determined based on the experimental measurement {Exp.) and the droplets dynamics analysis (DA) methods) as a function of the subcooling temperature for samples Cu2 and Cu4.
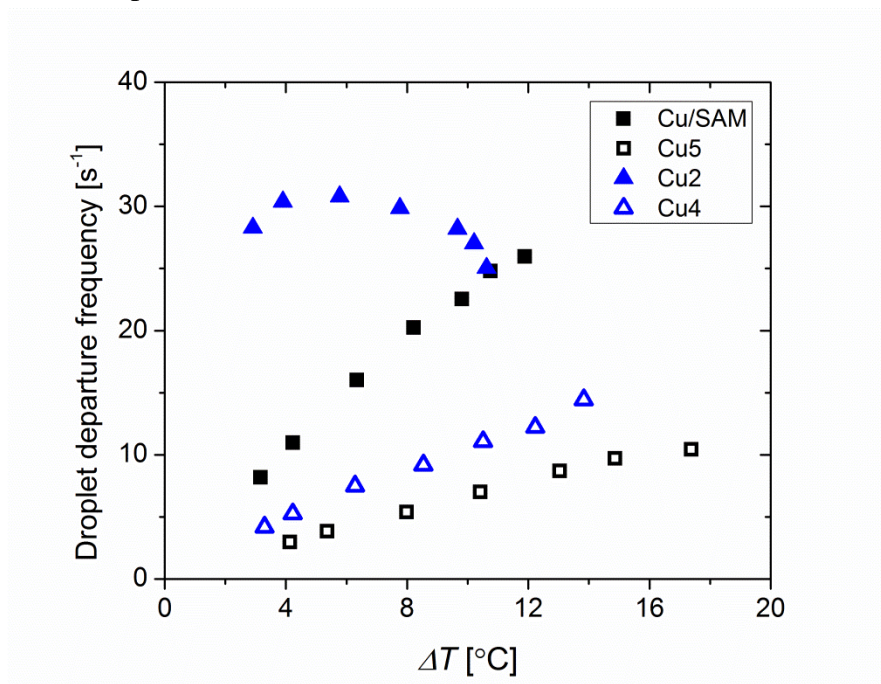
Figure 8.38: The droplet departure frequency as a function of the subcooling temperature for samples Cu/SAM, Cu2, Cu4 and Cu5.

230
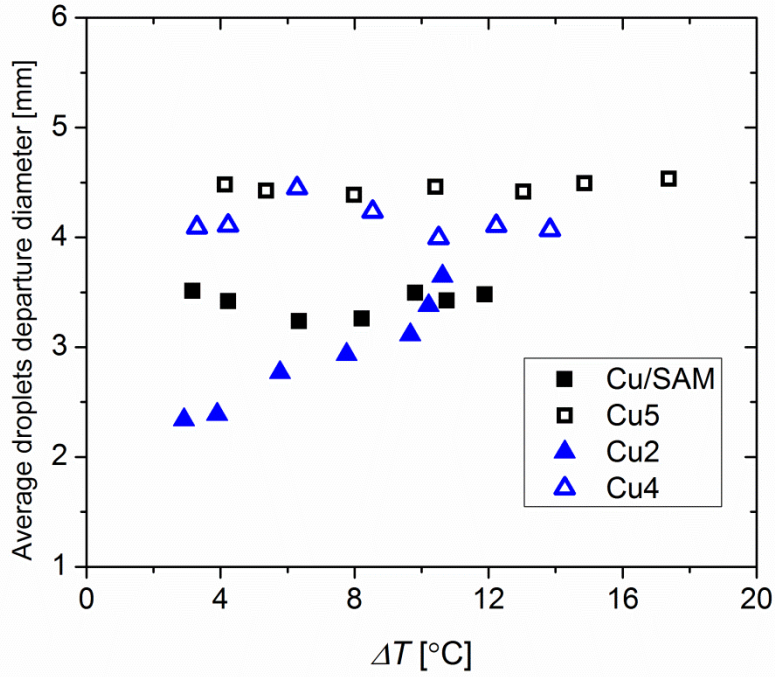
Figure 8.39: The average droplet departure diameter as a function of the subcooling temperature for samples Cu/SAM, Cu2, Cu4 and Cu5.

CHAPTER 9

CONCLUSIONS AND FUTURE WORKS

9.1 Conclusions

Experimental investigation on the condensation heat transfer characteristics of steam on horizontal copper tubes at the saturation condition and in the presence of the non-condensable gases has been performed. The influence of hydrophobic and superhydrophobic coatings on the copper tube with different surface structures including smooth, Sub-microscale porous with nanoscale pores size, microscale porous structure with microgrooves and micro/nanostructures on the dropwise condensation enhancement was examined. The current research consists mainly of three parts. In part one, the influence of the superhydrophobic nanostructured copper oxide (CuO) surface and the microstructured green patina surface $(Cu_4SO_4(OH)_6$ with three different thicknesses on condensation performance was first investigated. The objective of this part is to investigate the effects of the coating thickness and the role of oxygen and carbon on the dropwise condensation performance. The following conclusions have been drawn from this part of study.

- Coating thickness plays a critical role in determining nucleation, droplet mobility, and additional thermal resistance,

- Large pore size is unfavorable to DWC

232

- High oxygen concentration on the surface would absorb high carbon after the SAM coating, which can produce more hydrophobic surfaces, but retarding droplet nucleation as well increasing the thermal resistance.

- The influence of the micro/nanostructures thickness is significant on promoting the steam dropwise condensation. With a coating thickness of 1.0 μm or less, the dropwise condensation could be achieved and enhanced compared to the filmwise condensation due to the lower thermal resistance related to the coating and the less pinned condensate droplets in the cavities of the structure. In this work, for the patina surface with a coating thickness less than or about 1.0 μm the condensation heat transfer performance was enhanced by (40.1-87.1) % at the low and high subcooling temperatures, respectively. However, the performance was degraded below the values of the filmwise condensation by about (12.08-29.6) % and (44.5-49.05) % for the patina surfaces with coating thicknesses of about 50.0 μm and 200.0 μm, respectively.

- The condensation heat transfer was improved on the superhydrophobic copper oxide surface (CuO) compared to that of the filmwise condensation. The maximum improvement was about 48.7 % at a surface subcooling of 20.3 ℃. However, the results were then lowered to be close to the FWC after testing the sample the next day. The SAM coating was degraded to form a flooded surface with large and irregular shapes. This indicates that the nanostructured copper oxide surface is not reliable for promoting the steam dropwise condensation for long-term endurance.

233

In order to overcome the reduction in the dropwise condensation performance due to the condensate water droplets penetration into the structures, the micro/nanostructured coating was removed by polishing the surface after the self-assembled monolayer treatment. After the polishing process, it was demonstrated that a large amount of carbon is still deposited on the polished surface. Then, when the polished surface treated with the SAM coating, a white layer of carbon was deposited on the surface. The thickness of this white layer depends upon the time of the SAM treatment since it increases with the increase in the treatment time.

The polished superhydrophobic copper oxide and patina surfaces showed higher and reliable condensation enhancement compared to those with the micro/nanostructured surfaces. The mechanical polishing process was successful without any damaging for the surface. This is due to the highly strong bonding between the cuprite film and the copper substrate as well as the superior mechanical properties of the cuprite surface even compared to the polished plain copper surface. The measured values of the modulus and hardness of the cuprite surface using a Nanoindentation test at a maximum load of 1.0 mN were about 24.0189 GPa and 732.967 MPa, respectively.

Furthermore, the dropwise condensation heat transfer performance was enhanced by 1.87, 1.48, 2.2 and 2.59 times for the fresh samples of the microstructured patina surface with about 1.0 μm thickness, the nanostructured copper oxide surface, the polished copper oxide, and green patina surfaces, respectively compared to that surface with complete filmwise condensation. The fresh testing sample revealed a high improvement at the high subcooling temperatures, but then the improvement was reduced

234

and maintained consistently after some days of testing referring to the stability of the nucleation density and the droplet removal rate on the SAM coating..

In part two of this study, the effect of sub-microscale Cuprite Coatings (Cu_2O) with a coating thickness between (300 nm-1.6 μm) and nanopores less than 500 nm on the dropwise condensation enhancement was studied. Four cuprite surfaces with different colors (red, orange, mixed red/orange, dark orange) were examined to investigate the DWC performance. From this part of study the following conclusion can be summarized as;

- Thinner coatings with nanoscale pores can further enhance DWC, but still come with additional thermal resistance.

- The red cuprite coating can be oxidized under relatively high temperature vapor at the beginning of tests. Therefore, a further oxidization of cuprite coating by hydrogen peroxide can greatly control the coating thickness and improve the surface stability as well as sustain DWC performance. This process gives the ability to control the coating thickness highly compared with the other method used the alkaline solution to prepare the wick structures of the copper oxide, since it was extremely challenging to control the coating in only five minutes of surface preparation during this method.

- The enhancements in the condensation heat transfer for the not fresh and fresh samples of the cuprite surface with the red color were about 2.28 and 2.8 times, respectively higher than that for the filmwise condensation surface. Moreover, the maximum enhancements in the heat flux for the fresh samples of the cuprite surface with the red, orange, mixed red/orange and dark orange colors as well as

235

the oxidized cuprite surface in the hydrogen peroxide were about 180.41%, 124.65%, 212.04%, 143.58%, and 116.7%, respectively.

- The dropwise condensation heat transfer rate on the cuprite coatings is higher than that on the micro/nanostructured copper oxide and green patina surfaces. This is due to the less thermal resistance related to the substrate, coating thickness as well as to the adhesion forces associated with the interfacial interaction between the droplets condensate and the porous condensation surface, resulting to shedding droplets with a smaller size. Another reason is the high capillary forced achieved on the condensate droplet owing to the narrow nanoscale cavities of the porous structure with the sub-microscale thickness (300 nm-1.6 μm). This capillary action helps the condensate droplet to transform from the immersed state to the suspended state and thereby prevents the droplets from penetrating into the cavities of the porous structures.

In part three of this study, the cuprite surface was removed ultrasonically by acid, acetone, and ethanol, and then washed with distilled water to develop a rough-yellow copper surface with microscale porous structures and microgrooves (1-2 μm). The dropwise condensation performance on the novel superhydrophobic yellow copper surface and the hydrophobic plain copper surface was investigated. Additionally, the two copper surfaces were oxidized in the hydrogen peroxide solution to enhance the chemical stability by increasing the content of oxygen on the surface and to improve the chemical bonding between the low surface energy promoter and the substrate. From the experimental results from this part of study, the following conclusions can also be withdrawn as follow,

236

- Removing the additional thermal resistance of cuprite coating led to enhance the DWC performance with a novel copper surface with microscale porous structures and microgrooves.

- The oxidization of the microscale porous Cu surface with microgrooves can greatly improve the surface stability and sustain DWC performance, compared to the hydrophobic plain-oxidized surface.

- The microporous structures with microgrooves can prevent droplets from sucking into the pores and enhance the droplet departure frequency with smaller droplet departure diameter.

- For the superhydrophobic copper surface with the microporous structures and microgrooves, the improvements in the heat flux and the heat transfer coefficient were about 12.65 % and 13.43 %, respectively compared to the plain hydrophobic surface, whereas the enhancements were about 332.8 % and 339.96 %, respectively compared to the filmwise condensation model. The maximum values of the heat flux and heat transfer coefficient were about 797.05 (KW/m^2) and 76.72 ($KW/m^2.K$), respectively and they had been achieved at a subcooling temperature of 10.6 ℃. The highest enhancement compared to the smooth hydrophobic copper surface is due to the superhydrophobicity effects which led to enhance the droplet removal rate.

- The condensation heat transfer enhancements for the hydrophobic oxidized-plain copper surface and the superhydrophobic oxidized-rough copper surface were about 124.56% (2.24 times) and 235.72% (3.35 times) , respectively compared to the FWC model. The reduction in the condensation performance on the oxidized

237

plain surface is attributed to the high content of oxygen originated on the surface after the oxidation process. Thus, the carbon increased highly on the surface after the SAM treatment, resulting in increasing the conductive thermal resistance and decreasing the nucleation density since for efficient droplet nucleation the hydrophilic surface is required, while the superhydrophobic surface results in decreasing the nucleation density on the condensation surface.

In this part of dissertation, the droplet dynamics analysis method (DA) was also studied in order to confirm the experimental measurements results (Exp.) and to investigate the influence of the droplet departure frequency and the droplet departure diameter on the DWC performance. It was found good agreements between the experimental measurements and the DA methods. Moreover, it was found that the droplet departure frequency increases with decreasing the droplet departure diameter. However, for highly enhancement in the condensation rate, the increase in both the droplet departure frequency and droplet departure diameter is required.

Furthermore, and more interestingly the superhydrophobic yellow surface oxidized by hydrogen peroxide has higher heat transfer enhancement compared to the superhydrophobic oxidized plain copper surface as well as to the cuprite (Cu_2O) coatings. This is due to the lower thickness and the amount of oxygen on the surface which led to a less amount of carbon after the SAM coating, resulting in lower thermal resistance compared to the other coatings. Also, it was found that the oxidized yellow surface has higher departure frequency and droplet departure diameter compared to the oxidized plain copper surface,

238

Additionally, from this research, during the steam condensation, the measured contact angle on the surface is lower than that achieved in the air environment. This is attributed to the change in the droplet dynamic due to the droplet nucleation, growth, and departure during the condensation process compared to that stable one for the droplet with a specific size in the air environment. It was also noticed that even though the oxidized surfaces such as the cuprite, copper oxide, and the green patina surfaces showed the superhydrophobic behavior and droplet jumping phenomena in the air environment, the condensation performance on such surfaces is less than that of the complete dropwise condensation on the hydrophobic plain copper surface. This is attributed to some relevant factors such as the substrate thermal conductivity, the thermal resistance associated with SAM coating and the coating thickness, the thermal resistance of the condensate droplet, the interfacial interaction between the condensate droplet and the condensing surface, as well as the roughness of the condensing surface.

The interfacial interaction between the condensate droplets and the condensing surfaces with different structures such as smooth, porous and micro/nanostructures plays a major factor affecting the dropwise condensation characteristics. The droplet diameter departure on the micro/nanostructured surfaces is larger compared to that on the plain or porous structures. This is because of the high adhesion forces affecting the condensate droplet on micro/nanostructured surfaces. The droplet size increases until reaching the critical size so it can overcome the gravitational and steam drag forces and then shed off the surface. The larger size results in higher thermal resistance of the condensate droplet and thereby decreasing the dropwise condensation heat transfer performance.

239

9.2 Future works

In this work, the condensation heat transfer characteristics and the droplet dynamics analysis, at the saturation condition and in the presence of the non-condensable gases, on hydrophobic and superhydrophobic surfaces coated on horizontal copper tubes have been investigated. The developed coatings include different morphologies such as the smooth copper surface, cuprite surface (Cu_2O) with sub-microscale porous structures, rough copper surface with nanoscale porous structures, and micro/nanostructures of copper oxide (CuO) and green patina ($Cu_4SO_4(OH)_6$ surfaces. a series of studies have been achieved to examine effects of key parameters such as coating thickness, pore size, surface chemistry, and additional thermal resistance from the coatings. The current research focused on enhancing the performance of DWC and the chemical stability on the condenser surfaces. Further studies on these coatings can be carried out in the future. Some of these studies are discussed below.

1. Analyze the droplet jumping phenomena on the oxidized superhydrophobic surfaces.

2. Investigate the durability of the DWC on the developed coatings.

3. Developing the hybrid surface including the hydrophilic and hydrophobic patterns on the presented coatings to investigate the DWC enhancement.

4. Study the droplet dynamics on the condenser surfaces more deeply.

5. Investigate the effect of the developed hydrophobic coating on different heat transfer applications.

6. Investigate the effect of these coatings on enhancing the dropwise condensation (DWC) for the condensation section of the heat pipe.

240

REFERENCES

1. Averyt, K., et al., *Freshwater use by US power plants: Electricity's thirst for a precious resource*. 2011, Union of Concerned Scientists Cambridge, MA.

2. Kenny, J.F., et al., *Estimated use of water in the United States in 2005*. 2009, US Geological Survey.

3. Quality, C.o.E., *"Implementing Instructions: Federal Agency,Implementation of Water Efficiency and, Management Provisions of EO 13514,"*. 2013.

4. Bustamante, J.G., A.S. Rattner, and S. Garimella, *Achieving near-water-cooled power plant performance with air-cooled condensers.* Applied Thermal Engineering, 2016. **105**: p. 362-371.

5. Wang, P., et al., *Sweating-boosted air cooling using nanoscale CuO wick structures.* International Journal of Heat and Mass Transfer, 2017. **111**: p. 817-826.

6. Plawsky, J., et al., *Nano-and microstructures for thin-film evaporation—a review.* Nanoscale and microscale thermophysical engineering, 2014. **18**(3): p. 251-269.

7. Wei-Mon, Y., *Effects of film evaporation on laminar mixed convection heat and mass transfer in a vertical channel.* International journal of heat and mass transfer, 1992. **35**(12): p. 3419-3429.

8. Jang, J.-H., W.-M. Yan, and C.-C. Huang, *Mixed convection heat transfer enhancement through film evaporation in inclined square ducts.* International journal of heat and mass transfer, 2005. **48**(11): p. 2117-2125.

241

9. Saha, S., et al. *Simulation of Sweating/Evaporation Boosted Convective Heat Transfer Under Laminar Flow Condition*. in *ASME 2017 Heat Transfer Summer Conference*. 2017. American Society of Mechanical Engineers.

10. Van, W. and T. Lin, *Combined heat and mass transfer in natural convection between vertical parallel plates with film evaporation.* International Journal of Heat and Mass Transfer, 1990. **33**(3): p. 529-541.

11. Ren, C. and Y. Wan, *A new approach to the analysis of heat and mass transfer characteristics for laminar air flow inside vertical plate channels with falling water film evaporation.* International Journal of Heat and Mass Transfer, 2016. **103**: p. 1017-1028.

12. Fedorov, A., R. Viskanta, and A. Mohamad, *Turbulent heat and mass transfer in an asymmetrically heated, vertical parallel-plate channel.* International Journal of Heat and Fluid Flow, 1997. **18**(3): p. 307-315.

13. Cherif, A., et al., *Intensification of the liquid film evaporation in a vertical channel.* Desalination, 2010. **250**(1): p. 433-437.

14. Reuter, H. and N. Anderson, *Performance evaluation of a bare tube air-cooled heat exchanger bundle in wet and dry mode.* Applied Thermal Engineering, 2016. **105**: p. 1030-1040.

15. Ji, W.-T., et al., *Effect of vapor flow on the falling film evaporation of R134a outside a horizontal tube bundle.* International Journal of Heat and Mass Transfer, 2016. **92**: p. 1171-1181.

16.   Zavaleta-Aguilar, E. and J. Simões-Moreira, *Horizontal tube bundle falling film distiller for ammonia–water mixtures.* International Journal of Refrigeration, 2015. **59**: p. 304-316.

17.   Lecoq, L., D. Flick, and O. Laguerre, *Study of the water evaporation rate on stainless steel plate in controlled conditions.* International Journal of Thermal Sciences, 2017. **111**: p. 450-462.

18.   Terzi, A., et al., *Liquid film evaporation inside an inclined channel: Effect of the presence of a porous layer.* International Journal of Thermal Sciences, 2016. **109**: p. 136-147.

19.   Huang, C.-C., W.-M. Yan, and J.-H. Jang, *Laminar mixed convection heat and mass transfer in vertical rectangular ducts with film evaporation and condensation.* International journal of heat and mass transfer, 2005. **48**(9): p. 1772-1784.

20.   Debbissi, C., J. Orfi, and S.B. Nasrallah, *Evaporation of water by free convection in a vertical channel including effects of wall radiative properties.* International journal of heat and mass transfer, 2001. **44**(4): p. 811-826.

21.   Li, C., et al., *Nanostructured copper interfaces for enhanced boiling.* small, 2008. **4**(8): p. 1084-1088.

22.   Li, C. and G. Peterson, *Evaporation/boiling in thin capillary wicks (II)—effects of volumetric porosity and mesh size.* Journal of Heat Transfer, 2006. **128**(12): p. 1320-1328.

23. Li, C., G. Peterson, and Y. Wang, *Evaporation/boiling in thin capillary wicks (l)—Wick thickness effects.* Journal of Heat Transfer, 2006. **128**(12): p. 1312-1319.

24. Antao, D.S., et al., *Visualization of the Evaporating Liquid-Vapor Interface in Micropillar Arrays.* Journal of Heat Transfer, 2016. **138**(2): p. 020910.

25. Antao, D.S., et al., *Dynamic Evolution of the Evaporating Liquid–Vapor Interface in Micropillar Arrays.* Langmuir, 2016. **32**(2): p. 519-526.

26. Hanlon, M. and H. Ma, *Evaporation heat transfer in sintered porous media.* Transactions-American Society of Mechanical Engineers Journal of Heat Transfer, 2003. **125**(4): p. 644-652.

27. Dai, X., et al., *Capillary evaporation on micromembrane-enhanced microchannel wicks with atomic layer deposited silica.* Applied Physics Letters, 2013. **103**(15): p. 151602.

28. Dai, X., et al., *Micromembrane-enhanced capillary evaporation.* International Journal of Heat and Mass Transfer, 2013. **64**: p. 1101-1108.

29. Takata, Y., et al., *Effect of surface wettability on boiling and evaporation.* Energy, 2005. **30**(2): p. 209-220.

30. Nam, Y. and Y.S. Ju, *A comparative study of the morphology and wetting characteristics of micro/nanostructured Cu surfaces for phase change heat transfer applications.* Journal of Adhesion Science and Technology, 2013. **27**(20): p. 2163-2176.

31. Wang, P., et al. *Sweating-Boosted Air Cooling With Water Dripping*. in *ASME 2016 Heat Transfer Summer Conference collocated with the ASME 2016 Fluids*

244

Engineering Division Summer Meeting and the ASME 2016 14th International Conference on Nanochannels, Microchannels, and Minichannels. 2016. American Society of Mechanical Engineers.

32.   Zhang, L., N. Zhao, and J. Xu, *Fabrication and application of superhydrophilic surfaces: a review.* Journal of Adhesion Science and Technology, 2014. **28**(8-9): p. 769-790.

33.   Park, J.-J., et al., *Thermally induced superhydrophilicity in TiO2 films prepared by supersonic aerosol deposition.* ACS applied materials & interfaces, 2013. **5**(13): p. 6155-6160.

34.   Wong, W.S., et al., *Hierarchical amorphous nanofibers for transparent inherently super-hydrophilic coatings.* Journal of Materials Chemistry A, 2014. **2**(37): p. 15575-15581.

35.   Liu, Z. and Y. Qiu, *Critical heat flux of steady boiling for water jet impingement in flat stagnation zone on superhydrophilic surface.* Journal of heat transfer, 2006. **128**(7): p. 726-729.

36.   Takata, Y., et al., *Pool boiling on a superhydrophilic surface.* International Journal of Energy Research, 2003. **27**(2): p. 111-119.

37.   Liang, S., et al., *Highly hydrophilic polyvinylidene fluoride (PVDF) ultrafiltration membranes via postfabrication grafting of surface-tailored silica nanoparticles.* ACS applied materials & interfaces, 2013. **5**(14): p. 6694-6703.

38.   Tiraferri, A., et al., *Superhydrophilic thin-film composite forward osmosis membranes for organic fouling control: fouling behavior and antifouling*

mechanisms. Environmental science & technology, 2012. **46**(20): p. 11135-11144.

39.   Galopin, E., et al., *Selective adhesion of bacillus cereus spores on heterogeneously wetted silicon nanowires.* Langmuir, 2009. **26**(5): p. 3479-3484.

40.   Piret, G., et al., *Biomolecule and nanoparticle transfer on patterned and heterogeneously wetted superhydrophobic silicon nanowire surfaces.* Langmuir, 2008. **24**(5): p. 1670-1672.

41.   Byon, C., et al., *Drag reduction in Stokes flows over spheres with nanostructured superhydrophilic surfaces*. 2010, AIP.

42.   Wang, R., et al., *Light-induced amphiphilic surfaces.* Nature, 1997. **388**(6641): p. 431.

43.   A. Fujishima, K.H., T. Watanabe, *TiO2 Photocatalysis—Fundamentals and Applications. BKC, Inc;.* 1999.

44.   Fujishima, A., X. Zhang, and D.A. Tryk, *TiO 2 photocatalysis and related surface phenomena.* Surface Science Reports, 2008. **63**(12): p. 515-582.

45.   Srisitthiratkul, C., W. Yaipimai, and V. Intasanta, *Environmental remediation and superhydrophilicity of ultrafine antibacterial tungsten oxide-based nanofibers under visible light source.* Applied Surface Science, 2012. **259**: p. 349-355.

46.   Sun, R.-D., et al., *Photoinduced surface wettability conversion of ZnO and TiO2 thin films.* The Journal of Physical Chemistry B, 2001. **105**(10): p. 1984-1990.

47.   Houmard, M., et al., *Enhanced cleanability of super-hydrophilic TiO 2–SiO 2 composite surfaces prepared via a sol–gel route.* Surface Science, 2011. **605**(3): p. 456-462.

48. Liu, X., X. Du, and J. He, *Hierarchically Structured Porous Films of Silica Hollow Spheres via Layer‐by‐Layer Assembly and Their Superhydrophilic and Antifogging Properties.* ChemPhysChem, 2008. **9**(2): p. 305-309.

49. Jeong, Y.-M., et al., *Preparation of super-hydrophilic amorphous titanium dioxide thin film via PECVD process and its application to dehumidifying heat exchangers.* Journal of Industrial and Engineering Chemistry, 2009. **15**(2): p. 202-206.

50. Wang, L., et al., *Ultra-fast spreading on superhydrophilic fibrous mesh with nanochannels.* Applied Surface Science, 2009. **255**(9): p. 4944-4949.

51. Zhu, Y., et al., *Preparation of superhydrophilic α-Fe 2 O 3 nanofibers with tunable magnetic properties.* Thin Solid Films, 2006. **510**(1): p. 271-274.

52. Zang, J., et al., *Template-free electrochemical synthesis of superhydrophilic polypyrrole nanofiber network.* Macromolecules, 2008. **41**(19): p. 7053-7057.

53. Tang, K., et al., *Fabrication of superhydrophilic Cu 2 O and CuO membranes.* Journal of membrane science, 2006. **286**(1): p. 279-284.

54. Wang, D., et al., *Electrochemical characterization of the solution accessibility of CaTiO3 microstructures and improved biomineralization.* The Journal of Physical Chemistry C, 2008. **112**(41): p. 16123-16129.

55. Zhang, F., et al., *Nanowire‐Haired Inorganic Membranes with Superhydrophilicity and Underwater Ultralow Adhesive Superoleophobicity for High‐Efficiency Oil/Water Separation.* Advanced Materials, 2013. **25**(30): p. 4192-4198.

56. Song, X., H. Yu, and S. Sun, *Single-crystalline CuO nanobelts fabricated by a convenient route.* Journal of colloid and interface science, 2005. **289**(2): p. 588-591.

57. Liu, J., et al., *Hierarchical nanostructures of cupric oxide on a copper substrate: controllable morphology and wettability.* Journal of Materials Chemistry, 2006. **16**(45): p. 4427-4434.

58. Love, B. and P. Packman, *Effects of surface modifications on the peel strength of copper based polymer/metal interfaces with characteristic morphologies.* The Journal of Adhesion, 1993. **40**(2-4): p. 139-150.

59. Yun, H., et al., *Adhesion improvement of copper/epoxy joints.* Journal of materials science, 1992. **27**(21): p. 5811-5817.

60. Wen, X., et al., *Copper-based nanowire materials: templated syntheses, characterizations, and applications.* Langmuir, 2005. **21**(10): p. 4729-4737.

61. Wen, X., W. Zhang, and S. Yang, *Synthesis of Cu (OH) 2 and CuO nanoribbon arrays on a copper surface.* Langmuir, 2003. **19**(14): p. 5898-5903.

62. Livingston, R.A., *Influence of the environment on the patina of the Statue of Liberty.* Environmental science & technology, 1991. **25**(8): p. 1400-1408.

63. Fitzgerald, K., J. Nairn, and A. Atrens, *The chemistry of copper patination.* Corrosion science, 1998. **40**(12): p. 2029-2050.

64. Schweitzer, P.A., *Corrosion and corrosion protection handbook.* Vol. 1. 1989: CRC Press.

65. Atrens, A., *Research directions in magnesium corrosion arising from the wolfsburg conference.* Advanced Engineering Materials, 2004. **6**(1-2): p. 83-84.

66. Graedel, T., *Copper patinas formed in the atmosphere—II. A qualitative assessment of mechanisms.* Corrosion Science, 1987. **27**(7): p. 721-740.

67. Graedel, T., *Copper patinas formed in the atmosphere—III. A semi-quantitative assessment of rates and constraints in the greater New York metropolitan area.* Corrosion Science, 1987. **27**(7): p. 741-769.

68. Song, G. and A. Atrens, *Recent insights into the mechanism of magnesium corrosion and research suggestions.* Advanced Engineering Materials, 2007. **9**(3): p. 177-183.

69. Bastidas, J., et al., *Characterization of artificially patinated layers on artistic bronze exposed to laboratory SO2 contamination.* Journal of materials science, 1997. **32**(1): p. 129-133.

70. Coburn, S.K. *Atmospheric factors affecting the corrosion of engineering metals*. 1978. American Society for Testing and Materials.

71. Graedel, T., K. Nassau, and J. Franey, *Copper patinas formed in the atmosphere—I. Introduction.* Corrosion Science, 1987. **27**(7): p. 639-657.

72. Nassau, K., A. Miller, and T. Graedel, *The reaction of simulated rain with copper, copper patina, and some copper compounds.* Corrosion science, 1987. **27**(7): p. 703-719.

73. Rosales, B.M., R.M. Vera, and J.P. Hidalgo, *Characterisation and properties of synthetic patina on copper base sculptural alloys.* Corrosion Science, 2010. **52**(10): p. 3212-3224.

74. Selwyn, L.S., et al., *Outdoor bronze statues: analysis of metal and surface samples.* Studies in conservation, 1996. **41**(4): p. 205-228.

75. Squarcialupi, M.C., et al., *Characterisation by XPS of the corrosion patina formed on bronze surfaces.* Journal of Cultural Heritage, 2002. **3**(3): p. 199-204.

76. Cho, H., et al., *Durable superhydrophilic/phobic surfaces based on green patina with corrosion resistance.* Physical Chemistry Chemical Physics, 2015. **17**(10): p. 6786-6793.

77. S. R. Yoon, P.t., University of Utah, 1971, vol. 8

78. FitzGerald, K., et al., *Atmospheric corrosion of copper and the colour, structure and composition of natural patinas on copper.* Corrosion Science, 2006. **48**(9): p. 2480-2509.

79. Hayez, V., et al., *Micro Raman spectroscopy used for the study of corrosion products on copper alloys: study of the chemical composition of artificial patinas used for restoration purposes.* Analyst, 2005. **130**(4): p. 550-556.

80. Wenzel, R.N., *Resistance of solid surfaces to wetting by water.* Industrial & Engineering Chemistry, 1936. **28**(8): p. 988-994.

81. Cassie, A. and S. Baxter, *Wettability of porous surfaces.* Transactions of the Faraday society, 1944. **40**: p. 546-551.

82. Florence, A.T. and D. Attwood, *Physicochemical principles of pharmacy: In manufacture, formulation and clinical use*. 2015: pharmaceutical press.

83. Moffat, R.J., *Describing the uncertainties in experimental results.* Experimental Thermal and Fluid Science, 1988. **1**(1): p. 3-17.

84. Ameel, T.A., *Average effects of forced convection over a flat plate with an unheated starting length.* International Communications in Heat and Mass Transfer, 1997. **24**(8): p. 1113-1120.

85. Hsieh, C.-C. and S.-C. Yao, *Evaporative heat transfer characteristics of a water spray on micro-structured silicon surfaces.* International Journal of Heat and Mass Transfer, 2006. **49**(5–6): p. 962-974.

86. Raimundo, A.M., et al., *Wind tunnel measurements and numerical simulations of water evaporation in forced convection airflow.* International Journal of Thermal Sciences, 2014. **86**: p. 28-40.

87. Bhushan, B., *Biomimetics: lessons from nature–an overview*. 2009, The Royal Society.

88. Cheng, Y.-T. and D.E. Rodak, *Is the lotus leaf superhydrophobic?* Applied physics letters, 2005. **86**(14): p. 144101.

89. Parker, A.R. and C.R. Lawrence, *Water capture by a desert beetle.* Nature, 2001. **414**(6859): p. 33.

90. Zheng, Y., et al., *Directional water collection on wetted spider silk.* Nature, 2010. **463**(7281): p. 640.

91. Attinger, D., et al., *Surface engineering for phase change heat transfer: A review.* MRS Energy & Sustainability, 2014. **1**: p. E4.

92. Beér, J.M., *High efficiency electric power generation: The environmental role.* Progress in Energy and Combustion Science, 2007. **33**(2): p. 107-134.

93. Dehbi, A. and S. Guentay, *A model for the performance of a vertical tube condenser in the presence of noncondensable gases.* Nuclear Engineering and Design, 1997. **177**(1): p. 41-52.

94. Glicksman, L.R. and A.W. Hunt, *Numerical simulation of dropwise condensation.* International Journal of Heat and Mass Transfer, 1972. **15**(11): p. 2251-2269.

95. Liu, B.-T., K.-H. Chien, and C.-C. Wang, *Effect of working fluids on organic Rankine cycle for waste heat recovery.* Energy, 2004. **29**(8): p. 1207-1217.

96. Seo, D., C. Lee, and Y. Nam, *Influence of geometric patterns of microstructured superhydrophobic surfaces on water-harvesting performance via dewing.* Langmuir, 2014. **30**(51): p. 15468-15476.

97. Thomas, D.H., *Energy Efficiency through Combined Heat and Power or Cogeneration.* 2010: Nova Science Publishers.

98. Bian, J., et al., *Thermal vapor condensation of uniform graphitic carbon nitride films with remarkable photocurrent density for photoelectrochemical applications.* Nano Energy, 2015. **15**: p. 353-361.

99. Boreyko, J.B. and C.-H. Chen, *Vapor chambers with jumping-drop liquid return from superhydrophobic condensers.* International Journal of Heat and Mass Transfer, 2013. **61**: p. 409-418.

100. Chen, X., et al., *Nanograssed micropyramidal architectures for continuous dropwise condensation.* Advanced functional materials, 2011. **21**(24): p. 4617-4623.

101. Daniel, S., M.K. Chaudhury, and J.C. Chen, *Fast drop movements resulting from the phase change on a gradient surface.* Science, 2001. **291**(5504): p. 633-636.

102. Kim, M.-H. and C.W. Bullard, *Air-side performance of brazed aluminum heat exchangers under dehumidifying conditions.* International Journal of refrigeration, 2002. **25**(7): p. 924-934.

103.   Leach, R., et al., *Dropwise condensation: experiments and simulations of nucleation and growth of water drops in a cooling system.* Langmuir, 2006. **22**(21): p. 8864-8872.

104.   Miljkovic, N. and E.N. Wang, *Modeling and optimization of hybrid solar thermoelectric systems with thermosyphons.* Solar Energy, 2011. **85**(11): p. 2843-2855.

105.   Peters, T.B., et al., *Design of an integrated loop heat pipe air-cooled heat exchanger for high performance electronics.* IEEE Transactions on Components, Packaging and Manufacturing Technology, 2012. **2**(10): p. 1637-1648.

106.   Peterson, G.P., *An introduction to heat pipes: modeling, testing, and applications.* 1994.

107.   Rykaczewski, K., et al., *Three dimensional aspects of droplet coalescence during dropwise condensation on superhydrophobic surfaces.* Soft Matter, 2011. **7**(19): p. 8749-8752.

108.   Xiao, R., et al., *Immersion condensation on oil-infused heterogeneous surfaces for enhanced heat transfer.* Scientific reports, 2013. **3**: p. 1988.

109.   Humplik, T., et al., *Nanostructured materials for water desalination.* Nanotechnology, 2011. **22**(29): p. 292001.

110.   Khawaji, A.D., I.K. Kutubkhanah, and J.-M. Wie, *Advances in seawater desalination technologies.* Desalination, 2008. **221**(1-3): p. 47-69.

111.   Thickett, S.C., C. Neto, and A.T. Harris, *Biomimetic surface coatings for atmospheric water capture prepared by dewetting of polymer films.* Advanced Materials, 2011. **23**(32): p. 3718-3722.

112. Andrews, H., et al., *Three-dimensional hierarchical structures for fog harvesting.* Langmuir, 2011. **27**(7): p. 3798-3802.

113. Love, J.C., et al., *Self-assembled monolayers of thiolates on metals as a form of nanotechnology.* Chemical reviews, 2005. **105**(4): p. 1103-1170.

114. Milani, D., et al., *Evaluation of using thermoelectric coolers in a dehumidification system to generate freshwater from ambient air.* Chemical Engineering Science, 2011. **66**(12): p. 2491-2501.

115. Miljkovic, N., et al., *Jumping-droplet electrostatic energy harvesting.* Applied Physics Letters, 2014. **105**(1): p. 013111.

116. Wahlgren, R.V., *Atmospheric water vapour processor designs for potable water production: a review.* Water Research, 2001. **35**(1): p. 1-22.

117. Hong, K. and R. Webb, *Performance of dehumidifying heat exchangers with and without wetting coatings.* Journal of Heat Transfer, 1999. **121**(4): p. 1018-1026.

118. Li, B. and R. Yao, *Urbanisation and its impact on building energy consumption and efficiency in China.* Renewable Energy, 2009. **34**(9): p. 1994-1998.

119. Pérez-Lombard, L., J. Ortiz, and C. Pout, *A review on buildings energy consumption information.* Energy and buildings, 2008. **40**(3): p. 394-398.

120. Yau, Y.H., *Experimental thermal performance study of an inclined heat pipe heat exchanger operating in high humid tropical HVAC systems.* International journal of refrigeration, 2007. **30**(7): p. 1143-1152.

121. Ghosh, A., et al., *Enhancing dropwise condensation through bioinspired wettability patterning.* Langmuir, 2014. **30**(43): p. 13103-13115.

122. Ji, X., et al., *A vapor chamber using extended condenser concept for ultra-high heat flux and large heater area.* International Journal of Heat and Mass Transfer, 2012. **55**(17-18): p. 4908-4913.

123. Lee, J., S. Mahendra, and P.J. Alvarez, *Nanomaterials in the construction industry: a review of their applications and environmental health and safety considerations.* ACS nano, 2010. **4**(7): p. 3580-3590.

124. Lara, J.R. and M.T. Holtzapple, *Experimental investigation of dropwise condensation on hydrophobic heat exchangers part I: Dimpled-sheets.* Desalination, 2011. **278**(1-3): p. 165-172.

125. Anand, S., et al., *Enhanced condensation on lubricant-impregnated nanotextured surfaces.* ACS nano, 2012. **6**(11): p. 10122-10129.

126. Enright, R., et al., *Condensation on superhydrophobic surfaces: the role of local energy barriers and structure length scale.* Langmuir, 2012. **28**(40): p. 14424-14432.

127. Preston, D.J., et al., *Scalable graphene coatings for enhanced condensation heat transfer.* Nano letters, 2015. **15**(5): p. 2902-2909.

128. Wen, R., et al., *Droplet departure characteristics and dropwise condensation heat transfer at low steam pressure.* Journal of Heat Transfer, 2016. **138**(7): p. 071501.

129. *Human Development Report 2006, United Nations Development Program Publications, New York, NY, USA 2006.*

130. Stone, A., et al., *ENHANCED STEAM CONDENSATION AS AResult OF HEAT TRANSFER ADDITIVES.* International Journal of Environmentally Conscious Design & Manufacturing, 2001. **10**(4).

131. Rose, J., *Dropwise condensation theory and experiment: a review.* Proceedings of the Institution of Mechanical Engineers, Part A: Journal of Power and Energy, 2002. **216**(2): p. 115-128.

132. Schmidt, E., W. Schurig, and W. Sellschopp, *Versuche über die Kondensation von Wasserdampf in Film-und Tropfenform.* Technische Mechanik und Thermodynamik, 1930. **1**(2): p. 53-63.

133. Beysens, D., *Dew nucleation and growth.* Comptes Rendus Physique, 2006. **7**(9-10): p. 1082-1100.

134. Beysens, D., et al., *How does dew form?* Phase Transitions: A Multinational Journal, 1991. **31**(1-4): p. 219-246.

135. Fritter, D., C.M. Knobler, and D.A. Beysens, *Experiments and simulation of the growth of droplets on a surface (breath figures).* Physical Review A, 1991. **43**(6): p. 2858.

136. Dou, N.N.G., *Condensation on superhydrophobic copper oxide nanostructures.* 2012, Massachusetts Institute of Technology.

137. Rohsenow, J., *Hartnett and EN Ganic.* Handbook of Heat Transfer Application, 1985.

138. Dimitrakopoulos, P. and J. Higdon, *On the gravitational displacement of three-dimensional fluid droplets from inclined solid surfaces.* Journal of Fluid Mechanics, 1999. **395**: p. 181-209.

139. Kim, H.-Y., H.J. Lee, and B.H. Kang, *Sliding of liquid drops down an inclined solid surface.* Journal of Colloid and Interface Science, 2002. **247**(2): p. 372-380.

140. Boreyko, J.B. and C.-H. Chen, *Self-propelled dropwise condensate on superhydrophobic surfaces.* Physical review letters, 2009. **103**(18): p. 184501.

141. Vemuri, S. and K. Kim, *An experimental and theoretical study on the concept of dropwise condensation.* International Journal of Heat and Mass Transfer, 2006. **49**(3-4): p. 649-657.

142. Rose, J., *Proc. Inst. Mech. Eng. Part A-J.* Power Energy, 2002. **216**: p. 115.

143. Wen, R., et al., *Hydrophobic copper nanowires for enhancing condensation heat transfer.* Nano Energy, 2017. **33**: p. 177-183.

144. Chen, J.C., *Surface contact—its significance for multiphase heat transfer: diverse examples.* Journal of heat transfer, 2003. **125**(4): p. 549-566.

145. Kandlikar, S.G., *Handbook of phase change: boiling and condensation.* 1999: CRC Press.

146. Tanasawa, I., J. Ochiai, and Y. Funawatashi. *Experimental study on dropwise condensation-effect of maximum drop size upon the heat transfer coefficient.* in *Proceedings of the 6th International Heat Transfer Conference.* 1978.

147. Tanasawa, I., et al., *'Experimental Study on Dropwise Condensation Effect of Departing Drop Size on Heat-transfer Coefficients.* Trans. JSME, 1976. **42**: p. 2846-2852.

148. Young, T., *An assay on the cohesion of fluids. Philos.* 1805, TR Soc., 95: 65–87.

149. Miljkovic, N. and E.N. Wang, *Condensation heat transfer on superhydrophobic surfaces.* MRS bulletin, 2013. **38**(5): p. 397-406.

150. Dorrer, C. and J. Rühe, *Some thoughts on superhydrophobic wetting.* Soft Matter, 2009. **5**(1): p. 51-61.

257

151. Gao, L., A.Y. Fadeev, and T.J. McCarthy, *Superhydrophobicity and contact-line issues.* MRS bulletin, 2008. **33**(8): p. 747-751.

152. Quéré, D., *Wetting and roughness.* Annu. Rev. Mater. Res., 2008. **38**: p. 71-99.

153. Roach, P., N.J. Shirtcliffe, and M.I. Newton, *Progess in superhydrophobic surface development.* Soft matter, 2008. **4**(2): p. 224-240.

154. Miljkovic, N., et al., *Jumping-droplet-enhanced condensation on scalable superhydrophobic nanostructured surfaces.* Nano letters, 2012. **13**(1): p. 179-187.

155. Miljkovic, N., R. Enright, and E.N. Wang, *Effect of droplet morphology on growth dynamics and heat transfer during condensation on superhydrophobic nanostructured surfaces.* ACS nano, 2012. **6**(2): p. 1776-1785.

156. Sikarwar, B.S., et al., *Dropwise condensation studies on multiple scales.* Heat Transfer Engineering, 2012. **33**(4-5): p. 301-341.

157. Ma, X., et al., *Advances in dropwise condensation heat transfer: Chinese research.* Chemical Engineering Journal, 2000. **78**(2-3): p. 87-93.

158. Tanasawa, I., *Advances in condensation heat transfer.* Advances in heat transfer, 1991. **21**: p. 55-139.

159. Haraguchi, T., et al., *The effect of polyvinylidene chloride coating thickness on promotion of dropwise steam condensation.* International journal of heat and mass transfer, 1991. **34**(12): p. 3047-3054.

160. Holden, K., et al., *The use of organic coatings to promote dropwise condensation of steam.* Journal of heat transfer, 1987. **109**(3): p. 768-774.

161. Ma, X., et al., *Influence of processing conditions of polymer film on dropwise condensation heat transfer.* International Journal of Heat and Mass Transfer, 2002. **45**(16): p. 3405-3411.

162. Paxson, A.T., et al., *Stable dropwise condensation for enhancing heat transfer via the initiated chemical vapor deposition (iCVD) of grafted polymer films.* Advanced Materials, 2014. **26**(3): p. 418-423.

163. Qi, Z., Z. Dongchang, and L. Jifang, *Surface materials with dropwise condensation made by ion implantation technology.* International journal of heat and mass transfer, 1991. **34**(11): p. 2833-2835.

164. Zhao, Q. and B. Burnside, *Dropwise condensation of steam on ion implanted condenser surfaces.* Heat Recovery Systems and CHP, 1994. **14**(5): p. 525-534.

165. Enright, R., et al., *Dropwise condensation on micro-and nanostructured surfaces.* Nanoscale and Microscale Thermophysical Engineering, 2014. **18**(3): p. 223-250.

166. Das, A., et al., *The use of an organic self-assembled monolayer coating to promote dropwise condensation of steam on horizontal tubes.* Journal of heat transfer, 2000. **122**(2): p. 278-286.

167. Vemuri, S., et al., *Long term testing for dropwise condensation using self-assembled monolayer coatings of n-octadecyl mercaptan.* Applied thermal engineering, 2006. **26**(4): p. 421-429.

168. Nenad, M., et al., *Condensation on Hydrophilic, Hydrophobic, Nanostructured Superhydrophobic and Oil-Infused Surfaces.* 2013.

169. Blackman, L. and M. Dewar, *27. Promoters for the dropwise condensation of steam. Part I. Preparation of compounds containing monofunctional sulphur groups.* Journal of the Chemical Society (Resumed), 1957: p. 162-165.

170. Blackman, L., M. Dewar, and H. Hampson, *An investigation of compounds promoting the dropwise condensation of steam.* Journal of Applied Chemistry, 1957. **7**(4): p. 160-171.

171. Depew, C.A. and R.L. Reisbig, *Vapor condensation on a horizontal tube using teflon to promote dropwise condensation.* Industrial & Engineering Chemistry Process Design and Development, 1964. **3**(4): p. 365-369.

172. Marto, P., et al., *Evaluation of organic coatings for the promotion of dropwise condensation of steam.* International journal of heat and mass transfer, 1986. **29**(8): p. 1109-1117.

173. Stylianou, S. and J. Rose, *Dropwise condensation on surfaces having different thermal conductivities.* Journal of Heat Transfer, 1980. **102**(3): p. 477-482.

174. Lara, J.R. and M.T. Holtzapple, *Experimental investigation of dropwise condensation on hydrophobic heat exchangers. Part II: Effect of coatings and surface geometry.* Desalination, 2011. **280**(1-3): p. 363-369.

175. Yoshida, N., et al., *Sliding behavior of water droplets on flat polymer surface.* Journal of the American Chemical Society, 2006. **128**(3): p. 743-747.

176. Yang, Q. and A. Gu, *Dropwise condensation on SAM and electroless composite coating surfaces.* Journal of chemical engineering of Japan, 2006. **39**(8): p. 826-830.

177. Tanasawa, I. *Dropwise condensation: the way to practical applications.* in *Proceedings of Sixth International Heat Transfer Conference.* 1978.

178. Wilkins, D.G., L.A. Bromley, and S.M. Read, *Dropwise and filmwise condensation of water vapor on gold.* AIChE Journal, 1973. **19**(1): p. 119-123.

179. Schrader, M.E., *Ultrahigh-vacuum techniques in the measurement of contact angles. II. Water on gold.* The journal of physical chemistry, 1970. **74**(11): p. 2313-2317.

180. Bernett, M.K. and W.A. Zisman, *Confirmation of spontaneous spreading by water on pure gold.* The Journal of Physical Chemistry, 1970. **74**(11): p. 2309-2312.

181. Thelen, R.E.a.E., *Dropwisc condensation, Proc.First Internutionul Symposium on Wuter Desalination,pp. 18 -24, Washington. DC (1965).*

182. Woodruff, D.W. and J. Westwater, *Steam condensation on electroplated gold: Effect of plating thickness.* International Journal of Heat and Mass Transfer, 1979. **22**(4): p. 629-632.

183. O'neill, G.A. and J. Westwater, *Dropwise condensation of steam on electroplated silver surfaces.* International journal of heat and mass transfer, 1984. **27**(9): p. 1539-1549.

184. Finnicum, S.S. and J. Westwater, *Dropwise vs filmwise condensation of steam on chromium.* International journal of heat and mass transfer, 1989. **32**(8): p. 1541-1549.

185. Raj, R., S.C. Maroo, and E.N. Wang, *Wettability of graphene.* Nano letters, 2013. **13**(4): p. 1509-1515.

261

186. Zhao, Q., et al. *Industrial application of dropwise condensation*. in *Proc. 9th Intern. Heat Transfer Conf.* 1990.

187. Kananeh, A.B., et al., *Experimental study of dropwise condensation on plasma-ion implanted stainless steel tubes.* International Journal of Heat and Mass Transfer, 2006. **49**(25-26): p. 5018-5026.

188. Rausch, M., A. Fröba, and A. Leipertz, *Dropwise condensation heat transfer on ion implanted aluminum surfaces.* International Journal of heat and Mass transfer, 2008. **51**(5-6): p. 1061-1070.

189. Rausch, M., A. Leipertz, and A. Fröba, *Dropwise condensation of steam on ion implanted titanium surfaces.* International Journal of Heat and Mass Transfer, 2010. **53**(1-3): p. 423-430.

190. Lv, C., et al., *Departure of condensation droplets on superhydrophobic surfaces.* Langmuir, 2015. **31**(8): p. 2414-2420.

191. Lv, C., et al., *Condensation and jumping relay of droplets on lotus leaf.* Applied Physics Letters, 2013. **103**(2): p. 021601.

192. Rykaczewski, K., et al., *How nanorough is rough enough to make a surface superhydrophobic during water condensation?* Soft Matter, 2012. **8**(33): p. 8786-8794.

193. Carey, V.P., *Liquid vapor phase change phenomena: an introduction to the thermophysics of vaporization and condensation processes in heat transfer equipment*. 2018: CRC Press.

194. Varanasi, K.K., et al., *Spatial control in the heterogeneous nucleation of water.* Applied Physics Letters, 2009. **95**(9): p. 094101.

195. Kim, S. and K.J. Kim, *Dropwise condensation modeling suitable for superhydrophobic surfaces.* Journal of heat transfer, 2011. **133**(8): p. 081502.

196. Moulinet, S. and D. Bartolo, *Life and death of a fakir droplet: Impalement transitions on superhydrophobic surfaces.* The European Physical Journal E, 2007. **24**(3): p. 251-260.

197. Patankar, N.A., *Transition between superhydrophobic states on rough surfaces.* Langmuir, 2004. **20**(17): p. 7097-7102.

198. Cheng, J., A. Vandadi, and C.-L. Chen, *Condensation heat transfer on two-tier superhydrophobic surfaces.* Applied Physics Letters, 2012. **101**(13): p. 131909.

199. Hou, Y., et al., *Recurrent filmwise and dropwise condensation on a beetle mimetic surface.* ACS nano, 2014. **9**(1): p. 71-81.

200. Narhe, R. and D. Beysens, *Nucleation and growth on a superhydrophobic grooved surface.* Physical review letters, 2004. **93**(7): p. 076103.

201. Wier, K.A. and T.J. McCarthy, *Condensation on ultrahydrophobic surfaces and its effect on droplet mobility: ultrahydrophobic surfaces are not always water repellant.* Langmuir, 2006. **22**(6): p. 2433-2436.

202. Lo, C.-W., C.-C. Wang, and M.-C. Lu, *Scale effect on dropwise condensation on superhydrophobic surfaces.* ACS applied materials & interfaces, 2014. **6**(16): p. 14353-14359.

203. Huang, D.-J. and T.-S. Leu, *Condensation heat transfer enhancement by surface modification on a monolithic copper heat sink.* Applied Thermal Engineering, 2015. **75**: p. 908-917.

204. Kim, H. and Y. Nam. *Condensation heat transfer performance of nano-engineered Cu surfaces*. in *Journal of Physics: Conference Series*. 2014. IOP Publishing.

205. Zhao, Y., et al., *Copper-based ultrathin nickel nanocone films with high-efficiency dropwise condensation heat transfer performance.* ACS applied materials & interfaces, 2015. **7**(22): p. 11719-11723.

206. Lee, Y.A., et al., *Condensation heat transfer enhancement on surfaces with interlaced wettability.* Journal of Advanced Thermal Science Research, 2015. **2**: p. 27-32.

207. Zhong, L., et al., *Effects of surface free energy and nanostructures on dropwise condensation.* Chemical engineering journal, 2010. **156**(3): p. 546-552.

208. Parin, R., et al., *Nano-structured aluminum surfaces for dropwise condensation.* Surface and Coatings Technology, 2018. **348**: p. 1-12.

209. Lu, M.-C., et al., *Superhydrophobic Si nanowires for enhanced condensation heat transfer.* International Journal of Heat and Mass Transfer, 2017. **111**: p. 614-623.

210. Hoenig, S.H. and R.W. Bonner, *Dropwise Condensation on Superhydrophobic Microporous Wick Structures.* Journal of Heat Transfer, 2018. **140**(7): p. 071501.

211. Dietz, C., et al., *Visualization of droplet departure on a superhydrophobic surface and implications to heat transfer enhancement during dropwise condensation.* Applied physics letters, 2010. **97**(3): p. 033104.

212. Feng, J., Z. Qin, and S. Yao, *Factors affecting the spontaneous motion of condensate drops on superhydrophobic copper surfaces.* Langmuir, 2012. **28**(14): p. 6067-6075.

213. Narhe, R. and D. Beysens, *Growth dynamics of water drops on a square-pattern rough hydrophobic surface.* Langmuir, 2007. **23**(12): p. 6486-6489.

214. Chen, X., et al., *Activating the microscale edge effect in a hierarchical surface for frosting suppression and defrosting promotion.* Scientific reports, 2013. **3**: p. 2515.

215. He, M., et al., *Hierarchically structured porous aluminum surfaces for high-efficient removal of condensed water.* Soft Matter, 2012. **8**(25): p. 6680-6683.

216. Liu, T., et al., *Thermodynamic analysis of the effect of the hierarchical architecture of a superhydrophobic surface on a condensed drop state.* Langmuir, 2010. **26**(18): p. 14835-14841.

217. Rykaczewski, K., et al., *Multimode multidrop serial coalescence effects during condensation on hierarchical superhydrophobic surfaces.* Langmuir, 2013. **29**(3): p. 881-891.

218. Chen, C.-H., et al., *Dropwise condensation on superhydrophobic surfaces with two-tier roughness.* Applied Physics Letters, 2007. **90**(17): p. 173108.

219. Chen, X., J.A. Weibel, and S.V. Garimella, *Exploiting microscale roughness on hierarchical superhydrophobic copper surfaces for enhanced dropwise condensation.* Advanced Materials Interfaces, 2015. **2**(3): p. 1400480.

220. Rykaczewski, K., *Microdroplet growth mechanism during water condensation on superhydrophobic surfaces.* Langmuir, 2012. **28**(20): p. 7720-7729.

221. Kashchiev, D., *Nucleation: basic theory with applications. 2000.* Butterworth Heinemann: Boston.

222. Patankar, N.A., *Supernucleating surfaces for nucleate boiling and dropwise condensation heat transfer.* Soft Matter, 2010. **6**(8): p. 1613-1620.

223. Graham, C. and P. Griffith, *Drop size distributions and heat transfer in dropwise condensation.* International Journal of Heat and Mass Transfer, 1973. **16**(2): p. 337-346.

224. Kumagai, S., et al., *On the enhancement of filmwise condensation heat transfer by means of the coexistence with dropwise condensation sections.* EXPERIMENTAL HEAT TRANSFER An International Journal, 1991. **4**(1): p. 71-82.

225. Mahapatra, P.S., et al., *Key design and operating parameters for enhancing dropwise condensation through wettability patterning.* International Journal of Heat and Mass Transfer, 2016. **92**: p. 877-883.

226. Leu, T.-S., H.-W. Lin, and T.-H. Wu. *Enhancement of phase change heat transfer by using surface energy patterning techniques*. in *Nano/Micro Engineered and Molecular Systems, 2006. NEMS'06. 1st IEEE International Conference on*. 2006. IEEE.

227. Lee, Y.-A., et al., *Orientation effects of nanoparticle-modified surfaces with interlaced wettability on condensation heat transfer.* Applied Thermal Engineering, 2016. **98**: p. 1054-1060.

228. Peng, B., et al., *Analysis of condensation heat transfer enhancement with dropwise-filmwise hybrid surface: Droplet sizes effect.* International Journal of Heat and Mass Transfer, 2014. **77**: p. 785-794.

229. Peng, B., et al., *Experimental investigation on steam condensation heat transfer enhancement with vertically patterned hydrophobic–hydrophilic hybrid surfaces.* International Journal of Heat and Mass Transfer, 2015. **83**: p. 27-38.

230. Alwazzan, M., et al., *Condensation on hybrid-patterned copper tubes (I): Characterization of condensation heat transfer.* International Journal of Heat and Mass Transfer, 2017. **112**: p. 991-1004.

231. Egab, K.K., *A Comprehensive Evaluation of Hybrid Wetting Configurations on Dropwise Condensation.* 2017.

232. Lafuma, A. and D. Quéré, *Slippery pre-suffused surfaces.* EPL (Europhysics Letters), 2011. **96**(5): p. 56001.

233. Wong, T.-S., et al., *Bioinspired self-repairing slippery surfaces with pressure-stable omniphobicity.* Nature, 2011. **477**(7365): p. 443.

234. Epstein, A.K., et al., *Liquid-infused structured surfaces with exceptional anti-biofouling performance.* Proceedings of the National Academy of Sciences, 2012. **109**(33): p. 13182-13187.

235. Mishchenko, L., et al., *Design of ice-free nanostructured surfaces based on repulsion of impacting water droplets.* ACS nano, 2010. **4**(12): p. 7699-7707.

236. Quan, X., et al., *Enhanced dropwise condensation by oil infused nano-grass coatings on outer surface of a horizontal copper tube.* International Communications in Heat and Mass Transfer, 2018. **91**: p. 11-16.

237. Sieder, E.N. and G.E. Tate, *Heat transfer and pressure drop of liquids in tubes.* Industrial & Engineering Chemistry, 1936. **28**(12): p. 1429-1435.

238.	Rose, J.W., *Heat-transfer coefficients, Wilson plots and accuracy of thermal measurements.* Experimental Thermal and Fluid Science, 2004. **28**(2-3): p. 77-86.

239.	Bergman, T.L., et al., *Fundamentals of heat and mass transfer*. 2011: John Wiley & Sons.

240.	Kline, S.J., *Describing uncertainty in single sample experiments.* Mech. Engineering, 1953. **75**: p. 3-8.

241.	Enright, R., et al., *Condensation on superhydrophobic copper oxide nanostructures.* Journal of Heat Transfer, 2013. **135**(9): p. 091304.

242.	Miljkovic, N., R. Enright, and E.N. Wang, *Modeling and optimization of superhydrophobic condensation.* Journal of Heat Transfer, 2013. **135**(11): p. 111004.

243.	Xu, W., et al., *Directional movement of droplets in grooves: suspended or immersed?* Scientific reports, 2016. **6**: p. 18836.